UNIVERSITÀ DEGLI STUDI DI GENOVA

Scuola di Scienze Matematiche, Fisiche e Naturali
Dipartimento di Fisica

Ph.D Thesis
Physics and Nanoscience, XXXV cycle

Large area TMD-based van der Waals heterostructures featuring enhanced photoconversion in the flat optics regime

Candidate:
Matteo Gardella

Supervisors:
Prof. Francesco Buatier de Mongeot
Dr. Maria Caterina Giordano

“I call our world Flatland, not because we call it so, but to make its nature clearer to you, my happy readers, who are privileged to live in Space.”

Edwin A. Abbott, *Flatland: A Romance of Many Dimensions*

Contents

Introduction

One of the most urgent technological needs of this century concerns the research of innovative nanomaterials for applications in optoelectronics, nanophotonics and photovoltaics for renewable energy conversion. In fact, downscaling of the silicon-based devices (e.g. field-effect transistors) has come to an end due to intrinsic physical limitations such as size, inadequate carrier mobility, short channel effects, atomic-scale interactions, heat generation, and energy consumption at atomic scale thickness, requiring innovative materials to overcome such difficulties[1].

Graphene discovery in 2004 by Novoselov and Geim[2] arose a tremendous interest for the two-dimensional (2D) materials, in which the reduced dimensionality brings new properties with respect to their bulk counterparts. Despite the extraordinary properties exhibited by graphene, its gapless nature strongly limits the fabrication of graphene-based optoelectronic devices. For this reason, the interest of researchers shifted towards the class of 2D semiconductors. Among these materials, Transition Metal Dichalcogenides (TMDs) represent the most important family due to suitable bandgap energy values which match the Schockley-Queisser efficiency criterion for solar photoconversion, and to their extraordinary optical absorption coefficient[3].

Additionally, 2D materials can be vertically stacked to form the so-called van der Waals heterostructures that are endowed by pristine interface thanks to the relatively weak van der Waals interactions that keep the stack together[4]. This offers the opportunity to fabricate heterostructures of arbitrary 2D materials, independently by their crystal structure, with no limitations on the engineering of the optoelectronic and photonic properties of the new stacked metamaterial[5]. In particular, the possibility to realize van der Waals p-n junctions by coupling 2D-TMDs layers is very intriguing for photoconversion and photovoltaic applications.

So far, TMDs employment has been mostly limited to the fabrication of prototypical devices such as field-effect transistors and photodetectors, most of which were realized via mechanical exfoliation from single crystal of flakes with thickness ranging from one to few atomic layers. Despite their intriguing properties, these materials do not represent an industrially relevant alternative to traditional semiconductors, being the exfoliation a randomic process with very low yields and limited areas in the micrometer range. Consequently, one of the key frontiers of TMDs research is the large area growth of homogeneous ultra-thin layers with controlled thickness over macroscopic areas. To meet this requirement, several large area techniques have been studied to synthesize TMDs layers extending over cm^2 areas. However, in contrast with the exfoliation process, these techniques result in polycrystalline layers where the high concentration of grain boundaries degrades the macroscopic conduction.

The second crucial issue to be solved for ultra-thin TMD-based devices to be used in photoconductive and photodetection applications is the maximization of the optical absorption. Despite the excellent optical absorption coefficient, an ultra-thin TMD film indeed cannot absorb efficiently the incoming light due to the ultimately reduced thickness, which means a nanometric optical path. It is thus evident that new strategies for the optical absorption amplification in ultra-thin 2D semiconductors need to be developed to allow proper performances in TMD-based photodetection and photovoltaics applications. Because of the atomic thickness of the 2D layer, traditional solutions developed for the light harvesting amplification in conventional silicon-based photovoltaic devices, based on pyramidal microstructuring or on the addition of antireflective coatings, cannot be transferred to these materials.

Recently, the research group where I carried out my activity worked on large area ultra-thin MoS_2 films conformally grown on self-organized rippled substrate fabricated by ion beam sputtering[6–8]. Their results clearly showed a modification of the TMD optical and electronic properties grown on the nanostructured substrate with respect to a flat one. This observation was explained with the stress induced by the substrate morphology in the MoS_2 layer in correspondence to the high curvature regions given by the crests and valleys of the ripples, meaning that by control of the substrate morphology it is possible to engineer the material intrinsic properties[9].

Additionally, the nanostructures anisotropy adds a polarization-dependent optical response, offering a way to engineer the optical absorption of the 2D material in view of photoconversion applications. However, self-organized nanostructures suffer from a relevant size dispersion and long range disorder, whereas more interesting optical effects are expected for periodic nanogratings in which the subwavelength TMD layers reshaping provide them the functionality of flat optic diffractive elements[10].

Starting from here, I devoted the most of my research activity to face the two main challenges described above: developing a growth process for large area ultra-thin TMD films, and studying an efficient light harvesting strategy to maximize the optical absorption in few-layer semiconductor films. An overview of the state-of-the-art regarding 2D materials and nanophotonics approaches for light harvesting in ultra-thin films is given in Chapter 1, while the growth synthesis techniques are postponed in Chapter 2.

At the beginning of my PhD, MoS_2 films were grown by external collaborators of my group, thus limiting the activities. In the first phase of my research activity, I developed a novel large area growth process based on the physical deposition of solid precursor films and sulfurization, as I will describe in Chapter 2. This novel technique enabled not only the in-house growth of ultra-thin MoS_2 films for the first time, but also allowed to extend the process to ultra-thin WS_2 layers.

Having now the capability to control the deposition of two different TMDs layers, I moved to the growth of large area van der Waals heterostructures. Due to the type-II heterojunction formed by the band structure coupling of MoS_2 and WS_2, such heterostructures are expected to have a high potential in photoconversion applications. In Chapter 3 I will show the nanofabrication of planar MoS_2/WS_2 heterostacks, and their application in photocatalytic experiments and in a prototype of photonic device, featuring first evidence of photovoltage and photocurrent under illumination. This latter application also required me to develop large area transparent electrodes, so that I will dedicate a part of the chapter to indium tin oxide thin films and large area graphene.

In the second phase of my research activity, I focused on light harvesting in ultra-thin TMDs layers. Thanks to the conformality achieved by the physical deposition process, I explored a nanophotonic approach based on the optical anomalies arising from periodic modulation of the TMD layer at the subwavelength scale, obtained by conformal growth of the TMD layers onto nanostructured substrates. To this end, periodic nanogratings have been used as a template for the growth of ultra-thin MoS_2 layers. Differently from the self-organized nanostructures mentioned before, the periodicity induces diffractive effects that are exploited to steer the light parallel to the active 2D material enhancing the optical absorption, as demonstrated in Chapter 4 both directly by absorption measurements and indirectly by a photo-to-chemical energy conversion experiment where we detected enhanced photocatalytic performances.

In the final part of my project, I started preliminary studies on the elastic scattering properties of subwavelength periodical lattices based on nanostructured tilted TMD layers. By defocused ion beam sputtering, I was able to reshape the morphology of the initial nanograting templates to further engineer the TMD optical response. In particular, by off-normal incidence sputtering it is possible to tailor a specific slope of the tilted nanofacets, on top of which I deposited laterally disconnected MoS_2 nanostripes by grazing angle physical deposition. By developing a custom-made scatterometer, optical characterization of ultra-thin MoS_2 nanostripes and thicker MoS_2 films was performed, giving interesting preliminary results on the directional light scattering properties of these reshaped layers, as reported in Chapter 5. Finally, I adopted a similar deposition approach for the nanofabrication of large area heterostructures nanoarrays based on few-layer WS_2 nanostripes coated by a conformal MoS_2 layer, demonstrating further engineering of the optical response of few-layer TMD films with impact in photoconversion.

List of publications related to the thesis

- M. Bhatnagar*, M. Gardella*, M.C. Giordano, D. Chowdhury, F. Buatier de Mongeot *et al.*, “Broadband and Tunable Light Harvesting in Nanorippled MoS2 Ultrathin Films”, *ACS Appl. Mater. Interfaces* 2021, 13, 13508-13516 (*: equal contribution)
- M.C. Giordano, G. Zambito, M. Gardella, F. Buatier de Mongeot, “Deterministic Thermal Sculpting of Large-Scale 2D Semiconductor Nanocircuits”, *Adv. Mater. Interfaces* 2022, 2201408
- G. Ferrando, M. Gardella, G. Zambito, M. Barelli, D. Chowdhury, M.C. Giordano, F. Buatier de Mongeot, “Flat optics hybrid MoS2/polymer films for photochemical conversion”, *Nanoscale*, 2023, 15, 1953
- M. Gardella *et al.*, “Maskless synthesis of van der Waals heterostructure arrays engineered for light harvesting on large area templates”, *npj 2D Materials and Applications*, under submission
- M. Gardella *et al.*, “Large area van der Waals heterostructures for self-powered photonic devices”, *Adv. Funct. Mater.*, under submission
- M. Gardella *et al.*, “Resonant light manipulation and steering with large area 2D-TMD nanoresonators arrays”, manuscript in preparation

Chapter 1 – 2D materials, van der Waals heterostructures and nanophotonics approaching to light harvesting

Bulk semiconductor photonics represents one of the most widespread technologies for photodetection and energy conversion thanks to the high efficiency of conventional semiconductor materials. However, new frontiers and challenges have been recently opened in material science, aiming towards development of functional nanomaterials that could act as flexible building blocks for the Internet of Things and wearable electronics[11–13]. Towards the ambitious goal of a new generation of smart and multi-functional devices and nanosensors, a crucial role is played by the emerging class of two-dimensional (2D) materials, which exhibit exceptional optoelectronic response in devices confined to atomically thin dimensions[14–17].

Due to the weak out-of-plane interactions between the layers, dissimilar 2D materials layers can also be stacked to form the so-called van der Waals heterostructures characterized by sharp atomic interfaces[5] and by tailored optoelectronic properties determined by a proper choice of the stacked 2D-TMD pairs[18].

Among the main challenges related to development of real-world devices based on 2D semiconductors one can identify the increase of optical absorption in the atomically thin layers[19]. To this end, nanophotonics innovative approaches are required.

In paragraph 1.1 I will introduce the broad family of 2D materials. The main core of the paragraph will be dedicated to the Transition Metal Dichalcogenides family, which is at the basis of my activity research. The fundamental physical properties and application fields will be presented.

Van der Waals heterostructures by combination of different 2D materials and the possibilities opened by the intriguing physical properties that arise from their coupling will be discussed in paragraph 1.2.

Finally, in paragraph 1.3 I will present nanophotonics approaches applied to 2D materials with the aim of increasing light-matter interactions in atomically thin layers, since efficient light harvesting strategies are crucial towards a real-world application of 2D semiconductors.

1.1 2D materials

Two-dimensional materials and atomic van der Waals heterostructures have recently collected a strong scientific and technological interest over a broad community due to their exceptional properties, offering new solutions for device miniaturization down to the atomic scale[4,20–25].

Graphene is the first two-dimensional atomic crystal identified in 2004 by K.S. Novoselov and A.K. Geim[2]. Since then, graphene has been deeply studied in its fundamental properties, shifting the focus to the possible applications[26]. The scientific interest in graphene is owed to the peculiar characteristics it possesses: extremely high electron mobility, high current densities, high thermal conductivity, excellent mechanical properties, chemical functionalization and impermeability to any gas.

Due to its band structure graphene is a gapless semimetal[27], meaning that it cannot be used as active material in optics and optoelectronics despite its unparalleled electric properties. However, since graphene discovery the research on 2D materials has continuously expanded so that the 2D portfolio (**Figure 1.1a**) now includes materials with completely different crystalline structures and electronic properties, ranging from the gapless semimetal graphene to small bandgap semiconductors such as black phosphorus, visible bandgap semiconductors as molybdenum disulfide and insulating hexagonal boron nitride (**Figure 1.1b**).

Transition Metal Dichalcogenides (TMDs) are a family of two-dimensional layered semiconductors with general formula MX_2, where M is a transition metal and X is an element belonging to the chalcogens group. 2D-TMDs have gained broad attention due to their peculiar optoelectronic response within a broadband spectrum, and to their tunable bandgap that enables promising optoelectronic and photonic functionalities[7,28–34].

Due to its abundance in nature in form of molybdenite mineral, the most studied TMD is molybdenum disulfide (MoS_2), a material which was already industrially relevant by decades in its bulk form as a solid lubricant. In the following, I will mainly focus on MoS_2 to describe the general TMD properties. However, during my thesis I will also explore the growth of WS_2 – which bears many properties in common to MoS_2 – as a parent film for fabricating van der Waals heterostructures.

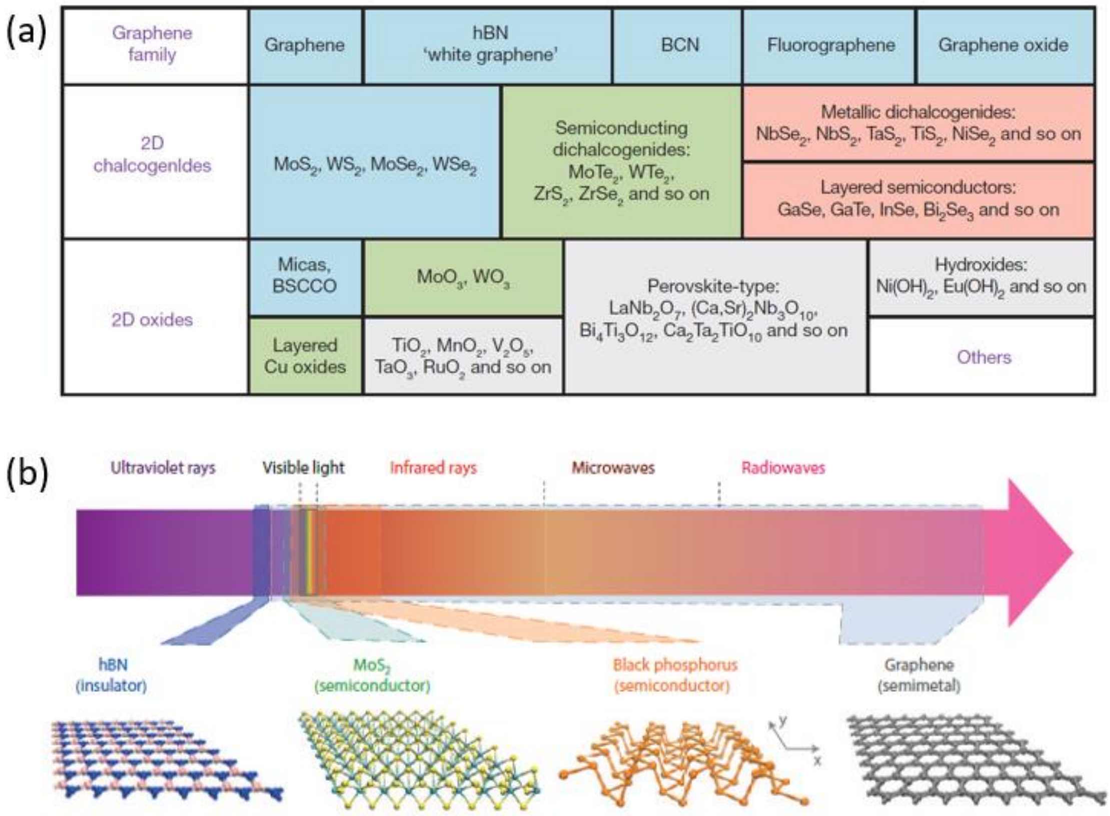

Figure 1.1 (a) Portfolio of available 2D materials, from ref [4]. (b) Collocation of different 2D materials bandgap in the electromagnetic spectrum, adapted from ref [35].

As shown by the three-dimensional representation in **Figure 1.2a**, a single TMD monolayer is formed by two planes of X atoms separated by a central plane of M atoms. The atoms inside the layer are bounded by strong covalent bonds, while the vertically stacked monolayers are bounded by weak van der Waals interactions. The latter are indeed responsible of the TMDs lubricant properties, related to the layers shear under mechanical stress[36].

The TMDs family is characterized by polymorphism with different possible crystallographic phases, as illustrated in **Figure 1.2b**. In the case of MoS_2, the unit cell contains two molybdenum atoms and four sulfur atoms, can be described with the lattice parameters *a* (in-plane) and *c* (out-of-plane). In its bulk form the crystalline structure is obtained by stacking layers along the *c* direction, with a monolayer having a total thickness of 0.65 nm. According to the relative disposition between adjacent layers, different phases are possible. The most common structure found in nature for MoS_2 is the hexagonal 2H-phase, which is also the most relevant for optics and optoelectronics applications since it is the only semiconducting phase[37]. Other possible MoS_2 polytypes are the rhombohedral 3R and the trigonal 1T. 2H and 3R are thermodynamically stable, with the former being more common, while the 1T showing metallic behavior is metastable[38].

TMDs are characterized by a band structure – and hence their optical and electronic properties – that is strongly correlated to the number of layers. In fact, bulk TMDs have an indirect bandgap but in the few-layer regime an increase of the bandgap energy value is observed as the number of layers decreases, with a transition from indirect to direct bandgap in the case of a monolayer. In **Figure 1.2c** the band structure for bulk, four-layer, bilayer and monolayer MoS_2 (from left to right, respectively) is reported. In view of optoelectronics, nanophotonics and photovoltaics, this strong dependence on the thickness represents an intriguing opportunity to tailor the TMD optoelectronic response. In particular, for a direct bandgap monolayer TMD a remarkable increase in the optical absorption coefficient and photoluminescence yield is expected.

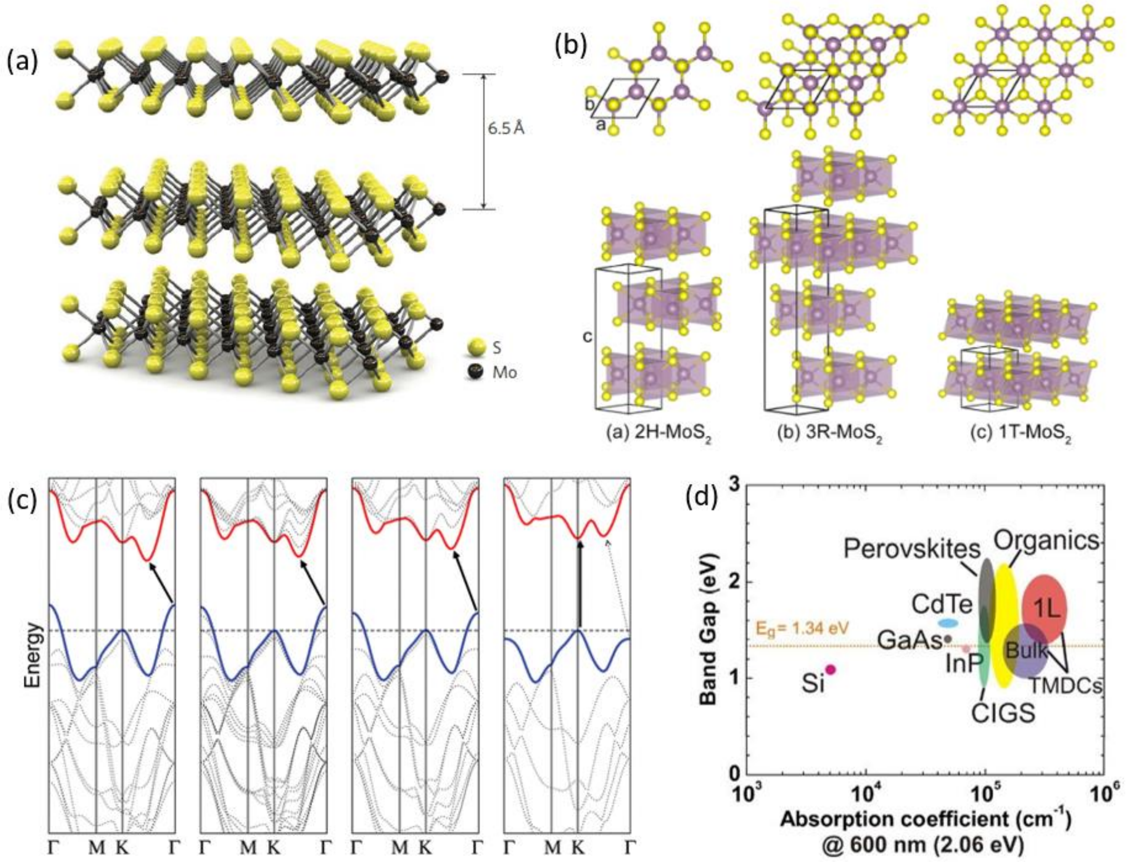

Figure 1.2 (a) Three-dimensional representation of MoS_2 crystalline structure, from ref [39]. (b) MoS_2 polytypes, adapted from ref [40]. (c) Band structure for bulk, four-layer, bilayer and monolayer MoS_2 (from left to right, respectively), from ref [28]. (d) Comparison between TMDs and other semiconductors energy bandgap values and absorption coefficients, from ref [3].

TMDs semiconductors are technologically relevant because their bandgap energy values are close to the optimal value of 1.34 eV imposed by the Shockley-Queisser limit, for which the highest efficiency is achieved in single junction solar cells[41]. For example, in the case of MoS_2 the energy bandgap varies from 1.2 eV in the bulk to 1.9 eV in the monolayer, and a similar trend is observed for all the TMDs with slightly different values. Additionally, the superior optical absorption coefficients in the Visible spectrum, enhanced of about two order of magnitude with respect to conventional bulk semiconductors such as silicon, selects the 2D-TMDs layers as optimal candidates for photodetection and photoconversion applications[3,42,43]. **Figure 1.2d** offers a straightforward comparison between TMDs and other semiconductors, highlighting the potential of these 2D semiconductors.

In **Figure 1.3a** the band structure of a MoS_2 monolayer is used to indicate the most important optical transitions, which determine its optical absorption. A and B arrows indicate the direct bandgap transitions arising from spin-orbit splitting, while C and D transitions arise from regions in which valence and conduction bands are parallel (band nesting region).

The TMDs layered structure results in a strong optical anisotropy as shown in **Figure 1.3b**, where the ordinary and extraordinary permittivities of various materials used in nanophotonics are reported[44]. In the plane of the layers, TMDs ordinary refractive index is higher than silicon, while in the out-of-plane direction the extraordinary refractive index is lower.

Figures 1.3c and **1.3d** show the imaginary and real part of the in-plane and out-of-plane components of MoS_2 permittivity tensor. The in-plane permittivity is dominated by the four excitonic resonances described in **Figure 1.3a**, while the out-of-plane permittivity is weaker and unstructured.

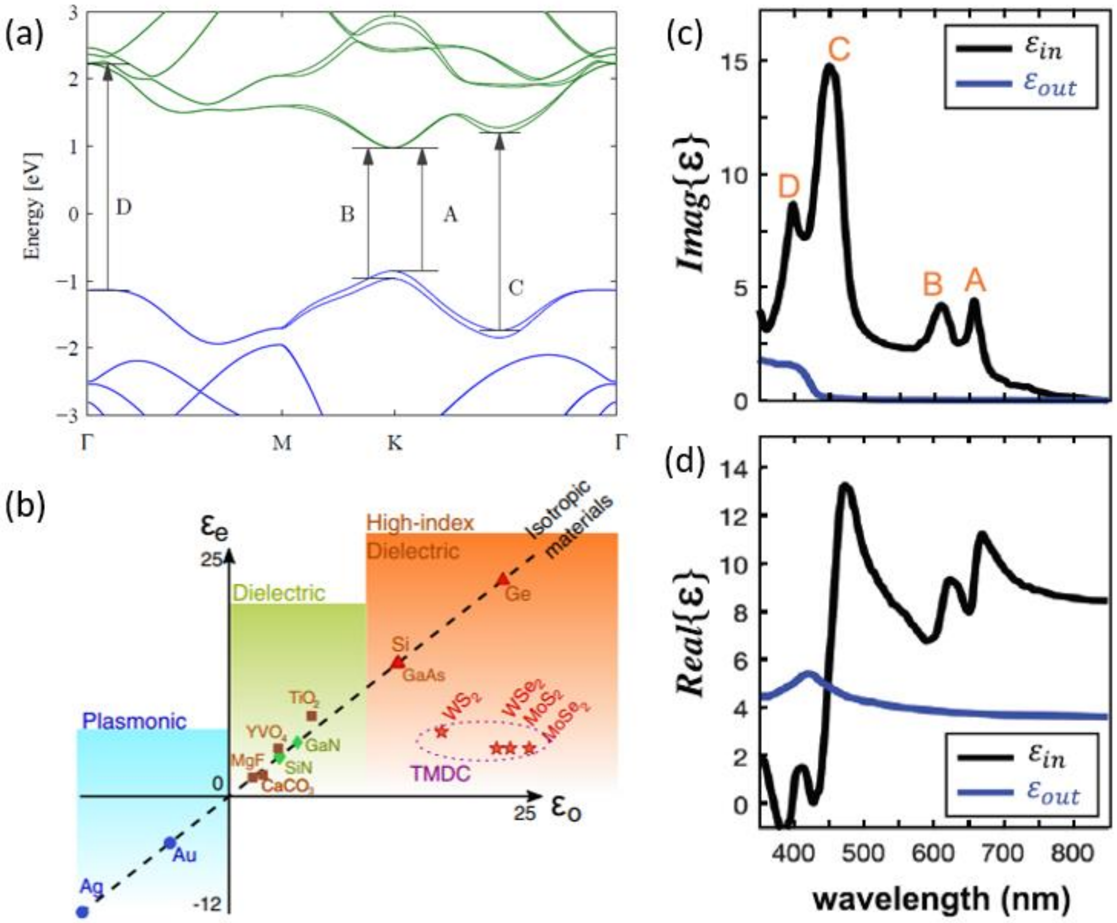

Figure 1.3 (a) MoS_2 relevant optical transitions, from ref [45]. (b) Ordinary and extraordinary permittivities for various materials, from ref [44]. (c,d) MoS_2 imaginary and real permittivity tensor, from ref [8].

Moving to the vibrational properties, **Figure 1.4a** shows the six phononic modes predicted from crystallography for the TMD hexagonal structure[46]. Four of them (E_{1g}, E^1_{2g}, E^2_{2g} e A_{1g}) are Raman active, while the remaining two are IR active (E^1_{1u} e A^1_{2u}). Raman spectroscopy indeed is a powerful characterization technique for the few-layer regime because of the strong correlation between the layers number and the position of the main peaks attributed to the in-plane E^1_{2g} and out-of-plane A_{1g} vibrational modes. **Figure 1.4b** shows the evolution of the Raman spectra as MoS_2 thickness increases, with the separation between the two peaks increasing and reaching a saturation value of about 25-26 cm^{-1} after six layers. In **Figure 1.4c** the spectral position for the two vibrational modes and their relative separation are reported as a function of the layers number.

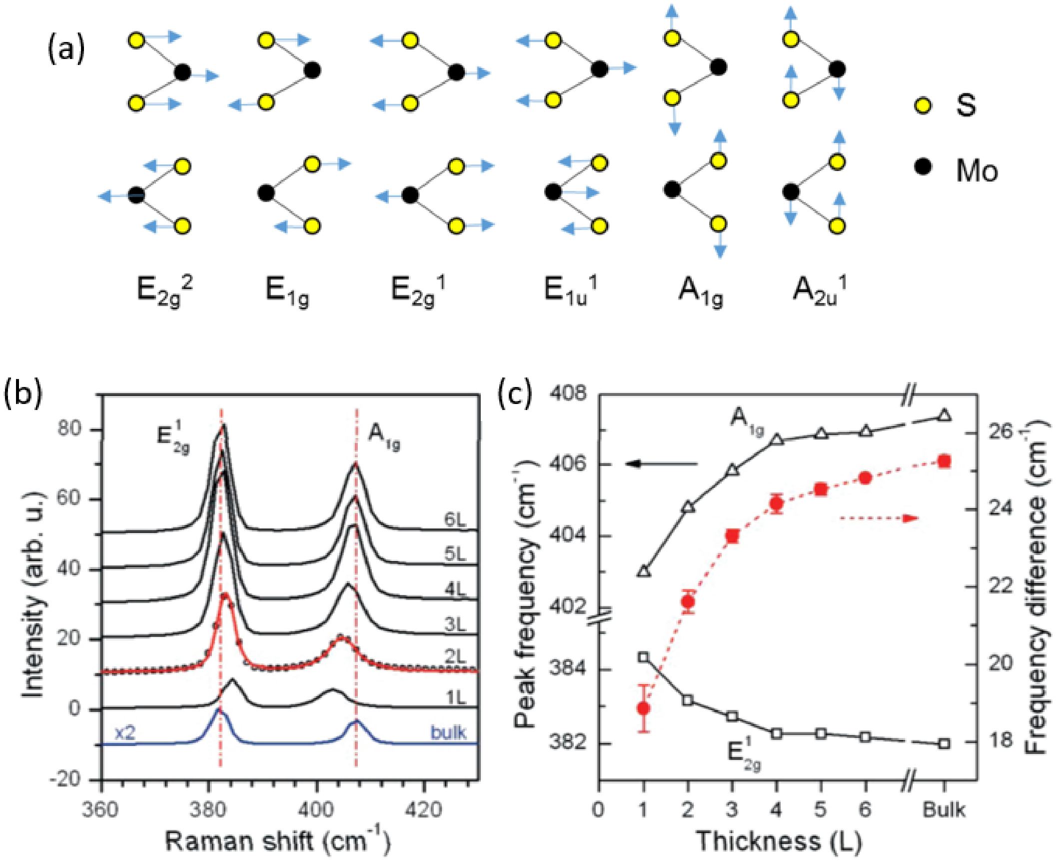

Figure 1.4 (a) MoS_2 phononic modes, from ref [46]. (b) Raman spectra for MoS_2 films with different thickness, from ref [47]. (c) Spectral position and separation value between the MoS_2 vibrational modes, from ref [47].

TMDs electrical and optical properties make them suitable materials for a variety of opto-electronic devices, such as photodetectors and solar cells, phototransistors and LEDs. A scheme with some TMDs applications and reference performance values is reported in **Figure 1.5**.

Photonic device designs combining 2D-TMDs and bulk semiconductors have been proposed for increasing the performances of new generation solar cells. Lin et al[48] demonstrated an improved power conversion efficiency up to 9% in MoS_2/GaAs heterojunction by suppression of the static charge transfer via insertion of an insulating h-BN layer.

Wu et al[49] demonstrated piezoelectricity in monolayer MoS_2 device, with an output power density of 2 mW m^{-2} and a 5% mechanical-to-electrical conversion. The piezoelectricity combining to the semiconducting properties in 2D-TMDs paves the way to applications in powering nanodevices, adaptive bioprobes and tunable/stretchable electronics and optoelectronics.

The ongoing miniaturization of electronic devices requires high performance energy storage devices on a small scale. Due to their large specific surface area and sheet-like structure, TMDs has attracted considerable attention for promising supercapacitor electrode applications. Choudhary et al[50] fabricated MoS_2 supercapacitor electrodes by magnetron sputtering deposition with high areal capacity (330 F cm^{-3}) and cycle stability. Detection of toxic gases and pollutants is a critical issue to industry, agriculture and public health. Therefore, the development of high sensitivity, low-cost and portable sensors with low power consumption is a challenge of technological relevance and TMDs are promising materials in this regard. For instance, Li et al[51] fabricated n-type MoS_2 field effect transistors (FETs) of different thickness demonstrating high NO sensitivity with a stable response over cycles.

TMD-based FETs can offer high sensitivity also to biomolecules, leading to applications in next-generation low-cost biosensors featuring label-free detection. In this field, Sarkar et al[52] demonstrated high sensitivity to pH changes and specific protein sensing in MoS_2 FET biosensors.

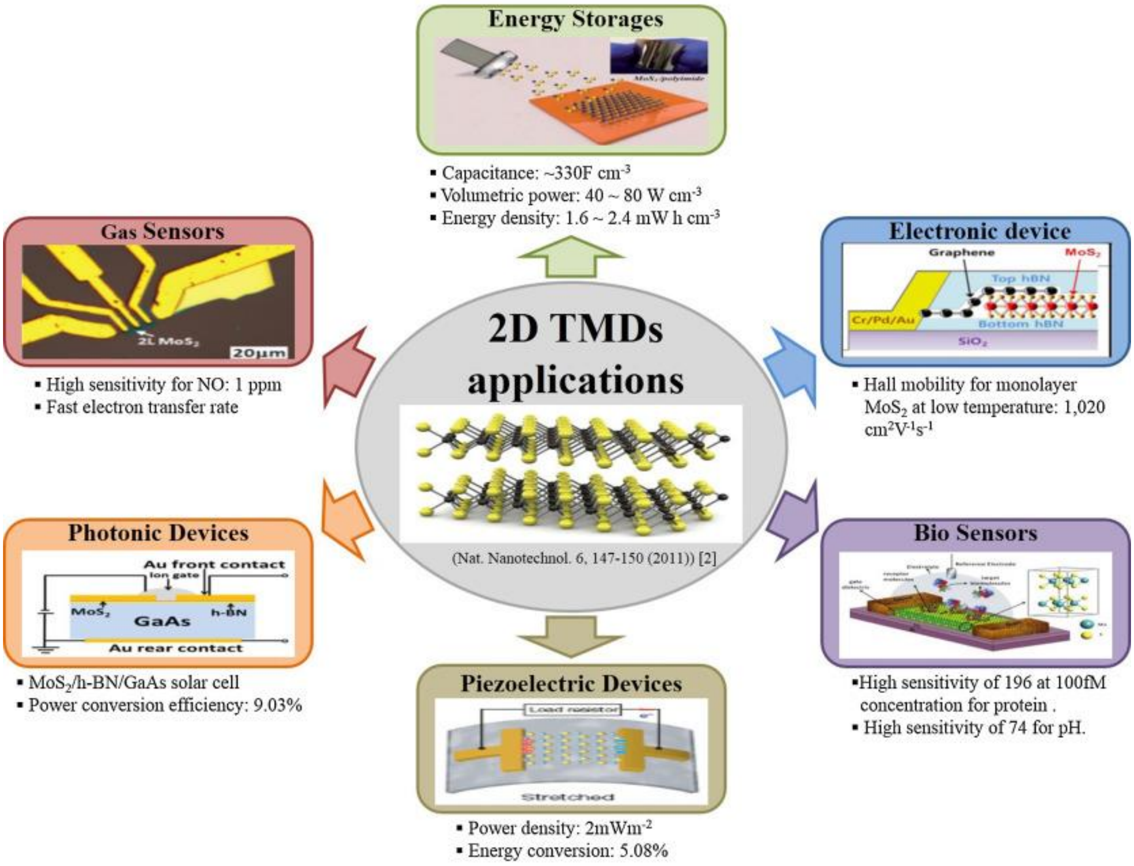

Figure 1.5 Applications of 2D-TMDs, from ref [29].

As briefly described above, the intrinsic properties of TMDs are intriguing for a plethora of applications ranging from the fields of electronics to photonics and enegy conversion and photocatalysis. However, the main challenge in real-world applications of TMD-based devices consists of the development of industrially scalable growth techniques, since fundamental studies and lab-scale devices are mostly based on exfoliated flakes or CVD grown crystals with lateral size usually in the range of tens of µm. The description of the TMDs fabrication techniques is postponed in Chapter 2, where I will refer to the state-of-the-art processes to better illustrate the large area growth process I developed during my PhD research activity.

1.2 Van der Waals heterostructures

The research on innovative semiconducting materials is fueled by the need of a sustainable energy future based on renewable energy, including photovoltaics and solar thermal generation. Silicon solar cells are the most established technology in the field of solar photoconversion, with state-of-the-art devices approaching the ideal Shockley-Queisser limit for a single junction solar cell[41]. To further increase the efficiency, silicon solar cells started to be coupled with other suitable semiconductors, from conventional III-V semiconductors to emerging polycrystalline thin-films as perovskite, forming multi-junction devices[53]. However, when designing a multijunction solar cell one should comply with specific criteria regarding the materials bandgap energy for optimized efficiency and lattice mismatch for high quality crystalline growth. Materials should be chosen with suitable energy bandgaps so that each junction generates approximately the same photocurrent, since the cell will be limited by the current through the junction with the smallest photocurrent in the typical series-connected configuration[54]. To maximize the solar cell efficiency, each junction should have a thickness high enough to virtually absorb all the incident above-bandgap light. However, there is a critical thickness above which epitaxially grown semiconductor layers start to develop dislocations due to strain induced by the lattice mismatch with the substrate. Along with impurities and other defects, dislocations are responsible for bulk recombination losses, contributing to deteriorate the solar cell performance in addition to recombination events that can occur at the interfaces as a consequence of lattice mismatch and surface defects[55].

In contrast with conventional bulk semiconductors heterostructures, 2D materials are characterized by atomically sharp and clean interfaces, with strong covalent and fully passivated in-plane bonds and weak out-of-plane van der Waals interactions. Therefore, they can be combined in what are called van der Waals (vdW) heterostructures by simply stacking them in sequence, as visually represented by the sketch in **Figure 1.6a**, to create multilayer devices with tailored electronic properties[56–62]. In **Figures 1.6b** and **1.6c** two examples of vertically stacked TMD-based heterostructures are reported, fabricated by alignment of mechanically exfoliated TMD flakes and CVD grown crystals, respectively. No epitaxy limitations apply to these systems, where individual layers can have different crystal symmetry and lattice parameters[5]. However, controlling the rotation angle between the crystalline orientation of the two stacked layers offers an additional opportunity to tailor the final properties of the heterostructure, entering in the field of twistronics[63].

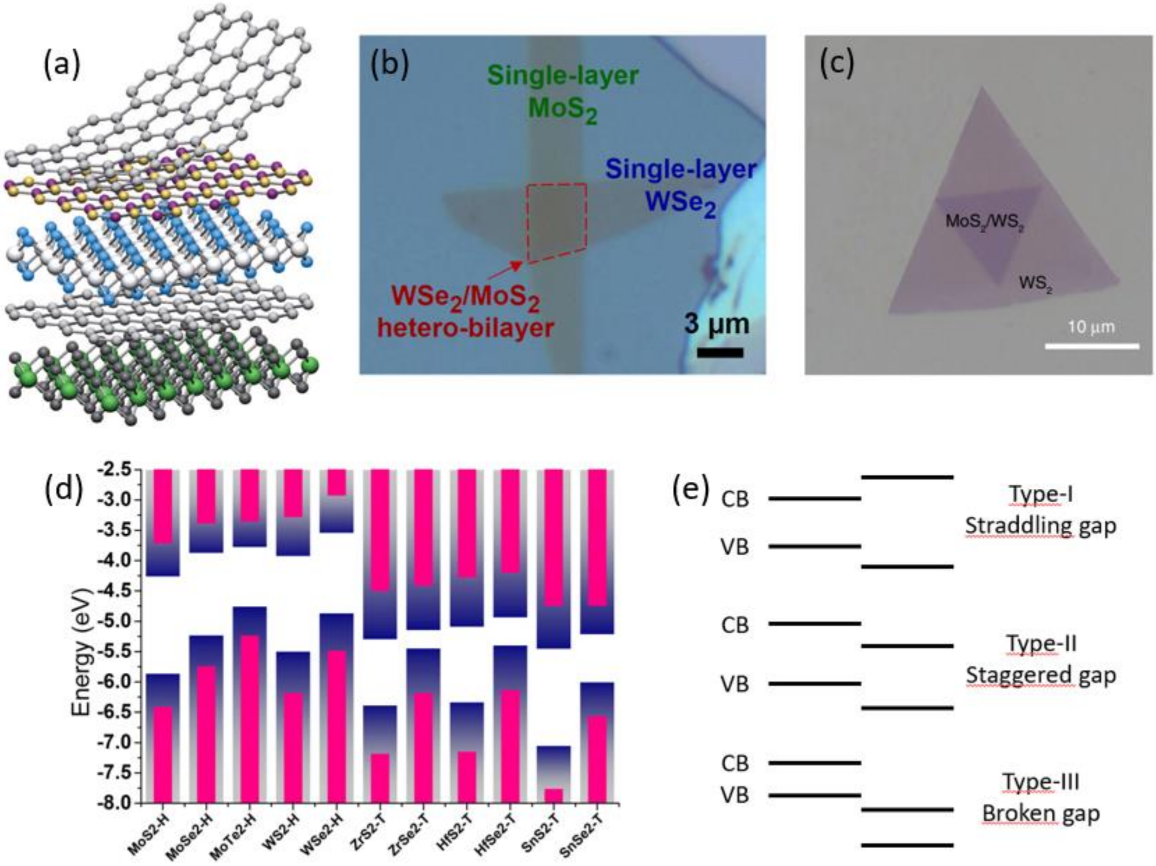

Figure 1.6 (a) Three-dimensional representation of 2D materials vertical stacking, from ref [4]. (b) Example of vertical heterojunction from mechanically exfoliated TMD flakes, from ref [64]. (c) Example of vertical heterojunction from CVD grown TMD crystals, from ref [65]. (d) Band edges for semiconducting TMDs with respect to vacuum, from ref [56]. (e) Band structure coupling in the possible heterojunction types.

Stacking two materials with different electronic band structures (TMDs band structures are reported in **Figure 1.6d**) gives rise to three possible band coupling, sketched in **Figure 1.6e**. In type-I heterojunctions a straddling gap is formed with enhanced luminescence properties since the maximum valence band and the minimum conduction band belonging to the same layer[66]. Type-II heterojunctions, in which a staggered gap is formed, are technologically relevant because the maximum valence band and the minimum conduction band belong to different layers, thus separating photogenerated electron-hole couples and increasing the carriers lifetime[67,68]. Consequently, type-II heterojunctions exploited both for energy conversion, since recombination rate is reduced, and for photocatalytic applications, since the separated charges on the surface can boost specific reactions[69–71]. Finally, in type-III heterojunctions the minimum conduction band is lower than the maximum valence band, forming a broken gap that can be exploited for instance in tunnel field-effect transistors[72].

Differently to bulk semiconductors heterostructures, 2D crystals can be also combined in lateral heterostructures. Though this configuration cannot be considered a van der Waals stacking, the physical phenomena arising from the coupling of different electronic structures are the same. Lateral TMDs heterostructures are typically synthesized recurring to Chemical Vapor Deposition processes based on lateral heteroepitaxial growth, with the second TMD growing on the edge of the first pre-existing crystal[73,74]. **Figure 1.7a** shows an example of CVD-grown $MoSe_2$/WSe_2 lateral heterostructure in which multiple junctions were achieved by repeating the process. The image on the left highlights the optical contrast between the different TMDs layers, while the photoluminescence map on the right demonstrates the high crystalline quality of each layer[74].

As evidenced by the STEM image reported in **Figure 1.7b** for a bilayer $MoSe_2$/WSe_2 lateral heterojunction (as represented in the above sketch), edge-epitaxy growth of TMD layers results in atomically sharp interfaces[75].

TMDs lateral heterojunction are crucial elements for the fabrication of two-dimensional p-n rectifying diodes, light-emitting diodes, photovoltaic devices, and bipolar junction transistors. **Figure 1.7c** reports the optical image of a monolayer WSe_2/$MoSe_2$ lateral heterostructure and its electrical transport curves. Since the coupling of these two materials intrinsically forms a p-n junction, metallic contacts were deposited to investigate its electrical properties. As shown by the I-V characteristics, the heterojunction indeed has a rectification behavior[76].

An alternative route to edge-epitaxy for the fabrication of lateral heterostructures – more promising in terms of scalability as it can be simultaneously performed on large areas – is selective area chemical doping, as already demonstrated by Chamlagain et al in 1 cm^2 MoS_2 and $MoSe_2$ films[77]. Another demonstration of scalable lateral heterostructures fabrication was given by Mahjouri-Samani et al by using lithographic techniques to selectively sulfurize a patterned monolayer $MoSe_2$ crystal in order to produce predefined arrays of lateral $MoSe_2$/MoS_2 heterojunctions[78].

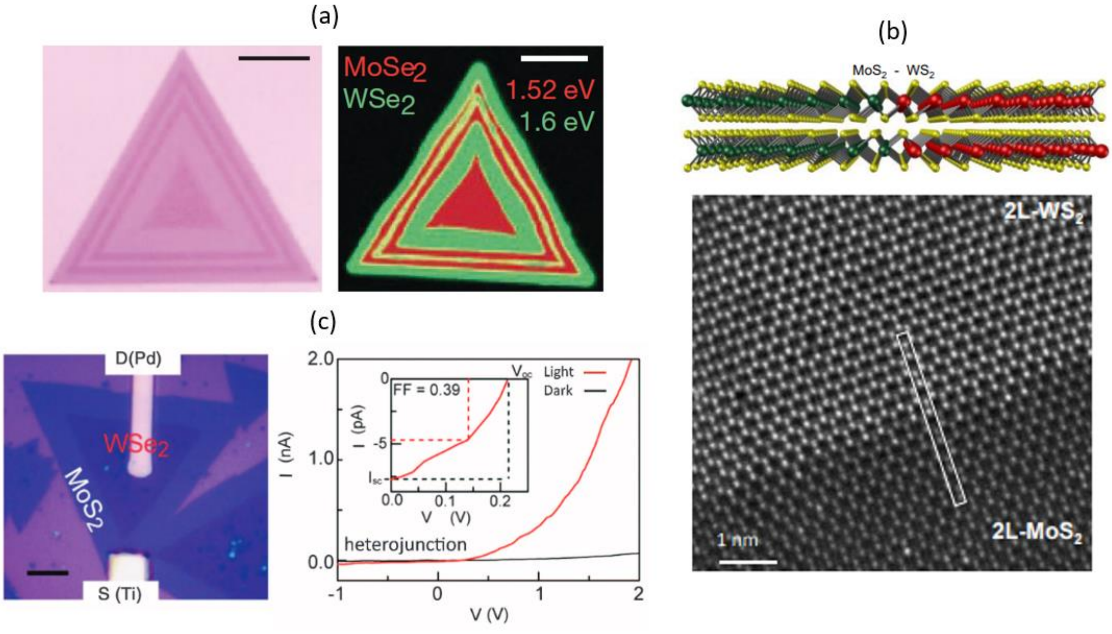

Figure 1.7 (a) Optical image of a multi-junction $MoSe_2$/WSe_2 lateral heterostructure and photoluminescence intensity map, adapted from ref [74]. (b) STEM image of a bilayer MoS_2/WS_2 lateral heterostructure, adapted from ref [75]. (c) Optical image of a WSe_2/$MoSe_2$ p-n junction device and its electrical transport curves in dark and under illumination, adapted from ref [76].

Thanks to their mechanical and opto-electronic properties and the possibility to functionalize them, 2D materials and their heterostructures are promising for next-generation electronics and optoelectronics, including smart application as flexible and self-powered devices for the Internet of Things besides more obvious applications in electronics and energy conversion[1]. In particular, TMDs van der Waals heterostructures represent optimal building blocks for the fabrication of self-powered photodetectors, by exploiting the charge separation of the photogenerated carriers at the 2D interface without any external bias[62,79–81].

Whatever materials are used, in solar conversion devices the ultimate aim is to design highly efficient, low cost and large-scale compatible cells and photocatalysts. To achieve this goal, the main step is the efficient coupling of light into active layer. If an efficient design is already needed for bulk semiconductors with active layer thickness higher than light penetration depth, even more crucial the problem is for ultrathin semiconductor such as TMDs and their van der Waals heterostructures where light must be absorbed in a subwavelength thickness[19].

1.3 Nanophotonics approaches for light harvesting in 2D semiconductor layers

Thanks to their peculiar optoelectronic response, 2D semiconductor layers represent a promising platform in view of ultra-thin photoconversion devices operating in different spectral ranges from the Visible to the Far Infrared. In this context Transition Metal Dichalcogenide semiconductors are particularly interesting due to their tunable bandgap in the Visible (e.g. MoS_2, WS_2) or Near-Infrared (e.g. $MoTe_2$) spectral range, combined with the characteristic transition from an indirect bandgap in bulk to direct bandgap in monolayer form, resulting in a high photoluminescence quantum yield[82], in turn corresponding to high radiative efficiency. These properties make the TMDs attractive as candidates not only for photonics and quantum applications but also for photovoltaic and energy storage applications[3].

In this perspective, it is particularly relevant the high photon absorption coefficient of TMD semiconductors; for instance, MoS_2 is characterized by an absorption coefficient that is enhanced up to about two orders of magnitude with respect to conventional bulk semiconductors (e.g. Si, GaAs). However, the inherently low overall optical absorption in the atomic layers (e.g. a free-standing TMD monolayer absorbs about 10% in the Visible[3]) represents a crucial limit that currently hinders competitive applications. Even considering thicker TMD layers with bulk-like response, the maximum above-gap absorption is limited to 40-60% (depending on the substrate) due to the high refractive index that implies the loss of a large fraction of the light due to reflection[83].

One possible solution known since long to drastically reduce reflectance from an interface is offered by nature, taking inspiration from the nanostructured corneas of night-flying moths (**Figures 1.8a** and **1.8b**). The so called biomimetic moth eye inspired designs are generally made of tapered geometries with subwavelength periodicity, in which the nanostructures act as an effective medium that gradually match the air impedance into the underlying substrate by progressive refractive index gradation[84]. **Figure 1.8c** shows an example of refractive index variation under different geometries for a UV-curable resin coating[85]. In the case of an unstructured coating layer (i), light would experience two sharp interfaces across three different media (air with refractive index n_{air}, resin with refractive index n_{UV} and substrate with refractive index n_s). For a columnar subwavelength structures array (ii), the nanostructured thickness adds an effective medium layer with refractive index n_1 controlled by the fill factor of the layer. A conical structures array with triangular profile (iii) instead induces a linear variation of the refractive index from n_{air} to n_{UV}, while a moth eye structures array with parabolic profile (iv) induces a gradual variation that drastically reduce reflection at the interfaces.

This biomimetic approach can be integrated to semiconductor technology to minimize the reflection losses, e.g. in solar cell to improve their efficiency[19] or in light-emitting diodes to enhance the emission[86].

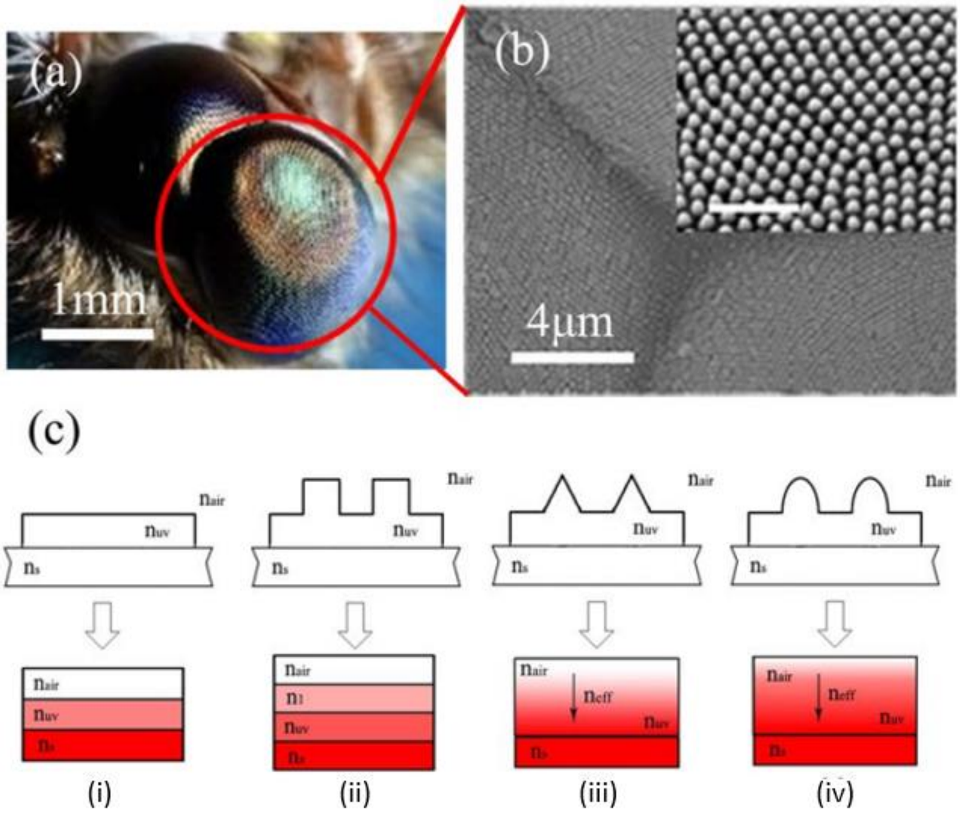

Figure 1.8 (a) Photograph of a moth eye. (b) Magnified SEM image of a moth eye showing subwavelength nanostructures array. (c) Refractive index variation under different interface geometries. Figure from ref [85].

In bulk semiconductors as silicon, another possible route to reduce reflection losses is based on antireflection coatings made of thin layers of dielectric materials with thickness satisfying the destructive interference condition, resulting in zero net reflected energy[87]. Combined with antireflection coatings, the surface can be additionally textured so that reflected light can bounce back on the semiconductor instead of getting lost. Due to the crystalline nature of silicon, a typical texturing process is based on the chemical anisotropic etching resulting in pyramidally shaped microstructures[88].

Due to their atomic thickness, it is not possible to adopt for the 2D materials the same light harvesting solutions already implemented for conventional semiconductors as bulk silicon. In view of the fabrication of photo-detection or photo-conversion devices, it is thus necessary to develop novel photon harvesting strategies[3].

Possible light trapping configurations based on plasmonic nanoparticles, shells or resonators[89,90] or even more complex architectures based on lossless dielectric optical cavities[91] have already been reported. However, for large area photovoltaic devices the desired solution should involve little or no micro/nanofabrication at all to minimize the costs while improving the performance. To this end, an interesting opportunity is given by thin film interference, which represents a lithography-free fabrication approach. Two possible configurations are reported in **Figures 1.9a** and **1.9b**, both using a highly reflective metal mirror as part of an open cavity in which light is resonantly coupled to the 2D material: in the first case the absorbing layer is spaced $\lambda/4$ away from the metal to induce destructive interferences at the interface enhancing the absorption[92], while in the second case the 2D material is directly in contact with the metal used as back reflector to increase the absorption by multipass interactions[93].

Figures 1.9c and **1.9d** represent more sophisticated designs in which light trapping is further enhanced by the use of nanostructured resonators coupled to thin film absorbers[94,95]. In the case of high refractive index TMDs, trapping nearly 100% of the incident light may be achieved for few nm thick active layers.

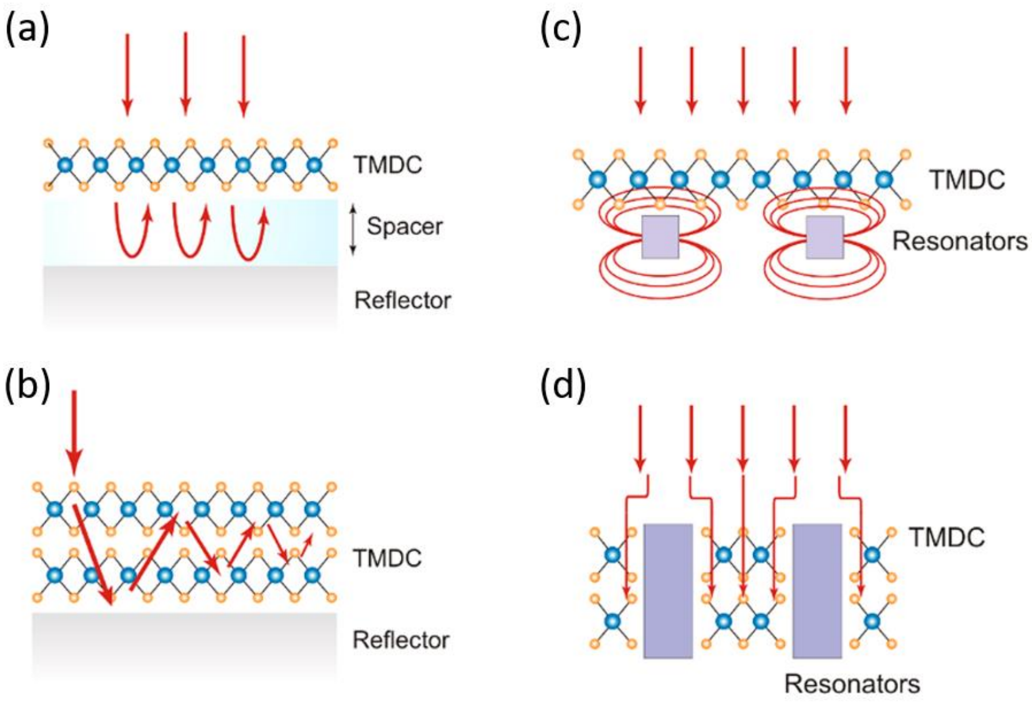

Figure 1.9 Light trapping configurations for optical absorption enhancement in 2D materials, adapted from ref [3].

It is important to note that besides the high optical absorption, high refractive index 2D materials also feature strong elastic light scattering. These interactions can be in fact exploited for manipulating the flow of the light using atomically thin optical elements. Contrary to conventional optical components, in which light wavefront is manipulated over distances larger than the wavelength, the use of high refractive index 2D materials or nanostructured metasurfaces can produce abrupt changes of light phase, amplitude and/or polarization on a subwavelength scale. This optical regime is referred to as flat optics[96]. Recently, a demonstration of flat optics based solutions was given by fabrication of optical and diffractive elements based on 2D-TMDs[10,97].

The high refractive index in TMDs is responsible for a giant optical path length (OPL) even in few nm thick layers, as a consequence of strong multiple reflections at the interfaces. In **Figure 1.10a** the simulated OPL for different materials in the sub-nm regime is reported, showing a strong dependence on the refractive index and a OPL value for MoS_2 that is significantly higher than the other materials.

The TMDs giant OPL enables phase-front engineering in atomically thin lenses, as the one fabricated by Yang et al[10]. In **Figure 1.10b** the intensity distribution pattern of a MoS_2 microlens measured by Scanning Optical Microscopy is reported. The inset schematically shows the lens bowl-shaped structure, which was achieved by focused ion beam milling of a 9-layer thick MoS_2 flake.

An even thinner and tunable lens in the ultimate limit of a WS_2 monolayer was demonstrated by van de Groep et al[97]. In their work, they patterned a CVD-grown WS_2 monolayer in the form of concentric rings so to obtain constructive interference of the diffracted light from the rings into a sharp focus. A scheme of the lens is reported in **Figure 1.10c**.

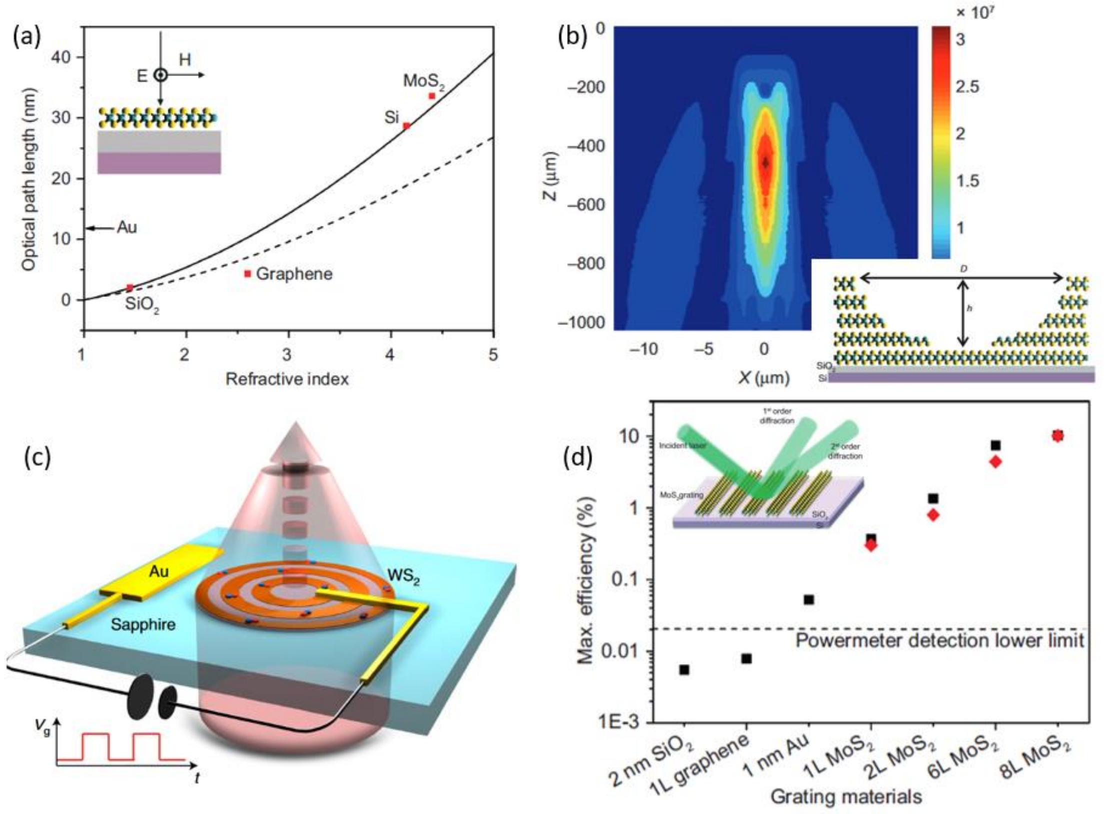

Figure 1.10 (a) Simulated OPL values for light reflected from 2D material (0.67 nm in thickness) with different indices on a SiO_2 (275 nm) / Si substrate (solid line) and SiO_2 substrate with infinite thickness (dashed line), from ref [10]. The calculated OPLs of 0.67 nm Au, 0.67 nm SiO_2, 1L (0.34 nm) graphene, and 1L (0.67 nm) MoS_2 are represented by markers. (b) Intensity distribution pattern of the MoS_2 micro-lens (sketched in the inset), adapted from ref [10]. (c) Schematic of a WS_2 zone plate lens, from ref [97]. (d) Comparison of the simulated (black squares) and measured (red diamonds) maximum grating efficiencies for different materials. The inset shows a sketch of the grating for diffraction efficiency measurements. Adapted from ref [10].

Besides the optical path length, another crucial parameter for efficient light manipulation is the scattering efficiency. In few-layer TMDs the high refractive index, combined with the atomically thin structure that results in a strong electric field inside the material, is responsible for an extraordinarily high scattering efficiency, thus enabling light manipulation by the collective scattering from TMDs nanostructured patterns, e.g. nanostripes arrays. Besides the thin optical lens discussed in **Figure 1.10b**, Yang et al[10] also recurred to focused ion beam to pattern diffractive nanograting in MoS_2 flakes (see sketch in the inset of **Figure 1.10d**) with different number of layers. In **Figure 1.10d** the maximum diffractive efficiency for gratings based on a variety of materials, showing an efficiency for MoS_2 nanogratings that is orders of magnitude higher than conventional materials.

The works I resumed in the previous figure were based on either exfoliated or CVD-grown flakes limited in size and only focused on the elastic scattering interactions for light wavefront manipulation, without studying the absorption in the TMD layer. However, they demonstrate the potential of flat optics applied to 2D semiconductors in view of light harvesting strategies in large area TMDs layers for photoconversion applications. One possibility to effectively couple light with the active 2D material is indeed given by flat optics metasurfaces based on subwavelength lattices, which amplify the overall optical absorption in the 2D active layer by tailoring light-matter interaction at the nanoscale via light scattering and/or near-field confinement[96,98–101]. By interacting with subwavelength periodic nanostructures, diffraction can be exploited to steer light parallel to the absorbing layer. This evanescent condition is referred to as Rayleigh anomaly and occurs at a specific wavelength. Lattice resonances and Rayleigh anomalies in photonic arrays represent an effective light trapping strategy, inducing strong in-plane light deflection and confinement[102–106].

This light trapping approach has been widely reported in the case of noble metal or dielectric nanostructures, but a strong potential is expected in the case of 2D-TMDs, such as MoS_2, provided light trapping and enhanced photo-conversion and/or -detection functionalities can be obtained by direct patterning of the atomically thin material[10,107]. During my research activity I thus worked on the fabrication of periodically nanostructured templates for the growth of conformal TMD layers. The diffraction effects induced by the subwavelength nanostructuring are exploited for increasing light-matter interactions with the ultra-thin 2D semiconductor, consequently enhancing the optical absorption as I will prove in Chapter 4.

At the same time, the nanostructured platform I fabricated can be used for the growth of nanostructured TMD layers for light wavefront manipulation via elastic scattering interactions. I will report some preliminary results on this in Chapter 5.

Chapter 2 – Large area growth of 2D-TMD films

In Chapter 1 I have discussed the scientific and technological interest for two-dimensional Transition Metal Dichalcogenides (2D-TMDs) and their optoelectronic properties. Here, I will continue the overview on the 2D semiconductors by focusing on the TMDs synthesis techniques, a topic largely covered by several reviews in literature[108–110]. Indeed, the development of high quality, uniform growth processes over wafer-scale is crucial for a real-world application of TMDs in electronics, optoelectronics and nanophotonics.

The first part of this chapter deals with the state-of-the-art synthesis of TMDs materials, with paragraph 2.1 dedicated to top-down approaches based on exfoliation and paragraph 2.2 dedicated to bottom-up large area growth processes that have been recently developed to overcome the main limitations of the exfoliation process.

In paragraph 2.3 I will cover the beginning of my PhD research activity, in which I worked at the in-house development of an innovative large area growth technique of few-layer TMD semiconductors (MoS_2) based on a novel physical deposition process. The achieved results set a milestone in my thesis and started new activities in the research group, previously limited to few-layer MoS_2 films grown in the framework of an external collaboration by recurring to a different process based on the high temperature sulfurization of MoO_3 films[111,112].

In paragraph 2.4 I will present an application of the large area growth combined with a nanolithographic technique to prove the capability to engineer deterministic 2D-TMD semiconductor nanostructures over large scale.

Finally, in paragraph 2.5 I will present the extension of the growth process to an alternative TMD semiconductors such as the ultra-thin WS_2, offering the possibility to grow a second TMD layer that is promising when combined to MoS_2 because they form a type-II van der Waals heterostructure with strong impact in photoconversion devices[113], as explained in Chapter 1.

2.1 TMDs exfoliation

The most common approach to the study of the TMDs fundamental properties is the exfoliation from the bulk crystal[114], in analogy with graphene that was first discovered by mechanical exfoliation from its bulk counterpart[2]. In particular, MoS_2 owes its fortune to the abundance in nature of its bulk mineral form, i.e. the molybdenite, thus making it the most studied TMD.

The standard micromechanical exfoliation process is based on the scotch tape method, described in the scheme reported in **Figure 2.1a**: a tape is pressed on the bulk material, from which flakes are peeled-off. The exfoliated flakes are then released on the desired substrate to complete the transfer. **Figure 2.1b** shows examples of few-layer flakes with different thicknesses down to a single monolayer fabricated by mechanical exfoliation[115]. Exfoliated flakes possess high crystalline quality and atomically thin interfaces, thus ensuring the best optoelectronic performances for the investigation of the material fundamental properties[51,116,117]. It is for this reason that most of the seminal studies and devices based on TMD materials rely on exfoliated flakes[118]. Additionally, different methods have recently developed for the controlled transfer of exfoliated 2D flakes by using polymeric matrices thus enabling the fabrication of vertically stacked Van der Waals heterostructures at the micro-scale[17,20].

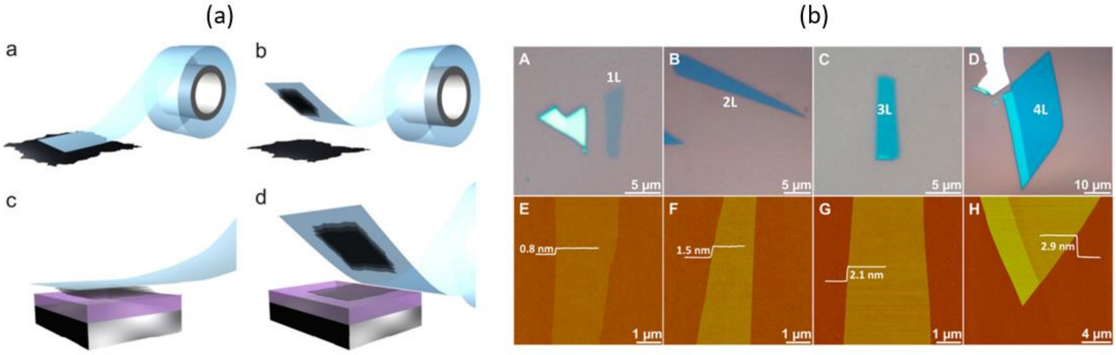

Figure 2.1 (a) Scheme of the scotch tape method for the exfoliation and transfer of 2D flakes, from ref [119]. (b) Exfoliated flakes of different thicknesses, from ref [115].

However, the exfoliation process also poses several limitations. First, the 2D flakes typically have limited size at the micrometer scale, as it can be inferred from the same **Figure 2.1b**, and the exfoliation yield is very low. Moreover, the flake thickness is not controlled and a distribution of different flakes randomly spread over a macroscopic sample is achieved after an exfoliation process[120]. A time-consuming optical microscope or AFM analysis is thus required to identify the target 2D flake (typically in the few-layer regime), that can be eventually transferred onto a pre-existing microscopic 2D layer with a precise alignment procedure controlled in-situ with an optical microscope[121].

It is thus straightforward to conclude that exfoliation cannot be considered a scalable approach since it involves low throughput flake transfer techniques, as well as cumbersome lithographic techniques such as Electron Beam Lithography to design contacts aligned to the microscale-size flakes.

To compensate for the low yield of mechanical exfoliation, an alternative large area route is represented by liquid-phase exfoliation, that results in highly concentrated solutions of flakes[122,123]. By use of proper solvents, stable dispersions of few- to monolayer TMDs flakes can be obtained, as described in literature[124–126]. The scheme in **Figure 2.2a** shows some examples. In the case of TMDs, intercalation is the most interesting alternative to micromechanical exfoliation: guest molecules (usually ionic species) are adsorbed by the layered material and increase the layers spacing, weakening the adhesion between them and facilitating the exfoliation via subsequent sonication in a liquid. Another possibility for TMDs is to expose them to ultrasonic waves in a solvent to exfoliate nanosheets. Depending on the solvent surface energy, exfoliated or reaggregated nanosheets can be obtained.

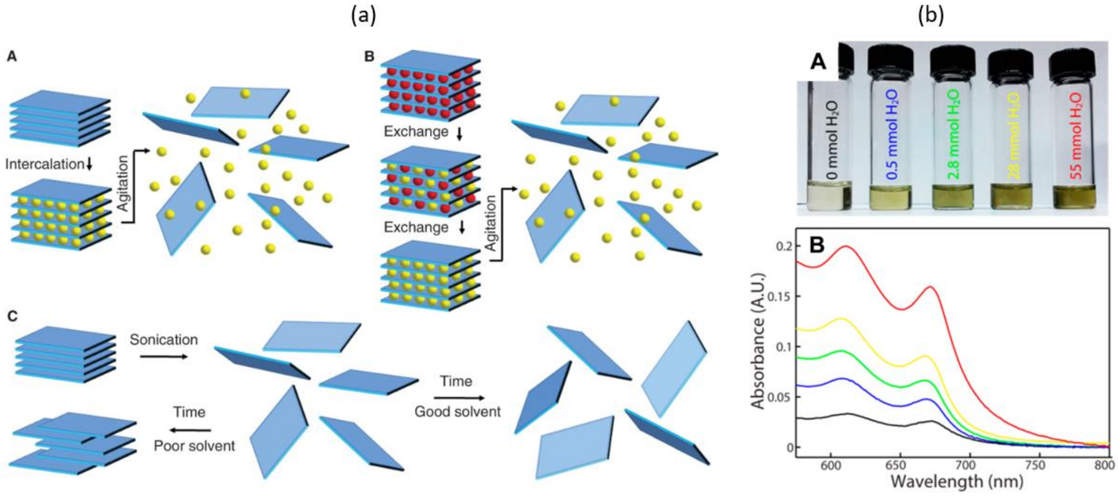

Figure 2.2 (a) Scheme of liquid-phase exfoliation mechanisms from ref [122]. (b) Optical absorption spectra of MoS_2 exfoliated flakes solutions at different concentrations depending on the solvent, from ref [123].

Figure 2.2b shows an example of MoS_2 exfoliated solutions at different concentrations depending on the solvent, with their optical absorption spectra. It can be noticed the strong excitonic response of the MoS_2 flakes, giving rise to the A and B exciton resonances at 675 nm and 625 nm respectively, as already discussed in Chapter 1.

Although on the one hand liquid exfoliation processes can be transferred to some technological applications, on the other hand issues such as the weak homogeneity of the layers over large area and the inter-flakes percolation dynamics at the microscopic scale still do not meet the scalability requirements for semiconductor industries and circuit integration.

2.2 Large area synthesis

The main limitations of the exfoliation approaches (random distribution of 2D flakes and sizes limited to the microscale) have just been presented. The urgent demand for potentially scalable platform and devices has recently motivated alternative growth methods for TMDs layers mainly relying on the Chemical Vapor Deposition (CVD) approach[112,127–134], which leads to a non-uniform distribution of triangularly shaped 2D-TMD islands typically limited at the microscale over large area substrates. A challenge of the CVD growth indeed is the control of lateral-to-vertical ratio of growth rates, in order to control the size and thickness of the crystalline flakes. An interesting feature of the CVD is the possibility to differently shape the CVD grown crystals by playing with the process parameters[135], as shown in **Figure 2.3a**. As in the case of exfoliated flakes, the high quality of the TMD crystals is reflected in good optoelectronic properties. Different applications of CVD-grown TMD devices can be found in literature, from photodetectors to transistors[136,137].

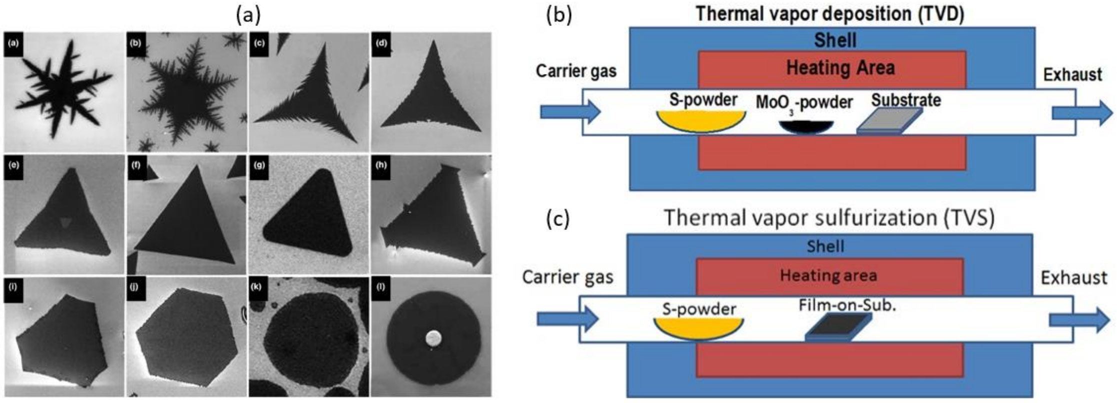

Figure 2.3 (a) Morphologies of TMD flakes grown by CVD process at different conditions, from ref [135]. (b) Scheme of Thermal Vapor Deposition process, from ref [138]. c) Scheme of Thermal Vapor Sulfurization process, from ref [138].

The term CVD is commonly used to group two different types of processes, the Thermal Vapor Deposition (TVD) and the Thermal Vapor Sulfurization (TVS)[138]. While the former is a proper CVD process, where vapor phase precursors react and deposit on the substrate (**Figure 2.3b**), the latter is rather based on the thermal annealing of a thin precursor film in a reactive sulfur atmosphere (**Figure 2.3c**). In literature, alternative names can be found to refer to this type of process based on a thin film annealing, such as Solid Film Source[111] (SFS-CVD) or Solid Precursor Film[7] (SPF-CVD), which I will adopt in the following to refer to this process. In contrast to conventional CVD processes that result in TMD flakes endowed with micrometer scale lateral size and random distribution on the surface, the physical deposition of a thin metal precursor film that is subsequently recrystallized at high temperature using a sulfur precursor is a promising alternative to obtain continuous layers with controlled thickness[6,7].

Relevant for the following experimental section is the sulfurization mechanism of MoS_2 layers in the SPF-CVD process based on Mo/MoO_x ultra-thin films. In the proposed model in literature, sulfurization is based on the sublimation of the molybdenum oxide that reacts in vapor phase with sulfur and reprecipitate on the substrate surface[139]. The complete sulfurization reaction is[111,140]:

$$2MoO_3 + 7S \rightarrow 2MoS_2 + 3SO_2$$

Being the process based on oxide sublimation, vapor phase reaction and disulfide precipitation, lateral diffusion is expected during the process. If on the one hand this mechanism is useful for smoothing of the surface offering a homogeneous growth, on the other hand it poses a fundamental limitation for the fabrication of laterally resolved nanostructures, since lateral resolution is lost.

To complete the picture of large area synthesis techniques, I will just mention some other processes that have been developed for the synthesis of large area TMD layers.

Atomic Layer Deposition (ALD) is a self-limiting layer by layer growth process that is the result of alternate injection of reactants into the growth area[141]. After each reaction step, a monolayer is formed and the excess species and by-products are removed before the next cycle, thus enabling exact control on the film thickness. Additionally, MoS_2 films can be synthesized by ALD even at low temperatures, making the process compatible with photolithographic and lift-off patterning and front-end-of-line integration in semiconductor technology[142].

Pulsed Laser Deposition (PLD) is a physical vapor deposition technique in which a high-power pulsed laser beam is focused inside a vacuum chamber on a target of the material to be deposited, resulting in the ablation of the target with a deposition flux on the substrate. PLD has been also extended to the growth of large area MoS_2 films[143]. By this process, the thickness can be controlled by controlling the frequency and energy of the laser and the deposition pressure, that determine the growth kinetics. Since the high laser energy is absorbed in a very small volume of the target, the ablated material preserves the target stoichiometry during the transfer on the substrate, though the crystalline phase may change. In contrast with other methods such as CVD, PLD avoids expensive and potentially dangerous precursors.

Molecular Beam Epitaxy (MBE) was also extended to the growth of large area MoS_2 on epitaxial substrates such as mica and sapphire[144]. In this kind of process, molecular beams of molybdenum and sulfur are used as reaction precursors and the substrate is used as a platform for orientated growth of the TMD. As a result, highly crystalline films with controlled orientation and negligible grain boundaries (which would degradate the electrical performances) can be achieved.

2.3 Growth of ultra-thin MoS_2 films

After having described the state-of-the-art in MoS_2 synthesis, in this paragraph I will cover the experimental results that I have achieved in the development of a novel process for the large area growth of homogeneous ultra-thin MoS_2 layers. In subparagraph 2.3.1 I will present two different custom-made set-ups, based on RF-sputtering and Ion Beam Sputtering respectively, that I have developed during my thesis work and that I used for the physical deposition of the precursor thin films. In subparagraph 2.3.2 I will describe the first growth trials starting from oxidized Mo thin films, presenting the optimization of the sulfurization process based on the initial failures. The limits of this approach will be highlighted to explain why I moved to sputtering based physical deposition of MoS_2 films, described in subparagraph 2.3.3.

2.3.1 Deposition of TMD precursor films

In this subparagraph, I will describe the two sputtering deposition techniques that I employed for the fabrication of homogeneous, large area ultra-thin precursor films as the first step toward large area synthesis of few-layer MoS_2 samples. Being a physical process based on the sputtering from a bulk target, the main advantage is the possibility to easily change the target either to change the material growth process (from Mo/MoO_x precursor films using a Mo target in subparagraph 2.3.2 to MoS_x precursor films using a MoS_2 target in subparagraph 2.3.3) or to change the material itself (WS_2 target instead of MoS_2, paragraph 2.5). Here, I will focus on the sputtering of Mo as a general demonstration of the process.

The first deposition process is based on Radio Frequency (RF) magnetron sputtering and is schematically shown in **Figure 2.4a**. We adapted a custom-made vacuum chamber in which the material target is coupled to an antenna connected to a radiofrequency generator, while the substrate (usually fused silica wafers) is faced to the target. The chamber is kept to Ultra High Vacuum (UHV) condition at a pressure of about 10^{-6} mbar by a combination of a rotary primary pump and a turbomolecular pump. During the magnetron sputtering deposition step, the chamber is filled with ultrapure argon to 10^{-2} mbar in order to ignite a plasma at an incident power of 100 W. Finally, by gradual decreasing of pressure and power, deposition is performed at 10^{-3} mbar with an incident power of 10 W. A movable shutter is used to protect the substrate from uncontrolled deposition during the plasma ignition process. During the sputtering process, deposition flux and film thickness are monitored by means of a quartz crystal microbalance that is mounted inside the chamber.

The deposition process here described can be performed on a broad portfolio of substrates, ranging from silicon to borosilicate glass and flexible polymeric substrates, since it takes place at low temperature.

The second deposition process is based on Ion Beam Sputtering (IBS). The set-up is realized in a custom-made vacuum chamber that is equipped with an Ion Gun (ECR Plasma Source TPIS by TECTRA). The chamber is kept in UHV condition at 10^{-7}-10^{-6} mbar by use of rotative and turbomolecular pumps and then filled up with argon (up to 6.0×10^{-4} mbar). A plasma is then generated by the Ion Gun magnetron and the ions are extracted by use of two grids set at different electrostatic potentials, generating a 1.44 keV Ar^+ ion beam (gas purity N5.0). The result is a defocused ion beam that is used to sputter the selected target, from which the material is deposited onto the facing substrate. The ion beam is collimated by a pinhole in the shutter placed in front of the extracting grid, so that only the target is sputtered preventing deposition contaminations that would originate from the chamber walls. As in the case of the RF-sputtering deposition, the same considerations made for the for the targets and substrates versatility are valid for the IBS deposition.

The IBS deposition process is represented in **Figure 2.4b**, where I show a sketch of the new flange that we specifically designed for large area TMD growth. This set-up features two key advantages with respect to the previously shown RF-sputtering deposition. First, it allows to load multiple TMD targets enabling sequential stacking of different TMD layers in UHV condition. In Chapter 3, I will exploit this opportunity to grow large area WS_2-MoS_2 heterostacks in a single deposition process. Second, it allows the controlled tilt of the substrate with respect to the material target to perform grazing angle deposition. As I will explain in Chapter 5, this possibility combined with nanostructured substrates enables maskless nanofabrication of nanostripes arrays based on few-layer TMD heterostructures.

The preliminary experiments performed during my thesis did not allow to evidence the differences in morphology and crystalline structure of the deposited via RF sputtering and defocused ion beam sputtering, respectively. Here, as an example, I will describe the deposition of solid precursor films of different thickness, as determined by the reading of the quartz microbalance, by RF-sputtering of a metallic molybdenum target. We assume that in the few-nanometer regime the Mo films are almost fully oxidized when exposed to ambient pressure, whereas in the case of thicker films only the top layers are oxidized while the buried layers stay metallic[145].

As an indirect evaluation of the precursor film thickness, we performed far-field transmission spectroscopy measurements in the Near-UV, Visible and Near-Infrared spectrum with a custom-made apparatus composed by a deuterium-halogen lamp DH-2000-BAL and an Ocean Optics HR4000 spectrometer. The light is fiber-coupled to the sample at normal incidence via a collimating lens that illuminates a spot of $\sim 1\ mm^2$ area, while the transmitted light is also fiber-coupled and guided to the detector. In **Figure 2.4c** the transmission spectra of different precursor films characterized by increasing thickness are reported, showing a progressive reduction in the optical transmittance. These samples have been used for the first sulfurization trials, as described in the following subparagraph.

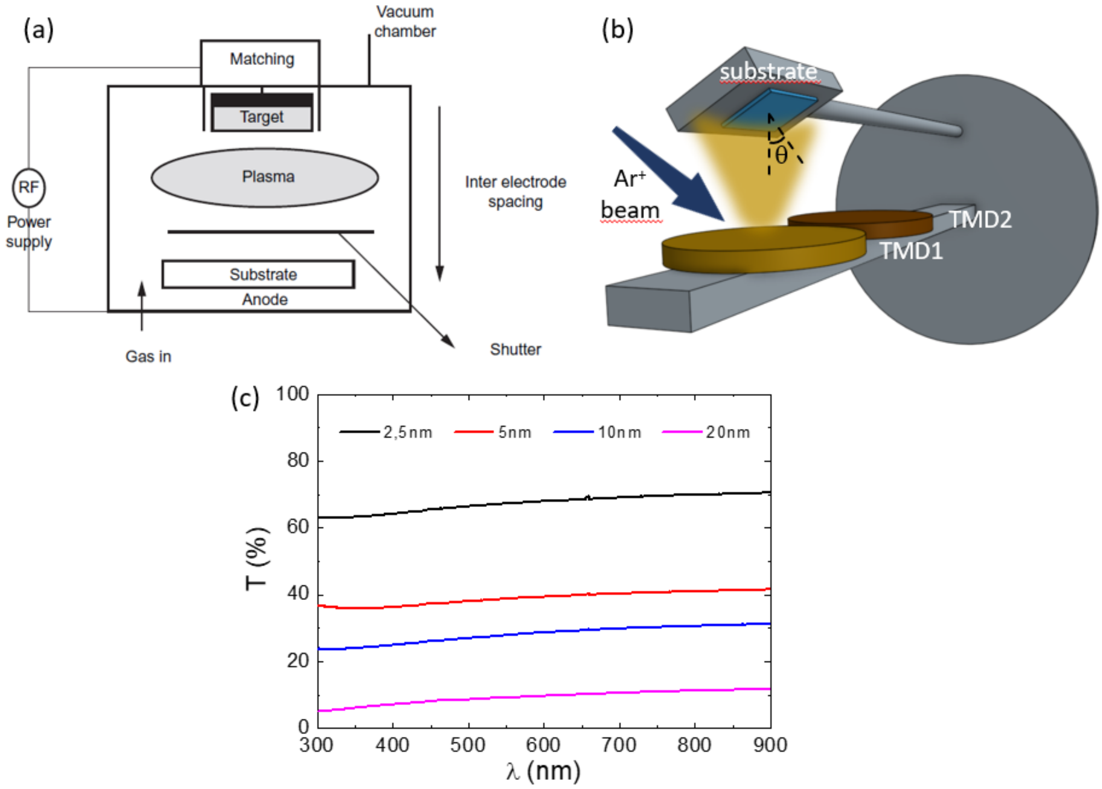

Figure 2.4 (a) Scheme of RF sputtering deposition, from ref [146]. (b) Scheme of our customized IBS deposition set-up, highlighting multiple targets loading and substrate tilting. (c) Optical transmission spectra of Mo precursor films with different thickness, deposited by RF-sputtering.

2.3.2 Solid Precursor Film – Chemical Vapor Deposition (SPF-CVD) of MoS_2 films

In the initial phase of my PhD research project, I implemented a SPF-CVD process to grow large area few-layer MoS_2 samples via high temperature sulfurization of pre-deposited Mo/MoO_x precursor films, as already shown in **Figure 2.3c**. The sulfurization has been performed adapting a single zone tube furnace, controlled by a CAL 3300 Autotune Temperature Controller equipped with a PID feedback system to regulate the heating process. A gas line system has been implemented to flux argon inside the 2-inch diameter quartz tube as inert carrier for the sulfur precursor. A sketch of the set-up is shown in **Figure 2.5a**. The sample is placed at the center of the furnace, where the sulfurization temperature is set by the controller, while sulfur powder used as sulfur precursor is placed upstream in a quartz boat. A custom sample carrier was manufactured from molybdenum foil to support large area substrates, properly tilted so to expose them to the sulfur flux.

The main criticality of the single-zone furnace is the absence of control on sulfur temperature, which is only determined by its position with respect to the furnace temperature gradient profile and required to initially proceed by a trial-and-error approach. For the first sulfurization experiments, I set the process parameters based on similar processes found in literature[145,147–149]. For this reason, I searched reference values for setting the sulfurization temperature and the sulfur sublimation temperature (determining the sulfur position inside the furnace). Combined to the sulfur position, sulfur powder amount and gas carrier flux determine the reactive sulfur flux reaching the sample, thus playing a crucial role in the process. Finally, other relevant process parameters I looked for were those related to the heating rate and the time interval during which the sample is held at high temperature (soaking).

Choudhary et al[147] synthesized large area Mo films with modulated thickness by working at 600°C (heat rate 20°C/min) in a Low Pressure Chemical Vapor Deposition system, by pumping down to 10^{-3} Torr and working with a 200 sccm Ar flux to carry the sulfur (1g).

Shazad et al[148] studied the effects of pressure and temperature on the sulfurization of RF-sputtered Mo films, reporting the synthesis of a fully sulfurized smooth film at 750°C rather than a mixed combination of 2D and 3D structures at 600°C or a discontinuous film at 450°C. The higher the pressure at a fixed flow of 100sccm N_2, the higher the concentration of sulfur that enables orientated growth after nucleation.

Heyne et al[145] used Mo and MoO_x precursor films with different thicknesses sulfurized at different temperatures (400°C, 600°C, 800°C). They show by XPS measurement the complete oxidation of ultra-thin Mo precursor films (2nm) while a partial metallic fraction is preserved for higher thicknesses (5nm). The S/Mo ratio increases with the sulfurization temperature and the initial oxidation of the solid precursor, though the sulfur precursor is H_2S instead of sulfur powder.

In contrast with these results, Romanov et al[149] report a weak dependence of the S/Mo ratio from the sulfurization temperature in the range from 500°C to 1000°, that mostly determines the morphology and microstructure. The higher the temperature, the larger the crystalline grains are, with the basal planes parallel to the substrate. The control on the orientation of the crystalline domains can improve the film functionality e.g. aiming at catalytic applications (in case of vertically aligned grains, exposing a higher number of reactive edges) or optoelectronic devices (in case of horizontally aligned grains.

Due to the different sulfurization set-ups used in the reported literature, I had to find a balance in the parameters I was able to control. I thus started by setting the sample temperature at 750°C with a heating rate of 20°C/min. A higher sulfurization temperature was not chosen due to the higher temperature gradient that would have reduced the reproducibility in the sulfur deposition, even though it would have improved crystalline quality and grain size. Since I employed a single zone furnace, I could not control the sulfur sublimation temperature that I wanted to set around 170°C, so I initially performed some heating ramps using a thermocouple to find the right position for the sulfur boat. In **Figure 2.5b** I show an example of a calibration heating ramp to determine the effective sulfur temperature (blue curve) as measured by means of the thermocouple placed in the same position. The considered case refers to a position at 3.5 cm inside the oven, with an Ar flux of 50 sccm. In this condition, the sulfur boat reaches about 170°C when the furnace reaches 750°C, ensuring sufficient sulfur flux during the sulfurization process. The red curve represents the temperature profile at the center of the furnace where the sample is placed: an infinite soaking time was set to determine the asymptotic temperature of sulfur, that reaches 225°C. Finally, the sulfurization process was optimized at an argon flux of 100 sccm and a 10 minutes soaking. Additionally, since the furnace is made by a resistive heater, there is no possibility to cool down except for quenching the sample by retracting it in a lower temperature zone. A quenching step was thus added to cool the sample faster, avoiding MoS_2 sublimation at high temperature.

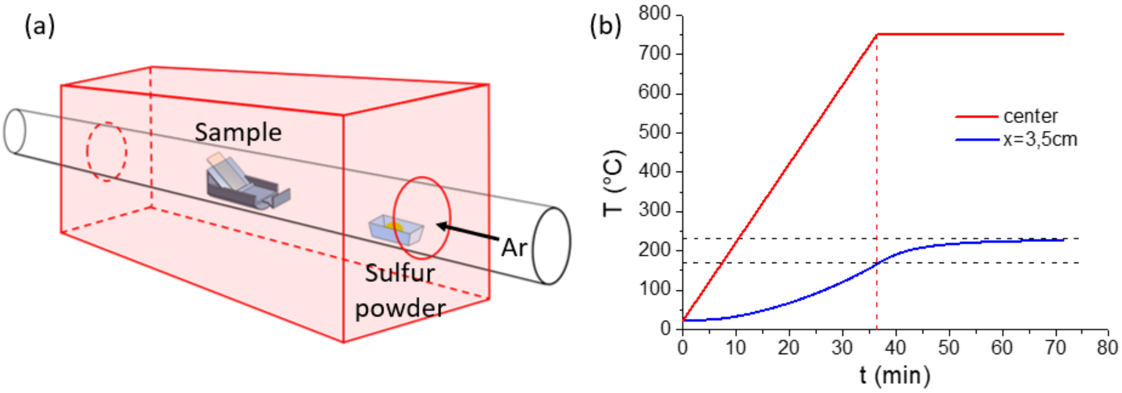

Figure 2.5 (a) Scheme of the sulfurization set-up based on a single zone tube furnace. (b) Calibration trial for the sulfur placement, monitoring virtual sulfur temperature (blu curve) by use of a thermocouple with respect to the set heating ramp (red curve).

The first sulfurization trial was performed on a 2 nm thick molybdenum precursor film and failed due to total sublimation of the precursor film. Being the reaction mechanism based on the sulfurization of sublimating molybdenum oxide, the most reasonable explanation for this first failure is in the low incoming sulfur flux: indeed, only 2 mg out of the loaded 23 mg evaporated.

I moved then to thicker precursor films and I increased the sulfur evaporation by loading a higher amount of sulfur powder at higher temperature with higher argon flux. After the soaking stage, quenching was performed to cool down the sample thus preventing the sublimation. The changes proved to be effective, obtaining a 10 nm thick MoS_2 film thanks to the sulfurization process. However, inhomogeneities at the millimeter scale are still present on the film and can be distinguished in the photograph of the sample shown in the inset of **Figure 2.6a**. Such observation is confirmed by the far-field extinction spectroscopy measurements reported in **Figure 2.6a**. Remarkably, all the extinction spectra show the excitonic features of MoS_2 with two peaks at about 672 nm and 620 nm (A and B excitons) and the band nesting region in the 400-450 nm range. A high extinction background (more than 20% towards the Infrared) is observed for all the spectra, indicating the presence of a metallic phase that reflects over a broadband range.

Having found a good condition for sulfur evaporation, I further optimized the sulfurization process by modifying the cooling phase: one hour after the quenching (with reduction of argon flux) the sample was reinserted in the center of the cooling oven to thermal anneal but at a temperature too low for sublimation (under 500°C). Additionally, it is in this occasion that I tested the new custom-made sample holder sketched in **Figure 2.5a**. In this way, I succeeded in the homogeneous growth of thinner precursor films. The photograph reported in the inset of **Figure 2.6b** for a sample prepared by sulfurization of an ultra-thin precursor layer (4 nm thick) shows a homogeneous surface over large cm^2 area. Optical extinction spectra acquired in different regions are shown in **Figure 2.6b** and confirm homogenous growth of MoS_2 over large area, since the characteristic exciton resonances of the TMD layer can be clearly identified. Interestingly, the optical extinction is higher than the previous sample though the initial precursor film was about half the thickness, confirming from one side a big loss of material in the previous case and on the other side the prevention of sample sublimation in this case.

To further investigate the optoelectronic properties of the few-layer film, Raman micro-spectroscopy measurements were performed in different spots over the large area sample excited by 532 nm laser line. The spectra are reported **Figure 2.6c** and show the MoS_2 characteristic vibrational modes with the in-plane E^1_{2g} mode at about 379 cm^{-1} and the out-of-plane A_{1g} mode at about 405 cm^{-1}. These positions are rigidly shifted at lower wavenumbers with respect to the expected values from literature[47]. Such shift can be can be attributed to a wrong instrumental calibration but also to possible effects of electron doping and residual strain depending on the growth technique[150,151]. However, the spectral separation of 26 cm^{-1} between the two modes is still useful to confirm the formation of a few-layer MoS_2 film, since the bulk limit value is already detected after six layers, corresponding to about 4 nm thick MoS_2 films.

However, the optical extinction spectra reported in **Figure 2.6b** still show a high background due to high reflectivity from a metallic layer, indicating a not complete sulfurization even for a 4-5 nm precursor film. The reported results demonstrate the difficulties in sulfurizing MoO_x precursor layers both in the limit of ultra-thin films, where the sample is lost due to oxide sublimation, and in the case of thicker films, where a consistent fraction of the layer remains metallic contributing to a high reflectivity. For these reasons, in the next subparagraph I will focus on a new physical growth process based on the deposition of ultra-thin MoS_x precursor films by direct defocused ion beam sputtering of a bulk MoS_2 target.

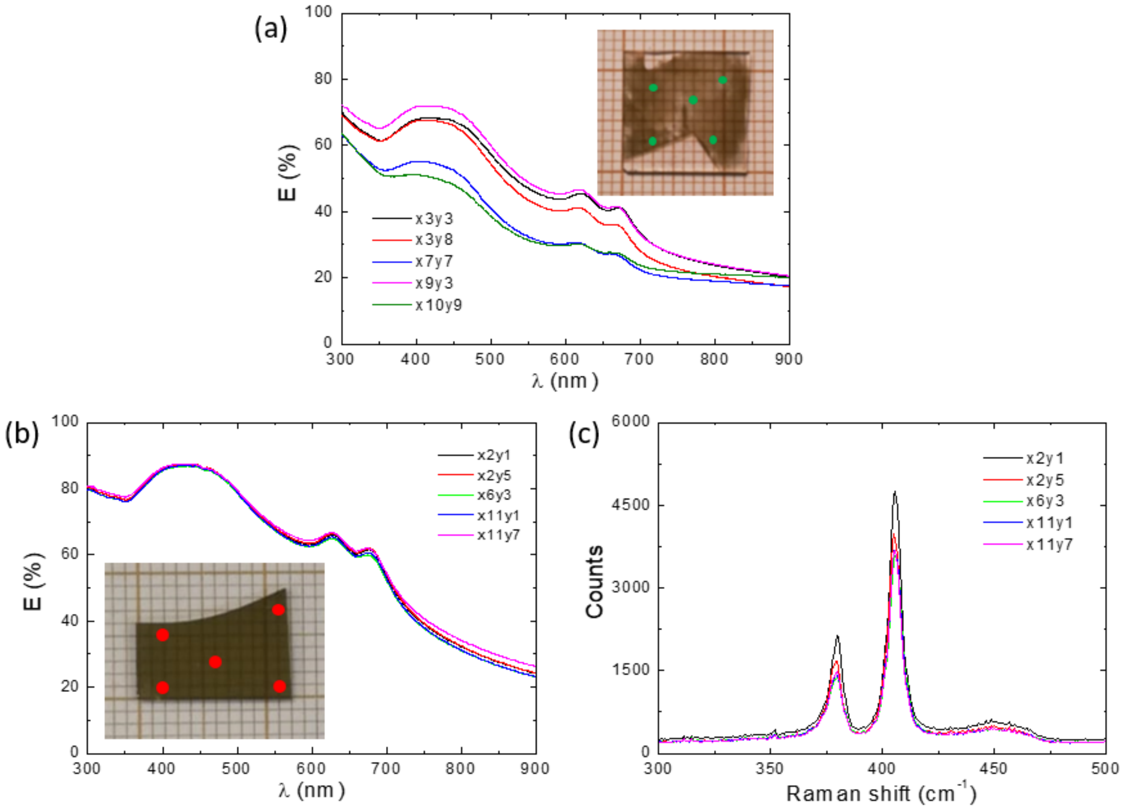

Figure 2.6 (a) Optical extinction spectra of inhomogeneous MoS_2 sample from thick molybdenum precursor (photograph shown in the inset). (b,c) optical extinction and Raman spectra of homogeneous MoS_2 sample from thin molybdenum precursor (photograph shown in the inset of panel b).

2.3.3 Physical deposition of MoS_2 films

The limits of the SPF-CVD deposition process have already been mentioned and mainly regard the sublimation of the oxide phase at high temperature, complicating the growth process for ultra-thin MoS_2 films, and the volatility of the precursor film. The latter may not be crucial in the case of large area homogeneous films but can be a crucial limitation in view of the fabrication of lithographic nanostructures, since the diffusion of the volatile precursor can be in the order of tens of micrometers[139] and can degrade the lateral resolution of lithographically defined nanostructures.

For this reason, we decided to develop a new large area growth process based on physical deposition of the TMD film by direct ion beam sputtering of a stoichiometric MoS_2 target. The precursor film deposited in this process is amorphous and slightly sub-stoichiometric (MoS_x), and for this reason is less volatile than the oxide precursor. The precursor film is then processed in the tube furnace with the same sulfurization process described in subparagraph 2.3.2. Due to the stochiometric MoS_2 target employed during physical deposition, we refer to this process as a high temperature recrystallization rather than a proper sulfurization, though the thermal annealing still occurs in a sulfur enriched atmosphere to preserve the stoichiometry. As I will show later in this chapter (paragraph 2.4) the process enables a more controllable growth of ultra-thin MoS_2 layers (down to 2-3nm) and the possibility to fabricate laterally confined nanostructures.

Large area homogeneous MoS_2 films can thus be achieved on areas exceeding several cm^2, as highlighted by the sample picture of **Figure 2.7a**, which shows a few-layer MoS_2 film (~6 nm) deposited on a transparent silica substrate. The deposition process of the pristine amorphous MoS_2 film takes place at room temperature and is thus compatible with flexible polymer substrates. The structural quality of the ultra-thin recrystallized TMD film is confirmed by the Raman micro-spectra (**Figure 2.7b**) characterized by the E^1_{2g} and by the A_{1g} mode, resonant at 383 cm^{-1} and 408 cm^{-1} respectively, as expected for an ultra-thin MoS_2 layer with a separation value of 25 cm^{-1} in agreement with a bulk-like response. The Raman response, detected over sub-micrometric optical spots, is homogeneous up to the cm scale, as demonstrated by the spectra acquired along a diagonal axis of the sample, 5-6 mm apart one from the other (colored spots in **Figure 2.7a**).

The presence of a MoS_2 ultra-thin film in the 2H-semiconducting phase is further confirmed by the optoelectronic response detected in far-field extinction spectroscopy

(**Figure 2.7c**), and characterized by the A and B exciton resonances, respectively detected at 670 nm and at 614 nm wavelength. The broader extinction signal detected in the 400-460 nm range can be attributed to the convolution of C and D resonances in few-layer MoS_2, also identified as band nesting transitions. These extinction spectra, uniform over large-scale, further confirm the good optoelectronic properties of these few-layer MoS_2 sample and homogeneity over cm^2 area.

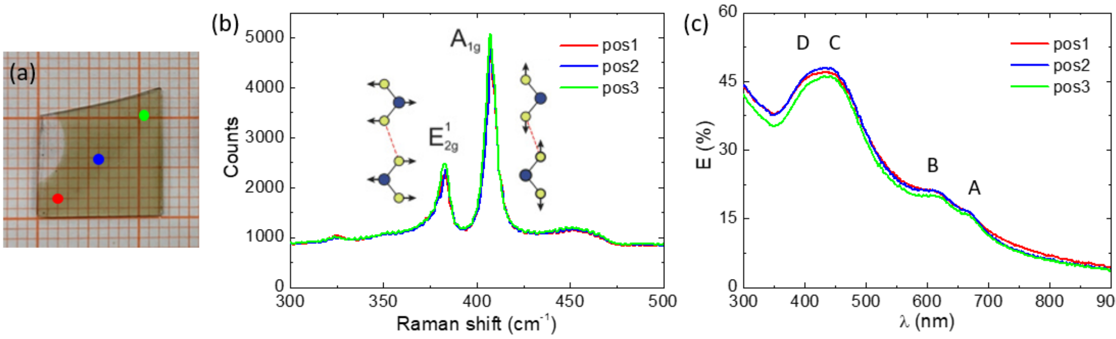

Figure 2.7 (a) Photograph of a homogenous large area recrystallized MoS_2 film. (b,c) Raman and optical extinction spectra acquired in correspondence to the colored spots in panel a.

We then explored different regimes of TMD thickness by incremental physical deposition of the MoS_2 layer, starting from 3 nm (4-5 layers, still in the few-layer regime) and increasing by 5 nm steps.

The Raman spectra at each different step are reported in **Figure 2.8a**. Except for the lower thickness, for which the separation between the two modes reads about 23 cm^{-1} close to the expected four monolayers, in all the other steps the separation reads about 26 cm^{-1}, that is the characteristic value of the bulk material response, thus giving no information on the effective thickness[152]. At contrary, the extinction spectra acquired for the different steps (**Figure 2.8b**) show an incremental increase of the extinction with the increase of the MoS_2 precursor film, demonstrating that we can effectively control the final thickness of the MoS_2 layers with our physical growth technique. The position of the A exciton redshifts from $\lambda = 670$ nm for the 3 nm thick film to $\lambda = 686$ nm for the 23 nm thick film, as expected from the literature for the increasing of the TMD thickness[153].

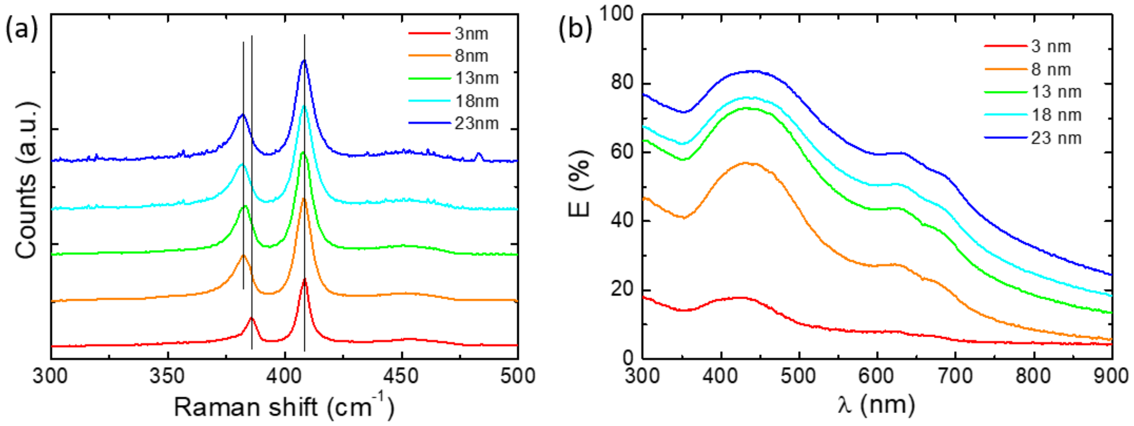

Figure 2.8 Raman (a) and optical extinction (b) spectra for different thicknesses of recrystallized MoS_2 films.

2.4 Few-layer TMD semiconductor nanocircuits

In this paragraph I will present the results recently published on Advanced Material Interfaces[154], where large area physical growth of 2D-TMDs layer was combined with high resolution thermal - Scanning Probe Lithography (t-SPL) to reshape the ultra-thin semiconducting layers at the nanoscale.

The possibility to achieve a controlled reshaping of TMDs layers is particularly attracting in order to develop engineered and/or quantum confined 2D materials as a building block for functional nanodevices in electronics, photonics and quantum technologies[21,97,155–160]. Recently the possibility to promote tuning of the optoelectronic response via shape engineering of 2D layers has been demonstrated using micrometric TMDs flakes[9,10,161], highlighting the impact of this approach in photonics and quantum optics. However, few attempts can be found on the arbitrary nanolithography of 2D-TMD layers on large-scale wafers, typically applied to isolated micro-flakes[162,163] or characterized by spatial resolution at the micro-scale[164]. Complex multi-step lithography processes requiring chemical or plasma etching of the 2D islands (subtractive approaches) are typically used for nanopatterning 2D-TMDs, introducing unwanted contaminations or surface damages to the fragile ultra-thin layers[165,166]. Scalable growth and non-invasive nanopatterning approaches are thus urgently required to engineer the optoelectronic and photonic response of 2D-TMD layers.

The thermal-Scanning Probe Lithography (t-SPL) has recently emerged as a very promising technique, uniquely providing local modification of materials properties in ambient conditions with nanoscale spatial resolution provided by a sharp conductive probe[167,168]. This approach is optimal for the fragile 2D layers as demonstrated by few recent experiments showing the nanolithography of high quality metallic contacts on 2D-TMDs[169], and thermomechanical reshaping when exfoliated as micrometric flakes randomly distributed on the surface[170,171].

In this work, we demonstrate the additive nanofabrication of few-layer MoS_2 nanostructures, grown in the 2H-semiconducting TMD phase, as shown by their Raman vibrational fingerprints and by their optoelectronic response. The capability to control the electronic transport properties at nanometer lateral scale is demonstrated via high-resolution Kelvin probe nanoscopy and local probing of the electric transport via conductive-AFM nanoscopy. The local electrical and compositional contrasts and the electrical conductivity, resolved at the nanometer scale on the MoS_2 nanopaths, qualify them as building blocks of next generation nanocircuitry. The exceptional uniformity of the 2D-TMDs layers over large area (cm^2), combined with the non-invasive t-SPL nanolithography enables the precise nanofabrication of ultra-thin nanocircuits and van der Waals heterostructures nanodevices over large-scale wafers, opening new perspectives in electronics, photonics and quantum technologies.

Specifically, my contribution to this work consisted of the large area MoS_2 growth on the lithographic template, the Raman characterization of the nanostructures and the initialization of the conductive AFM measurements.

2.4.1 Nanofabrication of TMD nanocircuits

Controlled deposition of ultra-thin semiconductor films is achieved via collimated ion beam sputtering (IBS) of a stoichiometric MoS_2 target according to the process described in paragraph 2.3.3, as demonstrated by the results shown in **Figure 2.7**. The large-scale homogeneity of our growth process, combined with the novel t-SPL technique, provides the unique opportunity to develop a scalable approach for the nanoscale-resolved reshaping of ultra-thin TMDs layers.

The t-SPL indeed exploits a sharp hot nanoprobe to pattern arbitrary nanopaths onto a thin polymeric bi-layer that we deposited by spin-coating onto a thermal oxide coated (SiO_2: 300 nm) p-doped silicon substrate (sketch in **Figure 2.9a**). The underlying film of the sacrificial bi-layer is a PMMA/MA (thickness 95 nm), while a thermally sensitive film of polyphthalaldehyde (PPA - thickness 25 nm) is spin-coated on the surface. The new Nanofrazor Scholar set-up (Heidelberg Instruments) enables the high-resolution t-SPL of the sensitive PPA film in ambient condition, thanks to the action of a sharp silicon tip (radius tip ∼10nm) locally heating the surface. The system provides temperature- and time-controlled heat pulses through the nanoprobe (temperature at the cantilever sensor tunable in the 500°C - 1100°C range), thus enabling the arbitrary nanolithography of complex shapes and/or local modification of material properties. In this way engineered nanopatterns can be written at high resolution (tip radius ∼ few nm) on the soft layer, which selectively exposes the patterned areas of the substrate after the chemical development of the underlying PMMA/MA film is finally performed solution of deionized water in isopropyl alcohol at 5% vol. (**Figure 2.9b**). The sacrificial bi-layer acts now as a mask with appropriate negative angle profile for the following MoS_2 growth (**Figure 2.9c**). The sample is finally rinsed in acetone for the lift-off of the non-patterned areas achieving MoS_2 nanopaths on the substrate, avoiding damages and contaminations by the lithographic process and leaving behind engineered few-layer MoS_2 nanopaths, as sketched in **Figure 2.9d**. Under this condition high quality MoS_2 nanostructures can be easily achieved with the high temperature recrystallization process.

The optical microscopy image of **Figure 2.9e** demonstrates the additive nanofabrication of few-layer MoS_2 nanocircuits (darker regions of the image) in arbitrarily defined positions on a scale that is dependent on the lithographic technique, since I already demonstrated that our TMD growth process results in homogeneous films over the cm^2 scale (**Figure 2.7**). The throughput of our nanofabrication process is only limited by our equipment, but could be further scaled up using industrial machines. The Scanning Electron Microscopy (SEM) image on a specific nanopattern (**Figure 2.9f**) shows well defined MoS_2 nanopaths (darker contrast in the SEM image) forming the logo of our facility and obtained thanks to the t-SPL nanolithography. The zoomed-in SEM image well highlights the contrast of the few-layer MoS_2 on the substrate with nm spatial resolution. Further MoS_2 nanopatterns designed at higher resolution with a thickness of 6.3 nm (∼9 layers) are shown in the AFM image of **Figure 2.9g**, which evidences nanostripes widths below 200 nm. High resolution AFM images have been acquired by a JPK NanoWizard AFM (Bruker) operating in Quantitative Imaging (QI) mode. Remarkably, the additive nanolithography approach here described enables fabrication of clean ultra-thin MoS_2 nanostructures, avoiding damaging and/or contamination of the 2D-TMDs layer intrinsic in the reactive ion etching based approach, typically used for nanopatterning 2D materials[165,172].

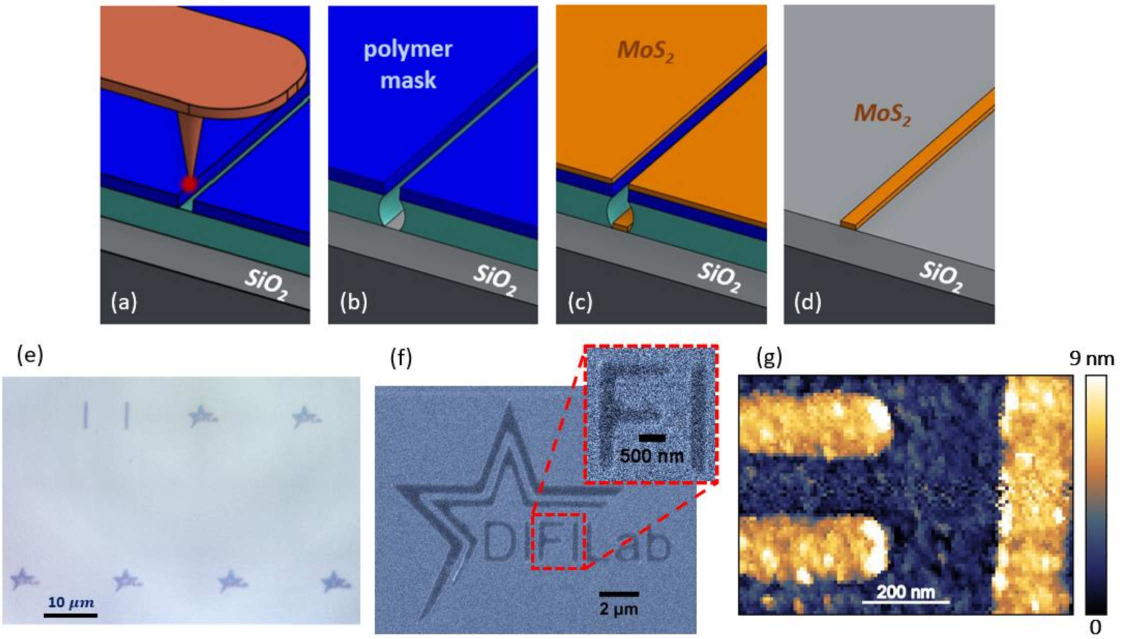

Figure 2.9 (a-d) Sketch of the t-SPL nanolithography process. (e) Large-scale optical microscopy showing a series of MoS_2 nanocircuits fabricated onto a Si/SiO_2 substrate. (f) SEM image of a few-layer MoS_2 nanocircuit (darker regions in the secondary electron signal) showing the logo of our laboratory (DIFILab facility - UNIGE) at the nanoscale and zoom on a detail of the MoS_2 nanopaths. (g) AFM image of a high resolution nanocircuit, showing ultra-thin MoS_2 nanopaths (scale bar 200 nm).

To confirm the material structure and to show the reshaping capabilities of the few-layer material, Raman micro-spectra and maps have been detected by using an NRS-4100 Raman microscope (JASCO) operating in back-scattering configuration with sample excitation with a 532 nm laser source.

Raman micro-spectra have been measured both on the engineered nanopaths (red curve in **Figure 2.10b** corresponding to blue regions of the optical microscopy image of **Figure 2.10a**) and few hundred nanometers apart on the bare substrate (black curve in **Figure 2.10b**). The Raman micro-spectrum detected on the MoS_2 nanopath shows the characteristic E^1_{2g} and A_{1g} vibrational modes excited at 383 cm^{-1} and 408 cm^{-1}, respectively, while on silica substrate (black curve) we measure an unstructured background.

In parallel, the high homogeneity of the few-layer MoS_2 nanopaths is demonstrated by the micro-Raman maps shown in **Figures 2.10c** and **2.10d** respectively, corresponding to the Raman image of a whole nano-logo and of a zoomed detail highlighted in **Figure 2.10a**. These Raman maps recover the morphology of the few-layer MoS_2 nanostructures, with a spatial resolution in the range of few hundred nm which is only limited by optical diffraction (**Figure 2.10d**).

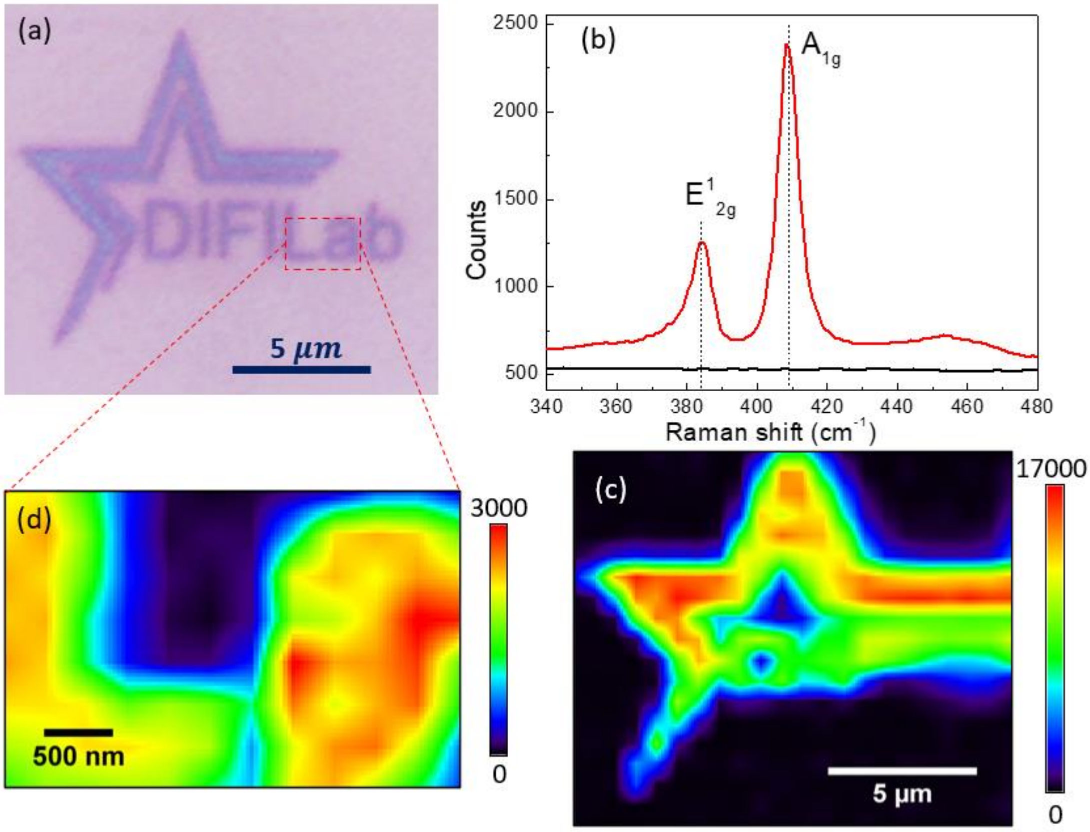

Figure 2.10 (a) Optical microscopy image of a few-layer MoS_2 nanocircuit. (b) Micro-Raman spectra detected on the MoS_2 nanopaths (red line) and on the neighboring Si region (black line). (c,d) Micro-Raman maps detected on the whole MoS_2 nanocircuit and onto a detail (highlighted region in panel a), respectively. The maps show the signal detected in the range from 370 cm^{-1} to 429 cm^{-1}, corresponding to E^1_{2g} and A_{1g} modes.

2.4.2 Electrical characterization of TMD nanocircuits

To reveal the spatial arrangement of the MoS_2 nanostructures overcoming the optical diffraction limit, and to investigate the local electrical properties Kelvin Probe Force Microscopy (KPFM) was employed. The Kelvin Probe Force Microscopy (KPFM) maps have been acquired by a Nano Observer AFM (Concept Scientific Instruments) operating in single-pass mode and equipped with a platinum-coated silicon tip, in order to extract contact potential difference maps of MoS_2 nanopaths lying on a Si/SiO_2 substrate. We define the contact potential difference (CPD) referred to SiO_2 work function as:

$$\Delta_{CPD} = \frac{1}{e}(\phi_{SiO_2} - \phi_s)$$

where e is the elementary electron charge, ϕ_{SiO_2} is the silica work function and ϕ_s is the work function of the surface underneath the tip during the scan. **Figure 2.11a** shows the Δ_{CPD} map obtained on the MoS_2 nanopaths, highlighting their strong electrical contrast in terms of surface potential.

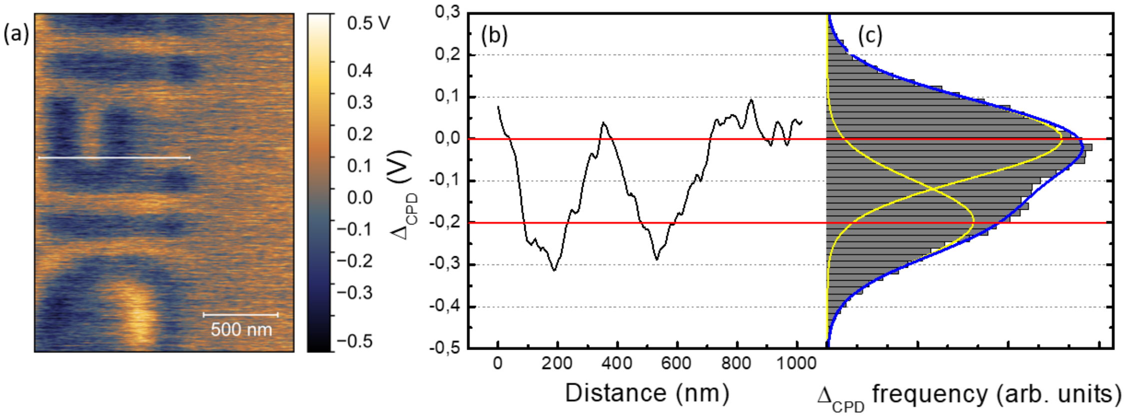

Figure 2.11 (a) Kelvin Probe Microscopy image showing the Contact Potential Difference referred to silica work function ϕ_{SiO_2} (Δ_{CPD}) signal, characterized by a strong electrical contrast of the MoS_2 nanocircuits. (b,c) Δ_{CPD} line profile corresponding to white line in panel a and histogram of the detected CPD signal, respectively.

An example of a Δ_{CPD} cross-section profile acquired across the MoS_2 nanotracks (white line in **Figure 2.11a** and corresponding profile in **Figure 2.11b**) shows a work function difference between MoS_2 nanopaths and silica substrate of about 200 meV. This electrical response is uniform over the CPD map, highlighting the MoS_2 to silica contrast with spatial resolution in the range of few tens of nm, determined by the Kelvin nanoprobe radius and by lock-in modulation voltage. In particular, the histogram of the Δ_{CPD} map (**Figure 2.11c**) is characterized by two distributions, respectively centered at 0 mV and -200 mV, as confirmed by the fit and by the cross-section profile at the MoS_2/silica edge. The former peak arises from the silica substrate and the latter from the MoS_2 nanopaths. Considering the value of SiO_2 work function ϕ_{SiO_2}~5.05eV, the measured Δ_{CPD} map characterized by 200 mV contrast at the MoS_2/SiO_2 interface allows to quantify the work function of the MoS_2 nanopaths as ϕ_{MoS_2}~5.25eV, in good agreement with respect to recent reports[173,174].

In order to show the potential of the 2D-TMDs nanocircuits as active optoelectronic interconnects, we devise a simple ultra-thin device thanks to the non-invasive t-SPL approach. High quality metallic contacts can be precisely aligned onto the nanocircuits by exploiting the peculiar in-situ imaging and real-time nanolithography capabilities (i.e. direct overlay method), avoiding undesired damage and contamination for the fragile layers[169]. In this way the electronic transport properties of the TMDs layers can be deeply investigated with nanoscale spatial resolution via conductive-AFM nanoscopy (c-AFM). This c-AFM approach enabled the high-resolution detection of current and resistance maps onto the MoS_2 nanodevice, avoiding damage of the sample and/or the probe[175,176]. The c-AFM maps (current, resistance) were acquired in contact mode by applying a DC bias voltage of 0.5 V to the sample (metallic nanoelectrode) with respect to a p-doped single crystal diamond tip, using the same Nano Observer AFM equipped with a ResiScope module enabling c-AFM nanoscopy over wide current (and resistance) ranges avoiding damage to the sample.

Figure 2.12 shows an example of 2D-TMD device based onto a few-layer MoS_2 nanofinger. A metallic nanocontact based on a Ti/Au thin film (thicknesses 2 nm / 20 nm) is precisely aligned onto the MoS_2 nanocircuits thanks to in-situ imaging and direct t-SPL overlay nanopatterning based on the polymeric bi-layer process. **Figures 2.12a** and **2.12b** show the local-current and -resistance map of the MoS_2 nanofinger device, detected in real-time with the topography (**Figure 2.12c**). A strong electrical contrast is detected at the MoS_2-substrate edges within both the current and the resistance map, as highlighted in **Figure 2.12d** by a comparison between topography and local current extracted along a horizontal profile (white dashed line in **Figures 2.12a** and **2.12c**). The electrical maps demonstrate the semiconducting behavior of the MoS_2 nanocircuit device with nanoscale spatial resolution, precisely corresponding to the AFM topography. The resistance (current) map shows a lower resistance (higher current) in proximity of the nanoelectrode, while a gradual resistance increase (current decrease) is detected as the electronic mean path to the contact increases. To quantify this effect, a current profile, extracted along a vertical profile of **Figure 2.12a** (dashed red line), is shown in **Figure 2.12e**. Due to the strong anisotropy of the MoS_2 nanofinger, endowed with nanoscale width, this curve well represents our system. The experimental data (black dots) are well described by a power law function $I(d) \propto d^{\alpha}$ with $\alpha = -1.1$ (red line in **Figure 2.12e**), where d is the distance between the metal nanoelectrode and the conductive nanoprobe. This behavior well fits with the response of a semiconducting few-layer MoS_2 channel of length d whose resistance R_c is expected to scale as $R_c \propto d^{-1}$. The local resistance maps allow to estimate a resistivity value of about 5 Ω·m for these large area few-layer MoS_2, under the approximation of a long channel device. This result is comparable to state-of-the-art

MoS_2 layers[160,177,178] and very promising in view of deterministic 2D-TMDs nano-interconnects.

Furthermore, this few-layer nanofinger configuration highlights the possibility to engineer even more complex few-layer van der Waals semiconducting nanodevices, taking advantage of the non-invasive t-SPL nanolithography for the arbitrary and precise alignment of 2D materials endowed with their original optoelectronic properties.

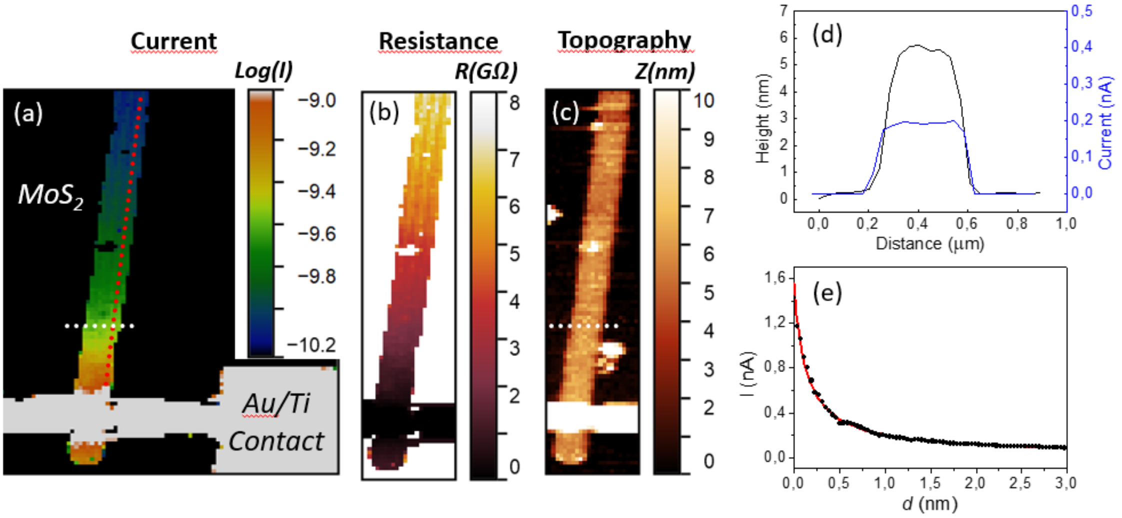

Figure 2.12 (a-c) AFM current and corresponding local resistance and topography map of a few-layer MoS_2 nanostripe device under 0.5V DC bias. (d) Current (blue) and corresponding topography (black) line profiles extracted across the substrate-finger edges (dashed white line in panel a and c). (e) Current profile extracted from the current map of panel a (dashed red line), showing a power law decay as the distance d from the nanocontact increases. A power law $I(d) \propto d^{-1.1}$ (red line) is superimposed to the data (black dots).

We have shown the additive nanolithography of few-layer MoS_2 nanocircuits arbitrarily and precisely engineered onto large-scale wafers, thanks to the non-invasive thermal-Scanning Probe Lithography approach combined with the homogeneous growth of few-layer TMDs across several cm^2. The thermal nanolithography of a sacrificial polymeric layer, combined with the large-scale physical deposition of the few-layer TMDs, uniquely enables the on-demand reshaping of ultra-thin TMDs layers with nanoscale spatial resolution. The so formed MoS_2 nanocircuits grow into the 2H-TMD semiconducting phase, as shown by their vibrational fingerprint in Raman micro-spectroscopy, and by their electrical work function in Kelvin probe nanoscopy. High quality few-layer TMDs nanodevices have been further engineered by exploiting the non-invasive t-SPL approach to precisely align metallic nanocontacts onto the MoS_2 nanocircuits. This configuration has enabled the local probing of the electronic transport properties of the few-layer MoS_2

nanocircuits, resolved via conductive-AFM nanoscopy. The local-conductivity maps highlight the competitive transport properties promising behavior of these reshaped MoS_2 nanodevices as few-layer semiconducting interconnects in ultra-thin devices and components. Remarkably these results highlight the possibility to engineer even more complex van der Waals heterostructure nanodevices by this original t-SPL based technique, uniquely preserving the optoelectronic properties of the fragile few-layer materials. These reshaped 2D-TMDs nanocircuits thus open new perspectives for the integration of 2D semiconducting layers in scalable new-generation devices with impact in electronics, photonics, renewable energies and quantum technologies.

2.5 Physical deposition of few-layer WS_2 films

In Chapter 1 van der Waals heterostructures based on 2D-TMDs were introduced, underlining the technological relevance of the new optoelectronic properties arising from the band structure coupling of two different materials. Having now developed a process for the growth of large area ultra-thin MoS_2 films, we explored the possibility to apply the same process to another TMD material. In particular, due to the interesting type-II staggered bandgap alignment between MoS_2 and WS_2, the natural choice was to extend the process to the latter material.

In paragraph 2.3.3. I described the growth process implemented for the synthesis of large area ultra-thin MoS_2 layers, based on the sputtering deposition from a bulk target of a sub-stoichiometric film that is relatively stable to high temperature of the recrystallization process. Due to the simplicity of the physical deposition process and to the possibility of changing the target material, I tried to extend the synthesis to the growth of WS_2 layers. To this end, a WS_2 target was loaded in the vacuum chamber for the sputtering deposition of a WS_x precursor, recurring to the Ion Beam Sputtering technique described in paragraph 2.3.1. The precursor was subsequently recrystallized at high temperature in a sulfur environment with the same process parameters optimized for MoS_2 films.
An example of recrystallized WS_2 ultra-thin film extending over cm^2 scale with thickness of about 3 nm is shown in **Figure 2.13a**. The recrystallized WS_2 films vibrational and optical response for such sample is reported in **Figures 2.13b** and **2.13c**, respectively. The Raman spectrum shows the typical vibrational modes of WS_2, with the in-plane E^1_{2g}

mode excited at 355 cm^{-1} and the out-of-plane A_{1g} mode excited at 421 cm^{-1}. In parallel, the extinction spectrum shows the A-B excitonic transition at 635 nm and 535 nm, while the band nesting region is detected in the range 380-460 nm.

The optical and vibrational characterization demonstrates the growth of large area semiconductor WS_2 films by simple change of the precursor film, thus proving that our physical deposition process is robust and can be extended to other TMD materials.

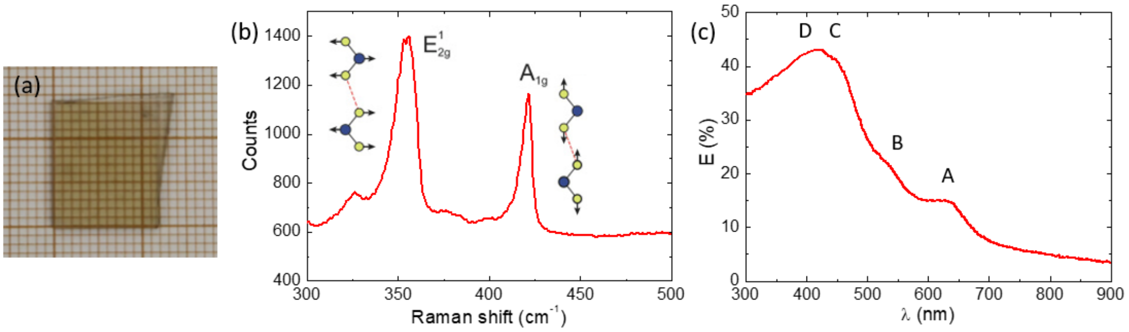

Figure 2.13 (a) Photograph of a large area WS_2 film. (b) Raman spectrum of recrystallized WS_2 film. (c) Optical extinction spectrum of an ultra-thin WS_2 film.

Chapter 3 – Large area van der Waals heterostructures

Having consolidated the growth process for large area ultra-thin films of MoS_2 and WS_2, the next step was to combine them to grow large area van der Waals heterostructures. The band structure coupling of these two TMDs is intriguing because it forms a type-II heterojunction in which photogenerated charges are separated in the two different layers, with consequent advantages in photoconversion applications.

In paragraph 3.1 I will present the fabrication of large area van der Waals heterostructure with a simplified geometry consisting of a simple vertical stack of MoS_2 and WS_2 layers extending at the cm^2 level. As a simple demonstration of the potential of TMD-based heterostructures I will show some preliminary results highlighting enhanced photocatalytic degradation of Methylene Blue dye molecules in solution.

In paragraph 3.2 I will address one of the fundamental steps required for the development of more complex TMD based large area optoelectronic device in superstrate configuration, i.e. the controlled fabrication of electrically conductive transparent window layers extending over large areas. In subparagraphs 3.2.1 and 3.2.2 I will respectively describe the results obtained for Indium Tin Oxide (ITO) and graphene.

In paragraph 3.3 I will show the experimental results for a large area van der Waals heterostructure fabricated on a large area graphene electrode, showing first evidence of photoconductive behavior, though with very low values of photovoltage and photocurrent due to the high sheet resistance of the graphene layers.

In paragraph 3.4 I will present preliminary results describing an innovative approach for reducing the sheet resistance of the graphene transparent contact, combining it with an ITO bottom layer. In subparagraph 3.4.1 I describe promising results obtained for a lower process temperature at 600°C, since the ITO layer is protected from sulfurization by graphene during TMD recrystallization.

3.1 Large area MoS_2/WS_2 vertical heterostructures

Large area vertically stacked MoS_2/WS_2 layers were sequentially deposited recurring to the ion beam sputtering process already described in paragraph 2.3.1. In this case, IBS deposition was preferred to RF sputtering since the set-up allows sequential in-situ deposition of two TMD precursor films from different stoichiometric WS_2 and MoS_2

targets. By shifting the linear stage holding the targets under the ion beam trajectory, we can easily control the selective sputtering deposition from a specific TMD target. The deposited TMD stack is then recrystallized in a single high temperature step, as described in paragraph 2.3.3, by exploiting the compatibility in the recrystallization parameters for the two different TMD layers. In this way I developed a controlled approach for the growth of large area TMD semiconductor heterostructures. **Figure 3.1a** shows a photograph of a fabricated sample based on vertically stacked MoS_2/WS_2 few-layer films homogeneously extending over large scale (cm^2), along with a sketch to clarify the heterostructure composition. The buried WS_2 layer has a nominal thickness of about 2.5 nm while the coating MoS_2 layer is about 10 nm thick.

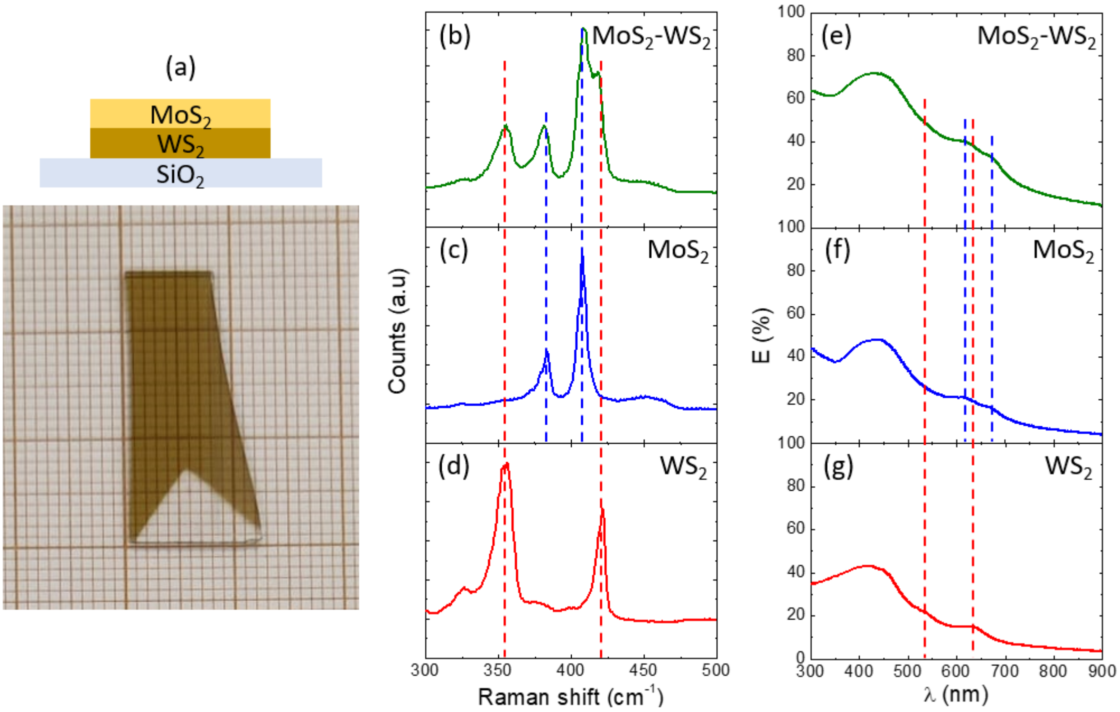

Figure 3.1 (a) photograph of a large area recrystallized vertically stacked bilayer of MoS_2 and WS_2. (b-d) Raman spectra for the bilayer, for MoS_2 and for WS_2. (e-g) Optical extinction spectra for the bilayer, for MoS_2 and for WS_2.

The heterostructure film was characterized by means of Raman microspectroscopy in different regions of the samples, observing a homogeneous vibrational response over large area. The spectrum of the heterostructure bilayer is reported in **Figure 3.1b** and clearly shows the characteristic E^1_{2g} and A_{1g} vibrational modes pertaining to MoS_2 and WS_2, already described in Chapter 2. The spectrum is directly compared with the Raman spectra independently acquired on the corresponding bare few-layer MoS_2 and WS_2 films, respectively (**Figures 3.1c** and **3.1d**). The presence of the vibrational modes of both materials clearly indicates the successful recrystallization of the bilayer which preserves the crystalline fingerprints of the individual layers.

Optical spectroscopy measurements were also performed to characterize the heterostructure. The extinction spectrum acquired for the sample is reported in **Figure 3.1e**. As in the Raman case, the reference optical spectra for the individual TMDs layers are reported for a direct comparison in **Figures 3.1f** and **3.1g**, respectively. Due to the spectral overlapping of the relevant features of the two materials, the optical signal of **Figure 3.1e** is dominated by the thicker MoS_2 layer: the WS_2 A exciton (640 nm) is covered by the MoS_2 A and B excitons (675 nm and 625 nm) and the WS_2 and MoS_2 band nesting regions spectrally match, while only a very shallow WS_2 B exciton (540 nm) can be detected.

3.1.1 Photocatalytic set-up and experimental procedures

As already described in Chapter 1, the physical and technological interest in TMD-based van der Waals heterostructures is broad ranged, especially if TMD pairs with type-II band alignment are stacked in view of self-powered photoconversion applications[62,79–81]. Here, I will now present a possible application of the vertically stacked MoS_2-WS_2 layers in photonics for boosting the efficiency of a test photocatalytic process. In this context, 2D-TMD materials represent a promising alternative for photo-to-chemical energy conversion applications due to their extremely high surface/volume ratio and to their optimal semiconducting gap which promotes the photogeneration of electron-hole couples[69–71]. In the experiments, Methylene Blue (MB) test molecules are chosen since they represent a typical organic pollutant as well as an ideal model probe to investigate photocatalytic degradation. Consequently, the MB photobleaching reaction is of particular interest for testing the efficiency of the photocatalysts in water remediation applications.

Before starting with the presentation of the photobleaching results, I will introduce in this subparagraph the photocatalytic set-up and the experimental protocol that we employed for this kind of experiments. Both the set-up and the protocol and implemented in the last years by two colleagues of mine, Matteo Barelli and Giulio Ferrando, while working on MB photobleaching using plasmonic nanostructures[179].

The set-up is shown in **Figure 3.2**. It is based on a tunable light source (Newport TLS130B-300X) equipped with a 300 W Xenon arc lamp, a CS130B monochromator and a 1-inch output flange. The monochromatized beam (±25 nm of bandwidth) passes through a wire grid polarizer (Thorlabs WP25M-UB), so that the electrical component of the electromagnetic radiation is linearly polarized. To ensure a uniform illumination, the cuvettes containing the MB solution are placed at 40 cm of distance from the lamp output flange. The source power is set in order to have a power density hitting the surface of the cuvettes equal to 2 mW cm^{-2} for all the experiments performed, as measured with a Newport 818-UV optical power detector connected to a Newport 1919-R optical power meter we measured the average beam power density.

For the experiments, we used two quartz cuvettes with 1 cm side square internal section and filled them with 2 mL of MB solution. One cuvette is used for the sample, the other one is used as a blank reference to determine the natural photodegradation rate of MB under exposure. By comparison of the two cuvettes, it is thus possible to calculate the photobleaching performances of the sample.

The MB concentration is kept constant during the various experiments at about 1.3×10^{-5} mol L^{-1} by diluting MB powder in mQ water. The concentration is estimated through a measurement of the solution absorbance ($A = -\log(T)$, where T is the measured transmittance) and using the Beer Lambert law resolved for the concentration $C = A\ d^{-1}\ \varepsilon^{-1}$, where d is the optical path expressed in cm and ε is the molar absorption coefficient, for which we used an average value from the literature of 7.5×10^4 L mol^{-1} cm^{-1} at $\lambda =$ 665 nm, corresponding to the MB absorption peak[180,181].

The cuvettes top is covered with parafilm to minimize the evaporation of the solvent, then they are left to stir at room temperature for 1 hour. At this point the sample is placed inside one cuvette and both of them are left to stir for another hour to reach a complete surface absorption/desorption equilibrium before the exposure. To even out the exposure of the cuvettes, they are swapped every 30 minutes of illumination. At regular intervals of photons dose the absorbance of both solutions is measured by measuring the optical extinction through the solution with a fiber-coupled optical transmission set-up.

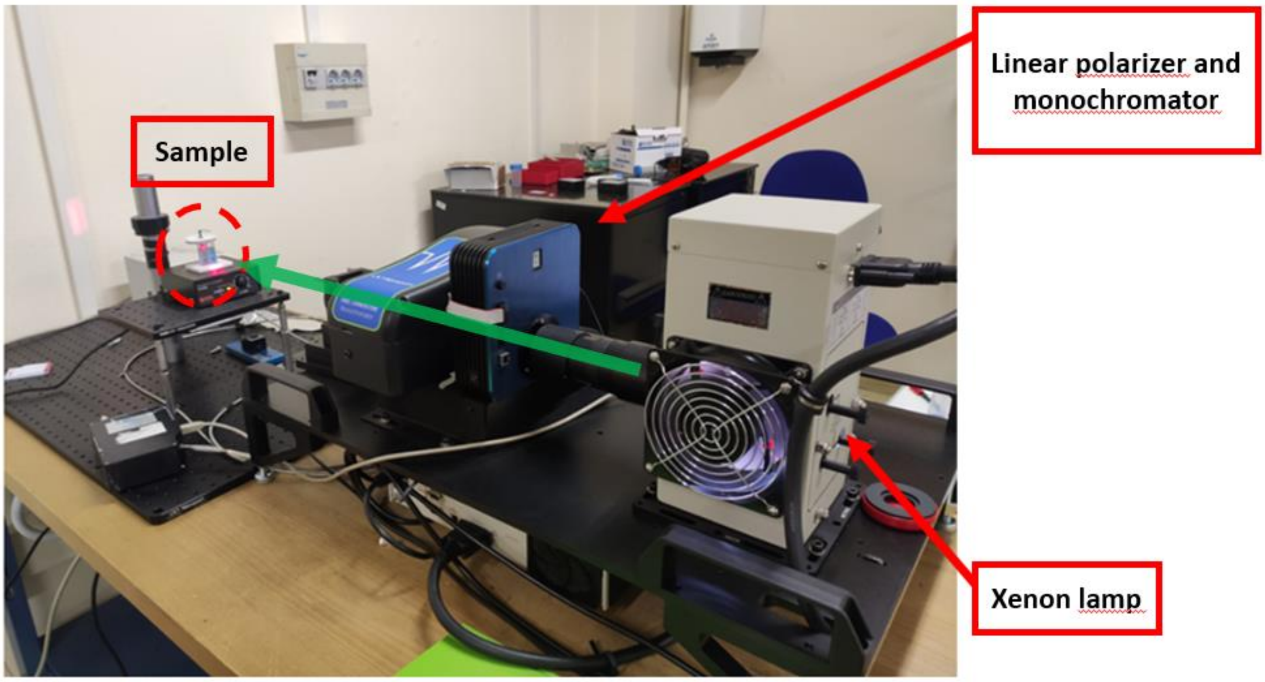

Figure 3.2 Photocatalytic set-up implemented in our laboratory.

3.1.2 Photocatalytic dissociation of organic pollutants from large area MoS_2/WS_2 vertical heterostructures

Using the set-up just described, we conducted photobleaching experiments adopting different 2D-TMD layers as photocatalysts. To this end, I fabricated a vertical heterostructure made by a 12 nm thick WS_2 layer coated by a 2 nm thick MoS_2 layer. To compare the heterostructure photobleaching performances with those of the individual TMD layers, I also fabricated a 12 nm thick WS_2 layer and an 8 nm thick MoS_2 layer (thickness chosen in order to have an optical absorption comparable to the heterostructure while maintaining the same MoS_2 surface chemistry).

In **Figure 3.3a** the optical transmission spectra for the initial MB solution, the heterostructure sample and the individual MoS_2 layer are reported.

The blue curve represents the transmission of the initial MB solution at a concentration $C_0 = 1.3\times10^{-5}$ mol L^{-1}. A double dip is observed in the spectral region from 550 nm to 700 nm, corresponding to the characteristic absorption peaks of MB. Almost full transmittance is observed for shorter and longer wavelengths respectively. The concentration of MB molecules in water solution is evaluated by measuring the characteristic transmittance of the solution in a quartz cuvette at a wavelength of 660 nm, in correspondence to the maximum of MB absorbance.

The red curve represents the transmission of the MoS_2/WS_2 heterostack. The optical spectrum is dominated by the spectral features of the thicker WS_2 layer, showing the characteristic excitonic modes at 630 nm (A exciton) and 540 nm (B exciton) and the band nesting region in the 400-450 nm spectral region.

The green curve represents the transmission of the individual MoS_2 sample, showing the characteristic A and B excitons (at 675 nm and 625 nm respectively) and the band nesting region at 400-450 nm. As already mentioned, its optical transmittance is comparable to the MoS_2/WS_2 heterostack.

For the MB photobleaching experiments, we illuminate the cuvettes containing the MB solution and the TMD samples with monochromatized light at a wavelength of 450 nm (25 nm bandwidth). As shown by the yellow band in the transmission spectra in **Figure 3.3a**, such wavelength on one side ensures the maximum reactivity from the TMD samples in correspondence to the band nesting region where optical absorption is higher, and at the same time reduces MB self-degradation because the molecule weakly absorbs light in the selected spectral region.

The results of the MB photodegradation experiments are reported in **Figure 3.3b**. The graph shows the evolution of MB concentration in solution (C/C_0), as a function of the photon exposure dose (Φ) expressed in photons/cm^2. The concentration is normalized to the initial MB concentration $C_0 = 1.3\times10^{-5}$ mol L^{-1}. The blue triangles refer to photodegradation of a blank MB solution illuminated at 450 nm. The red squares and green circles describe the experiments in presence of the WS_2 layer and of the MoS_2 layer, respectively: in both cases the TMD layer promotes photodissociation which is comparatively stronger in the MoS_2 case. Finally, the magenta triangles refer to the photobleaching experiment in the case of the WS_2/MoS_2 heterojunction, evidencing that the MB photodegradation rate is the highest among the selected TMD configurations, i.e. a factor 2.0 higher than for WS_2, and 1.3 higher than for MoS_2 films of comparable active area. Comparison with the latter sample is particularly relevant since they have in common the same MoS_2 outer interface, which determines an equivalent surface chemistry. In this way, since the optical extinction of the two samples at 450 nm wavelength is comparable (**Figure 3.3a**), it is possible to directly evaluate the effect of the charge separations in the type-II van der Waals heterostructure on the photobleaching reaction[182]. The type-II band alignment of the WS_2 and MoS_2 layers ensures a longer lifetime of the photogenerated carriers in the case of the heterostructure with respect to the bare TMD film, since the built-in field at the interface drives spatial separation of carriers with the electrons drifting towards the MoS_2 layer and the holes towards the WS_2 layer[113].

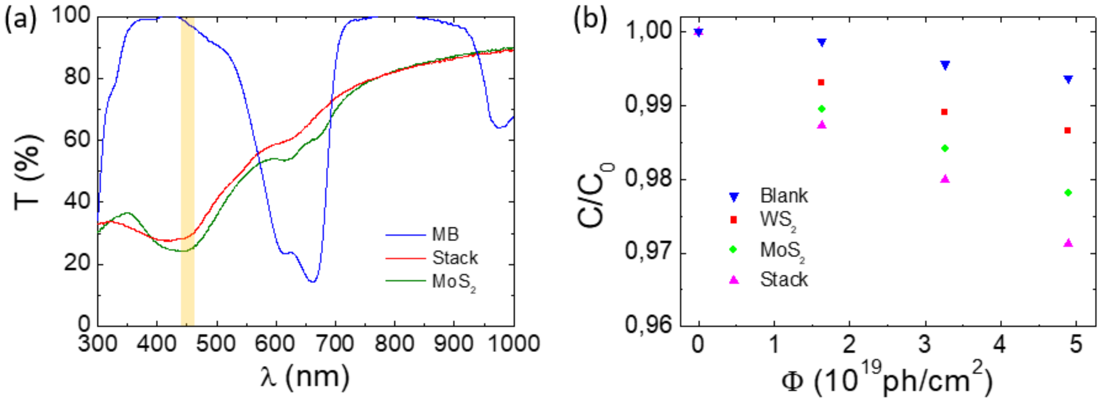

Figure 3.3 (a) Transmission spectra for initial MB solution, TMD stack sample and MoS_2 sample; yellow bar indicates the exposure wavelength. (b) MB solution concentration as a function of exposure dose for illumination with monochromatic light at 450 nm wavelength and different photocatalysts.

We have thus demonstrated the nanofabrication of a large area Van der Waals heterostructure platform that can effectively act as a photocatalyst by exploiting the peculiar type-II band alignment. These results are very promising and open several possibilities for integration of this large area 2D platforms in effective photo to chemical energy conversion devices with impact in photonics and energy storage.

3.2 Van der Waals heterostructures for photonics

The enhancement of photocatalytic dissociation of dye molecules represents a straightforward application of large area TMD-based heterostructures obtained following a straightforward and scalable approach, as I just demonstrated for the MB photobleaching. However, to fully exploit the potential of type-II band alignment in photonic devices, a vertical heterostructure device extending over macroscopic areas can be devised by introducing a transparent back electrode that supports the TMD heterostack and by coating the TMD layers with a top metallic contact, as shown in in **Figure 3.4** This is the so called superstrate configuration in a photonic device where the TMD active layers are vertically stacked on top of a transparent bottom contact, while the top contact is metallic and also works also as a back reflector effectively trapping the light shed from the back side of the device through the transparent SiO_2 substrate. In this way is possible to effectively collect the photogenerated carriers into a large area ultra-thin photoconversion device.

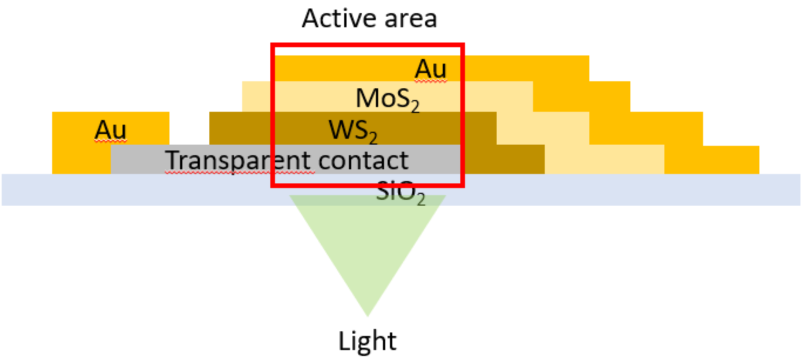

Figure 3.4 Photonic device based on vdW hetersotructures in superstrate configuration.

With respect to photocatalytic applications, here the design requires additional fabrication steps. Deposition of metallic top contacts (Au) was realized by physical growth (ion beam sputtering deposition) through a proximity mask, with the addition of an ultra-thin Ti adhesion layer. The latter step was simplified by the fact that devices fabricated on large area TMD films just require macroscopic contacts, while in the case of micrometric mechanically exfoliated or CVD-grown flakes a lithographic nanofabrication would have been necessary.

The fabrication of a transparent back electrode required to develop specific processes since we worked for the first time with Indium Tin Oxide (ITO) and graphene, two promising materials for application in transparent conductive window layers. I will focus on ITO in subparagraph 3.2.1 and on graphene in subparagraph 3.2.2, introducing their characteristics and their advantages and drawbacks.

3.2.1 Fabrication and test of Indium Tin Oxide transparent electrodes

Indium Tin Oxide (ITO) belongs to the family of Transparent Conductive Oxides (TCOs), i.e. materials characterized by good electrical conductivity and high optical transparency. In the case of ITO, this is obtained by heavily doping indium oxide with tin oxide (about 10%): the band structure of indium oxide has a bandgap of 3.7 eV, typical of an insulator, but the doping moves the Fermi level inside the conduction band. In this way it is possible to obtain a transparent material but with a relatively low sheet resistance (in the range of 20-100 Ω/□) that select these films as a suitable platform as transparent electrodes. A good compromise can be found between conductivity and transparency either by tailoring the film thickness (an increase results in a lower sheet resistance) or by threating the films at high temperature to optimize the electronic transport properties[183].

By using the RF sputtering set-up described in paragraph 2.2.1, I deposited 50 nm thick large area ITO films on dielectric silica substrates. In **Figure 3.5a** a photograph of an as-deposited ITO layer is shown, highlighting the high transparency of the film. The sheet resistance of the thin film was measured in a two-wire configuration by using two pressure contacts placed 6 mm apart, and reads about 600 Ω.

For our purpose, ITO films must be inert in sulfur atmosphere at high temperature. To verify this, a comparable ITO thin film was loaded in the furnace and subjected to a recrystallization process as in the case of TMD layers. The sample after this treatment is shown in **Figure 3.5b**: a yellowish and opaque film can be observed that have been attributed to undesired reactions between the ITO surface and the sulfur atmosphere occurred during the process. This has been confirmed by measuring the sheet resistance of the thin film after the high temperature process and observing an insulating behavior at difference of the pristine ITO film.

Raman characterization was then performed to investigate the samples and it is shown in **Figure 3.5c**. The black trace is the spectrum acquired on the as-deposited ITO, which shows no spectral features in the selected range. The red trace instead is the spectrum acquired on the treated sample, in which new peaks arise because of a change in the film composition induced by the reactions that occurred at high temperature in a sulfur atmosphere. Specifically, the vibrational modes that appear in the spectrum at 187 cm^{-1} (F_{2g}), 251 cm^{-1} (A_{1g}), 271 cm^{-1} (E_g), 311 cm^{-1} (A_{1g}), 329 cm^{-1} (F_{2g}) and 368 cm^{-1} (A_{1g}) can be attributed to the formation of β-In_2S_3 structure phase during the sulfurization process[184,185].

Optical transmission characterization was also performed. The spectra reported in **Figure 3.5d** evidence a decrease in transmission for the sulfurized ITO film, that is reduced from above 80% to about 60% and show a transmittance drop below 500 nm compatible with β-In_2S_3 transmittance[186,187].

These results clearly implicate that in our case ITO layers are not promising materials for the fabrication of transparent conductive electrodes to be used as bottom contacts in TMD-based van der Waals heterostructures, since the recrystallization process results both in a metal to insulator transition and in a reduction of the optical transmittance.

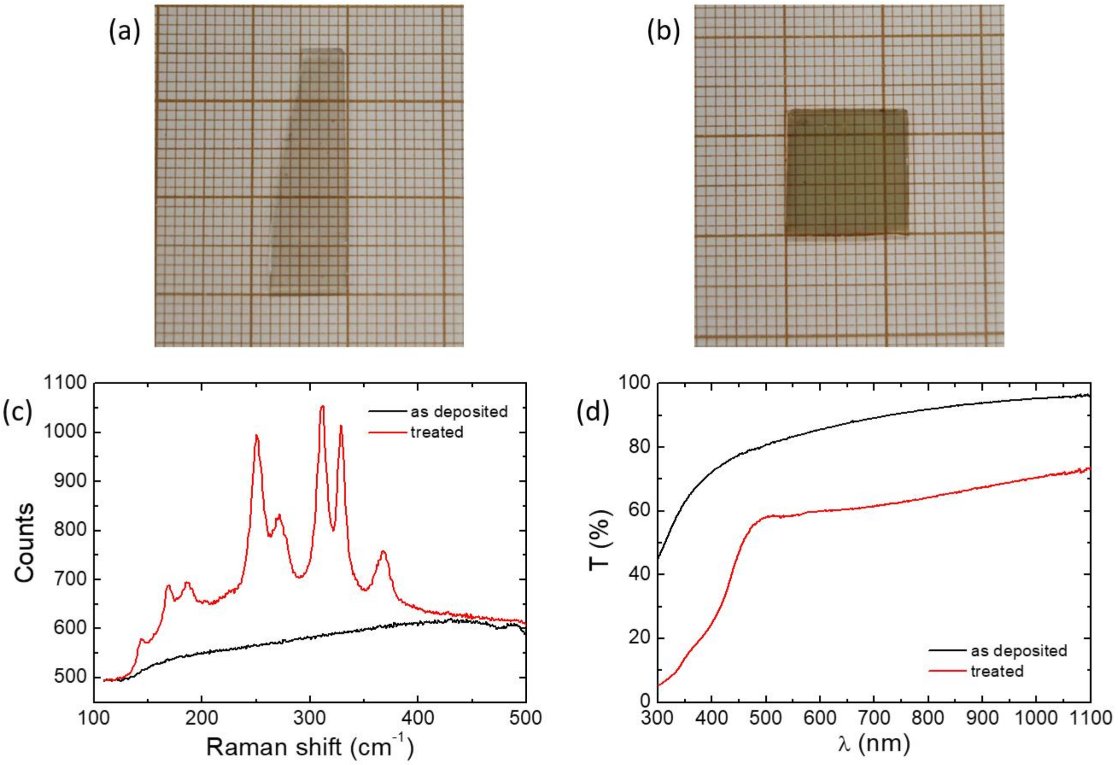

Figure 3.5 (a,b) Photographs of as-deposited and treated ITO layers. c) Raman spectra for the as-deposited and treated ITO layers. d) Optical transmission spectra for the as-deposited and treated ITO layers.

3.2.2 Fabrication and characterization of Graphene transparent electrodes for TMD layers

To circumvent the issues related to ITO sulfurization at high temperature, I moved to graphene as a possible alternative for the fabrication of large area transparent electrodes. Graphene is the first layer in the family of 2D materials[2], composed by a single layer of carbon atoms arranged in a hexagonal lattice with sp^2 coordination, behaving as a semimetal due to the presence of Dirac cones at the vertices of the hexagonal Brillouin zone. This band structure confers to graphene extraordinary electronic properties with an extremely high electron mobility (2×10^5 cm^2 V^{-1} s^{-1})[188]. In addition, graphene is highly transparent since the theoretical absorption is of 2.3% for a single monolayer[189]. For these properties, graphene is a promising choice as a conductive window layer.

In view of light harvesting applications, we chose to transfer commercial large area graphene layers onto transparent SiO$_2$ substrates. To electrically connect the TMD heterostructure on the side of the substrate, we deposited large area bilayer graphene transparent electrodes recurring to a wet transfer process in deionized water[190], as illustrated in **Figure 3.6a**. The substrates were treated in a custom-made set-up which allows to expose the surface to an ozone producing UV-C lamp. In this way the surface hydrophilicity is increased, promoting the graphene transfer process. Initially, the CVD grown graphene 1x1" (purchased from Graphenea) is provided supported on a polymer film and coated by a sacrificial layer for protection. By immersion in deionized water, the graphene film capped by the sacrificial layer detaches from the polymer support and starts floating. The surface treated silica substrate is then immersed beneath so to fish the floating graphene from below. The sample is then dried for 30 minutes in air and annealed for 1 hour at 150°C on a hot plate. After that, it is stored in vacuum for 1 day to increase the adhesion to the substrate. Finally, the sacrificial layer is removed by washing in hot acetone (50°C) for 1 hour and in isopropyl alcohol for another 1 hour. **Figure 3.6b** shows a photograph of a graphene electrode with area of about 1 cm^2 after transfer on the silica substrate. I highlight that the transfer process can be easily scaled up over larger areas.

The transferred graphene electrodes have a very low roughness reduced at the 2-3 nm level, as shown in the AFM image of **Figure 3.6c** and in the selected line profile in **Figure 3.6d.** Therefore, the graphene film represents a good platform for the growth of 2D-TMDs stack with clean interfaces. Indeed, unlike the ITO, graphene is a 2D material and allows the clean van der Waals stacking at the electrode-TMD interface.

In **Figure 3.6e** we show the characteristic Raman spectrum of the graphene sheet after the transfer process, which highlights the presence of characteristic vibrational modes located at 1589 cm^{-1} and 2690 cm^{-1}, corresponding to the G and 2D band respectively[14]. A very small peak can also be observed at 1350 cm^{-1} which is related to defects and disorder in the graphene layer. The reduced intensity of this defect mode in comparison to the G and 2D bands indicates the high quality of the material[192].

Figure 3.6f shows an optical transmission spectrum acquired on a transferred bilayer graphene. Extinction in the visible range is about 5%, in agreement with the expected theoretical absorption value of 4,6% for a bilayer graphene. The high transparency is crucial for graphene application as a transparent window layer in photonic devices in superstrate configuration.

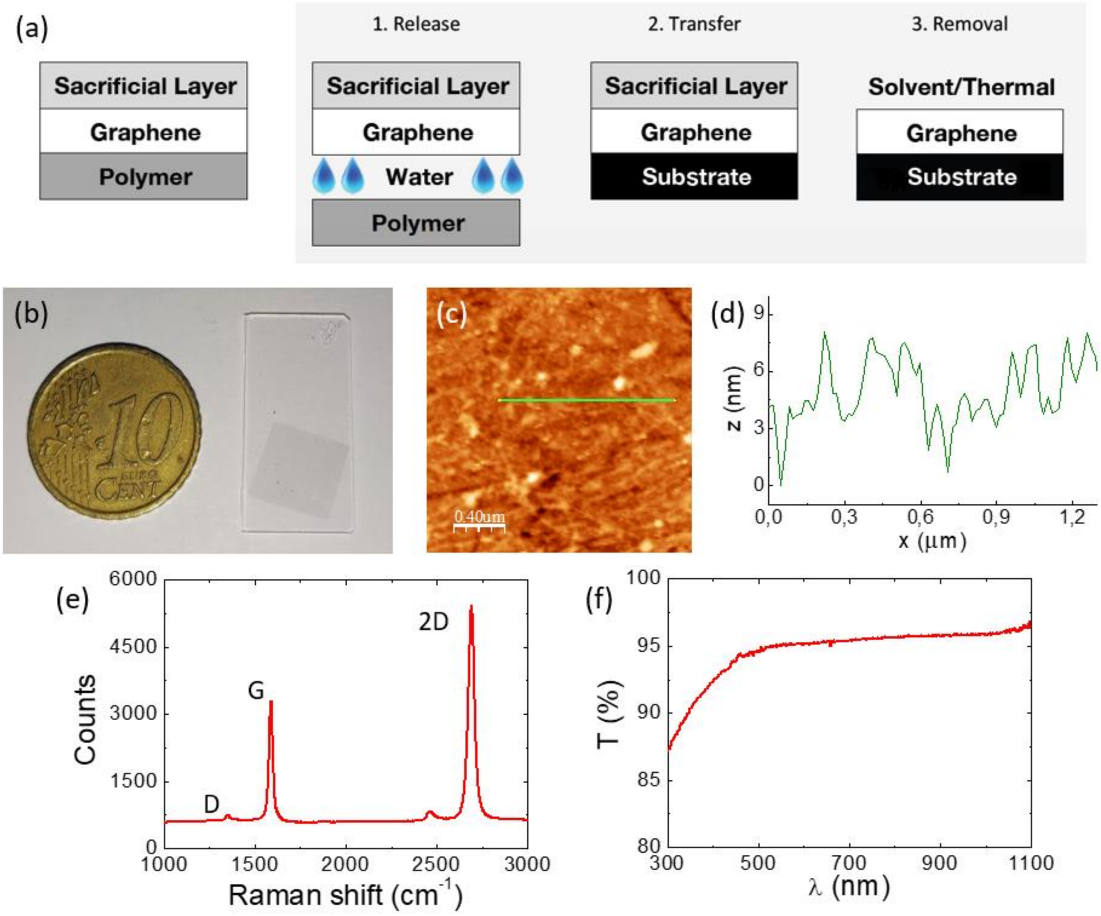

Figure 3.6 (a) Wet transfer process of graphene, from Graphenea EasyTransfer Instructions. (b) photograph of a large area bilayer graphene transferred on a dielectric silica substrate. (c,d) AFM image and extracted line profile for a transferred bilayer graphene. (e) Raman spectrum of a transferred bilayer graphene. (f) Optical transmission spectrum of a transferred bilayer graphene.

Two metal contacts were subsequently deposited through a proximity mask on a bilayer graphene electrode to determine the sheet resistance. For 2 mm wide contacts separated by a 2 mm gap, a sheet resistance value of about 1,5 kΩ is measured. This value is high and not comparable with that of the ITO films previously described, which however suffer degradation during the sulfurization process. For this reason, we tested graphene electrodes in the same conditions employed for TMDs recrystallization, to determine whether graphene remains transparent and conductive after being exposed to sulfur at high temperature.

Part of a graphene electrode was coated by a MoS_2 layer via IBS deposition. The MoS_2/graphene stack (sketch in **Figure 3.7a**) was then recrystallized according to the process described in paragraph 2.3.3. In this way, high quality few-layer MoS_2 films in the semiconducting 2H-phase are formed, as demonstrated by the micro-Raman spectrum reported in **Figure 3.7b**, which clearly shows the characteristic in-plane E^1_{2g} and out-of-plane A_{1g} vibrational modes, located at 378 cm^{-1} and 404 cm^{-1} respectively. The difference in the spectral positions of the two Raman peaks reads about 26 cm^{-1}, confirming the growth of a few-layer MoS_2 film.

The optical extinction measurements, performed across the UV-VIS-NIR spectral range on the same MoS_2/graphene sample, are reported in **Figure 3.7c**. The spectrum acquired on the stacked MoS_2/graphene (green trace) highlights the presence of the MoS_2 characteristic excitonic features, and further confirms the formation of a 2H-MoS_2 semiconducting phase. A and B excitons are excited at about 675 nm and 625 nm respectively, whereas the band nesting regions of C and D excitonic resonances are detected in the 400-450 nm spectral range. In the plot we also show the spectrum of the bare graphene bilayer sheet supported on the SiO_2 substrate (black trace), which is characterized by a weak and unstructured extinction in the range of 10%, spanning across the whole spectral range.

The high transmittance of graphene after the recrystallization process is encouraging in view of its application as transparent conductive electrode in optoelectronic devices.

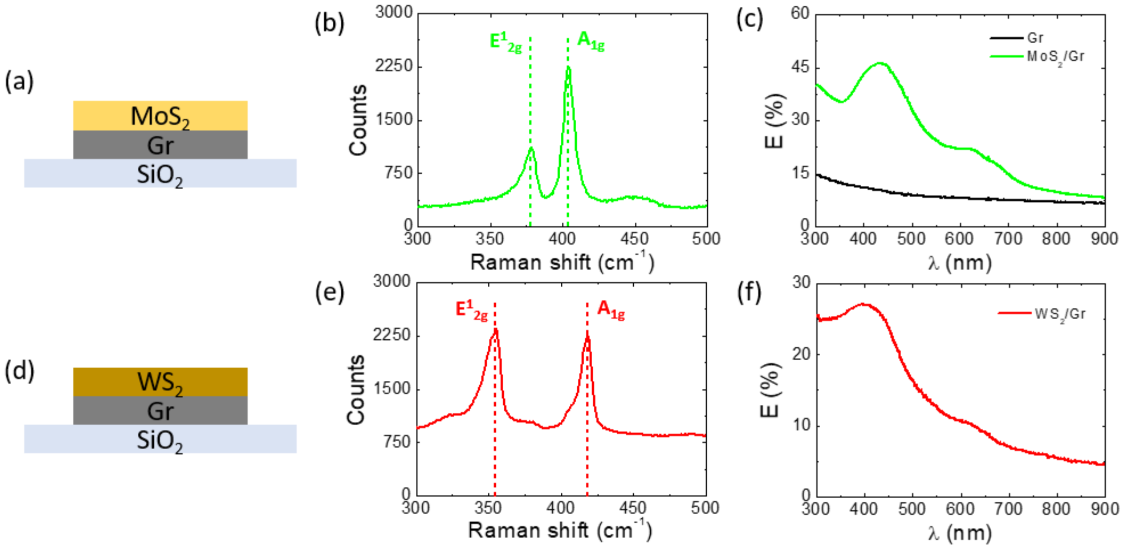

Figure 3.7 (a) Sketch of MoS_2/graphene/SiO_2 stack. (b) Raman spectrum of MoS_2 on graphene. (c) Optical extinction spectra acquired on bare graphene (black trace) and on MoS_2/graphene (green trace). (d) Sketch of a WS_2/graphene/SiO_2 stack. (e) Raman spectrum of WS_2 film on graphene. (f) Optical extinction spectrum acquired on WS_2/graphene.

A similar physical deposition approach has been followed for the growth of large area WS_2 films on graphene layers, in order to test WS_2 growth on graphene (sketch in **Figure 3.7d**). The micro-Raman spectrum reported in **Figure 3.7e** shows the characteristic vibrational in-plane mode E^1_{2g} and out-of-plane mode A_{1g}, located at 354 cm^{-1} and 418 cm^{-1} respectively, thus confirming the identification of a few-layer WS_2 film in the 2H-semiconducting phase.

Also the optical extinction spectrum, reported in **Figure 3.7f**, independently confirm that the few-layer WS_2 films are grown in the semiconducting 2H-phase. The main excitonic features of WS_2 are indeed located at about 630 nm (A exciton), 530 nm (B exciton, very shallow) and in the spectral range 400-450 nm (C and D transitions of the band nesting region).

Despite the higher sheet resistance compared to ITO, the excellent transparency combined to the 2D nature of graphene and its stability during the recrystallization process (both with MoS_2 and WS_2) make it the candidate material for the fabrication of a prototype photonic device.

3.3 Large area Van der Waals heterostructures MoS_2/WS_2/Gr for photonic applications

In the previous paragraph I introduced ITO and graphene as possible transparent conductive electrodes, describing the processes I developed for each of them. As I have just shown, ITO cannot stand with the high temperature process required by the TMD recrystallization, so in this paragraph I will discuss the results for a prototype device fabricated on a graphene layer used as electrode.

The possibility to devise self-powered photonic devices using 2D materials has been recently shown in van der Waals (vdW) metal-semiconductor-metal devices with engineered band alignment and in vdW MXene-silicon photodetectors[62,193]. Indeed, photon-to-current energy conversion in TMD-based heterostructures can be achieved at zero bias if the final energy band structure of the vdW 2D heterojunction intrinsically promotes the spatial separation of the photoexcited carriers thanks to a convenient band alignment between the semiconducting and/or metal component layers, as in the case of MoS_2/WS_2 heterojunctions[194]. A relevant example of this 2D scheme has been recently demonstrated in the case of type-II vdW heterostructures exhibiting energy and charge transfer effect[68,195,196]. Additionally, charge separation results in longer carriers lifetime which can be exploited for photocatalytic applications, being the charges involved in the reaction mechanism of crucial reactions as organic pollutants degradation[197]. Additionally, since the 2D materials are endowed with an extremely high surface/volume ratio, it is straightforward to foresee the potential of large area TMD-based heterostructures in photocatalytic applications[69,198].

Despite the optimal photoconversion properties of such kind of 2D devices are very promising, the scalability of this scheme towards real-world devices is still very poor since the device are typically based on exfoliated 2D semiconductor layer forming micrometric flakes. Continuous effort is put in the search for wafer-scale homogeneous growth techniques with thickness control, enabling the application of 2D materials in circuit integration[199]. At the same time, the development of large area transparent electrodes to be used as templates for the growth of van der Waals heterostructures is crucial for the fabrication of efficient photodetectors[200,201].

In the following I exploit the recent developments concerning large area physical deposition of 2D-TMD layers based on ion beam sputtering and recrystallization in sulfur enriched atmosphere, for the fabrication of van der Waals heterostructures. Vertical stacks of WS_2 and MoS_2 layers are synthesized on top of cm^2 scale graphene window electrodes. By contacting the graphene bottom electrode and WS_2/MoS_2 stack in superstrate configuration, photovoltage and photocurrent are measured across the type-II heterojunction formed by the two TMD layers. We also demonstrate an application of WS_2/MoS_2 stacked layers, without additional electrodes fabrication steps, as photocatalysts in Methylene Blue photodegradation reaction, showing higher dissociation rates with respect to individual TMD layers due to the favorable band structure. These results demonstrate the potential of TMD-based van der Waals heterostructures in the fields of energy conversion and photocatalysis.

Having demonstrated in the previous paragraphs the capability to grow by physical deposition the individual TMD on graphene layers placed deterministically on the SiO_2 wafer substrate, we now focus on the fabrication of a large area van der Waals MoS_2/WS_2 heterostructure supported on top of a transparent conductive graphene electrode (9×15 mm^2), as highlighted in the top sketch of **Figure 3.8a**. The TMD stack was then recrystallized in a single annealing step at 750°C since the experiments of **Figure 3.7** demonstrated that the individual components MoS_2 and WS_2 do successfully recrystallize in the semiconducting 2H-phase.

The photograph in **Figure 3.8a** shows a large-scale top view of the WS_2/MoS_2 heterostructure stack which covers a macroscopic active area of 1.2×1.2 cm^2 (0.9×1.0 cm^2 on graphene) defined by a deposition mask. Also visible in the photograph are the two macroscopic Au metal electrodes, respectively located on the uncoated edge of the graphene electrode (bottom contact) and on the graphene/WS_2/MoS_2 layer (top contact which also acts as optical back-reflector). A 2 nm thin Ti adhesion layer was deposited below the Au contact acting as an adhesion layer. Cross section sketches of the vdW heterostructure device have been added to clarify the device geometry. The design allows the direct contact of the graphene and prevents from shunts between the graphene and the MoS_2 layer. In the top sketch a cross sectional view of the device along the horizontal direction (black dashed line) is represented, showing the vertical stacking of graphene, WS_2 and MoS_2. The left sketch instead represents a cross sectional view of the device along the vertical direction (red dashed line), not showing the Ti adhesion layer for simplicity.

Figure 3.8b shows the Raman characterization of the TMD heterostructure, reporting a spectrum acquired on the vertically stacked MoS_2 and WS_2 layers (blue trace). The dashed lines have been added to the graph to highlight the spectral fingerprints belonging to the individual MoS_2 (green) and WS_2 (red) layers. The Raman spectrum of the TMDs heterostack shows the presence of the well separated E^1_{2g} modes corresponding to WS_2 and MoS_2, and of the A_{1g} modes which are partly overlapped spectrally, thus confirming that the thermal annealing process is effective in recrystallizing also the WS_2 layer buried below the MoS_2 layer. The Raman spectrum acquired on the bare graphene, close to the Au bottom contact (black trace), shows no spectral fingerprints of TMDs, thus demonstrating that the physical deposition process here described enables on-demand deposition of 2D-TMD semiconducting layers with a deterministic geometry defined by a proximity stencil mask. This is at variance with TMD deposition achieved by conventional CVD procedures, which lead to randomly nucleated flakes[136].

Figure 3.8c reports the extinction spectrum acquired in correspondence to the vertically stacked MoS_2/WS_2/graphene van der Waals heterostructure (blue trace). A comparison with the extinction spectra of bare graphene (black) and WS_2/MoS_2 stacked layers without graphene bottom layer (magenta) confirms that the graphene bilayer does not contribute with relevant spectral features to the observed extinction.

Due to the spectral overlap of the dominant excitonic features of the individual TMD layers, the optical response of the vertical heterostructure does not allow to resolve easily the individual components shown in **Figure 3.7**. In view of photoconversion applications, we highlight the substantial increase in the optical extinction with respect to the individual TMD layers, exceeding 60% in resonance to the band nesting region (C, D excitons around 400 nm) and reaching 30% in resonance to the A exciton transitions around 650 nm.

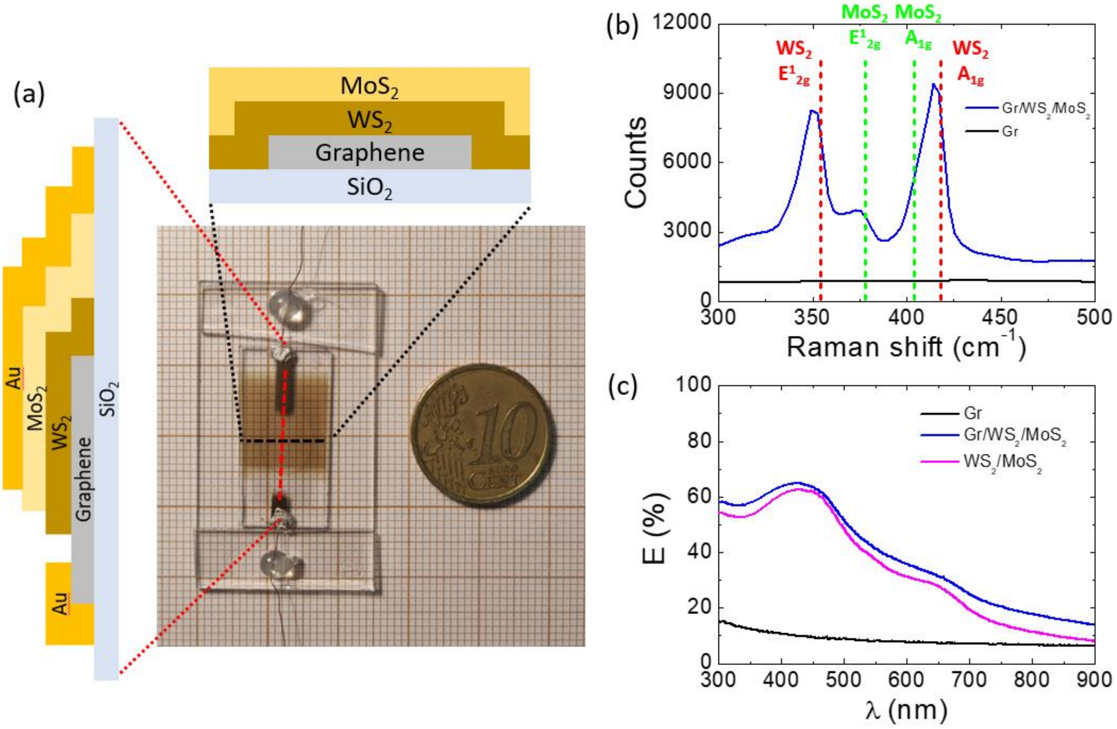

Figure 3.8 (a) Photograph of a large area van der Waals heterojunction composed by a stack of graphene, WS_2 and MoS_2. The top sketch represents a cross-section across the heterostructure stack along the horizontal direction (black trace), the side sketch represents a cross-section across along the vertical direction (red trace). (b) Raman spectra acquired in the heterojunction region (blue trace) and on the bare graphene (black trace). (c) Optical extinction spectra acquired on bare graphene (black trace), on WS_2/MoS_2 on top of graphene (blue trace) and on WS_2/MoS_2 outside the graphene (magenta trace).

The photoconversion response of the fabricated ultra-thin device has been investigated recurring to photovoltage and photocurrent measurements under controlled illumination conditions, with the light beam impinging from the side of the transparent silica support. Due to the type-II band structure of the TMD pair, the built-in voltage promotes vertical separation of the photogenerated charges across the van der Waals interface. The effective active area of the TMD heterostructure over which vertical transport occurs is defined by the top Au contact. In the current implementation the top contact active area, defined by sputtering through a lithographic proximity mask, spans across 2×4 mm^2, however we stress that for the heterostructure shown in **Figure 3.8a** the active area could be easily scaled up to about 9×10 mm^2 (corresponding to the graphene coated region) by enlarging the Au top electrode area. We also stress that the current size of the TMD heterostructure achievable are just limited by the lab-scale prototype set-up employed and by the extension of the transferred graphene layer, and straightforward scalability at wafer scale (4” and beyond) is expected since no fundamental constraints of the TMD physical deposition process are foreseen and larger CVD graphene layers can be transferred on demand.

In a first set of photoconversion experiments, a collimated broadband halogen light source (Osram 64255 8V 20W) covering the VIS-NIR spectral range was employed to illuminate the active area of the van der Waals heterojunction. **Figure 3.9a** reports the photovoltage $V_{OC}(t)$, acquired under open-circuit conditions with an HP 3478A Multimeter, as a function of time under alternating on-off illumination conditions, and for different illumination power density levels as measured by a thermopile power meter (Scientech Astral AI310).

The photovoltage time dependent variation under continuous broadband illumination was analyzed to extract the characteristic response time of the device. The first illumination cycle for each illumination power density level was fitted with a first order exponential decay described by the following formula: $V_{OC} = A_1 \cdot e^{(-t/\tau)} + V_0$. An error bar of 0.5 μV (noise level) was considered for each point. An example of one cycle fit is reported in **Figure 3.9b** for the power density level of 216 mW/cm^2, giving a response time of 15.5 ± 0.3 sec. In **Figure 3.9c** the extracted response time at each power density is reported, showing a characteristic time constant τ of about 16 seconds.

Under steady illumination conditions, the detected photovoltage saturation value $V_{OC,ss}$, increases proportionally to the incident optical power, as demonstrated by the plot in **Figure 3.9d**. A photovoltage as high as 43 μV at 252 mW/cm^2 is measured. A blue bar is added to the graph to highlight the background signal and noise level.

In a similar way the net short circuit photocurrent ΔI_{SC} was measured at different stationary illumination power levels, by using a Keithley 6487 Picoammeter / Voltage Source connected to the two terminals of the TMD heterostructure device. The results reported in **Figure 3.9e** show an approximately linear dependence of ΔI_{SC} from illumination power density P, with a net photocurrent increase up to 2 nA in correspondence to the maximum power density employed, P=236 mW/cm^2. Also in this case, the blue bar in the graph indicates the noise level after subtraction of a 0.4 nA offset determined in dark conditions.

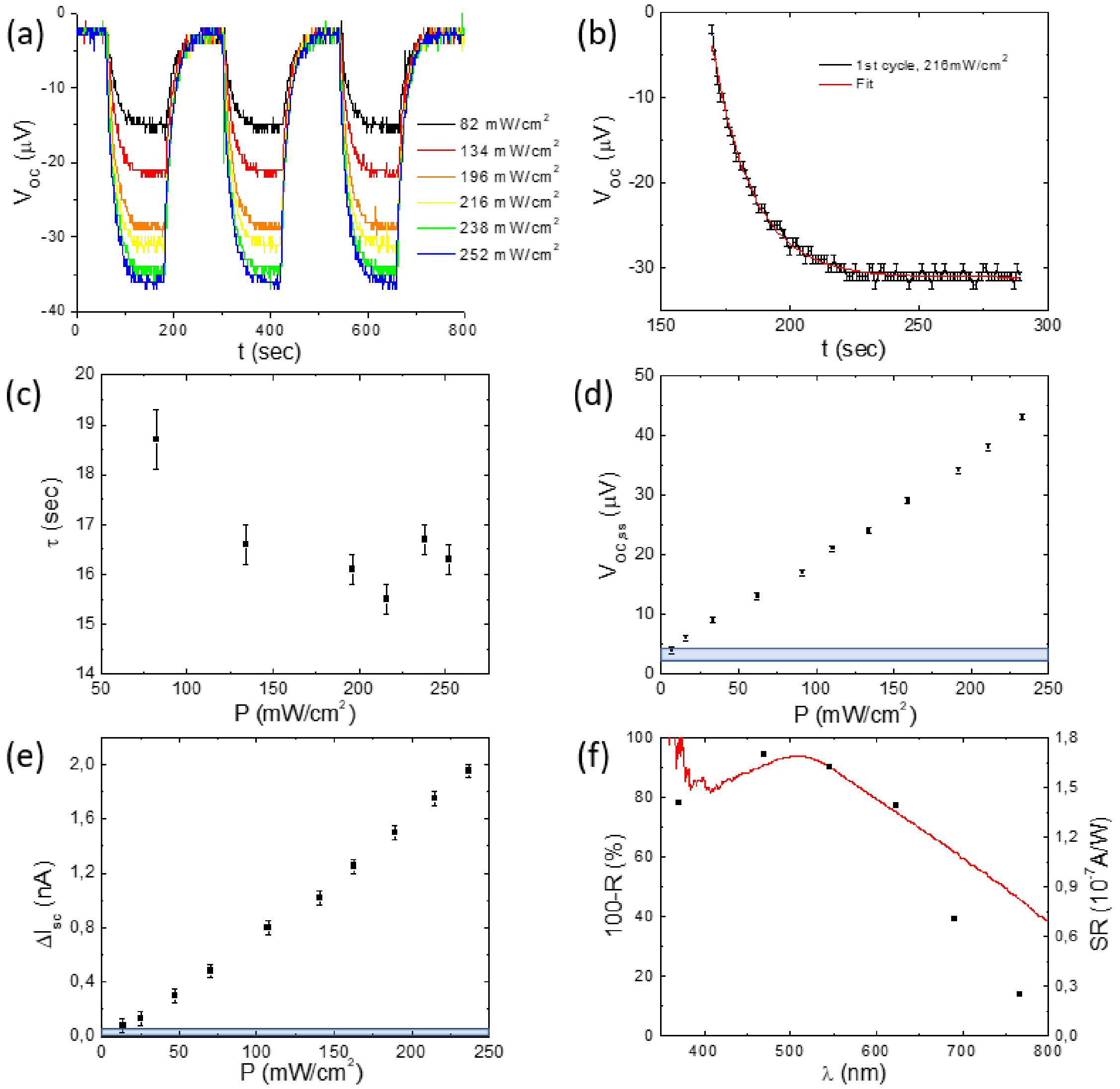

Figure 3.9 (a) Time-dependent open circuit photovoltage response $V_{OC}(t)$ under broadband illumination at different power. (b) Fit with a first order exponential decay of the first illumination cycle at 216mW/cm^2. (c) Response time as at different power density levels. (d,e) Steady state photovoltage $V_{OC,ss}$ and net photocurrent ΔI_{SC} under stationary conditions, as a function of incident power. (f) Comparison between optical absorption and spectral responsivity.

To evaluate the spectral responsivity of the device under monochromatic illumination conditions, a monochromatized Xenon light source (Newport TLS130B-300X) was employed for photoexcitation. Stationary illumination at different wavelengths λ, spanning from about 470 nm to 770 nm, was then achieved and the optical power P(l) was acquired with a calibrated photodiode power meter (Newport Power Meter Model

1919-R). The current/power spectral responsivity $SR(\lambda) = \Delta I_{SC}(\lambda) / P(\lambda)$, derived from the measured short circuit photocurrent and optical power, has been reported in **Figure 3.9f** (black squares). The spectral responsivity increases sharply when the wavelength decreases from the NIR across the TMD optical bandgap and spans across the spectral region of the excitonic transitions where optical absorption is higher.

In an independent way we determine the spectral dependence of optical reflectivity $R(\lambda)$ of the TMD heterostructure using a reflection/backscattering fibered probe. Since the reflectivity measurement is performed in correspondence to the Au contact which acts as a back-reflector, light transmission and scattering from the flat interfaces can be neglected and spectral absorption $A(\lambda)$ can be derived from the reflection spectrum according to $A(\lambda) = 100 - R(\lambda)$. The maximum of the absorption spectrum plotted in **Figure 3.9f** (red line) is found around 500 nm wavelength and closely matches the spectral trend of the current/power spectral responsivity.

We stress here that the low absolute values of photovoltage and photocurrent observed in this proof-of-concept large area TMD device are low and insufficient for any realistic electro-optical photoconversion application. This is mainly due to the very high series resistance of the graphene bilayer transparent bottom contact, as evaluated from a second graphene electrode transferred on a different silica substrate, showing a resistance in the range of 1.5 kΩ for contacts 2 mm apart. In fact, if we consider a simple Shockley equivalent circuit of the heterojunction, the high parasitic resistance forward polarizes the inner junction responsible for recombination in the TMD material thus hampering the photocurrent and photovoltage output[202]. Further developments, which go beyond the main focus of our paper, will require optimization of the bottom transparent conductive contact.

In summary, the physical deposition approach here described can be tailored for the deposition of large area TMDs films in the few-layer regime, as demonstrated by the presence of the characteristic response in Raman and optical spectra.

By stacked deposition of a MoS_2/WS_2 heterostructure on a graphene transparent electrode, an prototype large area photonic device was fabricated with measured photovoltage and photocurrent. We stress out that the currently achieved optoelectronic performances hinder any practical application since the effective photocurrent and photovoltage are hampered by the very high parasitic resistance. However, the electro-optical photoconversion can be considered as a proof-of-concept of the self-powered photoconversion recurring to a large area TMD deposition approach which is potentially scalable to the wafer level.

3.4 Future perspectives: graphene on ITO as improved transparent electrodes

The results I just discussed for the stacked MoS_2/WS_2 device highlight how crucial it is to develop highly conductive transparent electrodes to improve the optoelectronic performances. As a possible implementation, graphene could be transferred on top of the ITO layer which ensures a very low sheet resistance in the 10 Ω/□ range[203]. The basic idea of this approach exploits graphene as an impermeable membrane to prevent ITO sulfurization, while ensuring electron vertical conduction across the graphene/ITO interface. Additionally, the top graphene layer, characterized by sp^2 in plane coordination and weak out-of-plane interactions, also works as a 2D platform for the growth of TMD-based van der Waals heterostructures. I will now show preliminary results which demonstrate the performance of ITO-graphene samples sulfurized at different temperatures.

Figure 3.10a shows a photograph of an ITO film partly capped by a graphene bilayer film (inside the dashed area), after sulfurization at 750°C: the ITO region not protected by the graphene film obviously got sulfurized during the process (yellowish regions), and even under the graphene layer (at the center of the top edge) due to the high temperatures, the ITO sample evidenced substantial darkening becoming opaque, thus suggesting that at the high temperatures possible undesired reactions with sulfur can occur.

For this reason, a second ITO sample partly capped by a graphene bilayer was sulfurized at 600°C to verify temperature effects. The photograph shown in **Figure 3.10b** clearly indicates that ITO regions capped by graphene preserved their original transparency, confirming that the graphene layer is effective in blocking S diffusion.

The two samples were characterized by means of Raman spectroscopy to identify the spectral fingerprints of sulfurized ITO. The spectra reported in **Figure 3.10c** were acquired both on the graphene capped region (solid lines) and on the exposed ITO region (dashed lines) for the sample sulfurized at 750°C (blue lines) and the one sulfurized at 600°C (red lines). In both samples there is evidence of sulfurization outside the graphene since β-In_2S_3 Raman modes are well visible at 177 cm^{-1} (F_{2g}), 246 cm^{-1} (A_{1g}), 263 cm^{-1} (E_g), 308 cm^{-1} (A_{1g}), 326 cm^{-1} (F_{2g}) and 363 cm^{-1} (A_{1g}), while unstructured spectra are observed in the graphene capped region[184,185].

Though promising, the absence of vibrational modes is not sufficient to draw conclusive evidence on the quality of the ITO film, so we also performed optical transmission measurements, reported in **Figure 3.10d** (the same legend holds for colors and solid/dashed lines). For the uncapped ITO regions, a similar transmittance spectrum is observed after sulfurization at 600 and 750°C, with a sharp drop below 500nm that is compatible with β-In_2S_3 transmittance[186,187]. Conversely the graphene capped ITO film exhibits a transmission of about 80-90% in the case of 600°C, while after annealing at 750°C the transparency worsens sharply due to sulfur interdiffusion below the graphene capping layer.

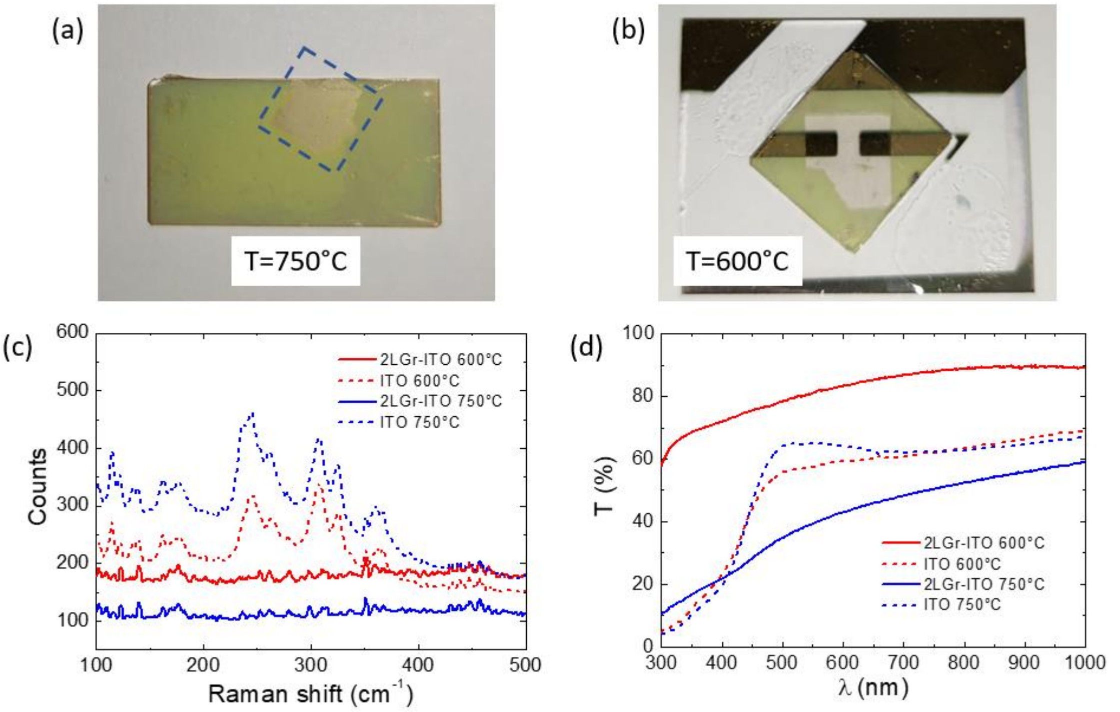

Figure 3.10 (a,b) Graphene/ITO stack treated in sulfur enriched atmosphere at 750°C and 600°C, respectively. (c) Raman spectra of graphene/ITO samples. (d) Optical extinction spectra of graphene/ITO samples acquired both on the exposed ITO and on the region coated by graphene.

A final conclusive test was performed by depositing metallic Au/Ti contacts (2mm width, 2mm gap as shown in **Figure 3.10b**), on top of the graphene/ITO layer. For the sample sulfurized at 600°C the sheet resistance attains a promising value of 50 Ω/□, which is comparable to the pristine ITO film prior to sulfurization.

The 2D platform formed by the graphene-ITO bilayer is thus characterized by a good transparency and a very low sheet resistance, even after sulfurization up to 600°C, and represents an ideal transparent conductive template for supporting van der Waals TMD heterostructures with optoelectronic functionality. Further tests with additional graphene/ITO samples would be required to verify if sulfurization steps at higher temperatures between 600°C and 750°C can be employed while still preserving the ITO functionality.

3.4.1 Low temperature recrystallization of TMD films supported on Graphene/ITO transparent layers

In the previous paragraph I have just shown that lower processing temperatures at 600°C ensure a good performance of the transparent conductive electrode based on graphene/ITO bilayer stack. It thus remains to be verified if MoS_2 and WS_2 precursor films deposited via IBS can be recrystallized at such reduced temperature. For this purpose, we modified the recrystallization process, by reducing the final temperature and correspondingly increasing the soaking time to 30 minutes, and by pushing the sulfur boat closer to the hot zone to compensate the reduction in sublimation rate.

In **Figure 3.11a** I show a photograph of a 3nm thick MoS_2 layer recrystallized at 600°C, homogenously extending over cm^2 scale. Raman characterization is shown in **Figure 3.11b**: by comparison with a MoS_2 layer of similar thickness sulfurized at 750°C it is possible to notice that the Raman vibrational modes are less sharp, with slightly lower counts and a higher FWHM, but still demonstrating recrystallization of MoS_2 in the semiconducting 2H-phase[148,204]. This conclusion is also confirmed by the optical transmission spectra reported in **Figure 3.11c**: though shallower than the layer recrystallized at 750°C (especially the A and B excitons), all the MoS_2 features are found also in the sample recrystallized at 600°C.

Similarly, the same process was employed to recrystallize a WS_2 layer. A photograph of a 3nm thick WS_2 sample is reported in **Figure 3.11d**, showing homogeneity over cm^2 scale. Raman spectra for such sample and for a sample with the same thickness recrystallized at 750°C are compared in **Figure 3.11e**. Even at 600°C, WS_2 vibrational modes are clearly visible in the spectrum, demonstrating effective recrystallization at a lower temperature. A direct comparison of the optical extinction spectra for the same samples is shown in **Figure 3.11f**, confirming the formation of the 2H-WS_2 phase even at 600°C since the characteristic excitonic features can be found in the spectrum.

However, the lower temperature results in a lower optical absorption due to lower crystalline quality, as demonstrated by the reduced intensity of the excitons.

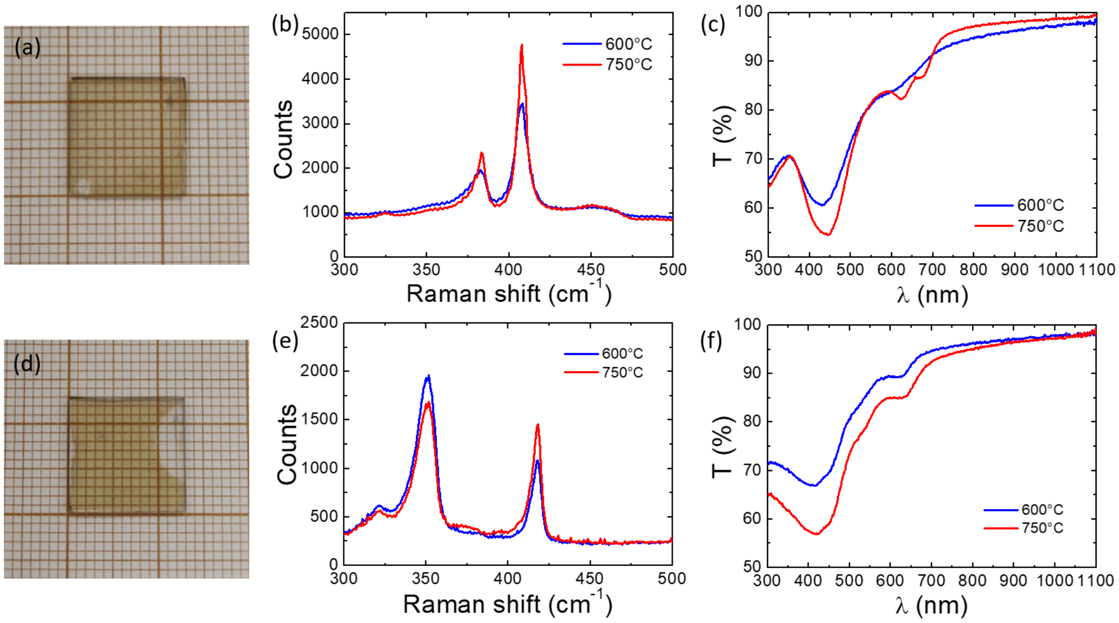

Figure 3.11: a) photograph of a MoS_2 layer recrystallized at 600°; b) Raman spectra comparison for MoS_2 layer recrystallized at 600°C and 750°C; c) optical transmission spectra comparison for MoS_2 layer recrystallized at 600°C and 750°C; d) photograph of a WS_2 layer recrystallized at 600°; e) Raman spectra comparison for WS_2 layer recrystallized at 600°C and 750°C; f) optical transmission spectra comparison for WS_2 layer recrystallized at 600°C and 750°C.

Summing up, these results show that TMD recrystallization is possible even at 600°C: if on one side this means a lower optical absorption, on the other side it is a promising result in view of the fabrication of a new large area van der Waals heterostructure device on top of ITO-graphene transparent conductive electrode. As already mentioned, we still have to explore the upper temperature limit of graphene/ITO protection in the range 600°C and 750°C which would ensure a improved quality of the TMD prototype device.

Chapter 4 – Light harvesting in ultra-thin TMD films

Two-dimensional (2D) Transition Metal Dichalcogenides (TMDs) semiconductors have recently emerged as very promising platform for new-generation atomic devices, due to their unique physical[29,205,206] and chemical properties[207–209]. Novel configurations employing TMDs and their van der Waals heterostructures[17,210,211] extending from monolayer to multilayer thickness offer rich prospects in diverse domains like nanophotonics,[212–214] optoelectronics,[30,215,216] quantum technologies[217,218] and photocatalysis[211,219] due to the tunable optoelectronic properties. In particular, the possibility to tailor the electronic band structure of 2D-TMDs such as MoS_2 achieving a transition from indirect to direct bandgap semiconductor in the monolayer form is very promising for applications in atomic scale photonics like photo-detection,[212,220] saturable absorption[221,222], two photon absorption[223,224] and nonlinear optics[225–228]. However, exploiting 2D materials as an active layer in nanophotonic devices is hurdled by low photon absorption due to the reduced thickness (despite the extremely high optical absorption coefficient, monolayer MoS_2 or WS_2 only absorbs around 10% of visible light)[210,229].

Light harvesting platforms and technologies are crucial in view of renewable photon to energy conversion technologies that can answer to the compelling global energy and environmental challenges. Two-dimensional (2D) Transition Metal Dichalcogenides semiconductor (TMDs) layers are particularly attractive in view of photoconversion applications but urgently require new ultra-compact photon harvesting schemes to mitigate the poor photon absorption properties.

In this chapter, I will focus on light harvesting in few-layer TMD films exploiting novel flat optics approaches derived from nanophotonics. Specifically, we propose a flat optics scheme based on nanogrooved ultra-thin MoS_2 layers conformally grown onto large area (cm^2 scale) nanopatterned templates[156,230]. The subwavelength reshaping of the 2D-TMDs layers promotes the excitation of photonic anomalies at the evanescence condition, either Rayleigh anomalies or Guided Mode anomalies (as described in Chapter 1), steering the light flow parallel to the active 2D-TMD film and boosting a strong in-plane electromagnetic confinement.

The effectiveness of the large area nanopatterning approaches will be demonstrated for the case of single component TMD films (in this chapter I will focus on nanostructured

MoS_2 only), however I anticipate that the more general validity of the approach also for complex heterostructure arrays will be confirmed in Chapter 5.

In section 4.1 I will describe the nanofabrication process that we developed, based on Laser Interference Lithography to form a polymeric pattern whose geometry is then transferred to the substrate via Reactive Ion Etching. A brief explanation of the physical principles on which this technique is based will be treated before the experimental details.
In section 4.2 I will present the results recently published on Advanced Functional Materials[156] about broadband and tunable absorption in nanorippled MoS_2 films conformally grown in the few-layer regime (4 ML thickness), supported by the nanostructured templates.
In section 4.3 I will study the optical response as the thickness of nanostructured MoS_2 films is gradually increased. Angle resolved extinction and absorption measurements will be used to characterize the evolution of the optical anomalies as the MoS_2 thickness increases.
In section 4.4 I will present the results that have been published this year in a Nanoscale paper[230]. Here, we showed that a periodically corrugated MoS_2 layer featuring flat optics light harvesting solutions can substantially enhance photodegradation rate of a typical water contaminant Methylene Blue (MB) with respect to a reference flat film.

4.1 Nanofabrication of large area nanostructured templates

The growth of few-layer conformal MoS_2 films on silica gratings was achieved by combining Lloyd Mirror Laser Interference Lithography (LIL) with Reactive Ion Etching (RIE) followed by conformal deposition of MoS_2 film. We adopted LIL since it is a cheap maskless lithography based on optical interference that allows to fabricate large area patterns with tunable periodicity following a simple parallel process. In this technique, the pattern is obtained from the interference fringes that are generated when two coherent laser beams interfere at the surface of a photoresist layer[231,232]. While in more complex set-ups such as multiple beam interferometers[233] the laser is split along different optical paths that generate the interference, in our case we adopted a Lloyd's mirror configuration[234] in which a second virtual laser beam is generated by the reflection of the laser source from a mirror mounted perpendicularly to the substrate, as depicted in **Figure**

4.1. The pattern is then a sequence of constructive and destructive interference fringes as the distance from the mirror increases, since the latter modulates the optical path difference between the direct laser beam illuminating the photoresist and the reflected beam. By controlling the rotation (θ_r) of the mirror-sample stage it is possible to tailor the angle of incidence (θ_i) of the laser on the photoresist, thus controlling the pattern periodicity (P) according to the following relation:

$$P = \frac{\lambda}{2 \cdot \sin \theta_i} \qquad (\text{eq. } 4.1)$$

where λ is the laser wavelength and θ_i is the half angle between the direct and reflected beams.

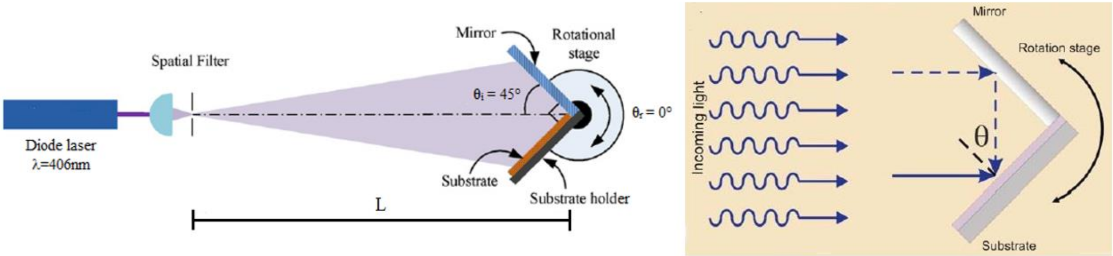

Figure 4.1: working principle of Laser Interference Lithography

In view of the application of the nanostructured substrates as templates for the growth of 2D-TMD semiconductor layers, we chose dielectric transparent silica wafers as initial substrates (**Figure 4.2a**) since they can withstand the elevated temperatures required during the TMD recrystallization process and have a high degree of transparency over a broad spectral range. The bare silica substrate was initially washed in acetone and isopropyl alcohol, then was spin-coated with a thin layer of diluted positive photoresist (AZ MIR 701 thinned with AZ EBR solvent) in order to produce a photolayer film 150-200 nm thick, followed by a soft baking treatment (**Figure 4.2b**). We employed our customized LIL set-up in Lloyd's mirror configuration in order to impress an optical interference fringe pattern onto the polymer. The positive-tone photoresist was thus exposed to AZ 726 MIF developer to selectively etch the optically irradiated areas which extend across cm^2 areas, thus achieving large area arrays of laterally separated polymer stripes. The parameters involved in LIL technique were optimized to develop a fringe pattern with desired periodicity between the stripes of the polymer resist (**Figure 4.2c**).

The second step involves preparing the polymer templates for Reactive Ion Etching, a sputtering process in which a chemically reactive plasma of CF_4 is used to selectively erode the exposed silica surface. To this end, Al mask was deposited on the polymer stripe pattern at normal incidence followed by removal of polymer stripes using ultrasonication in acetone for an optimized time duration (**Figure 4.2d**). The Al stripe covered silica substrate was then processed through RIE for developing well-ordered silica gratings with controlled surface profile, exploiting the different erosion rates due to chemical selectivity between exposed silica surface (fast erosion) and Al mask (slow erosion) (**Figure 4.2e**).

Remarkably, the fabrication process we adopted enables on one side the control on the periodicity and width of the pattern stripes by optimizing the LIL parameters (angle of incidence, exposure and development time) and on the other side the pattern vertical dynamics and – to some extent – shape by control on the RIE etching time (balance between vertical and lateral erosion as long as Al mask is not completely eroded).

At this point, the patterned silica substrate can be used as a template for the conformal growth of ultra-thin TMD layers (**Figure 4.2f**).

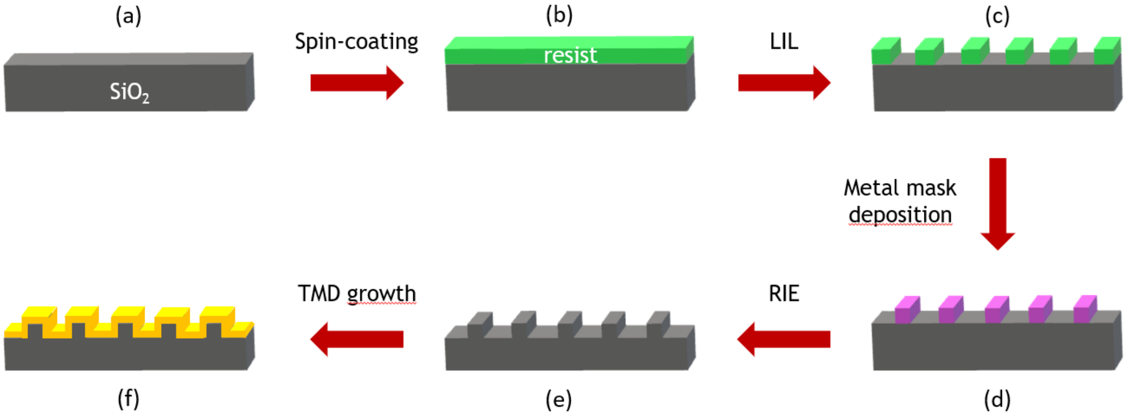

Figure 4.2: a) initial substrate; b) photoresist layer after spin-coating; c) polymeric pattern after LIL process; d) Al mask after normal incidence deposition and polymer lift-off; e) patterned substrate after RIE; f) nanostructured TMD layer conformally grown on top of the nanostructured pattern.

An example of a patterned template after the RIE process is shown in **Figure 4.3**, in which the initial morphology of the nanostructured silica substrate is studied. The AFM image reported in **Figure 4.3a** shows highly regular periodic structure with periodicity of about 300 nm and height of about 170 nm. A line profile extracted from the green line is reported in **Figure 4.3b**, showing few periods to identify the crests shape. It is interesting to notice that the crests top edge is flat and aligned, indicating the original silica surface that was protected by Al mask during the RIE process. A histogram of the heights is reported in **Figure 4.3c**, highlighting the presence of two peaks that can be attributed to the valleys and to the crests (sharper peak due to the flat top morphology), respectively. In **Figure**

4.3d the histogram of the topography first derivative is reported, giving information on the local slopes of the nanostructures. The peak around θ = 0° mainly arises from the flat top regions of the grating, while the two peaks at about θ = −65° and θ = 60° are attributed to the right and left side of the grating crests. Considering possible effects of tip-surface convolution and of feedback during the imaging, we consider this initial grating morphology to be symmetric, as expected from the RIE processing conditions at normal incidence.

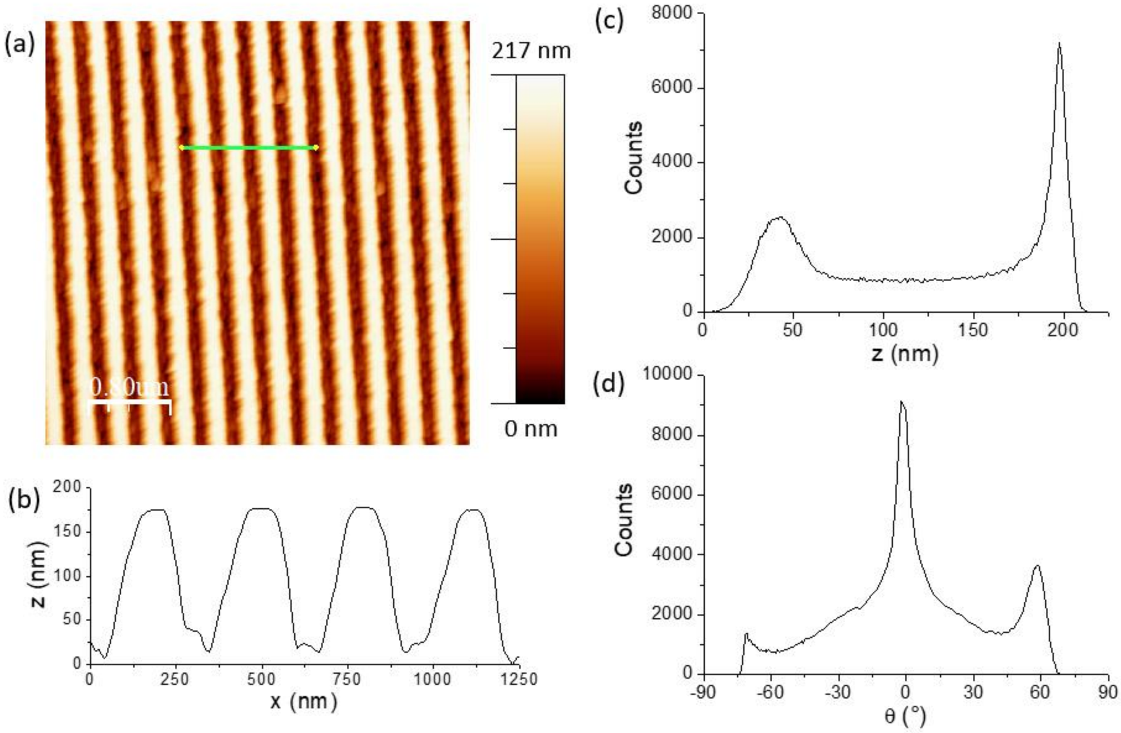

Figure 4.3: a) AFM image of a nanostructured silica template after LIL and RIE; b) extracted line profile; c) heights histogram of the AFM image; d) topography first derivative distribution.

4.2 Light harvesting in nanorippled ultra-thin MoS_2 films

In this paragraph I will show an application of the nanostructured silica templates as light harvesting platforms for ultra-thin MoS_2 layers. The core of the work and the figures of this section have been published on Advanced Functional Materials[156]. In this work, MoS_2 layers were still grown in the external collaboration with the CNR research group of Alessandro Molle in Agrate Brianza, by electron beam deposition of MoO_3 layers as precursor films that were subsequently sulfurized at 850°C.

Reshaping the 2D layer in the form of highly ordered subwavelength lattices[235–237] provides a unique opportunity to control the electronic band structure due to local strain engineering[6,9,238] and, in parallel, to couple the incoming photons with the active material allowing to tailor the excitation of lattice resonances and/or Guided Mode Anomalies[10,100,107,239]. These narrowband diffraction modes emerging in monodisperse periodic templates induce strong in-plane light scattering and near-field confinement in proximity of the active 2D layer, thus enabling resonant enhancement of the photon absorption[103,239,240].

In parallel, the scalable nanofabrication of 2D-TMDs is a relevant issue in view of real-world photonic applications. To this end, new techniques are currently investigated to grow large area TMDs layers[132,241] with the further benefit of reshaping the 2D layers via conformal growth on top of self-organized nanopatterned templates[242–245]. This way, the capability to homogeneously tailor the optical and vibrational response of 2D MoS_2 layers has been demonstrated over large area. However, the intrinsic size-dispersion of the nanopattern inhibits the emergence of coherent optical diffraction effects which would strongly promote light confinement in the 2D material.

In this work, we combine Laser Interference Lithography (LIL) with Reactive Ion Etching (RIE) to fabricate well-ordered silica gratings that are scalable to a macroscopic area and are used to drive the nanoscale re-shaping of few-layer 2D MoS_2 grown on top. The subwavelength period of the gratings allows for the emergence of a polarization sensitive Guided Mode Anomaly (GMA) that promotes the enhanced photon absorption in the conformally nanorippled 2D-MoS_2 film, which act as a flat optic element. We demonstrate the capability to tune the resonant wavelength of the GMA in a broadband spectral range from the Near-Ultraviolet (NUV) to the NIR by changing the illumination angle and the grating period, thereby achieving relative enhancement of photon absorption up to 240% with respect to a comparable MoS_2 film grown on a flat silica substrate. Additionally, the high amplitude and subwavelength modulations of the hybrid 2D-TMD/SiO_2 rippled interface induce a broadband bio-mimetic reduction of reflectivity due to the refractive index grading (moth eye effect)[246]. The capability to tailor broadband photon harvesting combined with anti-reflection functionalities over large area templates highlights the potential of metastructures based on 2D-MoS_2 for applications in nanophotonics, optoelectronics and quantum technologies.

4.2.1 Conformal fabrication of large area nanogrooved MoS_2 arrays

The nanofabrication of large area flat optics metasurfaces, based on few-layer MoS_2 homogeneously coating the top of nanopatterned silica substrate, has been achieved by combining LIL and RIE techniques described in paragraph 4.1. The robustness of LIL and RIE allows us to fabricate controlled subwavelength gratings extending over large area (cm^2) on transparent silica substrates that are used as templates to grow thin conformal MoS_2 films. For MoS_2 synthesis, 4 nm thick MoO_3 films were evaporated on a flat reference substrate and on silica gratings by means of electron beam evaporation. The precursor films were then exposed to sulfur enriched atmosphere in a tube furnace by using Ar gas with flow rate 0.2-0.3 L/h to transport sulfur from the source (1-2 g, Sigma-Aldrich) to the sample. The furnace was heated to 850°C with 5°C/min rate and kept at this high temperature for 10 min followed by natural cooling, achieving growth of conformal MoS_2 thin films (4-5 layer thick, corresponding to a thickness of 2.8-3.5 nm) on the silica gratings. Indeed, the periodic modulation of the active 2D layer allows us to control the electronic band structure through local strain engineering, leading to tailored optoelectronic response[6,7,9,245].

The surface morphology of the silica gratings decorated by a few-layer MoS_2 film is imaged through Atomic Force Microscope (AFM) as represented in **Figures 4.4a** and **4.4b** (and schematically sketched in **Figures 4.4h** and **4.4i**). The deposition of the flat reference MoS_2 films of comparable thickness has been previously reported in ref [111]. From the statistical analysis of the AFM images, the grating period (P) reads P = 290±15 nm for sample 1 (**Figure 4.4a**) and P = 450±15 nm for sample 2 (**Figure 4.4b**). The controlled exposure of the silica surface to active agents in RIE allows us to easily modify the surface morphology and the amplitude of the gratings, as shown in line profiles in **Figures 4.4c** and **4.4d** corresponding to the AFM image shown in **Figures 4.4a** and **4.4b**. A broad ridge is observed for sample 1 whereas a sharp conical profile is seen for sample 2 due to a longer etching time, responsible for a larger lateral erosion of the crests. In the inset of **Figure 4.4b** we show a photograph of sample 1 which highlights that optical functionalization of the nanorippled MoS_2/silica interface is achieved over large areas and induces a strong light scattering efficiency.

The vibrational response of the MoS_2 gratings has been investigated by micro-Raman spectroscopy. **Figures 4.4e**, **4.4f** and **4.4g** show the Raman spectrum from a continuous

2D MoS_2 film deposited on the flat silica substrate (black curve), sample 1 (blue curve) and sample 2 (red curve), respectively. The spectrum from each sample clearly shows the presence of the characteristic E^1_{2g} and A_{1g} modes which denote the in-plane and out-of-plane vibrations of MoS_2, respectively. The observed response in the Raman measurements (beam diameter ≈ 700 nm for a 100× objective with N.A.: 0.90) generates from an ensemble of crystalline grains of MoS_2, up to 50 nm in size[6], that conformally cover the silica grating. Specifically, the frequency separation of the E^1_{2g} to A_{1g} Raman modes for the 2D-MoS_2 film amounts to 24-25 cm^{-1}, compatible with 4-5 monolayers and an absolute thickness of 2.8-3.5 nm (considering the thickness of a monolayer 0.7 nm). Such figures are independently in agreement with TEM characterization of the reference MoS_2 films grown in the same conditions[111,112].

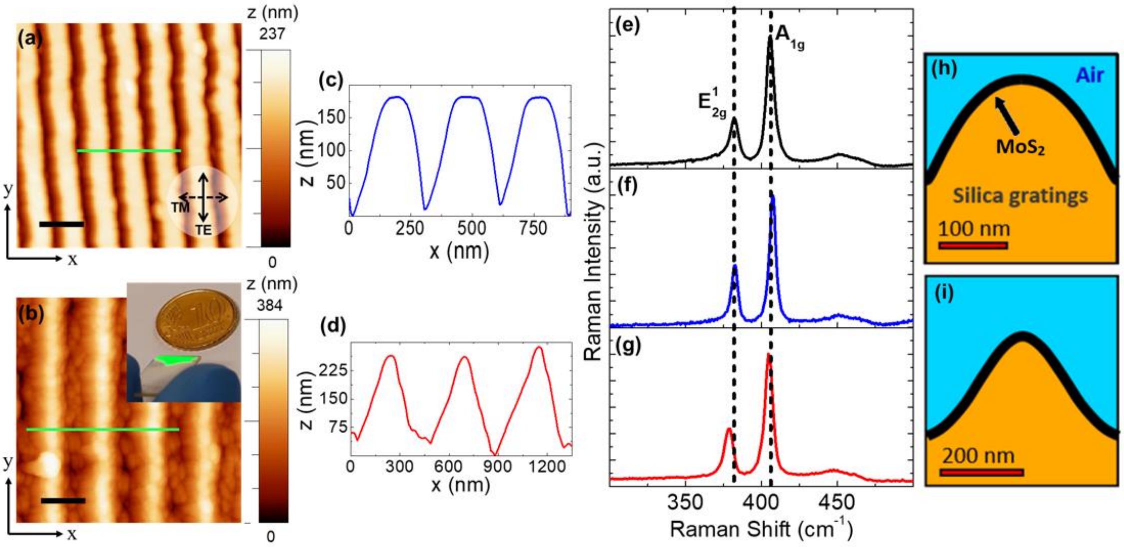

Figure 4.4: (a,b) AFM images for sample 1 and 2, respectively. Scale bar reads 400 nm. Inset of panel b shows a photograph of sample 1. (c,d) Line profiles corresponding to the horizontal green line in AFM images of sample 1 and 2, respectively. (e-g) Raman spectrum acquired for a flat MoS_2 reference film (black curve) compared to the spectrum from sample 1 (blue curve) and sample 2 (red curve). (h,i) FEM geometry used in the simulations for sample 1 and 2, respectively.

4.2.2 Optical characterization of nanogrooved MoS_2 arrays

The uniform periodic modulation of the 2D layer over a large area enables us to measure the optical response of these metasurfaces via NUV-VIS-NIR extinction spectroscopy by exploiting a macroscopic optical spot (diameter ≈ 2 mm)[247]. **Figure 4.5a** shows the recorded optical extinction spectra at normal incidence from a flat 2D MoS_2 film and from a 2D MoS_2 grating (sample 1) for polarization of the electric field oriented parallel (TE) and perpendicular (TM) with respect to the long axis of the nanoscale grating (see inset in **Figure 4.5a**). Each spectrum is referenced to air, including the contribution of reflection from the silica substrate. Of relevance for the photon harvesting functionality, we evidence that the subwavelength nanotexturing of the MoS_2/silica interface induces a substantial reduction of the Fresnel reflection losses (in the order of 50%) due to Moth Eye effect[84,246,248]. For instance, in **Figure 4.5a** one can see that above 750 nm, where absorption of MoS_2 is negligible, extinction is determined by the reflection at the air/MoS_2 interface and drops from about 9% for the flat MoS_2 film to about 4% from the rippled film.

The characteristic neutral excitonic resonances in the 2D MoS_2 are readily recognized in all spectra, where the low energy peaks labelled as A and B generate from spin-orbit splitting of the valence band at K-point of the Brillouin zone and the high energy C and D excitons are due to the band-nesting transitions at the edges of Brillouin zone[245,249]. The polarization dependent optical response detected in the case of MoS_2 gratings (sample 1) clearly shows a strong dichroism with enhanced extinction over a broadband NUV-VIS spectrum for TE polarization (solid blue curve) with respect to TM polarization (dashed blue curve). In particular, for TE polarization a narrowband optical extinction maximum is detected at the wavelength $\lambda \approx 320$ nm, giving rise to a relative enhancement of about 180 % with respect to the corresponding signal of the reference flat MoS_2 film.

The presence of an anomalous peak at $\lambda \approx 320$ nm leading to a strong extinction enhancement invokes a detailed investigation; therefore, we performed angle resolved optical extinction measurements for sample 1 (see **Figure 4.5b** for a schematic of the adopted set-up). In detail, the MoS_2 coated grating was illuminated by a NUV-VIS-NIR light from the substrate side in s-TE polarization tilting the sample at various angular configurations, thus allowing us to control the interaction between the incident light and the wave-vector component of MoS_2 grating ($2\pi/P$). **Figure 4.5c** shows the optical extinction spectra for $0° \leq \theta \leq 60°$. A clear and gradual redshift of the sharp spectral feature is seen from 320 nm to 565 nm as θ increases from 0° (black curve) to 60° (red curve). The dispersive nature of the peak is characteristic of photonic anomalies observed for highly ordered periodic arrays that can be classified to be either a Rayleigh Anomaly (RA) or a guided-mode anomaly (GMA)[250,251]. In particular, RA refers to diffracted light propagating parallel to the grating plane whereas in the GMA regime[250], the diffracted wave can couple with the underlying substrate therein propagating with the wave-vector parallel to the short axis of the grating. The latter behavior is possible due to the larger value of the refractive index in the substrate with respect to the effective medium formed by the diffraction grating and the surrounding medium that allows for total internal reflection of the wave coupled to the substrate. As the GMA wave is guided through the substrate, it can be further coupled to the 2D layer leading to resonant and non-resonant interactions of the scattered light with the nanograting. The dependence of the peak wavelength (λ_p) for the two diffractive anomalies on the illumination angle (θ) can be explained by the following equation[250,251]:

$$m\lambda_P = P(n + n_0 \cdot \sin\theta) \qquad (\text{eq. } 4.2)$$

where the integer m is the diffraction order, P is the grating period, n is the effective refractive index at the internal/external interface of the corrugated MoS_2 layer where the light is confined at the evanescent condition and n_0 is the refractive index of the medium where light travels before interacting with the sample.

In particular, in the GMA induced at the MoS_2-silica interface, n corresponds to the effective refractive index of the hybrid MoS_2-silica metastructures. As shown in **Figure 4.5d**, the photonic anomaly of **Figure 4.5c** could be fitted by using equation (4.2) and setting m = 1, P = 290 nm and n_0 = 1 (air) for varying θ. A very good match is found between the experiment (black squares) and the model (orange line) when an effective refractive index n = 1.07±0.05 is adopted for the MoS_2 coated silica metastructures. In **Figure 4.5d** the error bars are not visible because they are comparable or smaller than the symbol size. In particular, the angular accuracy of the goniometer reads about 1° and the wavelength resolution at the resonant peaks amounts to 1 nm.

These flat optics silica gratings homogeneously coated with atomically thin MoS_2 layers demand for electromagnetic computations aiming at a detailed investigation of their optical response. To this end we established a collaboration with professor Giuseppe Della Valle (Physics Departement and IFN-CNR, Politecnico di Milano), expert in the use of Finite Element Method solver (Comsol Multiphysics 5.4). The simulation assumes as model structure a single ridge morphology, resulting from the AFM line profiles of sample 1 (**Figure 4.4c**) and sample 2 (**Figure 4.4d**), respectively. In **Figures 4.4h** and **4.4i** we show the schematic of the unit cell with the grating geometry employed for simulating sample 1 and sample 2, respectively, highlighting the regions with different refractive indexes (in the sketch the thickness of the MoS_2 layer is exaggerated for the sake of visibility). To investigate the nature and the coupling of the diffractive anomaly to 2D MoS_2, we performed FEM computations for sample 1 (P = 290 nm). The simulated

MoS_2 coated grating is excited with s-TE polarized light at a specific illumination angle, θ. **Figure 4.5e** shows the calculated spectrum for each θ bringing out the characteristic neutral excitonic resonances and two different modes of the Rayleigh Anomaly that redshift with the increase in the incident angle (the latter have been clearly identified by inspecting the numerical derivatives of the simulated spectra, as detailed in the **Figure 4.5f**). We attribute the high energy mode to the scattering of incident light along the MoS_2 grating - air interface (RA_{air}) while the low energy mode (RA_{sub}) emerges due to the scattering of incident light along the MoS_2 grating - silica interface. These modes arise due to the different refractive indices of the media surrounding the periodically modulated MoS_2 layer, on one side the air ($n = 1.0$) for RA_{air}, and on the other side the silica ($n = 1.46$) for RA_{sub}, thus allowing for a change in the magnitude of the wave-vector component of the scattered light in the two media. In particular, the RA_{air} spans through the high energy C and D excitonic resonances, while the $RA_{sub.}$ moves through the low energy A and B excitonic resonances of the 2D MoS_2 film. **Figure 4.5d** also shows the dispersion of the resonant wavelengths for the two simulated RA modes (RA_{air} - blue trace and diamonds, RA_{sub} - green trace and circles) compared to the experimental data (black squares) which were fitted by using equation (4.2). The discrepancy between the experimental position of the photonic anomaly and the values of the RA anomalies is due to occurrence of a GMA confined in the silica substrate (thickness ≈ 700 μm)[250]. Indeed, the finite thickness of the dielectric substrate can sustain a continuous spectrum of guided modes (see sketch in **Figure 4.5b**) which leak from the MoS_2 coated nanotextured layer, provided its effective refractive index is lower compared to the silica supporting slab. In our case, the fit to the experimental data highlights an effective refractive index $n = 1.07 \pm 0.05$ for the MoS_2 coated silica metastructure. This value is intermediate between the refractive index of the substrate ($n = 1.46$) and air ($n = 1$), demonstrating that the observed modes are compatible with GMA leaking from the MoS_2 coated nanopatterned surface.

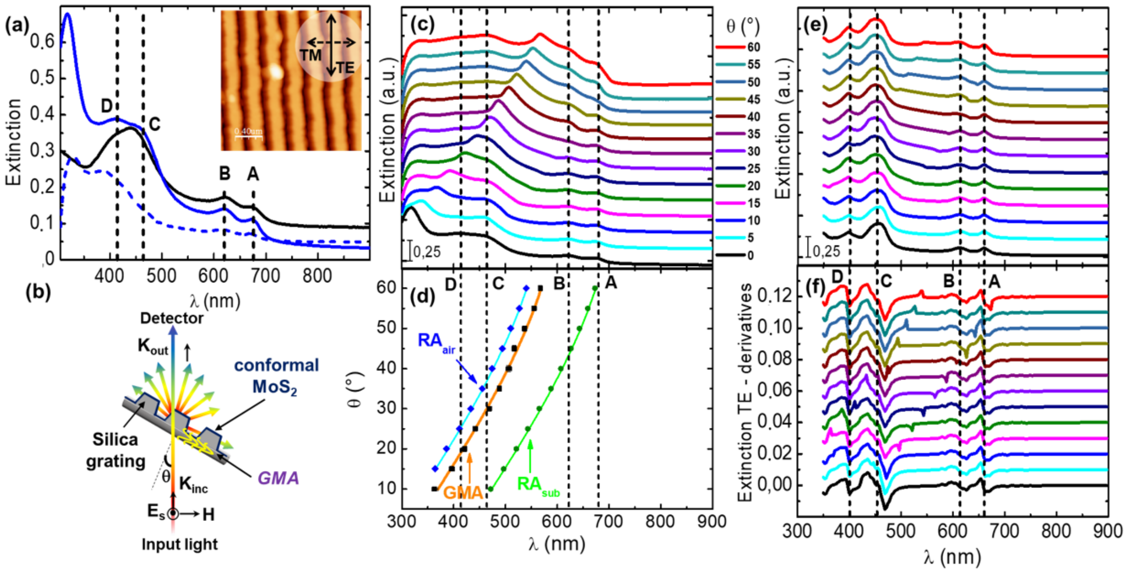

Figure 4.5. (a) Normal incidence optical extinction spectra for a reference flat MoS_2 film (continuous black) and for sample 1 (solid blue: TE polarization, dashed blue: TM polarization). Inset shows the direction of polarization superimposed on the AFM image of sample 1. (b) Schematic of the transmission set-up used for the angle-resolved optical measurements. (c) Angle resolved extinction spectra of MoS_2 grating (sample 1) for increasing incidence, θ, from 0° (black curve) to 60° (red curve). A relative offset of 0.2 has been introduced from one spectrum to the other for clarity purpose. (d) Comparison of the resonant wavelength for the experimentally observed diffractive anomaly (black squares, continuous orange) with RA modes captured through computations; RA_{air} (blue diamonds) and RA_{sub} (green diamonds). (e) Simulated angle-resolved extinction spectra in s-TE polarization for sample 1. (f) Numerical derivatives of the simulated extinction spectra of panel e, aimed at identifying the RAs of sample 1.

The experimental observations in **Figure 4.5c** and the quantitative agreement with the theory of diffractive anomalies are evidence of the fact that the GMA can be tuned by varying the illumination angle. At the same time equation (4.2) suggests that the GMA can be independently redshifted by increasing the grating period, thus leading to a spectral overlap of the guided-mode anomaly with low energy excitonic resonances in the active 2D layer. In sample 2 we thus modified the grating period to P = 450±15 nm (**Figures 4.4b** and **4.4d**) recording the angle resolved extinction spectra as performed previously for sample 1. **Figure 4.6a** shows the optical extinction curves for different illumination angles leading to the redshift of the guided-mode anomaly from 475 nm at θ = 0° (black curve) to 770 nm at θ = 40° (red curve). The larger period of the array allows the resonant mode to span over broadband wavelength range, now also including the low energy A and B excitonic resonances in MoS_2 at illuminating angles far from grazing conditions.

Figures 4.6b and **4.6c** show the zoomed-in view of the optical extinction from the experiment and the FEM simulations assuming as model structure for sample 2 the single ridge morphology sketched in **Figure 4.4i**. Looking carefully at the dispersion of GMA and RA_{air}, showing slight deviations in resonant wavelength between the two anomalies as they crossover low energy excitonic resonances A and B in MoS_2. **Figure 4.6d** shows a comparison between the dispersion of GMA wavelength for sample 1 and sample 2 for θ varying between 0° and 35°. The figure clearly elucidates the dependence of the GMA upon the grating period and the illuminating angle; while for sample 1 (P = 290 nm) it is possible to tune the resonant wavelength of the diffractive anomaly from NUV to VIS across the high energy C and D excitonic resonances of MoS_2, the larger period of sample 2 (P = 450 nm) allows the GMA to crossover low energy A and B excitonic resonances (open red circles). Thus, a simple modification of the period of the nanopatterned template allows us to enhance interaction of incident photons with specific MoS_2 excitonic resonances spanning from low to high energy. **Figure 4.6e** shows the simulated electric field intensity in s-TE polarization for $\theta = 25°$ at fixed illumination wavelength 660 nm for sample 2 and for the flat MoS_2, as a function of the distance along the unit cell. The values of angle and wavelength have been chosen in order to have the resonant excitation of GMA for sample 2 in proximity to the A exciton in the 2D MoS_2. The calculated intensity of the electric field shows a clear enhancement (up to threefold) for sample 2 (solid green) when compared to the flat MoS_2 film (dotted blue). The comparison between the near-field cross-section profile of the flat layer (**Figure 4.6e** top inset) and the patterned layer (**Figure 4.6e** bottom inset) permits to identify in a straightforward way the selective confinement of electromagnetic hot-spots on the illuminated MoS_2 ridges of the patterned sample. These results clearly show the capability to tailor photon trapping and absorption in corrugated 2D MoS_2 nanosheets, by simply reshaping the 2D material and tailoring the periodicity of the underlying grating nanopattern. This is a promising outcome for the use of 2D-TMD coated gratings for amplifying excitonic absorption along with applications devoted to photocatalysis and sensing over a broad wavelength range.

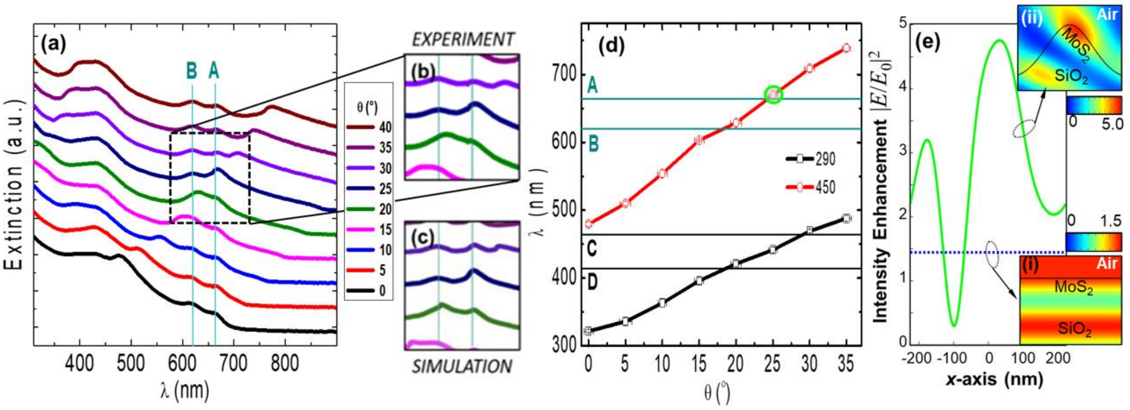

Figure 4.6. (a) Angle-resolved extinction spectra for sample 2 (P = 450 nm). (b,c) Focus on redshift of the dispersion of GMA and RA_{air} through characteristic A and B excitonic resonances in 2D-MoS_2 from the experiment and simulations, respectively. (d) Dispersion of the GMA resonant wavelength plotted as a function of the illuminating angle for sample 1 and 2. (e) Simulated electric field intensity for illumination at θ = 25° at fixed light wavelength 660 nm (green circle in panel d) when the x-coordinate moves across the unit cell, for a flat (dotted blue) and modulated 2D-MoS_2 (continuous green), supported on a semi-infinite silica substrate. The color images show the simulated magnitude of the near field for the flat film (bottom inset) and for sample 2 (top inset).

4.2.3 Total integrated optical absorbance of nanogrooved MoS_2 arrays

In order to highlight the impact of the proposed nanopatterned configuration for enhanced photon absorption in few-layer MoS_2, we performed measurements of total integrated absorbance using an integrating sphere set-up[247], able to collect the integral optical transmission (direct transmission, specular reflection and diffused forward/backward scattering at any angle) through the sample which is mounted inside the integrating sphere. A scheme of the integrating sphere is reported in **Figure 4.7a**. We used a NKT Photonics broadband white laser (SuperK COMPACT) as an illumination source coupled to an integrating sphere through a polarizer. The output from the sphere was coupled to the PC controlled HR4000 Ocean Optics spectrometer through an optical fiber (core diameter 600 μm). We measured the optical absorption in the following manner. First, a constant dark spectrum was acquired with light source off so as to read the detector noise level. Second, the integrated signal was recorded in indirect illumination ($T_{indirect}$, sample kept within the sphere and away from the incident light to capture optical background) followed by the recording of the signal in direct illumination (T_{direct}, sample mounted in the line of sight of the incident light). The normalized integrated signal (T) is then given by (T_{direct} − dark) / ($T_{indirect}$ − dark). The total absorption spectra (A) are hence extracted from the integral transmission measurements as A = (1 − T).

The integral transmittance spectra of the rippled MoS_2 films corresponding to sample 1 and sample 2 have been detected and compared with the spectra of a reference flat MoS_2 film. The possibility to control the incidence angle (θ) of the excitation beam on the sample has also allowed to collect a set of data that characterizes the angular dispersion of the detected absorption features in MoS_2 nanogratings. All the spectra were detected for s-TE polarization of the excitation beam, as sketched in **Figure 4.5b**. **Figures 4.7b** and **4.7c** show the absorption spectra respectively corresponding to the flat MoS_2 film and to the MoS_2 nanogratings (sample 1). The spectra have been detected under different illumination angle θ = 0° (green), θ = 35° (blue), θ = 40° (orange) and θ = 45° (black). In all the spectra referred to periodically modulated MoS_2 (**Figure 4.7c** - sample 1) we observe a broadband increase of optical absorption in the whole active window of MoS_2, with respect to the case of the reference flat layer (**Figure 4.7b**). Additionally, an absorption maximum is clearly detected as θ exceeds 30° and can be tuned from about 480 nm to 525 nm wavelength by tailoring the light incidence angle θ from 35° to 45°. Such dispersive behavior is in agreement with the redshift of the extinction maximum detected in **Figure 4.5c** and can be clearly attributed to the excitation of a GMA propagating at the nanopatterned silica/MoS_2 interface. Under GMA excitation at θ = 45° in MoS_2 nanogratings, a resonant absorption enhancement as high as 240% is detected with respect to the corresponding signal from a flat 2D layer. This effect is not merely confined to the GMA resonant wavelength but extends over a broadband VIS spectral range from 470 nm to 750 nm, with an averaged absorption gain which reads about 110% at θ=45°. This enhancement is due to the interaction of the non-resonant scattered light, guided into the bulk substrate, with the 2D nanogratings.[57,58] Similar optical behavior has been observed for sample 2 (**Figure 4.7d**) where we observe a narrowband maximum at 490 nm wavelength for normal incident excitation (θ=0°, pink curve). This characteristic feature redshifts to about 504 nm wavelength for θ=5°, showing a dispersive behavior in agreement with that of the GMA mode observed in the extinction spectra (**Figures 4.6a** and **4.6d**). In analogy to sample 1, a broadband absorption amplification effect is detected in the whole MoS_2 active band, confirming the interaction of non-resonant scattered light with the nanogratings.

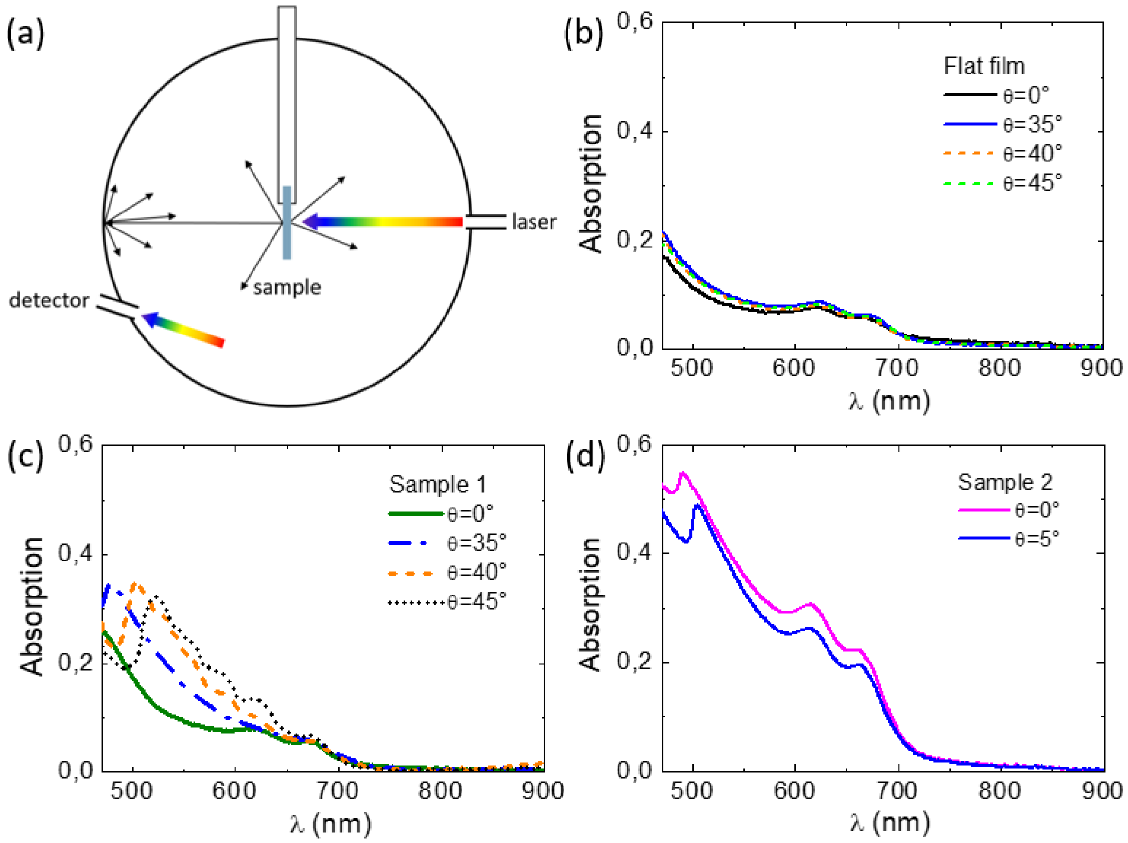

Figure 4.7 (a) Scheme of the integrating sphere set-up. (b-d) Optical absorption spectra extracted from integral transmission measurements performed under different incidence angle illumination conditions and s-TE polarization of the incident light for flat MoS_2 film (b), sample 1 (c) and sample 2 (d), respectively.

The dispersive GMA feature enables a strong resonant absorption of photons into the MoS_2 layers and is easily tunable over a broadband range from the NUV to the NIR by simply tailoring the illumination conditions and/or the grating periodicity. In parallel, a further broadband amplification of absorption is achieved in the VIS spectral range from 470 nm to 750 nm thanks to a non-resonant light scattering from the nanogratings which leads to an enhancement of integrated photon absorption up to 110% in nano-rippled 2D MoS_2 with respect to the reference flat MoS_2. Furthermore, the moth-eye anti-reflection effect induced in the VIS-NIR wavelength range by the MoS_2 coated gratings, determines a further route towards efficient light collection.

Given the large (cm^2) area and high throughput nature of the novel approach here described, we envisage a strong impact in view of possible development of scalable 2D layered nanophotonic devices featuring broadband photon harvesting.

4.3 Light harvesting in nanorippled thicker MoS_2 films

Contrary to the case of MoS_2 monolayers and bilayers, a 4/5-layer MoS_2 nanosheet as those considered in the previous paragraph can be described in terms of a bulk permittivity. It is therefore expected that the kind of absorption enhancement retrieved in our study cannot be affected by slight local variations in the number of layers. However, for MoS_2 thickness beyond 8-10 nm the onset of retardation-based regime in the nanosheets is expected in view of the very high optical density of MoS_2. For such optically thick MoS_2 structures, the GMA mechanism can take place also within the MoS_2 film itself, giving rise to a further enhancement of absorption, even though on a narrow range of wavelengths. Having demonstrated tunable and broadband absorption enhancement in subwavelength periodically reshape MoS_2 ultra-thin layers, we thus proceeded to further engineer the TMD optical response by increasing its thickness via incremental steps.

4.3.1 Conformal fabrication of large area nanogrooved MoS_2 arrays of variable thickness

An AFM image of the nanostructured silica substrate used as template for the growth of MoS_2 films in different thickness regimes is shown in **Figure 4.8a**. An extracted line profile is reported in **Figure 4.8b** to represent the initial morphology of the template, having a periodicity of about 300 nm with nanostructures as high as 300 nm. In the first growth step, a 3 nm thick MoS_2 layer was conformally grown on top of the template, replicating a sample like the one considered in the previous paragraph. The thickness was then increased by 5 nm for each growth step, up to a final MoS_2 thickness of 23 nm.

Having already demonstrated conformal growth of 3 nm thick MoS_2 films on nanostructured silica substrates, in **Figures 4.8c** and **4.8e** I report the AFM images, along with some extracted line profiles, in the case of the intermediate (13 nm) and higher (23 nm) MoS_2 thicknesses. Even for the higher TMD thickness, high vertical structures are preserved, demonstrating conformal growth even for increasing MoS_2 thicknesses.

In **Figures 4.8d** and **4.8f** Raman spectra for the considered steps are reported, each of them showing the characteristic in-plane (E^1_{2g}) and out-of-plane (A_{1g}) MoS_2 vibrational modes. MoS_2 in different thickness regimes

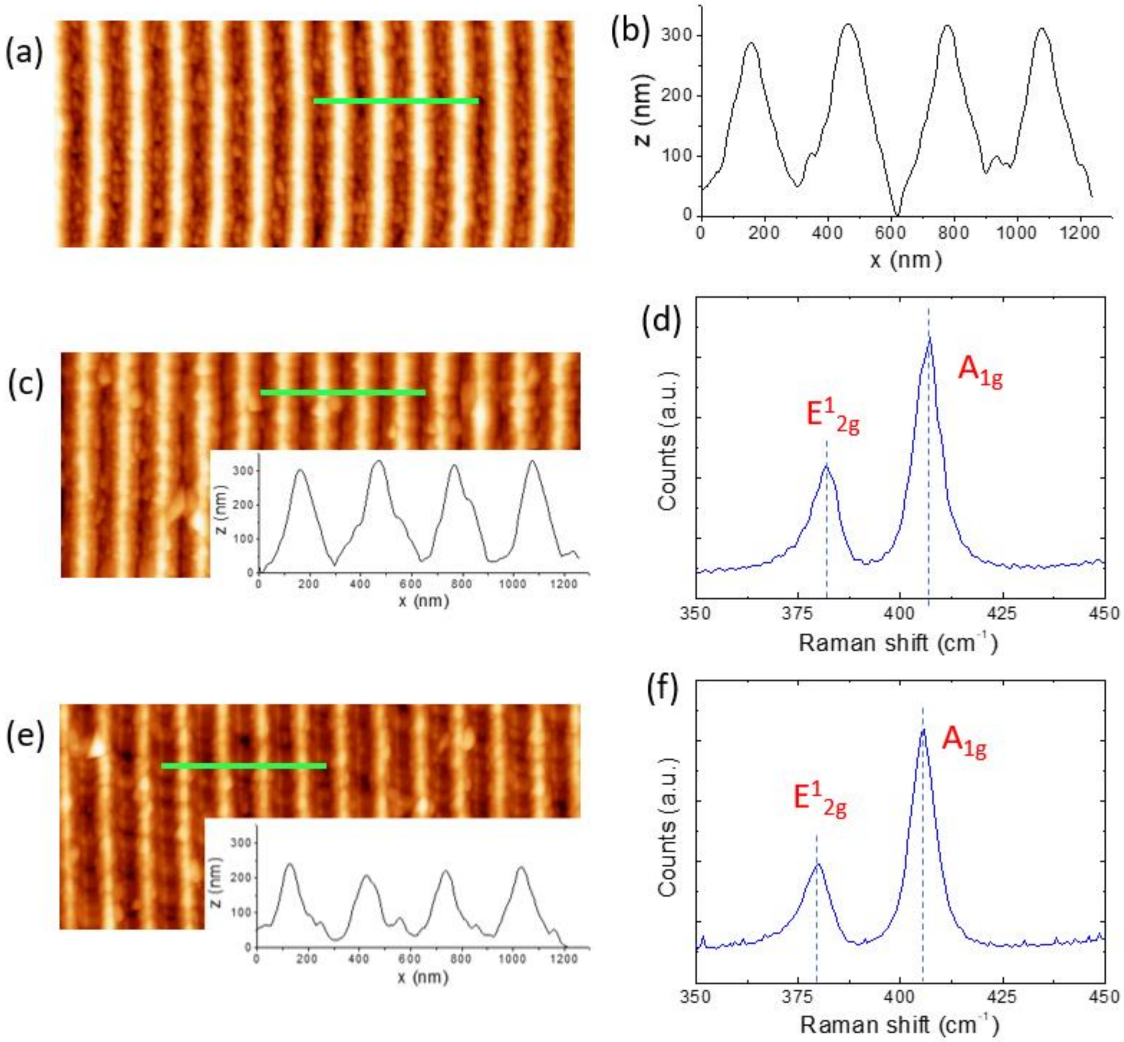

Figure 4.8 (a) AFM image of the initial silica template. (b) Extracted line profile from the AFM image in panel a. (c,e) AFM images and extracted line profiles for the 13 nm and 23 nm thick MoS_2 films respectively, demonstrating conformality on the nanostructured template even at higher thicknesses. (d-f) Raman spectra for the 13 nm and 23 nm thick MoS_2 films respectively.

4.3.2 Optical characterization of nanogrooved MoS_2 arrays with variable thickness

Figure 4.9a-e shows the angle resolved extinction spectra for the different growth steps. Obviously, the optical extinction increases with the MoS_2 thickness, but what is interesting to notice is the behavior of the photonic anomalies. For the case of the lowest thickness (3nm) the results substantially agree with those found in the previous section, with only one visible photonic anomaly that can be attributed to the external Rayleigh anomaly, whereas the internal Rayleigh anomaly can be only individuated by the derivatives of the spectra. As the MoS_2 thickness increases, a second optical anomaly at longer wavelengths can be clearly seen starting from the 13nm thick MoS_2 layer, reaching for the final thickness of 23 nm extinction values as high as 80% with very narrow peaks for grazing illumination. For this thickness, the extinction also reaches values higher than 90% in the C-D excitonic region.

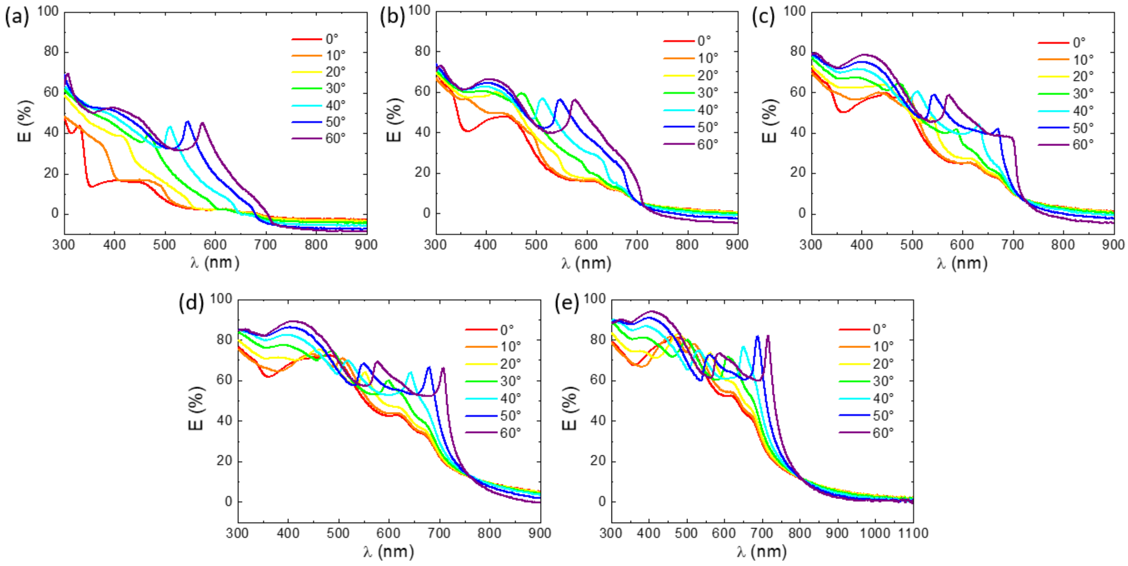

Figure 4.9 (a-e) angle resolved optical spectra at increasing MoS_2 thicknesses (3 nm, 8 nm, 13 nm, 18 nm and 23 nm respectively).

To investigate the dispersion of the optical anomalies detected in the angle-resolved extinction spectra the first derivatives of the spectra were calculated. For simplification, in **Figures 4.10a** and **4.10b** only the derivatives of the spectra for 13 nm and 23 nm thick MoS_2 films are reported. As already obvious from the extinction spectra, the two anomalies become more evident as the MoS_2 thickness increases, suggesting a stronger light-matter interactions and wavefront manipulation.

By recurring to the derivatives of the spectra, the photonic anomalies were fitted using equation (4.2) to extract the effective refractive indices. As an example, in **Figures 4.10c** and **4.10d** I report the anomalies dispersions and the fits obtained for the 13 nm and 23 nm thick MoS_2 films, respectively. In the first case, we found an effective refractive index n_{ext} = 1.00±0.02 for the external Rayleigh anomaly and n_{int} = 1.48±0.02 for the internal Rayleigh anomaly, whereas in the second case we found n_{ext} = 1.06±0.09 and n_{int} = 1.57±0.05. A more complete evolution of the effective refractive indices as a function of the MoS_2 thickness considering all the growth steps is reported in **Figure 4.10e**. The large error bar for the 18nm step is due to difficulties in tracking the anomaly position in the derivatives of the spectra. For the photonic anomalies at lower wavelengths an effective refractive index slightly higher than 1.0 is observed, compatible with an external Rayleigh anomaly propagating at the MoS_2-air interface, while a value of about 1.5 is found for the photonic anomaly at longer wavelengths, close to the silica refractive index and thus confirming the hypothesis of an internal Rayleigh anomaly propagating at the MoS_2-silica interface.

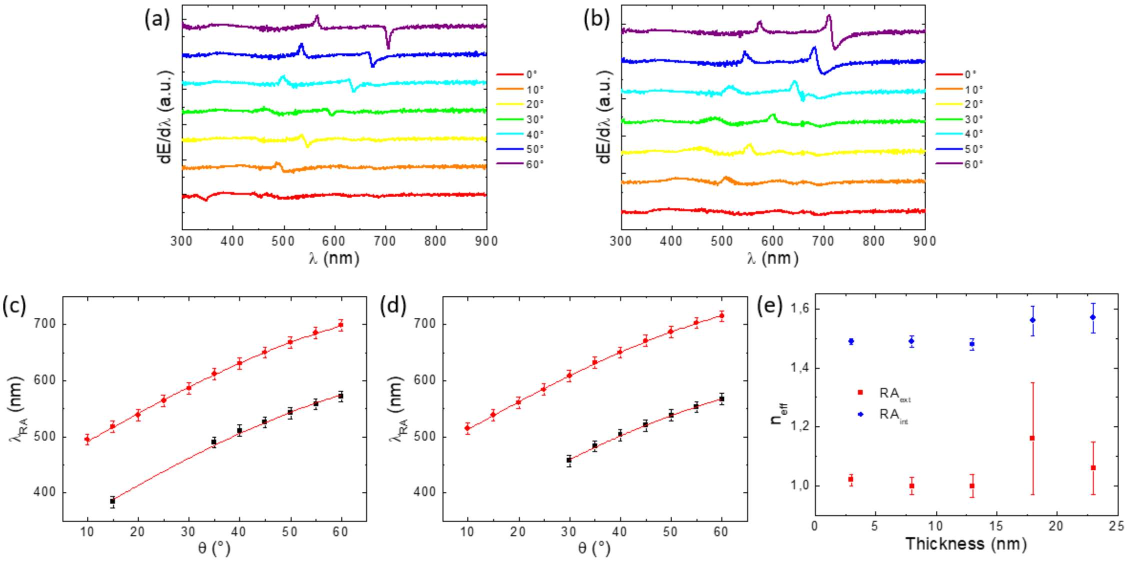

Figure 4.10 (a,b) Derivatives of the spectra for 13 nm and 23 nm thick MoS_2 films, respectively. (c,d) Optical anomalies dispersion and fits for 13 nm and 23 nm thick MoS_2 films, respectively. (e) Evolution of the effective refractive indices for the two anomalies in function of the MoS_2 thickness.

For a better understanding, in **Figure 4.11** a comparison of the extinction at fixed angles (0°, 20°, 60°) is shown. For normal incidence conditions (**Figure 4.11a**) a progressive extinction increase with the thickness is observed with an amplification of the extinction maxima in correspondence to the C-D excitons (400-480 nm) and to the A-B excitons (630-675 nm). However, the extinction maximum at 340nm for the lower thickness (3 nm, black trace), which is attributed to the Rayleigh anomaly, becomes less evident as the thickness increases. This observation suggests a convolution with the excitonic features of the MoS_2 in the spectral regions highlighted in blue and orange, respectively. Especially in the second case, weak local maxima in correspondence to the C and D excitons for thicknesses higher than 8nm.

The evolution of the photonic modes is monitored by tailoring the illumination conditions: a similar comparison is shown in **Figures 4.11b** and **4.11c** for the spectra acquired at $\theta = 20°$ and $\theta = 60°$.

For θ = 20° two maxima are observed for every thickness at about 420-500 nm (blue region) and 530-580 nm (orange region). Both the modes are spectrally sharp and are characterized by a gradual redshift and an intensity increase as the thickness increase. Considering the refractive index of the involved materials in the effective medium (silica, MoS_2, air), the photonic mode in the blue region can be attributed to the Rayleigh anomaly propagating at the external interface (MoS_2-air) whereas the photonic mode in orange region can be attributed to the Rayleigh anomaly propagating at the internal interface (MoS_2-silica).

For θ = 60° a further redshift of these modes is observed with a strong amplification of the internal anomaly, which becomes even stronger than the external anomaly for thicknesses higher than 13nm. Interestingly, in these conditions it is possible to tune the internal anomaly in the spectral region of the A exciton (675 nm). For grazing illumination conditions, in-plane light steering is thus expected to cause an absorption enhancement in the TMD layer.

These results demonstrate that by tailoring the thickness and the illumination angle it is possible to control the excitation intensity of photonic anomalies at the MoS_2 interfaces, tuning their spectral position in correspondence to the material excitonic transitions.

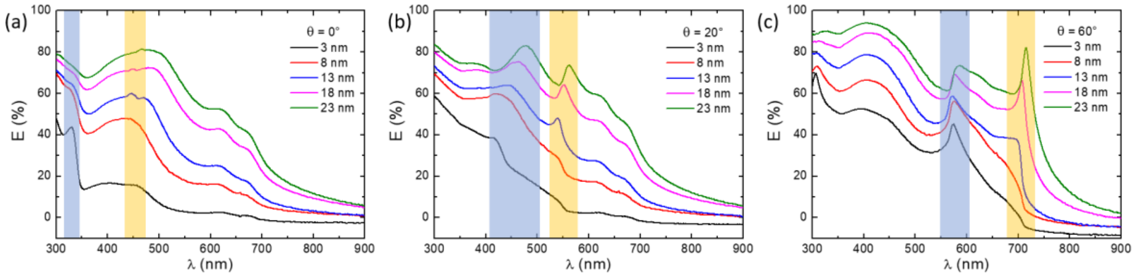

Figure 4.11: comparison of the extinction spectra for different MoS_2 thickness at fixed angles of 0° (a), 20° (b) and 60° (c).

4.3.3 Angle resolved integrated optical absorbance of MoS_2 arrays with variable thickness

In analogy to the extinction spectra discussed, **Figures 4.12a**, **4.12b** and **4.12c** report the comparison of the angle-resolved absorption spectra acquired at the same angles for increasing thickness. Also in this case it is evident the excitation of two dispersive photonic modes (internal and external Rayleigh anomalies) that result in the resonant amplification of the optical absorption, in particular in the case of the internal anomaly which is very narrowband with an absorption values up to 60%. For the external anomaly, the enhanced absorption reaches values up to 80% in the wavelength range between 470 nm and 500 nm.

The absorption spectra demonstrate that the periodic nanostructuring of the TMD layers in the flat optics regime is an effective light harvesting strategy. However, the comparison between extinction and absorption at some fixed angles for the thicker MoS_2 layer, reported in **Figure 4.12d**, clearly shows a strong difference in intensity, meaning that either reflection or scattering are not negliglible, especially in correspondence to the Rayleigh anomalies wavelengths. This observation will be studied in more detail in the next chapter, when considering the scattering properties of nanostructured TMD layers (see paragraph 5.3).

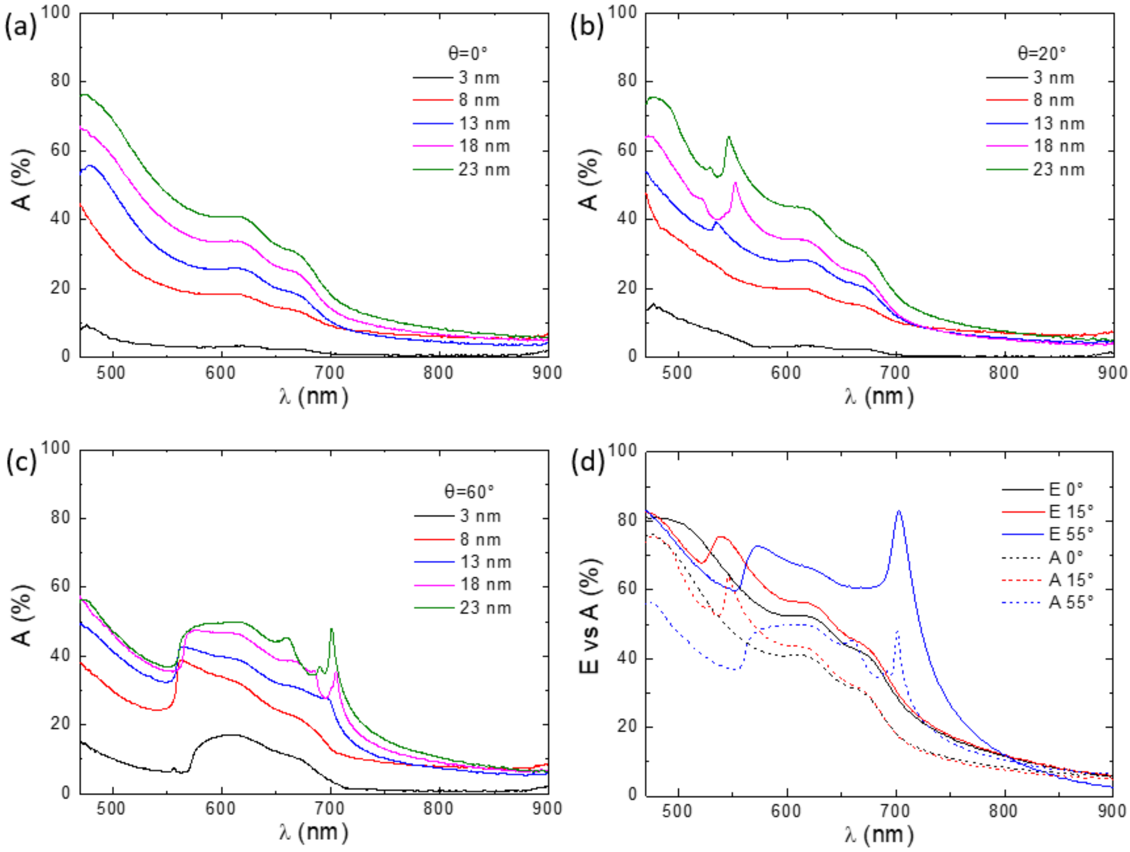

Figure 4.12: a-c) comparison of the extinction spectra for different MoS_2 thickness at fixed angles of 0°, 20° and 60°; d) comparison between extinction (solid lines) and absorption (dashed lines) at fixed angles for the 23 nm thick MoS_2 layer

As already explained, in the nanostructured layers an absorption increase is expected due to the excitation of photonic modes at the interfaces. In **Figure 4.13a** the comparison of the absorption spectra for $\theta = 60°$ for the nanostructured layers and their reference flat films with equal thickness is reported. As expected, the nanostructured layers always absorb more than their reference samples. In the spectral range between the two anomalies, for all the thicknesses a strong and broadband absorption enhancement is observed due to the presence of a non-resonant component in addition to the resonant photonic anomalies. The clear contribution of the internal Rayleigh anomaly though is only evident for the larger thicknesses. In the 23 nm case, an absorption enhancement higher than 200% with respect to the flat reference is observed in correspondence to the internal anomaly.

To quantify the average absorption in the nanostructured layers, the integral absorption in the spectral range from λ = 470 nm (laser lower emission limit) to λ = 750 nm (above the MoS_2 excitonic transitions) was calculated. In **Figure 4.13b** this trend is reported as a function of the thickness for the absorption spectra at different incidence angles (from 0° to 60° at 15° steps). The absorption obviously increases with the thickness, increasing from 3-9% for 3 nm layer to 40-44% for the 23 nm case. For $\theta=0°$, the absorption increases of a factor 13 from the lower to the higher thickness.

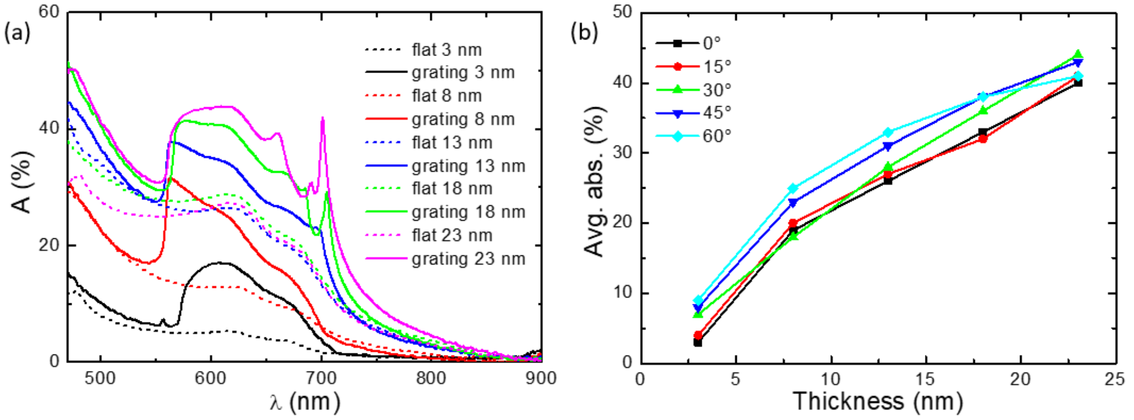

Figure 4.13: a) absorption comparison at θ = 60° for nanostructured and flat MoS_2 layers of different thickness; b) average absorption in the spectral range 470-750nm as a function of MoS_2 thickness

The results I have just shown demonstrate in a straightforward manner the possibility to tailor the optical response of MoS_2 layers all the way from the few-layer to the thick film regime. Particularly relevant is the possibility to shift coupling of the evanescent modes from the outer Rayleigh anomaly to the internal Rayleigh anomaly by increasing film thickness. In view of light harvesting and photoconversion applications this proves particularly relevant since light couples more efficiently to the 2D-TMD material.

4.4 Flat optics hybrid MoS_2/polymer films for photochemical conversion

In the previous sections, I demonstrated a flat optics light harvesting strategy based on subwavelength periodic nanostructuring of 2D-TMD films. In the flat optics regime optical anomalies arising at the evanescence condition substantially increase light-matter interactions. The effectiveness of our approach has been so far demonstrated by optical absorption measurements. In this section, I will present results which emphasize the potential of the novel large area TMD fabrication process for realistic photoconversion applications. More in detail, I will report the results published in a Nanoscale paper in 2023, which demonstrates the improved photocatalytic performances of nanostructured MoS_2 layer compared to a flat reference film[230].

Here, we propose a flat optics scheme based on nanogrooved ultra-thin MoS_2 layers conformally grown onto large area (cm^2 scale) nanopatterned templates. The subwavelength re-shaping of the 2D-TMDs layers promotes the excitation of photonic Rayleigh Anomaly (RA) modes, uniquely boosting a strong in-plane electromagnetic confinement. By tailoring the illumination conditions, we demonstrate effective tuning of the photonic anomalies over a broadband Visible spectrum across the absorption band of relevant polluting dye molecules. Thanks to the strong photonic in-plane confinement we achieve a resonant enhancement of the photodissociation rate of Methylene Blue (MB) molecules, well above a factor 2.

These results point out the potential of this flat optics scheme to photon harvesting in large-scale hybrid 2D-TMD/polymer layers with strong impact in various applications ranging from new-generation photonics to waste-water remediation and renewable energy storage. One possible instance deals with water remediation from chemical and pharmaceutical wastes and by-products. MoS_2 and more in general TMDs layers are actively analysed as renewable photocatalysts for boosting chemical reaction rates, harvesting photon energy[252]. In this context we highlight that the traditional photocatalysts, e.g. those based on TiO_2 films and nanoclusters, typically do not efficiently exploit the whole available solar spectrum due to their wide energy band gap[253].

Conversely, the photocatalytic properties of MoS_2 have been recently demonstrated in different processes among which Hydrogen Evolution Reaction (HER) for splitting water molecules[254,255], an efficient method to convert and store solar power, and for environmental water remediation[256,257]. The main process responsible for molecular dissociation is the injection of the photogenerated MoS_2 carriers into the HOMO/LUMO orbitals of the adsorbed molecule. In other instances MoS_2 can be used as a co-catalyst forming an heterostructure with another photocatalyst (for example CdS in HER processes) promoting efficient carrier injection and improved lifetime[254].

However, the low overall photon absorption of a single layer MoS_2, in the range of ∼10%, still represents a crucial bottleneck towards the development of high efficiency devices[258], and demands for novel photon harvesting and light trapping solutions specifically tailored for atomically thin absorbers.

In this work flat optics platforms based on periodic nanogrooved ultra-thin MoS_2 layers have been achieved over large-scale, promoting enhanced photon absorption and conversion within the few-layer material. Large area (cm^2) periodic templates fabricated by a Laser Interference Lithography (LIL) have been exploited to drive the formation of periodic gratings on transparent and flexible substrates. We developed an original large area physical growth approach of TMDs films, based on the conformal deposition of ultra-thin MoS_2 layers supported onto the periodic templates, forming hybrid polymer/few-layer MoS_2 flat optics nanogratings. These 2D-TMDs nanoarrays feature a light absorption enhancement compared to a reference few-layer MoS_2 promoted by the Rayleigh Anomaly (RA), which steers light flow parallel to the atomically thin 2D semiconductor absorber. Under these conditions we demonstrate the capability to resonantly enhance the photo-chemical degradation process of polluting Methylene Blue (MB) molecules, by effectively tuning the RA mode in resonance to the molecular absorption band.

4.4.1 Fabrication and characterization of MoS_2 layers

In Chapter 2 I described a large area physical deposition approach we developed for the growth of few-layer MoS_2 via RF sputtering of a MoS_2 target performed under high vacuum conditions and at room temperature. This technique thus leads to conformal growth of amorphous MoS_2 films (a-MoS_2) both on flat and nanostructured templates and it is fully compatible with polymeric substrates.

In this way few-layer TMDs can be easily confined on flexible templates as shown in **Figure 4.14a**, extending their applications with respect to the growth on conventional silica substrates. Under these conditions we obtain a uniform a-MoS_2/polymer hybrid film extending over macroscopic areas (cm^2 scale - **Figure 4.14a**), whose thickness reads 10 nm.

A reference a-MoS_2 layer grown onto a silica substrate is thermally recrystallized after growth[7]. To confirm the effect of the recrystallization process both a-MoS_2 and crystalline MoS_2 (c-MoS_2) layers, thickness of both reading 10 nm, are optically characterized. The optical extinction spectra detected over a broadband Near-UV (NUV) - Visible (VIS) - Near-Infrared (NIR) spectral range (**Figure 4.14b**) present markedly different signatures. While in the a-MoS_2 case an unstructured spectrum is detected (red trace), in the c-MoS_2 case (black trace) three well defined transmission minima become evident and allow to identify the semiconducting 2H-MoS_2 phase[259]. The two minima at 675 nm and 625 nm wavelength correspond to the characteristic A and B excitons, while the broader minimum detected at 400 nm is due to higher energy electronic transitions (so called 'band nesting' region)[260]. These conclusions are independently confirmed by the micro-Raman spectra (**Figure 4.14c**) which show the typical E^1_{2g} and A_{1g} vibrational modes excited at 380 cm^{-1} and 406 cm^{-1}, corresponding to the in-plane and out-of-plane Mo-S stretching modes respectively. These typical features are only visible in the c-MoS_2 film (black line). In the following the recrystallization step to form c-MoS_2 will be performed only for reference TMDs films supported on thermally stable silica substrates, while the remaining part of the experimental observation will be performed on a-MoS_2 films as they can be supported by soda lime glass and polymeric substrates which do not tolerate thermal annealing.

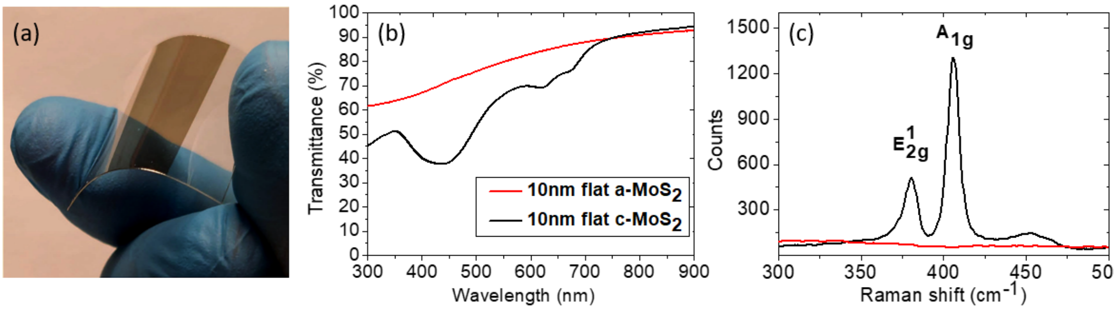

Figure 4.14 (a) Photograph of a large-scale RF sputtered few-layer MoS_2 film (10 nm thickness) deposited onto a flexible polymer substrate. (b) Transmission spectra of a few-layer a-MoS_2 (10 nm thickness -red line) and c-MoS_2 (10 nm thickness - black line). (c) Raman spectra of a-MoS_2 (red line) and c-MoS_2 (black line).

The optical transmittance through the c-MoS_2 film amounts to a value as high as 65% at 675 nm wavelength, corresponding to the A exciton, while above 780 nm wavelength, the optical transmittance of the sub-bandgap photons (i.e. energy below 1.55 eV) exceeds 90%. It is thus clear that effective light-harvesting solutions must be adopted to substantially increase the light harvesting properties of the 2D-TMD semiconductor films if one aims at real world photoconversion applications.

In order to enhance the light matter interaction within the ultra-thin MoS_2 layers we adopt an original approach based on flat optics to redirect the light wavefront parallel to the active layer reshaped to form an anisotropic and periodic nanogrooved medium. Ultra-thin a-MoS_2 layer has been conformally deposited on top of a polymer nanostructured template (as sketched in **Figure 4.15a**), thus forming a periodic subwavelength grating that is capable to excite lattice resonances.

These templates have been nanofabricated using Laser Interference Lithography (LIL), as described in paragraph 4.1. The optical interference fringes are impressed onto a transparent polymeric thin film coating that can be supported both on a rigid glass substrate as well as on flexible polymer (such as polycarbonate). The periodic nanogrooves extend over large areas, at the cm^2 scale, and contribute to steer propagation of the light wavefront, as clearly shown in the picture of **Figure 4.15b**. The interference conditions are chosen to form a periodic array of anisotropic nanostructures characterized by a height of (160±10) nm and by a subwavelength periodicity of (296±10) nm, as highlighted by the AFM image and by the cross-section profile (**Figures 4.15c** and **4.15d** respectively).

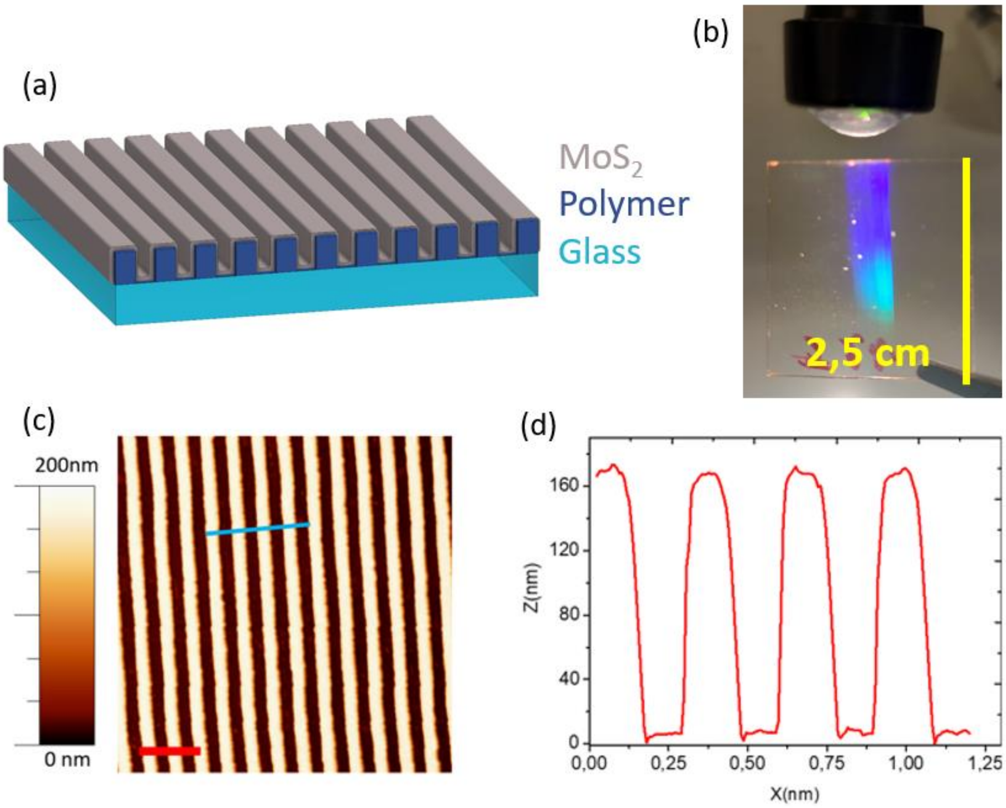

Figure 4.15: a) Sketch of the sample analysed, that is composed of an ultra-thin layer of MoS_2 deposited conformally on a polymeric grating on a glass substrate b) Photograph of the diffraction effect induced by the periodic grating (the yellow scale bar amounts to 2.5 cm) c) AFM topography of a bare polymeric template. The red scale bar amounts to 800 nm d) Extracted AFM line profile corresponding to the blue segment in panel c.

On top of the nanogrooved polymer template we deposit a large area 30 nm thick a-MoS_2 layer, which conformally adapts to the corrugated ripples profile, recurring to physical sputtering from a stoichiometric MoS_2 target. Thanks to the high optical density of the 2D-TMDs layer, the nanorippled film acquires flat optics functionality, boosting light-matter interaction and photo-conversion efficiency even in the limit of ultra-thin films, as revealed by the optical extinction spectra shown in **Figure 4.16b**.

We detected the optical response via angle-resolved NUV-VIS-NIR extinction spectroscopy. The sample was illuminated by a linearly polarized collimated beam (diameter ≈ 2 mm) at a given incidence angle θ with respect to the surface normal (as shown by the sketch of **Figure 4.16a**), with the electric field oriented perpendicular to the incidence plane and parallel to the elongation axis of the periodic nanostructures (s-TE polarization). The extinction spectra detected at different light incidence angles (θ), shown in **Figure 4.16b** with a relative offset for the sake of clarity, clearly underline the presence of a dispersive optical mode, that redshifts by increasing the light incidence angle (blue bars). The dominant extinction mode coherently shifts from 450 nm to 720 nm wavelength as θ increases from 0° (black curve) to 60° (violet curve). In the extinction spectra of **Figure 4.16b** a second weaker feature (red bars), blueshifted by about 150 nm, is also visible. Such optical features launched by the periodic a-MoS_2 array are attributed to evanescent Rayleigh Anomalies (RA) which resonantly redirect the light flow parallel to the periodically corrugated MoS_2 interface, either at the air or at the substrate side, thus coupling efficiently the incident light to the thin TMDs layers. In this way it is possible both to increase light scattering and to induce a strong in-plane light deflection and confinement in the active layer[10]. As a result, photon absorption is enhanced in the 2D-TMDs material itself boosting the photogeneration of electron-hole pairs, and at the same time strong electromagnetic confinement is induced in proximity of the few-layer MoS_2 lattice. To confirm the attribution of the optical modes to the Rayleigh Anomalies we fitted their dispersion recurring to equation (4.2).

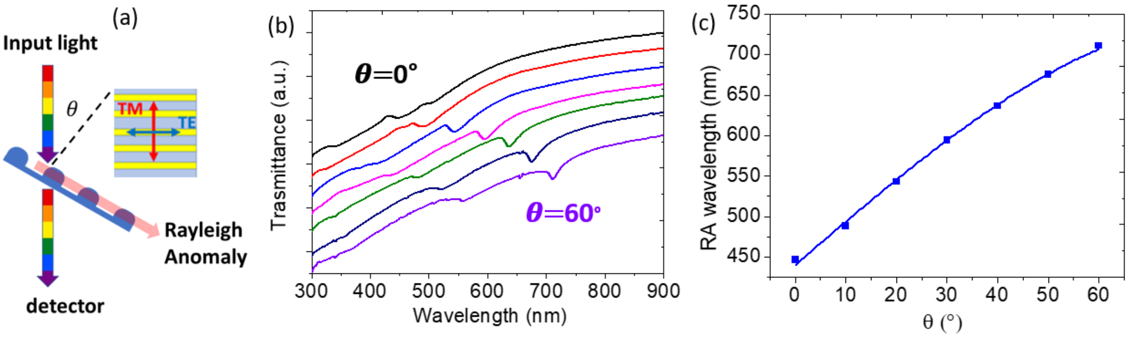

Figure 4.16 (a) Schematic of the optical configuration adopted for the angle-resolved extinction measurements. The incident light is linearly polarized perpendicular to the incidence plane and parallel to the grating long axis (TE polarization). (b) Experimental angle-resolved transmission spectra measured for increasing incidence θ from 0° (black curve) to 60° (purple curve). A relative offset of 10% has been introduced from one spectrum to the other for better reading. The red/blue squares underline the RA modes corresponding to the external/internal interface. (c) Position of the RA minima corresponding to the external (red dots) and to the internal (blue squares) interface, measured for different angles. Solid curves represent the theoretical position of RA (red and blue curves), obtained from equation (4.2).

As highlighted in **Figure 4.16c** the detected dispersion of the transmission dips corresponding to the RA modes at the external/internal interface (red/blue squares respectively) is in good agreement with the model according to equation (4.2), in which the only free parameter is the effective refractive index n. In the model we fix m = 1, n_0

= 1 (air) and a periodicity value P = 290±10 nm compatible with the AFM images. The blue and red lines represent equation (4.2), respectively assuming n_{int} = 1.55±0.03 and n_{ext} = 1.05±0.03. Such effective index values are compatible with an effective medium formed at the inner interface between MoS_2 and silica, and at the outer interface with air. Such results also demonstrate the capability to tune the spectral position of the RA modes within the VIS spectral range, enabling a fine tuning of the photon harvesting properties by simply controlling the illumination geometry or the TMDs nanoarray periodicity.

4.4.2 Photocatalytic experiments

A direct demonstration of the light harvesting enhancement in the nanorippled MoS_2 film can be provided by measuring the photobleaching rate of molecular dye probes such as Methylene Blue (MB) in proximity to the MoS_2 surface. This photochemical reaction is of great interest for waste-water remediation as MB is a polluting molecule widely used in the textile sector. By employing the photocatalytic set-up described in subparagraph 3.1.1, in a first experiment we checked the photocatalytic properties of 10 nm thick MoS_2 films deposited via PVD on flat substrates. We compare the MB photobleaching rate on as-deposited a-MoS_2 films and on recrystallized c-MoS_2 films.

The photocatalytic properties of both the samples have been measured using a custom developed set-up which allows to illuminate the 2D-TMDs layers immersed in the MB solution at variable angles, as sketched in **Figure 4.17a**. To this end, we fabricated a custom 3D-printed sample holder that allows to rotate the sample inside the cuvette and to perform illumination at a specific angle θ, as represented in the sketch.

In **Figure 4.17c** the evolution of the concentration *C* of the MB solution, normalized to the initial value C_0, in presence of 10 nm thick c-MoS_2 film (red dots) and a-MoS_2 film (black squares) is plotted as a function of the photon dose incident on the reference flat films. For both the exposures the samples are kept at normal incidence with respect to the illumination beam. The plot qualitatively evidences that the MB photobleaching rate is almost equivalent in the two cases.

In order to compare more quantitatively the photocatalytic activity of the samples we calculate the kinetic constant k according to the first order reaction kinetic law $[C] = [C_0]e^{-kt}$ where C is the MB concentration as a function of the time t and C_0 is the concentration of MB at the beginning of the exposure. Due to the low photon doses used, the exponential law can be approximated to first order by a linear law $[C] =$

$[C_0](1 - kt)$. In the case sample illumination is performed under non-normal incidence conditions the rate k is corrected by a factor $1/\cos(\theta)$ to consider the reduced photon flux. For the two experiments of **Figure 4.17c**, almost equivalent rates $k_{c\text{-}MoS2}$ = 0.030±0.002 h^{-1} and $k_{a\text{-}MoS2}$ = 0.026±0.002 h^{-1} are found. For both samples, the photodissociation rate is higher than that of the bare MB solution illuminated at 660 nm, which reads k_{bare_MB} = 0.020±0.001 h^{-1}. This result highlights the intrinsic photocatalytic properties of both c-MoS_2 and a-MoS_2 flat reference films.

Since the difference in photobleaching rate between the two reference films is almost negligible, in the following of our work we will focus on the study of the photocatalytic performance of the a-MoS_2 films. These are indeed particularly attractive in view of real-word water remediation applications based on 2D-TMDs because their growth occurs at room-temperature and is compatible with low cost and large area flexible templates, which would not withstand a high temperature recrystallization process.

After observing photocatalytic properties of the planar a-MoS_2 film, in a second set of observations we thus aimed to maximize the photochemical reactivity exploiting the flat optics photon harvesting configuration sketched in **Figure 4.15a**.

In **Figure 4.17d** we investigate the reactivity of a nanogrooved 30 nm thick a-MoS_2 film for different illumination angles θ (0°, 25° and 35°) by plotting the evolution of the concentration C of the MB solution, normalized to the initial value C_0, as a function of photon dose at a fixed illumination wavelength λ = 660 nm. At normal incidence (θ=0°, black squares) we observe a slight enhancement of the reaction kinetic constant for the nanopatterned sample with respect to the reference flat sample, k_{0° = 0.038±0.002 h^{-1}. This is attributed to the increased MoS_2 thickness, and to the larger effective surface area of the nanogrooved sample, estimated by AFM line profiles to be 1.5 times higher than the reference flat sample. Remarkably, the reaction kinetic constant is sharply boosted when the nanopatterned sample is illuminated at an angle θ = 25° (red squares) for which the RA, measured in water, is resonant with the illumination (**Figure 4.17b**). In this case we observe k_{25° = 0.089±0.005 h^{-1}. For this condition the kinetic constant is 2.3 times larger than the same sample illuminated at normal incidence and 3.4 times respect to the reference flat sample. A further increase of the illumination angle to θ = 35° (black squares) detunes the RA and the reaction kinetic constant drops down to k_{35° =0.044±0.003 h^{-1}. This observation is confirmed in an additional set of experiments in which the illumination angle θ is varied systematically, while leaving the illumination wavelength constant at 660 nm, in correspondence to the maximum absorption of the MB solution (**Figure 4.17b**).

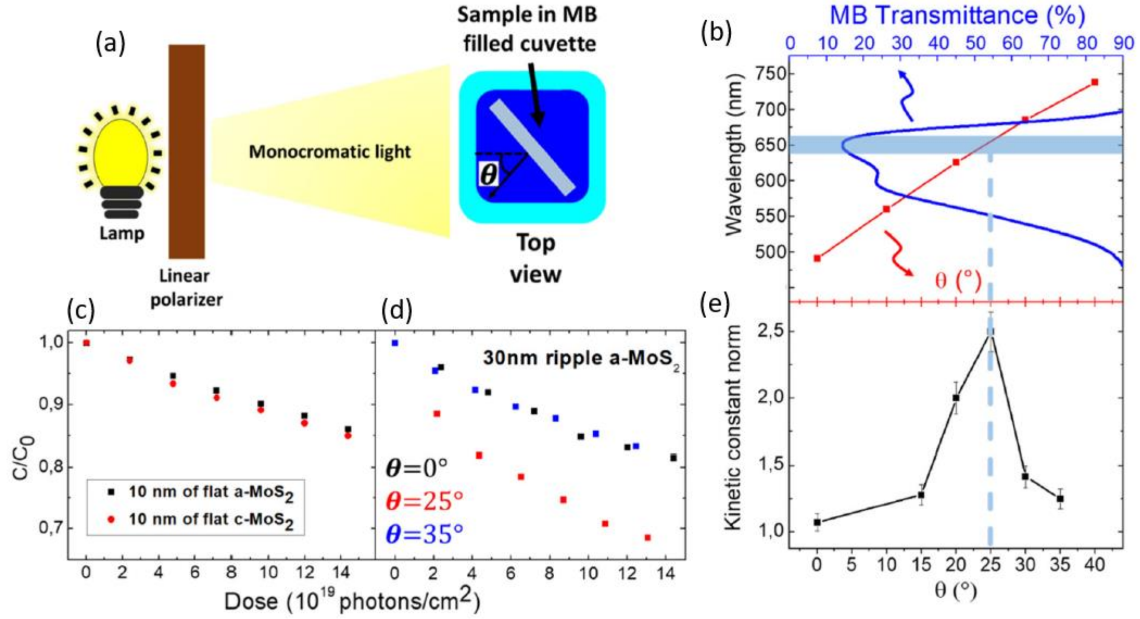

Figure 4.17 (a) Top view sketch of the experimental set-up. (b) Transmission spectra of the MB solution at normal incidence (blue line) compared with the dispersion curve of the RA detected in water (red squares). The blue box represents the excitation beam. (c) Normalized concentration of the MB solution containing a sample with 10 nm of a-MoS_2 (black squares) and solution containing a sample with 10 nm of c-MoS_2 (red circles) as a function of photons dose (pump source wavelength λ = 660 nm). (d) Normalized concentration evolution of the MB solution containing a 30 nm thick rippled film of a-MoS_2 at $\theta = 0°$ (black squares), $\theta = 35°$ (blue squares) and $\theta = 25°$ (red squares) plotted as a function of photon fluence (pump source wavelength λ = 660 nm). For the concentration values shown in panels c and d, the relative error on the measurement is 1%. (e) Plot of the kinetic constant of the photo-bleaching reaction detected for different light incidence angle θ. The red line at $\theta = 25°$ represents that the RA is resonantly excited under the narrowband illumination conditions.

Each of these experiments at variable angle has been analysed in terms of first order kinetic model, determining the kinetic constant normalised to the value $k_{0°}$ measured for normal incidence illumination. In **Figure 4.17e** we summarise the result of such experiments finding a remarkable dependence of photobleaching rate on the illumination angle, leading to a sharp maximum at $\theta = 25°$ (**Figure 4.17b**). Under these conditions the kinetic photobleaching constant is amplified by a factor 2.3 with respect to the non-resonant conditions found for non-optimised illumination at normal incidence, as shown before.

This result is attributed to the flat optics functionalization of the surface and, more specifically, to the ability to modify the spectral match of the inner RA with the chosen illumination wavelength at 660 nm and with the maximum of molecular absorbance (**Figure 4.17b**). Under such optimised illumination condition the incident light beam is redirected by the photonic anomaly, to flow parallel to the surface, thus determining both a local enhancement of the electromagnetic field in the near-surface region and an increased absorption in the active TMDs semiconductor film. Both these features contribute to the photobleaching of dye molecules, as recently demonstrated in the case of plasmonic nanoarrays[179]. In the present case the absorption enhancement is linked to the photogeneration of excited carriers and excitons in the TMD film, which play an important role in the photobleaching process.

In order to evaluate in a direct way the relevance of the absorption channel in the nanogrooved TMDs sample, we analyse the total absorption in a custom modified integrating sphere set-up, which allows to insert the sample inside the sphere with a controlled illumination angle θ in s-TE polarization. Specifically, thanks to a further 3D printed miniaturized rotating sample holder attached to the integrating sphere, the optical set-up allows us to detect the signal $T(\theta)$ due to the sum of direct transmission, diffused forward/backward and specular reflection at a specific illumination angle θ. Optical absorption from the sample is then defined in a straightforward way as $A(\theta) = 1 - T(\theta)$.
In **Figure 4.18a** the absorption spectra for different illumination angles corresponding to a 30 nm thick flat reference MoS_2 (dashed lines) and to a 30 nm thick nanorippled MoS_2 (continuous lines) are reported. For all the spectra corresponding to the nanorippled sample a broadband and omnidirectional enhancement of absorption is visible. The latter is attributed to the increase of light scattering in the Mie regime, effectively promoted by the high index 2D-TMDs nanostructures[261], and to waveguiding and trapping in the supporting dielectric substrate. In addition, for the spectra acquired under tilted illumination conditions, a further resonant and dispersive absorption band is visible, whose spectral position redshifts with increasing illumination angle, in good agreement with the extinction feature corresponding to the RA optical anomalies (**Figures 4.16b** and **4.16c**). To better analyse the absorption gain, in **Figure 4.18b** we report the ratio between the absorption spectra of the nanostructured sample and the flat sample. From these spectra the absorption of the sample results more than doubled in a broadband region corresponding to a spectral range ranging from 500 nm (lower limit of the

supercontinuum laser employed for illumination) to 800 nm (onset of MoS_2 absorption in correspondence to the A exciton transition - **Figure 4.14b**). Moreover, for the tilted samples a sharp resonant enhancement of absorption is visible and reaches up to 300% in correspondence to the inner RA anomalies confined at the buried MoS_2 interface, observed in the transmission spectra (**Figure 4.16b**). The observation of the absorption gain in the nanostructured MoS_2 films is an evidence that the MoS_2 photogenerated carries may play a role in the previously observed increased rate of the MB photobleaching. As expected, the outer RA anomalies which predominantly concentrate the electromagnetic field at the air interface contribute in a limited way to the optical absorption gain in MoS_2, reported in **Figure 4.18b**.

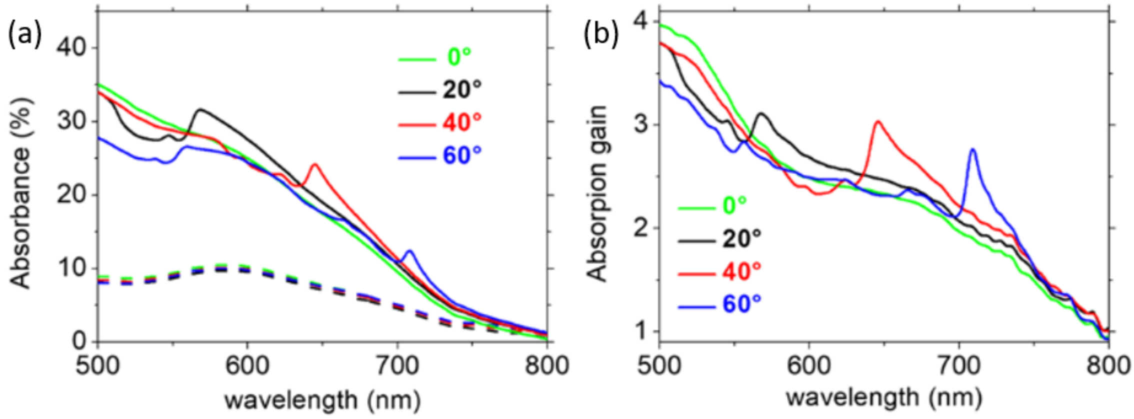

Figure 4.18 (a) Optical absorption spectra extracted from integrating sphere set-up performed under different incidence angle illumination conditions and TE polarization the of the incident light. The dashed lines correspond to a 30 nm flat MoS_2 film while the continuous lines correspond to a 30 nm rippled MoS_2 film. (b) Absorption gain at different illumination angles defined as the ratio between the absorption spectra of the nanostructured sample and the flat sample.

We demonstrate the optimal photon harvesting properties of nanogrooved few-layer a-MoS_2 by using these templates into a standard photobleaching reaction of polluting MB dye. We made different expositions at fixed excitation wavelength, tailoring the incidence angle of the light. The narrowband excitation of the RA tuned in resonance to the molecular absorption strongly boosts the photochemical properties of the solution, giving rise to a clear maximum of the photobleaching kinetic constant. This behaviour is due to the enhanced light-matter interaction promoted by the RA mode, that can strongly confine the light within the ultra-thin reshaped MoS_2 layer. The resonant RA excitation induce both an enhancement of the photon absorption, with higher carrier photogeneration within the active layer, and an amplified local field with boosted reactivity at the surface. The enhanced photobleaching of MB demonstrates the efficiency of this light trapping solution for photon harvesting and photo-conversion in ultra-thin TMDs layers.

4.5 Discussion

To sum up the results presented in this chapter, we demonstrated a novel photon harvesting scheme for few-layer 2D MoS_2 nanogratings which exploits large area nanostructured dielectric templates extending over cm^2 areas.

We employed a Laser Interference Lithography approach to fabricate homogenously patterned large area samples in the form of subwavelength periodic nanogratings. These lattices are able to support the conformal growth of ultra-thin MoS_2 films precisely following the nanogrooves. For the deposition we employed a physical vapor deposition method that is compatible with large area and scalable processes and, in addition, can be used in flexible polymeric samples. In our works, we either transferred the lithographic pattern geometry to the dielectric silica substrates recurring to a Reactive Ion Etching process or directly exploited the nanostructured photoresist mask.

We demonstrate the capability to achieve shape engineering of ultra-thin TMDs layers conformally grown on top of large-scale periodic nanogrooved templates, featuring flat optics functionalities. A subwavelength silica grating conformally coated with large area recrystallized MoS_2 layers promotes light coupling within the 2D material thanks to the excitation of a Guided-Mode Anomaly confined at the substrate-2D layer interface. We demonstrate the potential of this flat optics approach combining both resonant light confinement and non-resonant wave guiding in the dielectric template for broadband photon-harvesting in few-layer MoS_2. The strong and broadband photon harvesting efficiency of these flat optics configurations opens the possibility to exploit this large area nanofabrication approach in a new generation of macroscopic 2D nanodevices with a strong impact in nanophotonics, photovoltaics and quantum technologies.

With a simpler fabrication approach, we deposited conformal amorphous MoS_2 layers directly on the lithographic polymer mask. The hybrid polymeric/MoS_2 interface still enables manipulation of the optical wavefront, redirecting it parallel to the active interface when the Rayleigh Anomalies are resonantly excited with a narrowband illumination beam, thus promoting photon harvesting and enhanced photobleaching of polluting dye probes. The nanogrooved amorphous MoS_2 layers support photonic anomalies which can be tailored across the VIS-NIR region from 450 nm to 720 nm by simply optimizing the illumination angle. Tuning the Rayleigh anomaly with the molecular optical absorption, we demonstrate enhanced photobleaching of a polluting die probe.

These results thus qualify the large area hybrid 2D-TMDs/polymer layers as promising candidates for the implementation of cost-effective photocatalytic waste-water remediation applications. Additionally, this flat optics approach is very promising in order to promote efficient light trapping in ultra-thin semiconductor layers for wider applications in optoelectronics, photonics, and quantum technologies.

Chapter 5 – Light wavefront manipulation in nanostructured TMD layers

In Chapter 4 a flat optics light harvesting strategy based on subwavelength periodic reshaping of large area TMD layers was proposed. Effective optical absorption enhancement was obtained in the case of few layer MoS_2 layers conformally grown by physical deposition on top of nanostructured silica substrates. Engineering of photonic anomalies which steer light parallel to the TMD film either at the outer or inner interfaces was obtained by optimizing the MoS_2 thickness. In this last chapter instead, I will focus on the following main issues: engineering nanofabrication of the silica templates, optimized for the maskless fabrication of large area arrays of TMD nanostripes (MoS_2), and for the fabrication of periodic nanoarrays of vertically stacked TMD heterostructures (MoS_2/WS_2). Additionally, I will address my attention at a direct investigation of the potential of the high refractive index TMD nanoarrays as flat optic nanoantennas for launching scattered and waveguided radiation. The latter measurements, though still preliminary, are made possible by a custom fabricated scatterometer set-up.

In paragraph 5.1 I will present some results on the morphological modification of the nanostructured silica templates via Ion Beam Sputtering experiments, achieving different reshaping whether the sputtering occurs at normal or grazing incidence angles. In particular, grazing incidence sputtering enables slope selection and faceting, introducing asymmetry in the templates.

In paragraph 5.2 I will present more detailed scattering measurements performed on a continuous nanorippled MoS_2 film and compare it with the scattering of a bare silica template, showing a strongly enhanced scattering signal in case of a high refractive index MoS_2 layer. These results demonstrate the possibility to manipulate the light wavefront in a flat optics regime with 2D-TMD films.

In paragraph 5.3 I will introduce a maskless deposition process for large area nanoarrays of MoS_2 nanostripes, by off-normal incidence deposition of laterally disconnected MoS_2 stripes on a nanostructured asymmetric silica template, in which slope selection offers the possibility to control the tilt of the TMD nanostripes array. Under such configuration, interesting scattering effects are expected from the MoS_2 nanostripes, operating as optical antennas. To study these interactions, in subparagraph 5.3.1 I will describe the implementation of a custom scatterometer set-up, while in subparagraph 5.3.2 I will present some preliminary results, showing the possibility not only to increase optical absorption, but also to manipulate the optical wavefront with atomically thin TMD layers. In paragraph 5.4 I will use a similar maskless deposition process for the fabrication of large area nanoarrays of van der Waals heterostructures, based on nanostructured templates to laterally confine WS_2 nanostripes by off-normal incidence deposition, followed by deposition of a conformal MoS_2 layer. For such system, improved light harvesting is found due to the insertion of the WS_2 nanostripes array. In view of photocatalytic application, this geometry is favorable not only because of the higher absorption, but also because of the formation of type-II heterojunctions arrays, which for planar films have already been shown to be more reactive than the individual layers in Chapter 3. Unfortunately, ultimate photocatalytic experiments were not performed since the strict limitations on the sample shape were not satisfied.

5.1 Templates reshaping via Ion Beam Sputtering

In Chapter 4 I described a large area nanofabrication process based on Laser Interference Lithography and Reactive Ion Etching to pattern nanostructured SiO_2 templates. Here, I will demonstrate the possibility to further reshape the morphology of the silica template (either controlling the pattern height or the local facet slope and roughness) via erosive Ion Beam Sputtering (IBS), employing a defocused Ar^+ ion beam at 800eV at variable incidence angles.

In conventional ion beam nanopatterning experiments an initially flat substrate exposed to defocused ion beam irradiation typically develops a ripple-like nanopattern induced by self-organized mechanisms described by the Bradley-Harper model and its non-linear refinements[262]. The model takes into account competition between the erosive action of the ion beam (destabilizing mechanism) and the relaxation by thermally- and ion-activated diffusion of surface adatoms (stabilizing mechanisms) which assume different importance when sputtering is performed at off-normal incidence angles[263]. For intermediate angles, a periodic ripple pattern with a spatial wavevector oriented parallel to the ion beam projection results, while for sputtering at grazing incidence angles the ripple pattern develops with spatial wavevector orthogonal to the ion beam projection[264]. A transition to a flattening regime is normally observed for near normal incidence conditions for which the erosive action is minimized, and ballistic energy transfer from the impinging ions to mobile adatoms results in a net stabilizing mass flow from the top of the ridges to the bottom of the valleys[265]. Other important pattern formation mechanisms come into play if the ion beam alters the elemental composition of the top surface layers by preferential sputtering so that they develop a compressive strain[238]. In this case, provided sufficient mobility of the surface atoms is granted (either thermally activated or by ion induced viscous flow), a wrinkling destabilization mechanism takes place in order to reduce the surface energy, leading to efficient formation of a high aspect ratio faceted morphology. Under ion irradiation conditions for which mass transport is relevant, it is also possible to define at will the slope of the faceted profile by appropriately choosing the local ion beam incidence angle close to maximum of the angular dependent sputtering yield[238].

In my work I chose a different regime of nanopatterning by Ion Beam Sputtering, in which the silica substrates are irradiated by the defocused Ar ion beam in a pre-patterned condition, i.e. after high aspect ratio nanogratings have been formed by the LIL+RIE nanofabrication process described in paragraph 4.1 and shown in **Figure 4.2**. In a first set of experiments, I performed irradiation experiments at normal incidence with the aim of smoothing the substrate reducing the local roughness, and the aspect ratio of the surface profile from flat-top into a saw-tooth faceted one. We initially performed normal incidence sputtering experiments on two silica templates with periodicity (P) of about 300 nm and 1100 nm, respectively. Initial morphology line profiles of few periods directly after the RIE process are reported in **Figure 5.1a** (black trace) for the sample with P = 300 nm and in **Figure 5.1b** for the sample with P = 1100 nm, both clearly showing flat-top crests maintaining the original silica wafer surface. **Figure 5.1a** also shows the evolution of the line profile for the template with P = 300 nm at different steps of the sputtering process. After 20 seconds of sputtering (red trace), the structures have become narrower and the flat-top crests have shrunk to a cusp. In parallel, the crests height has globally increased due to different erosion rates of crests and valleys[262]. By further sputtering to a total time of 80 seconds (blue trace) the height has decreased while preserving the nanostructures aspect ratio, and the initially rough valleys have been smoothed.

In **Figure 5.1c** the height evolution as a function of the sputtering time is reported for both the short and long period templates. The first observation is that the higher periodicity (meaning a larger gap between the Al mask stripes) enables higher vertical dynamics since vertical etching can last longer before the lateral erosion make the sacrificial metal mask collapse. Interestingly, for both the sample an initial height increased is observed with the sputtering dose, though on longer times for the larger period. After that, a rather constant decrease rate of about 1nm/sec is observed at longer sputtering times.

Figure 5.1d reports the evolution of the facets slopes (ϕ) showing a slow shallowing of the structures that maintain their aspect ratio, as already highlighted by the line profiles. These results show that IBS can effectively smooth and reshape the surface morphology. The local slope of the facets ϕ = ±65° turns out to be selected around the maximum of the sputtering yield of Ar ions[238]. I stress here that if IBS sputtering experiment would have been performed starting from an initially flat SiO_2 substrate only shallow ripple patterns with very small local slope would have been formed[266]. The use of pre-patterned template thus open-up new possibilities for engineering specific details of the nanopattern via self-organized ion beam sputtering.

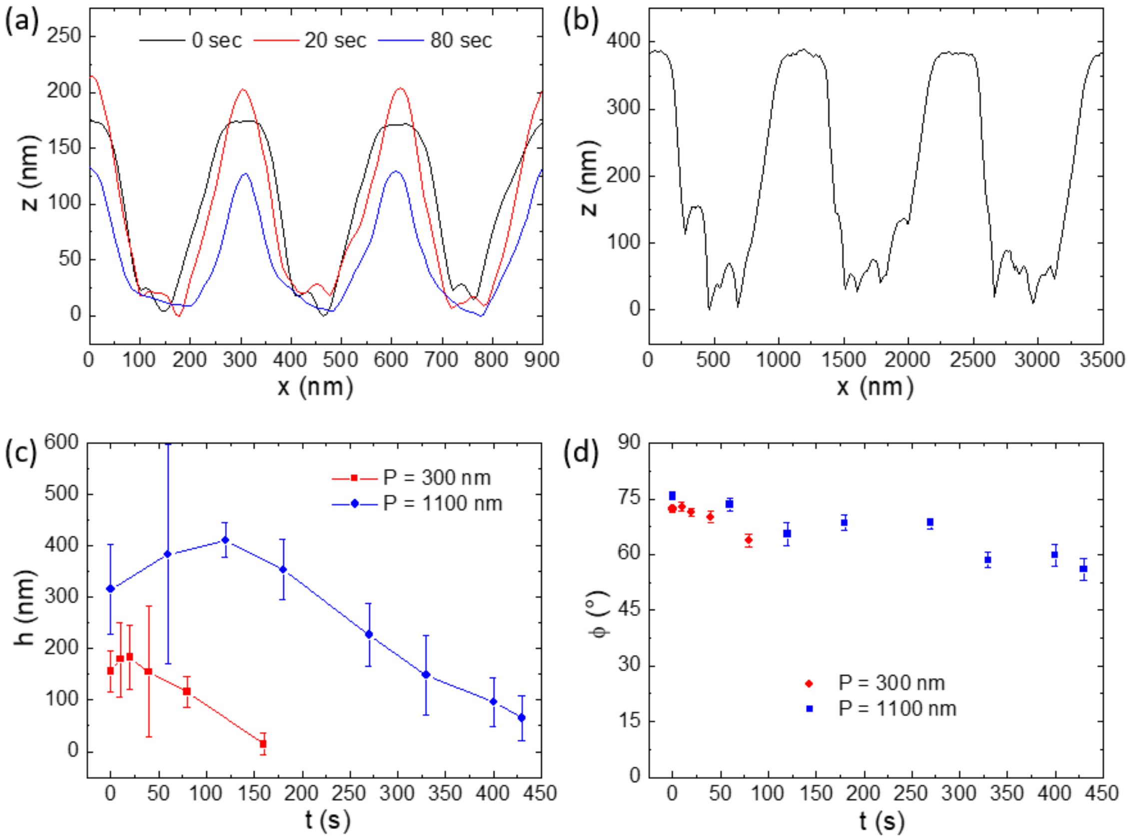

Figure 5.1 (a) Line profile of few periods at different sputtering times for the template with P = 300 nm. (b) Initial morphology for the template with P = 1100 nm. (c,d) profile height and slope evolution for both P = 300nm and P = 1100nm samples as a function of sputtering times.

In the following, I will describe an additional opportunity offered by the IBS nanopatterning at an off normal sputtering angle θ, as sketched in **Figure 5.2a**. Under these conditions, for a symmetric template with slopes of ±ϕ sputtered at an off-normal angle θ a different local sputtering angle occurs on the two sides of the crests, so that the difference in sputtering yield results in the anisotropic faceting of the template.

In **Figure 5.2b** I show the AFM image and an extracted line profile of a nanostructured silica template (P = 300 nm) that has been sputtered at θ=15° with the ion beam impinging from the left side as in the previously shown sketch. As a result, the right side of the template crests appears flattened with respect to the steep left side slope.

Figure 5.2c shows the slopes distribution evolution as a function of the sputtering time at θ=15° for the considered sample. Starting from the symmetric initial situation (black trace) it is evident that after 120 seconds of sputtering long facets with slope ϕ = −35° (right side) have formed, while short steep facets with ϕ=65° (left side) have preserved themselves on the template side facing the ion beam.

In **Figure 5.2d** a comparison of the slopes distribution at fixed sputtering time (t = 90 sec) for templates sputtered at different θ angles is reported. If we focus on the negative slopes with the predominant peak in the histogram (right side of the crests, the one illuminated downhill by the ion beam), it is possible to notice a shift of the peak facet slope histogram (from −42°, to −37°, and −22°) which follows proportionally the increase in the sputtering angle θ from 15°, to 25° and 40°. This result further confirms that we can control the slope of our faceted templates by selecting the ion beam incidence angle in correspondence to the maximum of the local sputtering yield on the facet. These results can be of particular interest for several applications such as color routing with plasmonic nanostructures[267,268] or tilted Mie optical resonators for light wavefront manipulation. A preliminary demonstration of the potential application of these asymmetric templates will be shown in the next paragraph for supporting the growth of tilted and disconnected MoS_2 nanostripes grown in registry with the faceted substrate by glancing angle deposition.

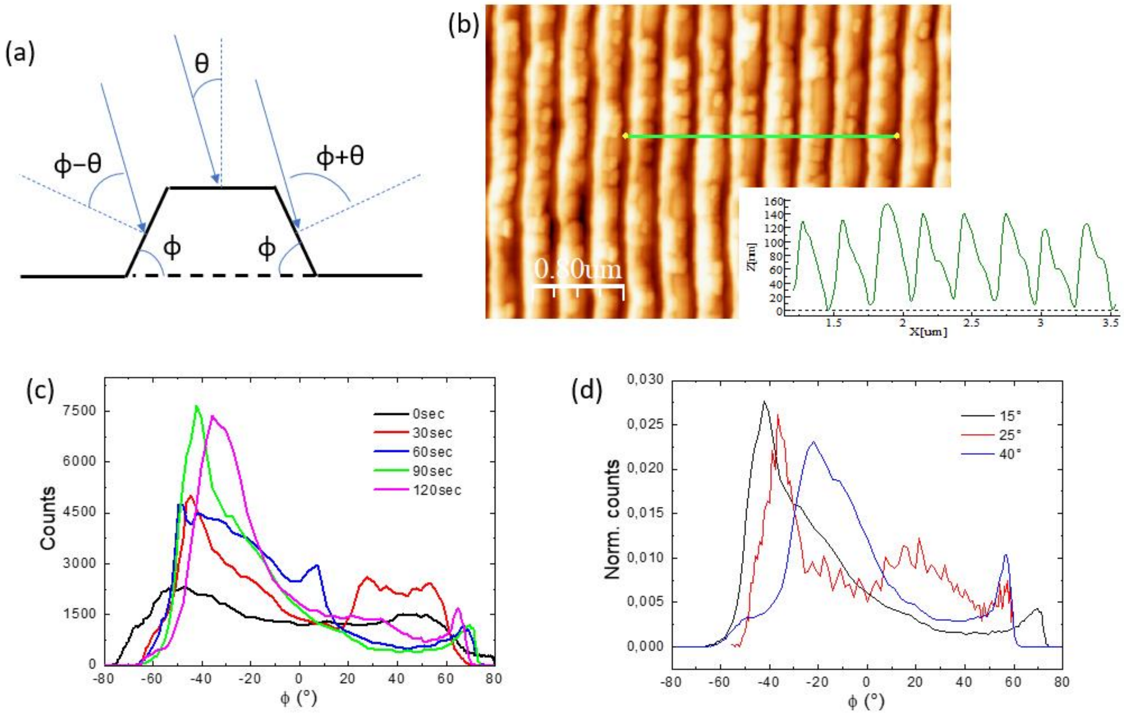

Figure 5.2 (a) Sketch of the off-normal sputtering of nanostructured templates. (b) AFM image and extracted line profile for a template sputtered at θ=15°. (c) Slopes distribution evolution as a function of sputtering time at θ=15°. (d) Slopes distribution at fixed sputtering time for different sputtering angles.

5.2 Large area maskless fabrication of MoS_2 nanostripes arrays

Reshaping of SiO_2 templates via Ion Beam Sputtering was introduced in paragraph 5.1 and a representative example of asymmetric templates with slope selected facets was shown. Here, in the first instance I will describe how the uniaxial silica templates can represent an ideal platform which enables large area nanofabrication of laterally disconnected MoS_2 nanostripe arrays. The latter are formed over cm^2 areas by glancing angle shadow deposition of the TMD precursor in a single maskless step.

Since TMDs are characterized by an extremely high optical density compared to conventional semiconductors[3], it is expected that the nanostripes exhibit strong light scattering properties and perform as nanoantennas already in the ultra-thin flat optics regime. In the final part of my thesis, I have thus embarked in a preliminary exploratory study aiming to assess the potential of the disconnected MoS_2 nanostripes for enhancing electromagnetic field localization and scattering in the Mie regime. For this purpose, I developed a custom scatterometer set-up capable of varying both polarization and incidence angle of the illuminating beam as well as the scattering angle across the whole VIS-NIR spectral range.

The fabrication of a large area array of laterally disconnected MoS_2 nanostripes was achieved by means of IBS deposition at grazing angles on nanostructured templates, using the set-up described in Chapter 2. A silica template was previously sputtered at off-normal incidence to reshape the grating morphology forming faceted ridges on top of which the nanostripes are deposited exploiting shadowing effects. **Figure 5.3a** shows the morphology of the template, which has been sputtered at 15° to obtain facets with a selected slope of about 35°. Given the template morphology, we decided to deposit 3 nm of MoS_2 by Ar sputtering from a stoichiometric target, at a grazing incidence angle of 50°, as shown in **Figure 5.3b**. Under these conditions geometrical shadowing from the steep ridges ensures that 200 nm wide disconnected MoS_2 nanostripes are deposited on the illuminated facet of the SiO_2 ripples. The self-organized maskless deposition process thus ensures a straightforward nanofabrication of TMD nanostripes arrays, with full control of nanostripe width and thickness by controlling deposition angle and dose, as well as control on nanostripes periodicity and tilt by tailoring the SiO_2 template periodicity and slope.

After recrystallization of the MoS_2 nanostripes, angle resolved extinction spectra were acquired for positive and negative tilt angles (see sketch in **Figure 5.3c**) to characterize how the asymmetry of the sample affects its optical response even in this ultrathin TMD regime. The results are reported in **Figures 5.3d** and **5.3e** for positive and negative angles, respectively. At normal incidence a Rayleigh anomaly is observed around 300 nm as expected from a periodic array with period around 300 nm. A direct comparison of the two graphs, showing respectively optical extinction for positive and negative illumination tilt angles shows some differences: in general, the peak corresponding to the Rayleigh anomaly is more evident for positive tilt angles, and in general a slightly higher extinction from the MoS_2 excitonic features is observed for negative tilt angles (e.g. compare the spectra acquired at $\theta=\pm60°$ in the two panels). No difference would instead be expected in the case of a symmetrical SiO_2 template capped by a continuous and conformal MoS_2 film.

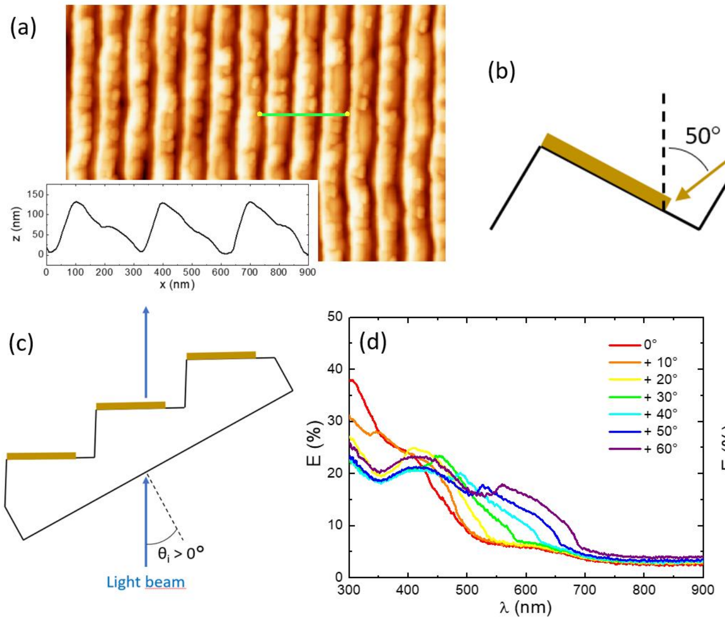

Figure 5.3 (a) AFM image of the asymmetric silica template used for the deposition of MoS$_2$ nanostripes. (b) MoS$_2$ nanostripes deposition geometry. (c) Sketch indicating positive θ angles. (d,e) Angle resolved extinction spectra for positive and negative θ, respectively.

In order to better highlight the differences between the extinction spectra for positive and negative illumination angles we chose a selected set of spectra which are plotted in **Figures 5.4a**, **5.4b** and **5.4c.** Here we show a comparison between the optical extinction spectra acquired at θ = 0° (illumination at normal incidence with respect to the sample macroscopic surface normal), at θ = +35° (illumination at normal incidence with respect to the MoS$_2$ nanostripes local normal) and θ = −55° (illumination parallel to the nanostripes long axis).

Given the subwavelength sizes of our MoS$_2$ nanostripes (200 nm width, 3 nm thickness, 300 nm period), the optical response in transmission configuration is a complex intermixing of diffraction from the periodic lattice conditions and of interaction (absorption, waveguiding and scattering) with the effective medium composed by MoS$_2$/SiO$_2$/air nanostructured interface. The optical spectra reported in **Figure 5.4d** show that extinction is higher when the long axis of MoS$_2$ nanostripes is oriented parallel to the light beam (θ = −55°, sketch in Figure 5.4c) rather than when it is perpendicular (θ = +35°, sketch in Figure 5.4b). Remarkably, the extinction enhancement occurs for the wavelengths corresponding to the MoS$_2$ excitons (C and D transitions in the range 400-450 nm, A and B transitions in the range 600-700 nm). This observation can be explained in terms of the interaction of light with the thicker effective medium formed by MoS$_2$ nanostripes: for θ = +35° the interaction along the propagation direction occurs with a very low thickness of 3 nm, whereas for θ = −55° the thickness of the effective medium becomes dominated by the width (200 nm) of the MoS_2 nanostripe, which favors stronger optical absorption.

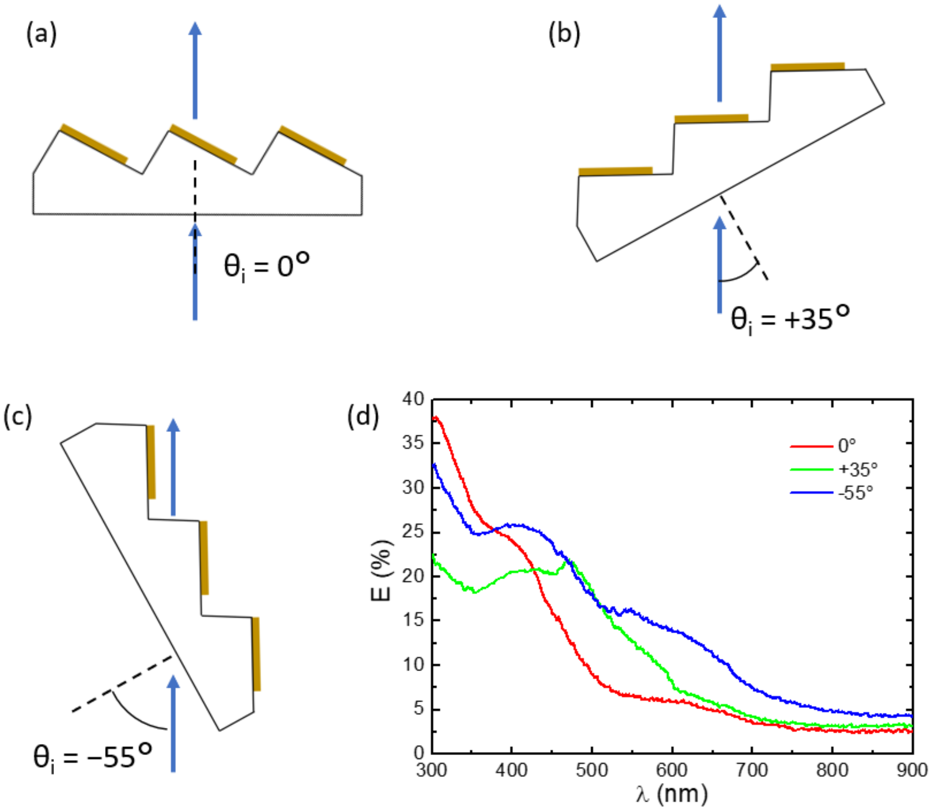

Figure 5.4 (a-c) Sketches of the significant illumination angles at θ = 0°, θ = +35° and θ = −55° adopted for the extinction measurements. (d) Optical extinction spectra acquired for the illumination angles shown in panels a-c.

For the case θ = 0° optical extinction is higher in the near UV, around 300 nm, since the Rayleigh anomaly dominates the spectrum, but overall it is lower in the remaining spectral range when compared to the other two configurations. For θ = +35° the Rayleigh anomaly is clearly observed at about 500 nm where the extinction is increased, whereas for θ = −55° a weak anomaly can be found at about 550 nm. We underline that the marked differences in the extinction spectra are already evident for TMD film as thin as 3 nm, and that a much stronger contrast is expected to occur by increasing further the thickness of the MoS_2 nanostripes in the range of 20 nm and beyond. Due to time limits, I did not have time to study optical extinction in this regime which will be explored in future experiments.

5.2.1. Scatterometer set-up

To characterize the light scattering properties of the nanostructured TMD layers I assembled a custom experimental set-up (scatterometer) as shown in **Figure 5.5**. The set-up is designed to work in transmission configuration with transparent substrates, though reflection measurements are also possible.

The illumination source is a NKT Photonics broadband white laser (SuperK COMPACT) that emits in the 450-2400 nm range. A combination of two polarizers is used to control the laser intensity (first polarizer used as attenuator) and polarization (second polarizer). A rotating sample holder is fixed to a goniometer to control the light incidence angle θ, defined with respect to the sample normal. We consider positive θ angles for counterclockwise rotation and negative θ angles for clockwise rotation. The scattered light is detected by a collimating lens that can rotate in the incidence plane and is fiber-coupled to a solid-state UV-VIS-NIR detector (Ocean Optics HR4000). A second goniometer is used to control the detection angle ϕ defined with respect to the sample normal. As sketched in **Figure 5.5**, we consider positive ϕ angles for clockwise rotation and negative ϕ angles for counterclockwise rotation.

The measurements have been acquired in transmission configuration, with incident light entering from the flat backside of the silica substrate and scattered light exiting from the nanostructured TMD side in the upper half-space defined by the nanostructured TMD surface. In order to quantitatively compare the scattering spectra acquired in different configurations, they have been normalized to the “white” laser emission spectrum (measured by illuminating a teflon lambertian diffuser that has constant 99% reflectivity in the spectral range of interest), also taking into account the differences in the laser attenuator and in the acquisition time of the spectrometer.

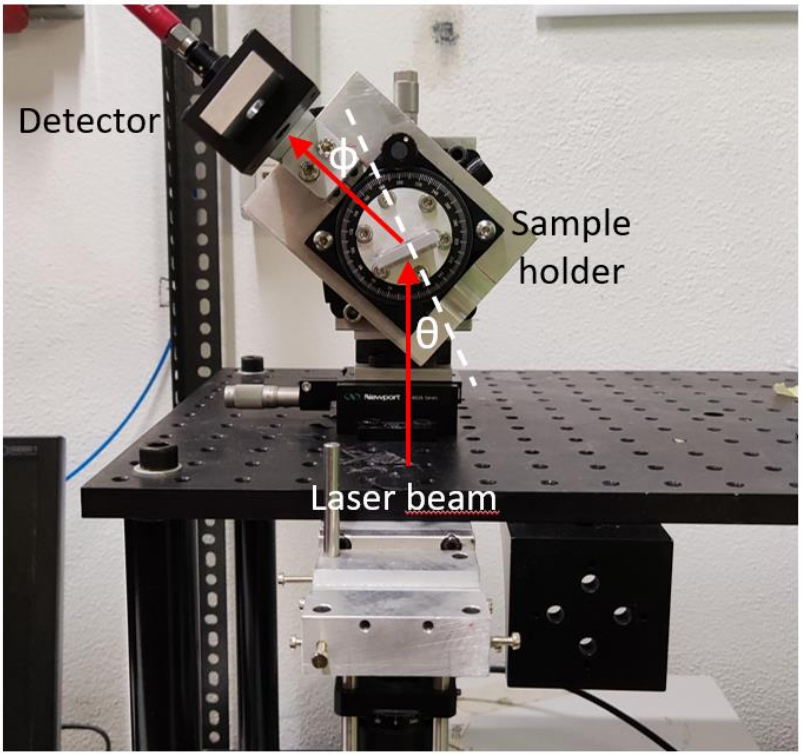

Figure 5.5 Custom scatterometer set-up; two independent goniometers allow to control incidence angle θ (positive in the shown geometry) and detection angle ϕ (negative in the shown geometry). The supercontinuum laser source is mounted in the bottom and shines light vertically.

5.2.2 Light scattering from MoS_2 nanostripe arrays

Due to time restrictions, so far I could only perform preliminary scattering measurements on the MoS_2 nanostripes which were described in the previous paragraph, in order to verify their potential application as optical nanoantennas. The scattered signal has been measured in a selected configuration sketched in **Figures 5.6a** and **5.6b** with illumination at normal incidence θ = 0°, and detection at some relevant configurations: ϕ = +35° (detection of scattering normal to the long axis of the MoS_2 nanostripes) and ϕ = −55° (detection of scattering parallel to the long axis of MoS_2 nanostripes). To evaluate the optical asymmetry of the sample, the scattered signal was also detected at ϕ = −35° and ϕ = +55°.

The scattering spectra recorded with the detector at ϕ = ±35° are reported in **Figure 5.6c**, while those recorded with the detector at ϕ = ±55° are reported in **Figure 5.6d**. It is straightforward to see that the spectra at ϕ = ±35° and ϕ = ±55° are not equivalent due to the morphologic asymmetry of the sample. Particularly relevant is the comparison between the scattering spectra detected at ϕ = +35° (blue trace) and at ϕ = −55° (black trace), when the detector is respectively aligned perpendicular or parallel to the long axis of the nanostripes: in the former case we observe a significant four-fold increase in scattered intensity since the MoS_2 nanostripe, endowed with a very high refractive index $n \approx 5$, acts as a dipole scatterer in the Mie regime[261].

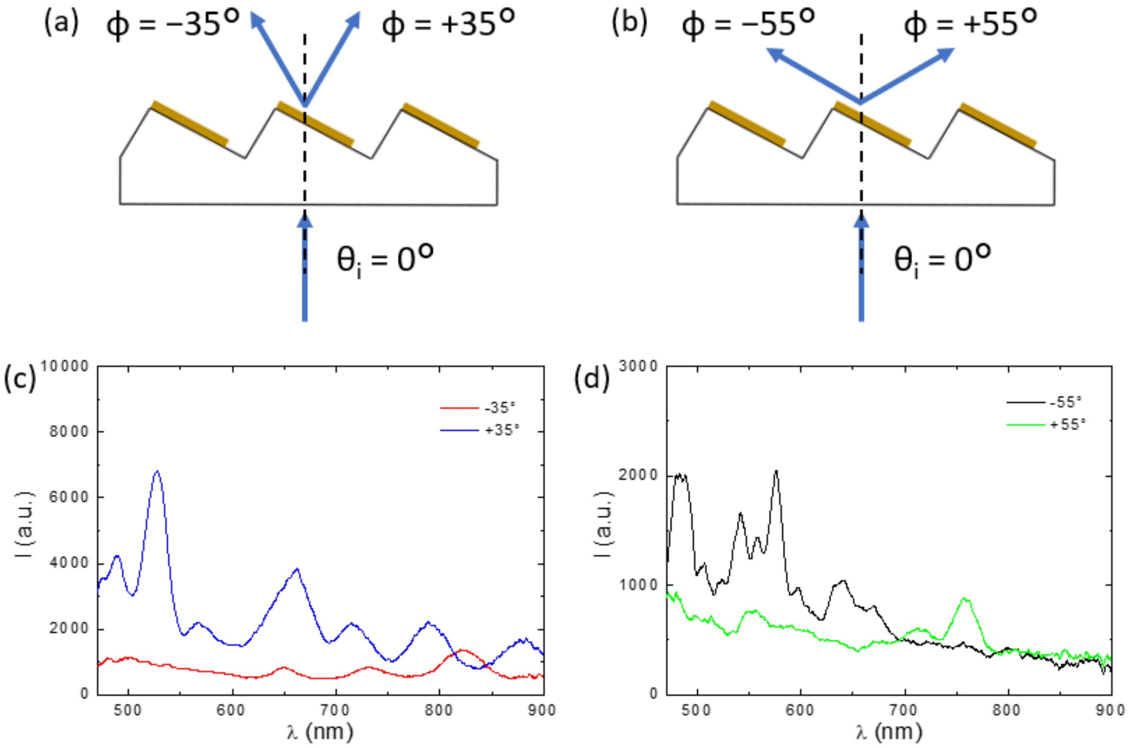

Figure 5.6 (a,b) Scattering measurements geometries. (c,d) Scattered signal detected for ϕ = ±35° and ϕ = ±55°, respectively.

Additionally, the scattering spectra shown in **Figure 5.6c** evidence strong intensity oscillations that are particularly relevant for ϕ = +35° when the detector is oriented perpendicular to the nanostripe long axis. The origin of such oscillations is attributed to the onset of Fabry-Perot resonances supported by the MoS_2 nanostripes. Such resonances are expected at a wavelength λ_m for which a MoS_2 nanostripe (width d) contains an integer number m of half-wavelengths[269]:

$$d = m\lambda_m/2n \qquad (\text{eq. } 5.1)$$

In **Figure 5.7a** I show the result of a simple heuristic calculation of the Fabry-Perot resonance for MoS_2 nanostripes of different width d, and with refractive index n derived from ref [270], according to equation (5.1). Though the calculation is oversimplified and does not take into account the very small thickness and the non-ideal shape of the MoS_2 nanostripes, the result highlights a qualitative agreement between the calculated resonant wavelengths and the observed scattering spectra. In order to describe in a more quantitative way the remarkable oscillations observed in the scattering spectra, finite elements electromagnetic simulations would be necessary quantitatively identify the origin of these optical modes. These simulations are planned in the framework of an external collaboration but unfortunately the results are not yet available at the present time.

Basing on the results of the preliminary simulations of **Figure 5.7a** we can conclude that the TMD nanostripes perform as Fabry-Perot nanoresonators and show a substantial four-fold enhancement in the scattering cross section with respect to the baseline (e.g. for the mode at 525 nm the intensity reads 7000 cts against a background of 1500 cts). The simulation in **Figure 5.7** also indicates that due to the very high refractive index of the MoS_2 film, which exceeds 5 in the visible range (**Figure 5.7b**), TMD nanoantennas with sizes in the 100 nm range can sustain Fabry-Perot and Mie resonances in the visible spectral range. The large scale nanostructured 2D-TMD arrays fabricated via scalable and low-cost processes thus prove effective also for light scattering and color routing applications in the flat optics regime in which just few atomic layers thick nanoantennas are employed.

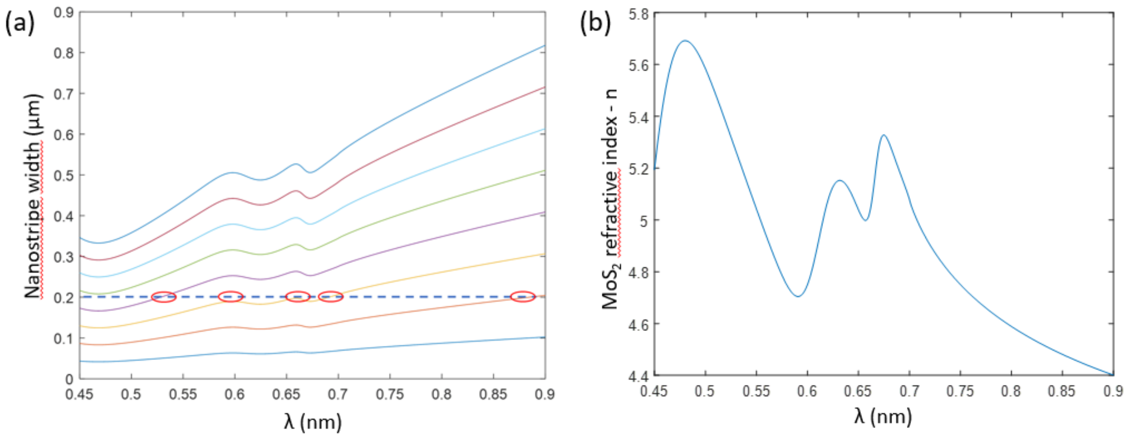

Figure 5.7 (a) Calculation of the Fabry-Perot resonance wavelength for MoS_2 nanostripes of different width (d). Dashed line represents nanostripe width d = 200 nm. (b) MoS_2 refractive index (real part n) accord to ref [270].

5.3 Light scattering from continuous MoS_2 nanorippled film

In Chapter 4 I described the growth and optical characterization of continuous nanorippled MoS_2 films with increasing thickness, conformally supported on silica templates. After each incremental growth step, I characterized optically the optical response by angle-resolved extinction and absorption measurements inside the integrating sphere set-up. In particular, in **Figure 4.12d** I showed a comparison between extinction and absorption for the highest MoS_2 thickness of 23 nm, highlighting the presence of a relevant contribution from either reflection or scattering to explain the different intensities.

Here, thanks to the custom scatterometer set-up described in the previous paragraph, I will focus on a direct characterization of waveguiding performance of the nanorippled MoS_2 layer in correspondence to the evanescent condition corresponding to the Rayleigh anomalies. The scattering signal at the evanescent condition will then be placed in comparison with a bare silica template used as a reference, in order to evaluate the flat optics performance of the high refractive index TMD layer. I will also provide a simple qualitative evaluation of the free-space diffracted component originating from the periodically undulated 2D-TMD nanolayer, since this component does not contribute to the enhancement of optical absorption of interest for photoconversion applications.

In **Figure 5.8a** a top view sketch representing the 23 nm thick nanostructured MoS_2 sample is shown. The patterned MoS_2 region is confined in the left edge of the sample (cross hatched area) while a flat MoS_2 film covers the right part of the silica substrate. Illumination with the supercontinuum laser source takes place from the bottom side in the middle of the MoS_2 nanograting. The asymmetry in the sample conformation must be kept in mind, as we will see later that differences arise when light is scattered and waveguided towards the near edge or the far edge of the sample.

In **Figure 5.8b** a photograph shows in a qualitative way the interaction of the light beam with the nanostructured 2D-TMD sample, for an illumination angle tilted at $\theta_i = -45°$. A white screen is placed on the right side of the sample to directly visualize the effects of diffraction and scattering: the photograph shows clearly both the free-space propagating diffractive modes and the evanescent Rayleigh anomaly (RA), as clarified by the sketch in **Figure 5.8c**.

The red spot in the direction tangent to the sample ($\phi = 90°$) is related to the Rayleigh anomaly arising at the evanescence condition that results in the propagation of light confined at the TMD interfaces. In such configuration we refer to a backward Raileigh anomaly since due to the interaction with the grating wavevector, the light $\vec{k}$ wavevector is reversed towards the half-space where the light source is placed. Under the experimental conditions of **Figure 5.8b**, i.e. $\theta_i = -45°$, the evanescence condition for the

Rayleigh anomaly occurs for wavelengths towards the red, as evident from the photograph and in agreement with the equation (4.2) described in subparagraph 4.2.2.

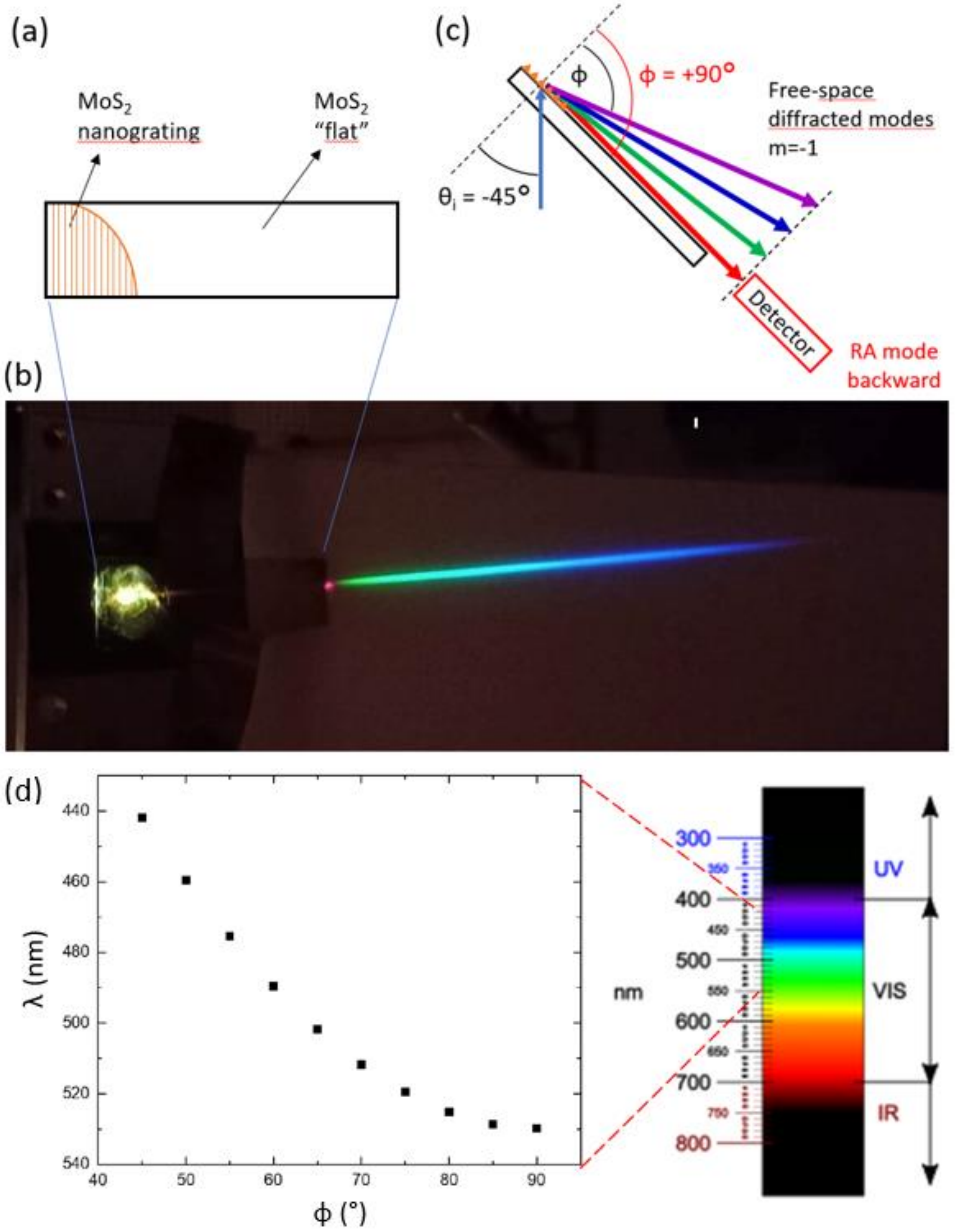

Figure 5.8 (a) Sketch of the measured sample, indicating the pattern position with respect to the substrate length. (b) Photograph qualitatively showing the light-grating interaction. (c) Sketch of Rayleigh anomaly and free-space diffracted modes. (d) Expected angular dispersion of the free-space diffracted modes in the m = −1 order.

The colored light blade, going from green to violet, is instead related to optical modes originating from the diffractive interaction of the light beam with the periodically nanostructured MoS_2 film. For wavelengths shorter than λ_P, light is diffracted in the free space modes that propagate in the upper half-space with decreasing wavelengths as the detector angle ϕ (defined from the sample normal) decreases. It is possible to qualitatively reproduce the dependence of the diffracted modes by use of the analytic expression for a transmission grating:

$$\lambda = \mathrm{P}/\mathrm{m}\,(-\sin\phi - \sin\theta_\mathrm{i}) \qquad (\mathrm{eq.\,5.2})$$

where P is the grating periodicity (about 300nm in our case), m (±1, ±2, …) is the diffractive order, θ_i is the incidence angle and ϕ is the scattering angle of the diffracted mode. In our case (**Figure 5.8b**), with P ~ 300nm, m = −1 and $\theta_\mathrm{i} = -45°$, the angles corresponding to the color blade projected on the white screen vary from $\phi = 45°$ (blue) to $\phi = 90°$ (green), in good qualitative agreement with the dispersion shown in **Figure 5.8d**. Given the low periodicity of our nanograting, only the m = −1 order and m = 0 order (direct transmission) give rise to free space propagation in the visible spectral range.

By placing the detector arm of the custom scatterometer set-up at a tangent angle $\phi = 90°$ it is also possible to directly collect the waveguided light component launched tangent to the MoS_2/silica interface at the evanescent condition. In **Figure 5.9** we study the backward Rayleigh anomaly behavior as a function of the incidence angle, ranging from $\theta_\mathrm{i} = -45°$ to $\theta_\mathrm{i} = +45°$ at 5° steps. The adopted experimental configurations are shown in **Figures 5.9a** and **5.9b** distinguishing two cases for positive θ_i and negative θ_i, since for the former case the backward anomaly is detected for the detector at $\phi = -90°$ while for the latter at $\phi = 90°$. As it will be relevant later in the discussion, please notice in the two sketches the different length of the optical path traversed by light confined in the Rayleigh anomalies for the two cases.

In **Figures 5.9c** and **5.9d** the detected scattered signal for negative and positive θ_i respectively is shown. The graphs show that the Rayleigh anomaly is almost monochromatic with a very narrow peak characterized by a half width at half maximum (HWHM) of about 3nm. In the case of **Figure 5.9d** the narrow RA peak is broadened by the presence of secondary peaks at shorter wavelengths arising from free-space diffracted modes that are collected by the collector lens its acceptance angle.

By changing θ_i it is possible to tune the spectral position of the internal Rayleigh anomaly across the visible range from about 470 nm to 660 nm, in optimal agreement with the angular dependent dispersion derived from the extinction spectra reported in paragraph 4.3 and summarized in **Figure 4.9e** and **Figures 4.10b** and **4.10d**. Thanks to its high refractive index, the nanostructured MoS_2 film is thus able to efficiently couple almost monochromatic radiation in the evanescent Rayleigh anomaly in the flat optics regime. In **Figures 5.9c** and **5.9d** it is also possible to notice at shorter wavelengths and for grazing incidence angles the presence of the second RA mode corresponding to evanescent propagation at the external interface.

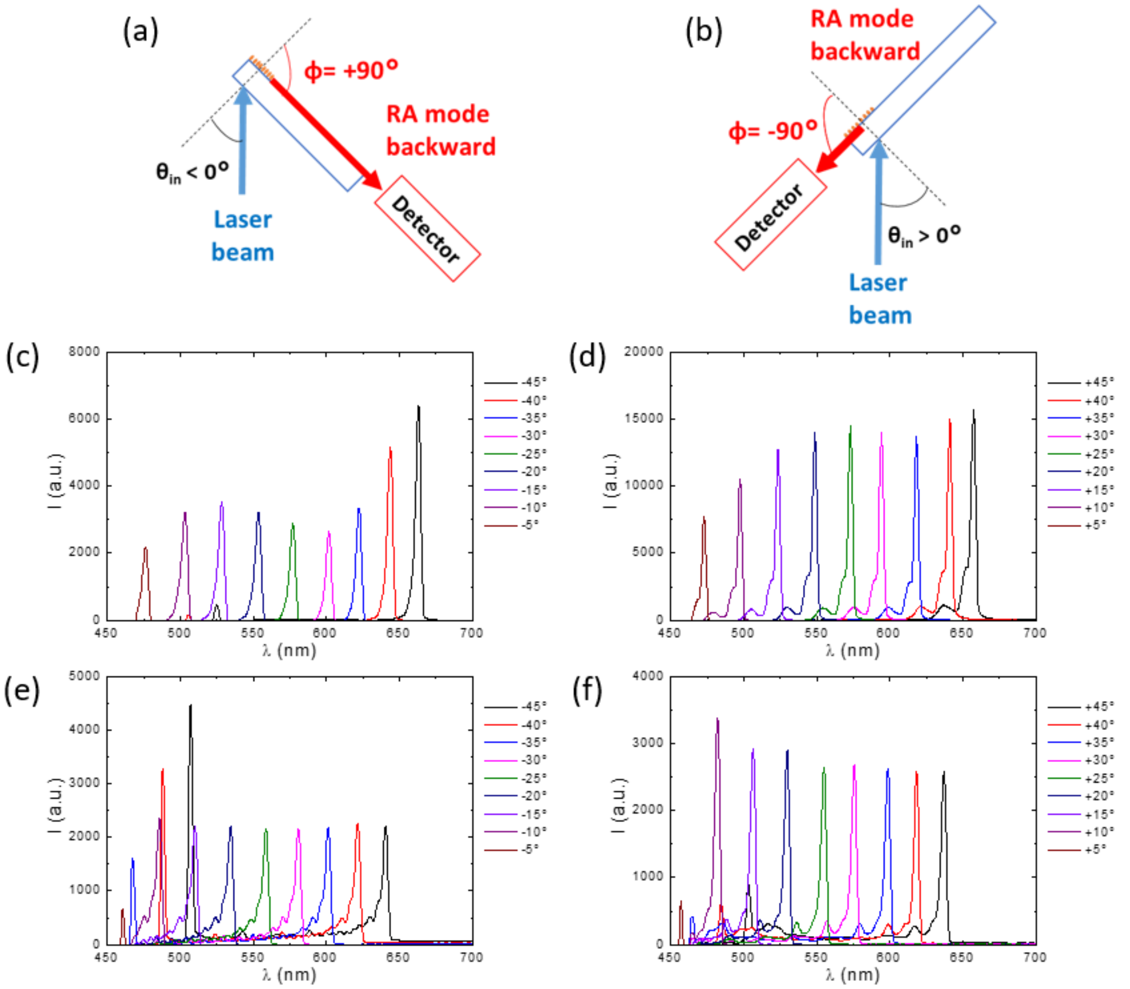

Figure 5.9 (a,b) Sketches of the backward Rayleigh anomaly for negative and positive θ, respectively. (c,d) Detected signal for nanostructured 23 nm thick MoS_2 layer at different incidence angles under the geometries shown in panel a and b, respectively. (e,f) Detected signal for bare silica template at different incidence angles under the geometries shown in panels a and b, respectively.

A direct comparison between the spectra of **Figures 5.9c** and **5.9d** allows to highlight a substantial difference in the scattered intensity (a factor between 2 and 4) depending on the sign of θ_i. As already mentioned, due to the sample asymmetry the waveguided light follows a different optical path at the MoS_2 interface for positive or negative incidence angle. Since the extinction coefficient of MoS_2 at visible wavelength presents a substantial value in correspondence to the excitonic transitions the waveguide must be considered lossy and a substantial degree of absorption losses is expected for light trapped in the waveguided modes. In the case $\theta_i > 0°$ the optical path is shorter which explains the higher detected intensity (e.g. 15000 counts at $\theta_i = +25°$ in comparison to 2000 counts at $\theta_i = -25°$).

To disentangle the effective contribution of the ultra-thin TMD layer from the scattering of the bare silica grating substrate, the light scattering from a second silica template with similar morphology and periodicity was measured. The rippled geometry of the sample is the same of the nanostructured MoS_2 film, with the patterned region close to an edge of the sample and a longer flat region towards the other edge. This similar asymmetry will be important for a comparison with the leaky waveguide described before. In **Figures 5.9e** and **5.9f** the backward Rayleigh anomalies at negative and positive θ_i are reported. For the bare silica grating too we observe a dispersion of the narrowband Rayleigh anomaly across the visible range, going from about 460 nm to 640 nm. The blueshift in the angular dispersion agrees with the lower refractive index of the bare silica with respect to the MoS_2 film. Interestingly, for the higher negative θ_i the external Rayleigh anomaly at shorter wavelengths is more intense than the internal Rayleigh anomaly.

The similar intensities of the scattered signal for negative and positive θ_i despite the different optical path length in the two directions can be explained by purely dielectric and non-lossy nature of the SiO_2 substrate. The results further confirm our previous conclusions which highlight the effectiveness of 2D-TMD nano arrays engineered with subwavelength periodicity as an effective flat optics light harvesting strategy.

Finally, by direct comparison of **Figures 5.9c** and **5.9d** with **Figures 5.9e** and **5.9f** it is straightforward to notice that the nanorippled MoS_2 film (thickness 23 nm), exhibits a scattering intensity enhanced up to a factor 6 in comparison to a SiO_2 nanograting with 200 nm pattern amplitude, demonstrating the potential of nanostructured 2D-TMD films for flat optics applications thanks to the high optical refractive index in the visible range ($n_{MoS2} \sim 5\text{-}6$ vs $n_{SiO2} \sim 1.5$).

5.4 Large area van der Waals heterostructure nanoarrays engineered for light harvesting

In this last paragraph I will show a more demanding application of the nanostructured silica templates as platform for the growth of large area arrays of vertically stacked TMD heterostructures (MoS_2/WS_2). Our physical deposition process based on ion beam sputtering combined with the nanostructured templates enables the engineering of a two-step maskless deposition process: first, tilted nanostripes arrays based on few-layer WS_2 are grown by glancing angles deposition, and then conformally coated by a continuous few-layer MoS_2, thus achieving large area van der Waals heterostructure nanoarrays.

On one hand, the periodic van der Waals heterostructures nanoarrays promote the excitation of photonic anomalies at the evanescent condition, which steer light flow parallel to the ultrathin active material. On the other hand, the periodic modulation of the refractive index provided by the tilted WS_2 nanostripes, which act as optical sensitizers, dramatically boosts photon absorption in the TMDs medium.

The enhancement of solar light harvesting in ultra-thin van der Waals heterostructures, functionalized following flat optics concepts, represents a promising step towards real-world application of large area 2D-TMDs heterostructures in photoconversion, nanophotonics, and energy storage applications.

5.4.1. Large area Nanofabrication of van der Waals 2D-TMD heterostructures

Large area arrays of 2D-TMDs heterostructures have been confined onto transparent silica templates with a maskless ion beam assisted growth process. Periodic nanogrooved silica substrates have been fabricated recurring to the custom variant of the Laser Interference Lithography (LIL) coupled to Reactive Ion Etching (RIE) described in paragraph 4.1. The characteristic morphology of the templates is investigated by means of Atomic Force Microscopy (AFM). **Figure 5.10a** reports an AFM image together with an extracted cross-section profile for one of the fabricated substrates, highlighting the high aspect ratio of our patterns. Specifically, the template considered in the following discussion is characterized by a vertical dynamic of about 200-250 nm and a periodicity of 300±15 nm, as assessed from the self-correlation of the AFM image (see Figure SI1 – Supporting Information). The nanoridges morphology has been also studied in terms of the slope (ϕ) distribution, obtained from the first derivative of the AFM topography and shown in **Figure 5.10b**. The two peaks in the slope distribution, observed at about $\phi = -$

65° and ϕ = 70°, arise from the opposite facets of the nanoridges and demonstrate the potential application of these templates for maskless confinement of tilted nanostructures arrays by shadow deposition over large areas.

To fully exploit the potential of our high aspect-ratio periodic templates for guiding the confined growth of self-organized TMD nanostructures, we developed the custom Ion Beam Sputtering deposition set-up for multiple TMDs deposition that is schematized in **Figure 5.10c** and has already been described in subparagraph 2.3.1. By rotating the substrate at an angle θ, we can have precise control on the deposition of laterally disconnected TMD nanostructures confined by maskless glancing angle growth on the illuminated facets.

The accurate control on the growth condition, combined with the faceted template morphology, offers the flexible nanofabrication of different heterostructures designs. Besides achieving large area growth of two-dimensional materials, our innovative approach enables to easily fabricate few layer TMD nanostructures tilted out-of-plane at difference of state-of-the-art lithographic techniques. Our proposed configuration favors peculiar optoelectronic response of the tilted ultra-thin layers, thus opening new possibilities in nanophotonics triggered by the various possibilities in nano-optics[6,8,154].

The heterostructure sample HS1 was fabricated starting from the nanopatterned substrate described in **Figures 5.10a,b**. Exploiting the high aspect ratio of the template, lateral disconnection of WS_2 nanostripes was achieved by performing deposition at an off normal incidence angle ϕ = 50° (sketch in **Figure 5.10d**). Considering the local incidence angle of the atom flux on the facets ($\phi - \theta = 65° - 50° = 15°$), we derive a deposited thickness of the WS_2 nanostripes of 9 nm. In a second deposition step, a 3 nm thick MoS_2 film was deposited at normal incidence onto the template, forming a conformal layer vertically stacked on top of the few-layer WS_2 nanostripes (sketch in **Figure 5.10e**). Two flat references of the TMD materials were also fabricated under the same deposition conditions employed for the heterostructure sample HS1 on flat silica substrates for the characterization of WS_2 and MoS_2 individual layers, namely sample Ref-WS_2 and sample Ref-MoS_2 respectively. We thus proceeded to recrystallize the TMD layers recurring to the sulfurization process described in subparagraph 2.3.2.

The picture shown in **Figure 5.10f** represents sample HS1 and demonstrates the high throughput of our lithographic approach which leads to the maskless fabrication of HS array extending over cm^2 areas. The blue reflex in the illuminated left region of the sample is due to coherent scattering and diffraction from the highly periodic array of van der Waals MoS_2/WS_2 heterostructures.

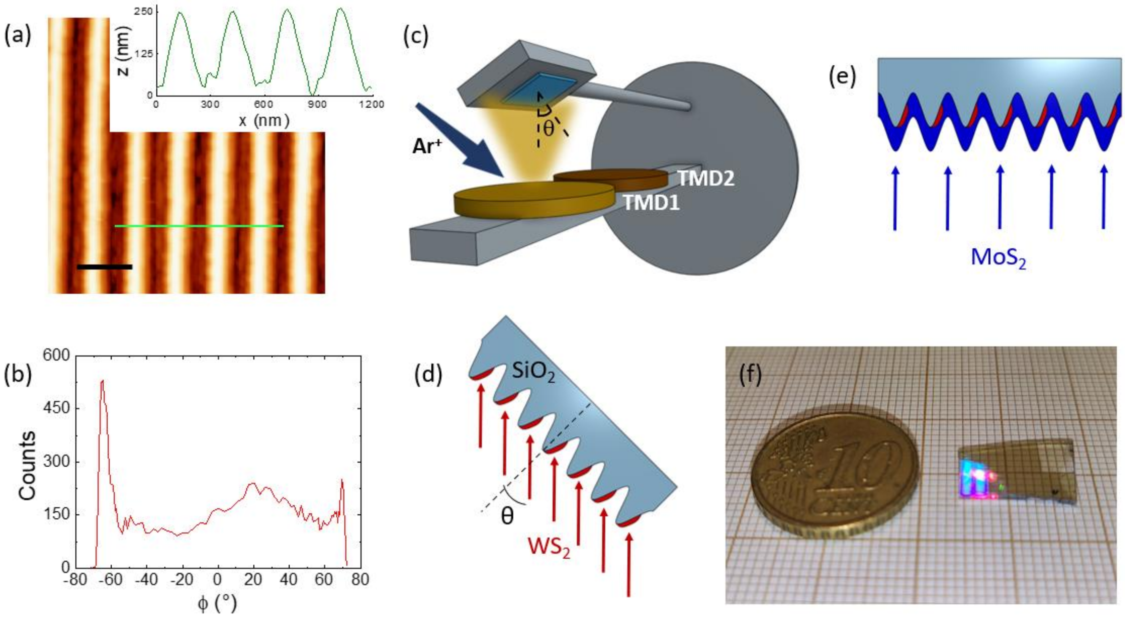

Figure 5.10 (a) AFM image of a nanogrooved silica used as a template for the growth of large area heterostructures (the scale bar reads 400nm); a line profile is extracted from the green line. (b) Slopes distribution of the template, as obtained from the derivative of the topography. (c) Sketch for the IBS deposition set-up with multiple TMD targets and rotating sample holder. (d) Sketch for WS_2 nanostripes maskless deposition at glancing angle. (e) Sketch for normal incidence deposition of a MoS_2 capping layer. (f) Photograph of sample HS1, demonstrating large area nanopatterning and TMDs growth.

Recrystallized samples have been characterized via SEM imaging, Raman micro-spectroscopy and optical spectroscopy. In **Figure 5.11a** a SEM image acquired using the Back Scattering Electron (BSE) signal of sample HS1 shows compositional contrast between the engraved WS_2 nanostripes on the right side of the substrate nanoridges and the MoS_2 signal on the left side, demonstrating that the maskless physical deposition process at glancing angles allows to obtain confinement of WS_2 nanostripes arrays. The upper half of the SEM image is shown in false colors to match the cross-section profile of the heterostructure (red for the WS_2 nanostripes, blue for the MoS_2 film). In **Figure 5.11b** a cross section SEM image of the heterostructures acquired in the Secondary Electron (SE) channel is shown, together with an inset showing a zoomed-in SEM-BSE image that better evidences the compositional contrast between the two TMD materials. One can clearly identify the morphology of the underling silica ridges, the presence of the WS_2 nanostripes lying tilted on the faceted template (contributing with a higher BSE signal due to the presence of tungsten atoms endowed with high Z-number) and the thin continuous MoS_2 capping layer.

The micro-Raman spectra acquired for the reference flat TMD films corresponding to the single component layers and the spectrum corresponding to the stacked heterostructures are shown in **Figures 5.11c-e**, respectively. The spectra of the individual layers Ref-MoS_2 and Ref-WS_2 (**Figures 5.11c** and **5.11d**) are characterized by the Raman vibrational modes of MoS_2 and WS_2, thus confirming the growth of high quality TMD layers. The in-plane mode E^1_{2g} and the out-of-plane mode A_{1g} are located at 383 cm^{-1} and 407 cm^{-1} for MoS_2 and at 354 cm^{-1} and 418 cm^{-1} for WS_2, in good agreement with literature[271,272]. Colored dashed lines (blue for MoS_2, red for WS_2) are traced in correspondence to the E^1_{2g} and A_{1g} modes of the reference samples in order to identify the Raman spectral signature of MoS_2 and WS_2 stacked layers also in the spectrum corresponding to the van der Waals heterostructures of sample HS1 (solid trace in **Figure 5.11e**). The combined presence of vibrational modes belonging both to MoS_2 and WS_2 in the Raman spectrum corresponding to sample HS1 independently confirms the formation of vertically stacked TMD heterostructures, as already suggested by the SEM cross sections.

Such conclusions are also reached if we analyze the optical extinction spectrum of sample HS1 in the VIS-NIR spectral region and compare it to those of the reference TMD layers. **Figure 5.11f** shows the optical extinction spectra at normal incidence for the reference MoS_2 and WS_2 films (blue and red curves), characterized by the excitonic modes of the two materials. A and B excitons are detected at $\lambda = 673$ nm and $\lambda = 623$ nm in the case of MoS_2 and at $\lambda = 631$ nm and $\lambda = 535$ nm in the case of WS_2, whereas band nesting spectral region is detected around $\lambda = 450$ nm for both the materials, confirming the growth of semiconducting TMD layers[8,273]. The spectrum of sample HS1, reported in **Figure 5.11g**, on one side shows the presence of the excitonic features of MoS_2 and WS_2 layers (the latter more pronounced due to the larger layer thickness) and on the other side shows a substantial increase of optical extinction in the whole spectral range, particularly relevant in correspondence to the excitonic features of the individual TMD components. Remarkably, we also highlight the appearance of a new prominent spectral feature, marked by the arrow, whose extinction increases up to 95% at about 480 nm. Such photonic anomaly is absent in the spectra of the planar MoS_2 and WS_2 reference samples (**Figure 5.11f**).

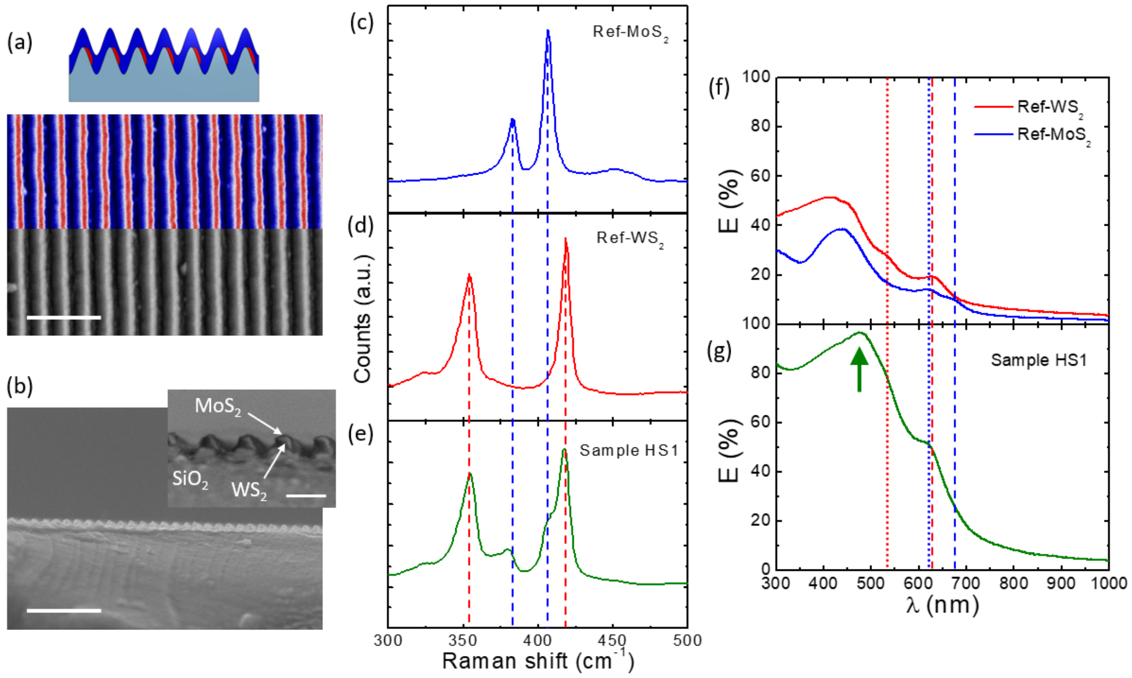

Figure 5.11 (a) SEM image (backscattering BSE signal) of the heterostructures array sample HS1 in false colors according to the sketch (scale bar reads 1μm). (b) Cross section SEM-SE image of sample HS1 (scale bar reads 2μm); inset shows a zoomed-in SEM-BSE image highlighting compositional contrast of the WS_2 coated nanostripes (scale bar reads 300nm). (c-e) Raman spectra of samples Ref-MoS_2 and Ref-WS_2 compared to sample HS1. (f) Normal incidence optical extinction spectra for samples Ref-MoS_2 and Ref-WS_2 and (g) of to the heterostructure array (TE polarization).

5.4.2. Optical characterization of van der Waals 2D-TMD heterostructure arrays

In order to attribute the nature of the photonic anomaly observed in the normal incidence extinction spectrum of sample HS1, we also performed a set of angle resolved extinction measurements which are plotted in **Figure 5.12** and allow to clearly evidence the presence of dispersive features. The angle resolved transmission spectra have been acquired in S-TE polarization, i.e. using linearly polarized light with the electric field oscillating perpendicular to the incidence plane and parallel to the ridges, by tilting the sample from θ=0° to θ=60° at steps of 5° according to the sketch shown in **Figure 5.12a**. For sake of clarity in **Figure 5.12b** we plot the angle resolved extinction spectra at 10° increment steps. The intense extinction peak observed at about 480 nm for normal incidence illumination redshifts up to 700 nm as the incidence angle increases from 0° to 60°. Remarkably, we observe that the extinction in correspondence to this maximum is higher than 90% at every incidence angle. At shorter wavelengths an additional dispersive feature, corresponding to an asymmetric dip, redshifts from about 350 nm to 550 nm as the tilt angle increases. The extraordinary light coupling of the 2D-TMD nanostructured array in the flat optics regime is made possible by the remarkably high dielectric constants of WS_2 and MoS_2.

To better trace the dispersion of these two features, the first derivatives of the spectra have been calculated and plotted with an offset for a better comprehension (**Figure 5.12c)**. The experimental dispersion data of the two photonic anomalies, identified by the wavelength for which the derivative is nulled, are shown in **Figure 5.12d**. The presence of two dispersive modes, originating from the periodic arrangement of 2D-TMD nanoridges, can be tentatively attributed to the resonant excitation of Rayleigh Anomalies at the onset of the evanescent condition at the outer or inner interfaces of the 2D layers, and to the broadband excitation of guided mode anomalies confined at the inner interface of the grating. The dispersion of the Rayleigh anomalies can be described according to equation (4.2).

In **Figure 5.12d** we show a fit of the experimental dispersion data corresponding to the two photonic anomalies by setting m = 1 and $n_0 = 1$ and optimizing the free parameters on P and n_{eff}. An error bar of ± 5 nm was attributed to the experimental wavelength data to take into account errors arising from the detector spectral resolution and from small angular errors (lower than 1°) in the tilting of the sample during the measurements. For the dispersive mode at shorter wavelengths (orange symbols), the effective refractive index has been determined as n = 1.02±0.04 and the periodicity as P_{fit} = 295±7 nm. The result is in excellent agreement with the attribution to an external Rayleigh Anomaly (RA_{ext} sketch in **Figure 5.12e**) since the parameters are compatible with $n_{air} = 1$ and sample periodicity P_{AFM} = 300±15 nm assessed by the AFM characterization. For the dispersive mode at longer wavelengths (green symbols), the best fit of the effective refractive index is n = 1.66±0.06 and of the periodicity is P_{fit} = 274±7 nm (still compatible at 1 σ with the AFM value). In this case the Rayleigh anomaly propagating at the inner interface (RA_{int}, sketch in **Figure 5.12e**) is affected by the higher refractive index of the effective medium composed by silica and the MoS_2/WS_2 heterostructures.

We expect that the excitation of these Rayleigh anomalies induces a strong in-plane light confinement in proximity to the ultra-thin TMD medium.

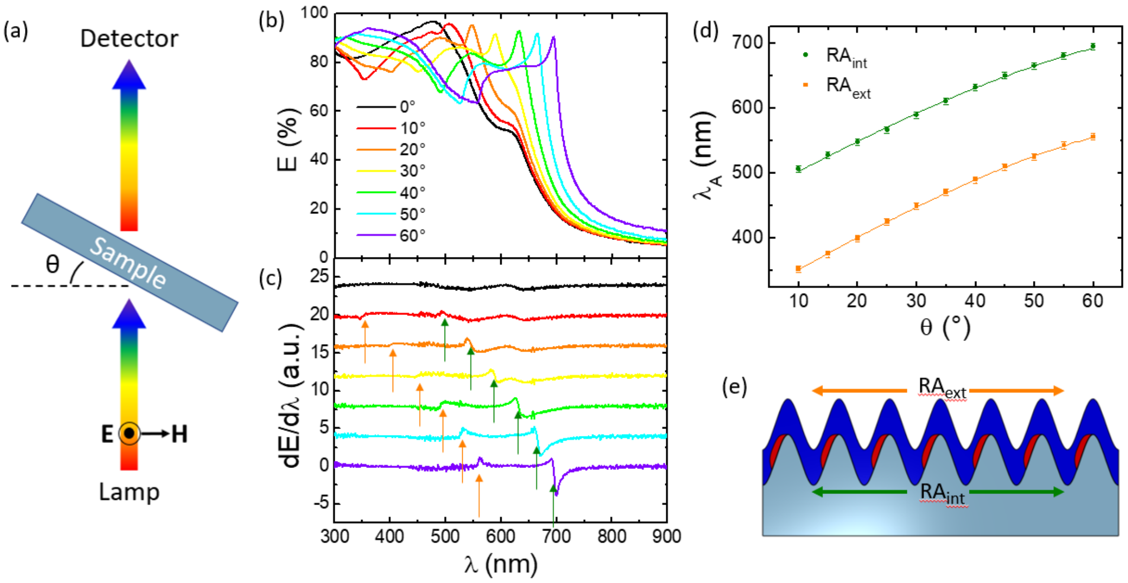

Figure 5.12 (a) Scheme of angle resolved extinction measurements. (b) Angle resolved extinction spectra for sample HS1, referenced to a flat silica substrate. (c) Derivatives of the spectra shown in panel b; d) dispersion of the Rayleigh anomalies as traced from the derivatives in panel c. (e) Sketch of the Rayleigh anomalies at the two different interfaces.

To study the influence of WS_2 nanostripes as optical sensitizers, we fabricated additional heterostructure samples by varying the WS_2 nanostripes thickness at fixed MoS_2 thickness on nanostructured silica templates with morphology equivalent to sample HS1. Sample HS2 was thus fabricated with halved WS_2 thickness (about 4.5 nm) and sample HS0 with no WS_2 at all.

In **Figure 5.13a** we report the optical extinction spectra acquired at a fixed angle $\theta = 15°$ for HS0 (blue curve), HS1 (black curve) and HS2 (red curve). The angle $\theta = 15°$ was chosen in order to reduce the contribution from the substrate reflection and to better evidence the Rayleigh anomalies, avoiding spectral overlap with the TMDs excitonic features. Overall, we notice as expected that the optical extinction of the heterostructures increases with the total thickness of the WS_2 nanostripes. Additionally, we highlight that the extinction spectrum of sample HS0 shows the typical excitonic features of MoS_2 along with a dispersive feature at about $\lambda = 390$ nm that corresponds to the external Rayleigh anomaly (orange dashed line), while the internal Rayleigh anomaly at about $\lambda = 530$ nm cannot be clearly identified unless recurring to the derivative spectrum. If thin WS_2 nanostripes are added to form heterostructures (sample HS2), the optical response becomes immediately dominated by the WS_2 excitonic features, and a very weak photonic anomaly can be distinguished in the extinction spectrum. When the WS_2 thickness is further increased up to 9 nm (sample HS1), the internal Rayleigh anomaly at about 530 nm, marked by the green dashed line, becomes extremely pronounced and dominates the optical extinction.

In **Figure 5.13b** we summarize the observed trend of the optical extinction as a function of the WS_2 thickness in the TMD heterostructures in correspondence to the inner/outer Rayleigh anomalies for θ = 15°. Remarkably, the extinction in correspondence to the inner anomaly, which is not observable in the bare MoS_2 film, reaches a value as high as 95% in presence of the thick WS_2 nanostripes which thus act as optical sensitizers, boosting light confinement inside the active TMD layer. On the other hand, the contribution to extinction from the outer anomaly, which steers light at the TMD/air interface, is already high in the case of simple MoS_2 corrugated films (for HS0 extinction is in the range of 60%) and increases just slightly around 80% when the WS_2 nanostripes are combined to form heterostructures.

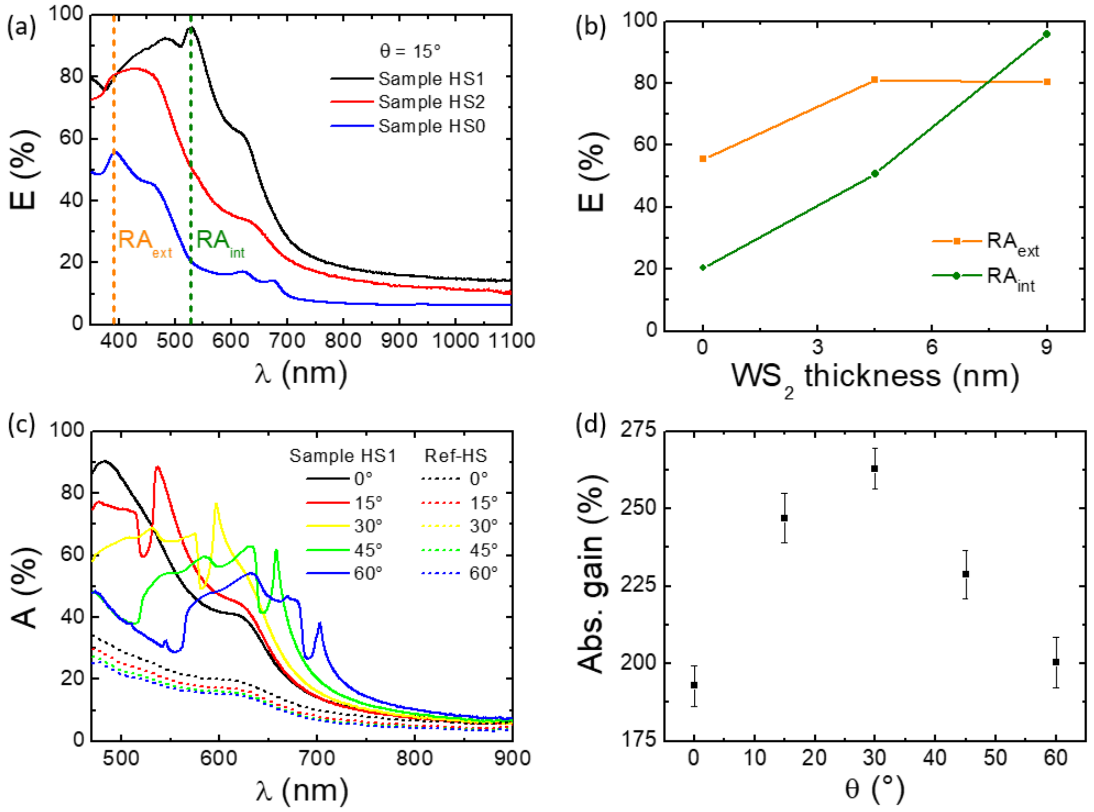

Figure 5.13 (a) Extinction spectra at fixed angle (θ = 15°) for sample HS1 (black curve), sample HS2 (red curve) and sample HS0 (blue curve), referenced to the signal in air. (b) Extinction variation as a function of the WS_2 thickness at θ = 15°, in correspondence to the external Rayleigh anomaly at λ = 390 nm and the internal Rayleigh anomaly at λ = 530 nm. (c) Absorption spectra at different angles for sample HS1 compared to Ref-HS. (d) Absorption gain in the spectral range 470-750 nm as a function of the incidence angle for sample HS1 compared to Ref-HS.

Actually, both scattering and absorption contribute to the optical extinction features detected in **Figure 5.12**. In order to precisely identify the contribution to the optical absorption of the outer/inner optical anomalies, and to unambiguously determine the light harvesting performance of the nanostructured van der Waals heterostructures, we thus performed integrated absorbance measurements in the custom-modified integrating sphere set-up, described in subparagraph 4.2.3 and in **Figure 4.7a**, which allows to record absorption spectra of the samples placed inside the sphere at variable illumination angle. In **Figure 5.13c** we compare the optical absorption of the periodic array of heterostructures for sample HS1 at different illumination angles (solid lines) with that of a reference flat bilayer stack of WS_2 and MoS_2 of equivalent thicknesses, namely sample Ref-HS (dashed lines). The absorption spectra of sample HS1 show both (i) the characteristic narrowband optical anomalies dispersing across the investigated spectral range for increasing incidence angle, and (ii) a broadband enhancement of absorption due to incoherent light scattering and waveguiding in the dielectric slab[274]. Both narrowband and broadband absorption enhancement are absent in the case of the reference bilayer despite the same amount of optically absorbing TMD material, since energy-momentum conservation rules prevent photon coupling and steering into the flat dielectric slab. In particular, we stress out for sample HS1 the extraordinary absorption enhancement up to 500% at 15° incidence angle at the resonant wavelength around 530 nm, corresponding to the inner Rayleigh anomaly (see Methods for further details).

A further relevant issue to be highlighted in view of real-world light harvesting applications based on ultra-thin TMD materials is the omnidirectional enhancement of the optical absorption when the illumination angle θ is varied in the range 0-60°, being such conditions indeed typical of non-concentrated solar applications in flat-plate absorbers. In order to quantitatively assess the latter feature, in **Figure 5.13d** we define the absorption gain G (averaged in the spectral range 470-750 nm) as the difference between the absorption of nanostructured sample A_{HS} and of flat reference stack A_{ref}, normalized to the latter according to $G = (A_{HS} - A_{ref}) / A_{ref}$. For near normal incidence angles the absorption gain of the heterostructure array reads around 180%, further increasing for larger angles with a maximum of 260% around $\theta = 30°$. Such results are remarkable in view of photoconversion applications based on ultra-thin TMD materials since critical angular alignment with respect to the light source is no longer required in the flat optics scheme here addressed. The peculiar maximum absorption gain observed for non-normal incidence angles θ around 30° is related to the tilted geometry of the WS_2 nanostripes which are supported on the steep SiO_2 facets (see **Figure 5.10b,d**).

Our results demonstrate that the physical deposition method here described enables the growth of large area arrays of 2D-TMD layers (MoS_2 and WS_2) conformally supported on nanostructured silica templates. The latters are patterned via laser interference lithography, forming uniaxial nanogrooves engineered with a high aspect-ratio faceted profile.

The faceted templates enable the confinement of uniaxial arrays of 2D-TMD nanostructures fabricated in a single maskless step over cm^2 areas by selective shadowed deposition of WS_2 nanostripes at glancing angles, followed by conformal MoS_2 deposition to complete the van der Waals heterostructure. We stress out that in the case of layered materials such as TMDs, characterized by a strong optical anisotropy, a slope selective fabrication process of the nanostructured substrate enables out-of-plane tilt of the material at a specific angle, and offers the possibility to finely control the optical response of the metasurface[8].

By carefully matching the periodicity of the template with the extraordinary dielectric constant of the TMD layers, our approach allows to engineer the optical absorption across a broad spectral range of interest for solar energy harvesting. The flat optics functionality of the WS_2 nanostripes array is manifested in two complementary ways: omnidirectional and broadband light harvesting performance arises from the light scattering and waveguiding into the dielectric slab, while resonant narrowband amplification of absorption is due to Rayleigh photonic anomalies which steer light at the onset of the evanescence condition.

The peculiarity of the periodic faceted templates ensures a simple and maskless nanofabrication of 2D-TMD heterostructure nanoarrays extending over cm^2 areas. The high refractive index WS_2 nanostripes act as an optical sensitizer media that boost optical absorption in comparison both to the single MoS_2 layer and to the equivalent flat reference WS_2/MoS_2 bilayer. The vertical stacking of type-II heterostructures with their staggered alignment of energy levels represents a crucial step towards the optimization of self-powered photoconversion devices aiming at solar energy harvesting for photocatalytic photodissociation of polluting dyes in solution and energy storage[179]. We stress out that upscaling of the process to wafer scale can be readily accomplished by adopting industrial scale interference lithography set-ups and sputtering deposition equipment.

In conclusion, we propose an original maskless deposition process for the fabrication of large area TMDs-based van der Waals heterostructures nanoarrays supported onto nanopatterned templates, acting as a flat optics media. Laterally confined WS_2 nanostripe arrays capped by a continuous MoS_2 layer are deposited over cm^2 areas by adopting a physical deposition process. By varying WS_2 facets thickness, template periodicity and photon incidence angle, the light-matter properties of the TMDs heterostructures can be engineered systematically, steering light flow at the evanescent condition. In particular, we demonstrate the role of the WS_2 nanostripes as optical sensitizers which boost the photonic Rayleigh anomalies confined at the inner interface. An absorption gain of the heterostructures nanoarrays as high as 450% is observed in correspondence to the specific resonant wavelength which matches the Rayleigh anomaly condition at the inner interface. Moreover, a broadband absorption gain as high as 230% with respect to a MoS_2 coated reference template is demonstrated by integrating over the whole visible spectrum. The successful large area integration of 2D-TMDs layers with faceted nanogrooved templates enables the straightforward formation of type-II van der Waals heterostructures which represents the fundamental building blocks required for competitive photoconversion applications. These results pave the way for the realization of real-world 2D devices promoting photon harvesting for a broad range of applications from energy conversion and storage, to sensing and quantum technologies.

Conclusions

Transition Metal Dichalcogenides (TMDs) are two-dimensional layered semiconductors endowed with extremely high optical absorption coefficient and bandgap energies in the Visible - Near Infrared. As a matter of fact, TMDs and their heterostructures are very attractive materials for photoconversion and photodetection applications and in next generation electronics. However, some technological challenges as the development of scalable fabrication processes and advanced design for efficient light absorption in the ultra-thin regime need to be faced.

In this context, during my PhD activity research I have been working on the growth of large area 2D-TMD layers and their optical functionalization achieved by nanostructuring.

During the first phase of my doctorate, I focused on the problem of large area deposition of few-layer TMD films recurring to a physical deposition approach in a custom developed set-up. As described in Chapter 2, I developed two different processes for the large area deposition of solid precursor films, either based on radio-frequency sputtering or on ion beam sputtering from stoichiometric TMD targets, both offering the possibility to control the initial precursor thickness. The subsequent optimization of a high temperature (750°C) recrystallization process in sulfur rich atmosphere, based on a single zone tube furnace, finally allowed to demonstrate the capability to grow ultra-thin MoS_2 and WS_2 layers on large area silica substrates in the range of 1 inch square.

I then showed that the novel TMD physical deposition process can be easily integrated in a state of a nanolithography process, thus demonstrating the capability to grow MoS_2 micro- and nanostructures with shape tailored at the nanometer level, deterministically located on large area wafers. Additionally, in this work a preliminary electronic characterization (work function and resistivity) was performed for the first time on our TMD layers, giving encouraging results in view of TMDs integration in electronics and nanocircuitry.

The possibility of growing in sequence MoS_2 and WS_2 precursor films has been exploited for the growth of vertical 2D-TMD stacks which are recrystallized in a single-step process. In Chapter 3, I demonstrated that in this way it is possible to achieve the synthesis of large area van der Waals heterostructures with type-II band alignment. As an immediate demonstration of the opportunities offered by such planar heterostructures, I showed the results of Methylene Blue (MB) photobleaching experiments performed using different TMDs layers as photocatalysts. The MoS_2/WS_2 heterostructure proved indeed to increase the MB degradation rate more than the individual MoS_2 and WS_2 layers as a consequence of a band structure coupling that favors charge separation and results in higher carrier lifetimes.

As a natural application of such TMD-based platform I identified the fabrication of electro-optic devices based on large area MoS_2/WS_2 heterostructures, which additionally required the development of transparent electrodes. In one approach I explored the use of ITO layers recurring to a sputtering-based deposition process. Though the electro-optical quality of the ITO layer is excellent, reaction with sulfur at high temperatures during the recrystallization process of the TMD film degrades the electrical conductivity. A natural choice for the development of van der Waals heterostructure was thus the use large area graphene electrodes, which I fabricated by optimizing a wet transfer process. The large area deposition process I developed enabled to form a SiO_2/graphene/WS_2/MoS_2 heterostack in a single step, in which the graphene window layer also acts as bottom contact. Deposition of a macroscopic Au top contact, which also acts as back reflector, made possible photoconversion measurements of the TMD device under illumination conditions. The preliminary electro-optical characterization of the WS_2/MoS_2 heterostructure evidences the presence of photovoltage (few tens of µV) and photocurrent (few nA), which are limited by the high series resistance of the graphene electrode.

In the course of my thesis, I explored a possible solution to the latter issue by capping the ITO film with a graphene layer, which acts as an impermeable membrane preventing ITO sulfurization. The latest results demonstrate that in this way – and by reducing the sulfurization temperature to 600°C – it is possible to prevent degradation of the ITO electrode and to still obtain sulfurization of MoS_2 and WS_2 layers. These results set the ground for the fabrication of a new device with improved series resistance, which unfortunately I did not have time to realize.

As mentioned in the beginning, light harvesting strategies are required in ultra-thin semiconducting films in order to enhance the optical absorption. In the rest of my thesis, I thus focused on this challenge. The approach which we explored is based on the subwavelength periodic reshaping of the TMD layers to induce strong diffractive effects at the onset of the evanescence condition, so to steer light parallel to the absorbing 2D material. In these conditions the periodic nanoarray launches Rayleigh anomalies and guided mode anomalies (i.e. diffracted leaky modes that are trapped inside the substrate by total internal reflection) which strongly enhance the effective optical path.

In Chapter 4 I presented a nanofabrication process based on Laser Interference Lithography and Reactive Ion Etching to form large area periodic patterns on silica substrates used as templates for the growth of conformally nanorippled MoS_2 films. By controlling the periodicity and the illumination angle, we demonstrated a tunable resonant and broadband non-resonant absorption enhancement up to 110% with respect to a flat MoS_2 film.

We then further engineered the MoS_2 optical response by exploring a higher thickness regime (from 3 nm to 23 nm) for which even stronger light-matter interactions are expected. Indeed, my results demonstrate that for thicker MoS_2 films the evanescent Rayleigh mode is shifted from the external interface to the internal one, thus boosting light coupling inside the 2D material itself.

Also, I independently demonstrated effective light harvesting in nanorippled MoS_2 films via MB photobleaching experiments, showing enhanced degradation rate with respect to a flat reference MoS_2 film as a consequence of increased light-matter interactions. In fact, the highest degradation rate was found when the Rayleigh anomaly was tuned with the MB molecular absorption band.

Finally, thanks to the custom sputtering deposition set-up developed during my thesis, I employed nanostructured silica templates to engineer the TMD deposition beyond the growth of conformal layers. In particular, by grazing angle deposition on silica nanogratings, I was able to fabricate laterally disconnected TMD nanostripes with a maskless process based on shadowing effects. In Chapter 5 I thus focused on the nanofabrication of periodic TMD nanoarrays (both arrays of nanostripes and of vertically stacked heterostructures) and investigated the elastic scattering properties of nanostructured TMDs films.

Initially, I presented an ion beam sputtering process to reshape the silica templates under different conditions. By sputtering at normal incidence, I demonstrated the possibility to control the height of the nanostructures while preserving the aspect ratio and the steep slopes of the facets. By sputtering at off-normal incidence angles instead, I demonstrated the faceting of the template into an asymmetric saw-tooth profile, in which the slope of the long facet can be controlled by the ion beam incidence angle.

By using an asymmetric silica nanograting, I achieved the fabrication of a large area array of few-nm MoS_2 nanostripes tilted at an angle imposed by the template faceting. Then, we developed a customized scatterometer to characterize the optical anisotropy of the asymmetric TMD nanostripes. The first scattering measurements in the few layer regime (3 nm) indeed point towards a strong role of Mie scattering and also evidence the presence of sharp Fabry-Perot resonances. A more systematic study of the scattering from TMD nanostripes could not be performed due to time limitations, nevertheless the preliminary data are promising and suggest that substantially stronger effects might become dominant in a higher MoS_2 thickness regime.

Scattering measurements were performed also on the thicker conformal MoS_2 layer (23 nm) considered in the previous chapter. Here, the focus was on the direct measurement of the in-plane scattered light, which showed a significantly stronger Rayleigh anomaly for the MoS_2 coated nanograting with respect to a bare silica one. The latter result demonstrates the fundamental role of high refractive index TMD layer for this flat optics light harvesting strategy.

Finally, I presented large area van der Waals vertical heterostructures arrays fabricated by maskless deposition of WS_2 nanostripes arrays and coated with a continuous MoS_2 film. Due to the insertion of WS_2 nanostripes acting as optical resonators, I demonstrated an even higher absorption enhancement than the case of nanorippled MoS_2 layer alone. These large area van der Waals heterostructures arrays are expected to feature a strongly improved photocatalytic performance as a consequence of light harvesting combined with charge separation. Such measurements could not be performed due to time limitations but are currently planned.

In conclusion, during my PhD I achieved important results concerning the growth of large area TMD layers and their heterostructures, offering new opportunities for the laboratory. I will here resume the next experimental steps to further explore the incomplete tasks left by thesis.

Preliminary sulfurization trials at lower temperatures demonstrates that optimization at lower temperatures can be done and this would be relevant in view of industrial transfer. Additionally, this would help in the development of transparent conductive electrodes.

Thanks to the TMD conformal growth, nanostructuring of the templates resulted in optical absorption enhancement. Photocatalytic results on van der Waals heterostructures arrays are still missing due to the lack of suitable samples, but work is in progress along this direction.

Finally, scattering measurements require a deeper investigation. Only few geometric conditions were measured and most importantly the nanostriped sample was in the ultra-thin regime (3 nm). Incremental growth of the MoS_2 thickness is already planned, expecting a strong enhancement of the scattering signal due to the increased optical path in high refractive index TMD.

I also stress that the growth and nanofabrication approaches here described currently allow the fabrication of 1 inch square samples whose size is only limited by the sample holder of the custom vacuum chamber. Since all the growth and nanofabrication steps here described can be expanded on large scale industrial coaters, we can foresee the scalability of our process towards the wafer level, a crucial issue in view of real-world photoconversion applications based on 2D-TMD.

References

1. Chakraborty, S. K., Kundu, B., Nayak, B., Dash, S. P. & Sahoo, P. K. Challenges and opportunities in 2D heterostructures for electronic and optoelectronic devices. *iScience* **25**, 103942 (2022).
2. Novoselov, K. S. *et al.* Electric Field Effect in Atomically Thin Carbon Films. *Science* **306**, 666–669 (2004).
3. Jariwala, D., Davoyan, A. R., Wong, J. & Atwater, H. A. Van der Waals Materials for Atomically-Thin Photovoltaics: Promise and Outlook. *ACS Photonics* **4**, 2962–2970 (2017).
4. Geim, A. K. & Grigorieva, I. V. Van der Waals heterostructures. *Nature* **499**, 419–425 (2013).
5. Castellanos-Gomez, A. *et al.* Van der Waals heterostructures. *Nat Rev Methods Primers* **2**, 58 (2022).
6. Martella, C. *et al.* Anisotropic MoS_2 Nanosheets Grown on Self-Organized Nanopatterned Substrates. *Adv. Mater.* **29**, 1605785 (2017).
7. Martella, C. *et al.* Designer Shape Anisotropy on Transition-Metal-Dichalcogenide Nanosheets. *Adv. Mater.* **30**, 1705615 (2018).
8. Mennucci, C. *et al.* Geometrical Engineering of Giant Optical Dichroism in Rippled MoS_2 Nanosheets. *Adv. Optical Mater.* **9**, 2001408 (2021).
9. Castellanos-Gomez, A. *et al.* Local Strain Engineering in Atomically Thin MoS_2. *Nano Lett.* **13**, 5361–5366 (2013).
10. Yang, J. *et al.* Atomically thin optical lenses and gratings. *Light Sci Appl* **5**, e16046–e16046 (2016).
11. Hussain, A. M. & Hussain, M. M. CMOS-Technology-Enabled Flexible and Stretchable Electronics for Internet of Everything Applications. *Adv. Mater.* **28**, 4219–4249 (2016).
12. Yi, F. *et al.* Wearable energy sources based on 2D materials. *Chem. Soc. Rev.* **47**, 3152–3188 (2018).
13. Pang, Y., Yang, Z., Yang, Y. & Ren, T. Wearable Electronics Based on 2D Materials for Human Physiological Information Detection. *Small* **16**, 1901124 (2020).
14. Xie, C., Mak, C., Tao, X. & Yan, F. Photodetectors Based on Two-Dimensional Layered Materials Beyond Graphene. *Adv. Funct. Mater.* **27**, 1603886 (2017).
15. Long, M., Wang, P., Fang, H. & Hu, W. Progress, Challenges, and Opportunities for 2D Material Based Photodetectors. *Adv. Funct. Mater.* **29**, 1803807 (2019).
16. An, J. *et al.* Perspectives of 2D Materials for Optoelectronic Integration. *Adv Funct Materials* **32**, 2110119 (2022).
17. Zhou, X. *et al.* 2D Layered Material-Based van der Waals Heterostructures for Optoelectronics. *Adv. Funct. Mater.* **28**, 1706587 (2018).
18. Ciarrocchi, A., Tagarelli, F., Avsar, A. & Kis, A. Excitonic devices with van der Waals heterostructures: valleytronics meets twistronics. *Nature Reviews Materials* **7**, 449–464 (2022).
19. Ghobadi, A., Ulusoy Ghobadi, T. G., Karadas, F. & Ozbay, E. Semiconductor Thin Film Based Metasurfaces and Metamaterials for Photovoltaic and Photoelectrochemical Water Splitting Applications. *Adv. Optical Mater.* **7**, 1900028 (2019).
20. Novoselov, K. S., Mishchenko, A., Carvalho, A. & Castro Neto, A. H. 2D materials and van der Waals heterostructures. *Science* **353**, aac9439 (2016).

21. Stanford, M. G., Rack, P. D. & Jariwala, D. Emerging nanofabrication and quantum confinement techniques for 2D materials beyond graphene. *npj 2D Mater Appl* **2**, 20 (2018).
22. McCreary, A., Kazakova, O., Jariwala, D. & Al Balushi, Z. Y. An outlook into the flat land of 2D materials beyond graphene: synthesis, properties and device applications. *2D Mater.* **8**, 013001 (2021).
23. Frisenda, R., Niu, Y., Gant, P., Muñoz, M. & Castellanos-Gomez, A. Naturally occurring van der Waals materials. *npj 2D Mater Appl* **4**, 38 (2020).
24. Akinwande, D. *et al.* A review on mechanics and mechanical properties of 2D materials—Graphene and beyond. *Extreme Mechanics Letters* **13**, 42–77 (2017).
25. Gibertini, M., Koperski, M., Morpurgo, A. F. & Novoselov, K. S. Magnetic 2D materials and heterostructures. *Nat. Nanotechnol.* **14**, 408–419 (2019).
26. Novoselov, K. S. *et al.* A roadmap for graphene. *Nature* **490**, 192–200 (2012).
27. Allen, M. J., Tung, V. C. & Kaner, R. B. Honeycomb Carbon: A Review of Graphene. *Chem. Rev.* **110**, 132–145 (2010).
28. Splendiani, A. *et al.* Emerging Photoluminescence in Monolayer MoS $_2$. *Nano Lett.* **10**, 1271–1275 (2010).
29. Choi, W. *et al.* Recent development of two-dimensional transition metal dichalcogenides and their applications. *Materials Today* **20**, 116–130 (2017).
30. Mak, K. F. & Shan, J. Photonics and optoelectronics of 2D semiconductor transition metal dichalcogenides. *Nature Photon* **10**, 216–226 (2016).
31. Dai, Z., Liu, L. & Zhang, Z. Strain Engineering of 2D Materials: Issues and Opportunities at the Interface. *Adv. Mater.* **31**, 1805417 (2019).
32. Parto, K., Azzam, S. I., Banerjee, K. & Moody, G. Defect and strain engineering of monolayer WSe2 enables site-controlled single-photon emission up to 150 K. *Nat Commun* **12**, 3585 (2021).
33. Ryu, Y. K. *et al.* Microheater Actuators as a Versatile Platform for Strain Engineering in 2D Materials. *Nano Lett.* **20**, 5339–5345 (2020).
34. Molina-Sánchez, A., Hummer, K. & Wirtz, L. Vibrational and optical properties of MoS2: From monolayer to bulk. *Surface Science Reports* **70**, 554–586 (2015).
35. Xia, F., Wang, H., Xiao, D., Dubey, M. & Ramasubramaniam, A. Two-dimensional material nanophotonics. *Nature Photon* **8**, 899–907 (2014).
36. Vazirisereshk, M. R., Martini, A., Strubbe, D. A. & Baykara, M. Z. Solid Lubrication with MoS2: A Review. *Lubricants* **7**, (2019).
37. Venkata Subbaiah, Y. P., Saji, K. J. & Tiwari, A. Atomically Thin MoS $_2$: A Versatile Nongraphene 2D Material. *Adv. Funct. Mater.* **26**, 2046–2069 (2016).
38. Krishnan, U., Kaur, M., Singh, K., Kumar, M. & Kumar, A. A synoptic review of MoS2: Synthesis to applications. *Superlattices and Microstructures* **128**, 274–297 (2019).
39. Radisavljevic, B., Radenovic, A., Brivio, J., Giacometti, V. & Kis, A. Single-layer MoS2 transistors. *Nature Nanotech* **6**, 147–150 (2011).
40. Mortazavi, M., Wang, C., Deng, J., Shenoy, V. B. & Medhekar, N. V. Ab initio characterization of layered MoS2 as anode for sodium-ion batteries. *Journal of Power Sources* **268**, 279–286 (2014).
41. Shockley, W. & Queisser, H. J. Detailed Balance Limit of Efficiency of *p-n* Junction Solar Cells. *Journal of Applied Physics* **32**, 510–519 (1961).
42. Gant, P. *et al.* A strain tunable single-layer MoS2 photodetector. *Materials Today* **27**, 8–13 (2019).
43. Gonzalez Marin, J. F., Unuchek, D., Watanabe, K., Taniguchi, T. & Kis, A. MoS2 photodetectors integrated with photonic circuits. *npj 2D Mater Appl* **3**, 14 (2019).

44. Green, T. D. *et al.* Optical material anisotropy in high-index transition metal dichalcogenide Mie nanoresonators. *Optica* **7**, 680 (2020).
45. Trolle, M. L., Seifert, G. & Pedersen, T. G. Theory of excitonic second-harmonic generation in monolayer MoS 2. *Phys. Rev. B* **89**, 235410 (2014).
46. Ye, M., Winslow, D., Zhang, D., Pandey, R. & Yap, Y. Recent Advancement on the Optical Properties of Two-Dimensional Molybdenum Disulfide (MoS2) Thin Films. *Photonics* **2**, 288–307 (2015).
47. Lee, C. *et al.* Anomalous Lattice Vibrations of Single- and Few-Layer MoS $_2$. *ACS Nano* **4**, 2695–2700 (2010).
48. Lin, S. *et al.* Interface designed MoS2/GaAs heterostructure solar cell with sandwich stacked hexagonal boron nitride. *Sci Rep* **5**, 15103 (2015).
49. Wu, W. *et al.* Piezoelectricity of single-atomic-layer MoS2 for energy conversion and piezotronics. *Nature* **514**, 470–474 (2014).
50. Choudhary, N. *et al.* Directly deposited MoS $_2$ thin film electrodes for high performance supercapacitors. *J. Mater. Chem. A* **3**, 24049–24054 (2015).
51. Li, H. *et al.* Fabrication of Single- and Multilayer MoS2 Film-Based Field-Effect Transistors for Sensing NO at Room Temperature. *Small* **8**, 63–67 (2012).
52. Sarkar, D. *et al.* MoS $_2$ Field-Effect Transistor for Next-Generation Label-Free Biosensors. *ACS Nano* **8**, 3992–4003 (2014).
53. Yamaguchi, M., Lee, K.-H., Araki, K. & Kojima, N. A review of recent progress in heterogeneous silicon tandem solar cells. *J. Phys. D: Appl. Phys.* **51**, 133002 (2018).
54. Friedman, D. J. Progress and challenges for next-generation high-efficiency multijunction solar cells. *Current Opinion in Solid State and Materials Science* **14**, 131–138 (2010).
55. Baiju, A. & Yarema, M. Status and challenges of multi-junction solar cell technology. *Front. Energy Res.* **10**, 971918 (2022).
56. Zhang, C. *et al.* Systematic study of electronic structure and band alignment of monolayer transition metal dichalcogenides in Van der Waals heterostructures. *2D Mater.* **4**, 015026 (2016).
57. Haigh, S. J. *et al.* Cross-sectional imaging of individual layers and buried interfaces of graphene-based heterostructures and superlattices. *Nature Mater* **11**, 764–767 (2012).
58. Trovatello, C. *et al.* Ultrafast hot carrier transfer in WS2/graphene large area heterostructures. *npj 2D Mater Appl* **6**, 24 (2022).
59. Choi, K., Lee, Y. T. & Im, S. Two-dimensional van der Waals nanosheet devices for future electronics and photonics. *Nano Today* **11**, 626–643 (2016).
60. Khelifa, R. *et al.* Coupling Interlayer Excitons to Whispering Gallery Modes in van der Waals Heterostructures. *Nano Lett.* **20**, 6155–6161 (2020).
61. Furchi, M. M. *et al.* Device physics of van der Waals heterojunction solar cells. *npj 2D Mater Appl* **2**, 3 (2018).
62. Zhou, C. *et al.* Self-driven WSe2 photodetectors enabled with asymmetrical van der Waals contact interfaces. *npj 2D Mater Appl* **4**, 46 (2020).
63. Jorio, A. Twistronics and the small-angle magic. *Nature Materials* **21**, 844–845 (2022).
64. Fang, H. *et al.* Strong interlayer coupling in van der Waals heterostructures built from single-layer chalcogenides. *Proc. Natl. Acad. Sci. U.S.A.* **111**, 6198–6202 (2014).
65. Zhang, J. *et al.* Enhancing and controlling valley magnetic response in MoS2/WS2 heterostructures by all-optical route. *Nat Commun* **10**, 4226 (2019).

66. Bae, H. *et al.* Light Absorption and Emission Dominated by Trions in the Type-I van der Waals Heterostructures. *ACS Photonics* **8**, 1972–1978 (2021).
67. Wang, Y. *et al.* Visible light driven type II heterostructures and their enhanced photocatalysis properties: a review. *Nanoscale* **5**, 8326 (2013).
68. Liu, J., Li, Z., Zhang, X. & Lu, G. Unraveling energy and charge transfer in type-II van der Waals heterostructures. *npj Comput Mater* **7**, 191 (2021).
69. Ren, K., Wang, K., Cheng, Y., Tang, W. & Zhang, G. Two-dimensional heterostructures for photocatalytic water splitting: a review of recent progress. *Nano Futures* **4**, 032006 (2020).
70. Shifa, T. A., Wang, F., Liu, Y. & He, J. Heterostructures Based on 2D Materials: A Versatile Platform for Efficient Catalysis. *Adv. Mater.* **31**, 1804828 (2019).
71. Kumar, P. *et al.* Boosting Photocatalytic Activity Using Carbon Nitride Based 2D/2D van der Waals Heterojunctions. *Chem. Mater.* **33**, 9012–9092 (2021).
72. Lei, C. *et al.* Broken-Gap Type-III Band Alignment in WTe2/HfS2 van der Waals Heterostructure. *J. Phys. Chem. C* **123**, 23089–23095 (2019).
73. Zhang, X.-Q., Lin, C.-H., Tseng, Y.-W., Huang, K.-H. & Lee, Y.-H. Synthesis of Lateral Heterostructures of Semiconducting Atomic Layers. *Nano Lett.* **15**, 410–415 (2015).
74. Sahoo, P. K., Memaran, S., Xin, Y., Balicas, L. & Gutiérrez, H. R. One-pot growth of two-dimensional lateral heterostructures via sequential edge-epitaxy. *Nature* **553**, 63–67 (2018).
75. Sahoo, P. K. *et al.* Bilayer Lateral Heterostructures of Transition-Metal Dichalcogenides and Their Optoelectronic Response. *ACS Nano* **13**, 12372–12384 (2019).
76. Li, M.-Y. *et al.* Epitaxial growth of a monolayer WSe2-MoS2 lateral p-n junction with an atomically sharp interface.
77. Chamlagain, B., Withanage, S. S., Johnston, A. C. & Khondaker, S. I. Scalable lateral heterojunction by chemical doping of 2D TMD thin films. *Sci Rep* **10**, 12970 (2020).
78. Mahjouri-Samani, M. *et al.* Patterned arrays of lateral heterojunctions within monolayer two-dimensional semiconductors. *Nat Commun* **6**, 7749 (2015).
79. Sundararaju, U., Mohammad Haniff, M. A. S., Ker, P. J. & Menon, P. S. MoS2/h-BN/Graphene Heterostructure and Plasmonic Effect for Self-Powering Photodetector: A Review. *Materials* **14**, 1672 (2021).
80. Li, S. *et al.* Ultra-sensitive self-powered photodetector based on vertical MoTe $_2$ /MoS $_2$ heterostructure. *Appl. Phys. Express* **13**, 015007 (2020).
81. Wu, W. *et al.* Self-powered photovoltaic photodetector established on lateral monolayer MoS2-WS2 heterostructures. *Nano Energy* **51**, 45–53 (2018).
82. Mak, K. F., Lee, C., Hone, J., Shan, J. & Heinz, T. F. Atomically Thin MoS 2 : A New Direct-Gap Semiconductor. *Phys. Rev. Lett.* **105**, 136805 (2010).
83. Jariwala, D. *et al.* Near-Unity Absorption in van der Waals Semiconductors for Ultrathin Optoelectronics. *Nano Lett.* **16**, 5482–5487 (2016).
84. Wilson, S. J. & Hutley, M. C. The Optical Properties of 'Moth Eye' Antireflection Surfaces. *Optica Acta: International Journal of Optics* **29**, 993–1009 (1982).
85. Sun, J. *et al.* Biomimetic Moth-eye Nanofabrication: Enhanced Antireflection with Superior Self-cleaning Characteristic. *Sci Rep* **8**, 5438 (2018).
86. Rao, J., Winfield, R. & Keeney, L. Moth-eye-structured light-emitting diodes. *Optics Communications* **283**, 2446–2450 (2010).
87. Zhao, J. & Green, M. A. Optimized antireflection coatings for high-efficiency silicon solar cells. *IEEE Trans. Electron Devices* **38**, 1925–1934 (1991).

88. Papet, P. *et al.* Pyramidal texturing of silicon solar cell with TMAH chemical anisotropic etching. *Solar Energy Materials and Solar Cells* **90**, 2319–2328 (2006).
89. Lin, J., Li, H., Zhang, H. & Chen, W. Plasmonic enhancement of photocurrent in MoS $_2$ field-effect-transistor. *Appl. Phys. Lett.* **102**, 203109 (2013).
90. Sobhani, A. *et al.* Enhancing the photocurrent and photoluminescence of single crystal monolayer MoS2 with resonant plasmonic nanoshells. *Applied Physics Letters* **104**, 031112 (2014).
91. Wu, S. *et al.* Control of two-dimensional excitonic light emission via photonic crystal. *2D Mater.* **1**, 011001 (2014).
92. Jang, M. S. *et al.* Tunable large resonant absorption in a midinfrared graphene Salisbury screen. *Phys. Rev. B* **90**, 165409 (2014).
93. Park, J. *et al.* Omnidirectional Near-Unity Absorption in an Ultrathin Planar Semiconductor Layer on a Metal Substrate. *ACS Photonics* **1**, 812–821 (2014).
94. Piper, J. R. & Fan, S. Total Absorption in a Graphene Monolayer in the Optical Regime by Critical Coupling with a Photonic Crystal Guided Resonance. *ACS Photonics* **1**, 347–353 (2014).
95. Kim, S. J., Fan, P., Kang, J.-H. & Brongersma, M. L. Creating semiconductor metafilms with designer absorption spectra. *Nat Commun* **6**, 7591 (2015).
96. Yu, N. & Capasso, F. Flat optics with designer metasurfaces. *Nature Mater* **13**, 139–150 (2014).
97. van de Groep, J. *et al.* Exciton resonance tuning of an atomically thin lens. *Nat. Photonics* **14**, 426–430 (2020).
98. Bliokh, K. Y., Rodríguez-Fortuño, F. J., Nori, F. & Zayats, A. V. Spin–orbit interactions of light. *Nature Photon* **9**, 796–808 (2015).
99. Zhou, Y., Zheng, H., Kravchenko, I. I. & Valentine, J. Flat optics for image differentiation. *Nat. Photonics* **14**, 316–323 (2020).
100. Giordano, M. C. *et al.* SERS Amplification from Self-Organized Arrays of Plasmonic Nanocrescents. *ACS Appl. Mater. Interfaces* **8**, 6629–6638 (2016).
101. Limonov, M. F., Rybin, M. V., Poddubny, A. N. & Kivshar, Y. S. Fano resonances in photonics. *Nature Photon* **11**, 543–554 (2017).
102. Vecchi, G., Giannini, V. & Gómez Rivas, J. Shaping the Fluorescent Emission by Lattice Resonances in Plasmonic Crystals of Nanoantennas. *Phys. Rev. Lett.* **102**, 146807 (2009).
103. Byelobrov, V. O., Zinenko, T. L., Kobayashi, K. & Nosich, A. I. Periodicity Matters: Grating or lattice resonances in the scattering by sparse arrays of subwavelength strips and wires. *IEEE Antennas Propag. Mag.* **57**, 34–45 (2015).
104. Baur, S., Sanders, S. & Manjavacas, A. Hybridization of Lattice Resonances. *ACS Nano* **12**, 1618–1629 (2018).
105. Tran, T. T. *et al.* Deterministic Coupling of Quantum Emitters in 2D Materials to Plasmonic Nanocavity Arrays. *Nano Lett.* **17**, 2634–2639 (2017).
106. Kang, G. *et al.* Broadband Light-Trapping Enhancement in an Ultrathin Film a-Si Absorber Using Whispering Gallery Modes and Guided Wave Modes with Dielectric Surface-Textured Structures. *Adv. Mater.* **25**, 2617–2623 (2013).
107. Wu, J. *et al.* Monolayer Molybdenum Disulfide Nanoribbons with High Optical Anisotropy. *Advanced Optical Materials* **4**, 756–762 (2016).
108. Chhowalla, M., Liu, Z. & Zhang, H. Two-dimensional transition metal dichalcogenide (TMD) nanosheets. *Chem. Soc. Rev.* **44**, 2584–2586 (2015).
109. Song, X. *et al.* Progress of Large-Scale Synthesis and Electronic Device Application of Two-Dimensional Transition Metal Dichalcogenides. *Small* **13**, 1700098 (2017).

110. Samadi, M. *et al.* Group 6 transition metal dichalcogenide nanomaterials: synthesis, applications and future perspectives. *Nanoscale Horiz.* **3**, 90–204 (2018).
111. Vangelista, S. *et al.* Towards a uniform and large-scale deposition of MoS $_2$ nanosheets via sulfurization of ultra-thin Mo-based solid films. *Nanotechnology* **27**, 175703 (2016).
112. Martella, C. *et al.* Engineering the Growth of MoS $_2$ via Atomic Layer Deposition of Molybdenum Oxide Film Precursor. *Adv. Electron. Mater.* **2**, 1600330 (2016).
113. Hong, X. *et al.* Ultrafast charge transfer in atomically thin MoS2/WS2 heterostructures. *Nature Nanotech* **9**, 682–686 (2014).
114. Ottaviano, L. *et al.* Mechanical exfoliation and layer number identification of MoS $_2$ revisited. *2D Mater.* **4**, 045013 (2017).
115. Li, H., Wu, J., Yin, Z. & Zhang, H. Preparation and Applications of Mechanically Exfoliated Single-Layer and Multilayer MoS $_2$ and WSe $_2$ Nanosheets. *Acc. Chem. Res.* **47**, 1067–1075 (2014).
116. Das, S., Chen, H.-Y., Penumatcha, A. V. & Appenzeller, J. High Performance Multilayer MoS $_2$ Transistors with Scandium Contacts. *Nano Lett.* **13**, 100–105 (2013).
117. Kim, J. *et al.* Observation of ultralong valley lifetime in WSe2/MoS2 heterostructures. *Science Advances* **3**, e1700518 (2017).
118. Lopez-Sanchez, O., Lembke, D., Kayci, M., Radenovic, A. & Kis, A. Ultrasensitive photodetectors based on monolayer MoS2. *Nature Nanotech* **8**, 497–501 (2013).
119. Novoselov, K. S. & Castro Neto, A. H. Two-dimensional crystals-based heterostructures: materials with tailored properties. *Phys. Scr.* **T146**, 014006 (2012).
120. Guo, H., Hu, Z., Liu, Z. & Tian, J. Stacking of 2D Materials. *Adv. Funct. Mater.* **31**, 2007810 (2021).
121. Qi, H. *et al.* Production Methods of Van der Waals Heterostructures Based on Transition Metal Dichalcogenides. *Crystals* **8**, 35 (2018).
122. Nicolosi, V., Chhowalla, M., Kanatzidis, M. G., Strano, M. S. & Coleman, J. N. Liquid Exfoliation of Layered Materials. *Science* **340**, 1226419 (2013).
123. Jawaid, A. *et al.* Mechanism for Liquid Phase Exfoliation of MoS $_2$. *Chem. Mater.* **28**, 337–348 (2016).
124. Adilbekova, B. *et al.* Liquid phase exfoliation of MoS $_2$ and WS $_2$ in aqueous ammonia and their application in highly efficient organic solar cells. *J. Mater. Chem. C* **8**, 5259–5264 (2020).
125. Shen, J. *et al.* Liquid Phase Exfoliation of Two-Dimensional Materials by Directly Probing and Matching Surface Tension Components. *Nano Lett.* **15**, 5449–5454 (2015).
126. Nguyen, E. P. *et al.* Investigation of Two-Solvent Grinding-Assisted Liquid Phase Exfoliation of Layered MoS $_2$. *Chem. Mater.* **27**, 53–59 (2015).
127. Liu, Y. & Gu, F. A wafer-scale synthesis of monolayer MoS $_2$ and their field-effect transistors toward practical applications. *Nanoscale Adv.* **3**, 2117–2138 (2021).
128. Zhang, Y. *et al.* Recent Progress in CVD Growth of 2D Transition Metal Dichalcogenides and Related Heterostructures. *Adv. Mater.* **31**, 1901694 (2019).
129. Tang, J. *et al.* In Situ Oxygen Doping of Monolayer MoS $_2$ for Novel Electronics. *Small* **16**, 2004276 (2020).
130. Cohen, A. *et al.* Growth-Etch Metal–Organic Chemical Vapor Deposition Approach of WS $_2$ Atomic Layers. *ACS Nano* **15**, 526–538 (2021).

131. Giannazzo, F. *et al.* Direct Probing of Grain Boundary Resistance in Chemical Vapor Deposition-Grown Monolayer MoS $_2$ by Conductive Atomic Force Microscopy. *Phys. Status Solidi RRL* **14**, 1900393 (2020).
132. Chiappe, D. *et al.* Controlled Sulfurization Process for the Synthesis of Large Area MoS $_2$ Films and MoS $_2$ /WS $_2$ Heterostructures. *Adv. Mater. Interfaces* **3**, 1500635 (2016).
133. Hamza Safeer, S. *et al.* CVD growth and optical characterization of homo and heterobilayer TMDs. *Journal of Applied Physics* **132**, 024301 (2022).
134. Martella, C. *et al.* Changing the Electronic Polarizability of Monolayer MoS $_2$ by Perylene-Based Seeding Promoters. *Adv. Mater. Interfaces* **7**, 2000791 (2020).
135. Zhang, J., Wang, F., Shenoy, V. B., Tang, M. & Lou, J. Towards controlled synthesis of 2D crystals by chemical vapor deposition (CVD). *Materials Today* **40**, 132–139 (2020).
136. Perea-López, N. *et al.* CVD-grown monolayered MoS $_2$ as an effective photosensor operating at low-voltage. *2D Mater.* **1**, 011004 (2014).
137. Zhang, Z. *et al.* High-performance transistors based on monolayer CVD MoS $_2$ grown on molten glass. *Appl. Phys. Lett.* **113**, 202103 (2018).
138. Liu, H. F., Wong, S. L. & Chi, D. Z. CVD Growth of MoS $_2$ -based Two-dimensional Materials. *Chem. Vap. Deposition* **21**, 241–259 (2015).
139. Taheri, P. *et al.* Growth mechanism of largescale MoS $_2$ monolayer by sulfurization of MoO $_3$ film. *Mater. Res. Express* **3**, 075009 (2016).
140. Pondick, J. V., Woods, J. M., Xing, J., Zhou, Y. & Cha, J. J. Stepwise Sulfurization from MoO $_3$ to MoS $_2$ via Chemical Vapor Deposition. *ACS Appl. Nano Mater.* **1**, 5655–5661 (2018).
141. Browning, R. *et al.* Atomic layer deposition of MoS $_2$ thin films. *Mater. Res. Express* **2**, 035006 (2015).
142. Jurca, T. *et al.* Low-Temperature Atomic Layer Deposition of MoS $_2$ Films. *Angew. Chem. Int. Ed.* **56**, 4991–4995 (2017).
143. Serna, M. I. *et al.* Large-Area Deposition of MoS $_2$ by Pulsed Laser Deposition with *In Situ* Thickness Control. *ACS Nano* **10**, 6054–6061 (2016).
144. Fu, D. *et al.* Molecular Beam Epitaxy of Highly Crystalline Monolayer Molybdenum Disulfide on Hexagonal Boron Nitride. *J. Am. Chem. Soc.* **139**, 9392–9400 (2017).
145. Heyne, M. H. *et al.* Multilayer MoS $_2$ growth by metal and metal oxide sulfurization. *J. Mater. Chem. C* **4**, 1295–1304 (2016).
146. Madhuri, K. V. Thermal protection coatings of metal oxide powders. in *Metal Oxide Powder Technologies* 209–231 (Elsevier, 2020). doi:10.1016/B978-0-12-817505-7.00010-5.
147. Choudhary, N., Park, J., Hwang, J. Y. & Choi, W. Growth of Large-Scale and Thickness-Modulated MoS $_2$ Nanosheets. *ACS Appl. Mater. Interfaces* **6**, 21215–21222 (2014).
148. Shahzad, R., Kim, T. & Kang, S.-W. Effects of temperature and pressure on sulfurization of molybdenum nano-sheets for MoS 2 synthesis. *Thin Solid Films* **641**, 79–86 (2017).
149. Romanov, R. I. *et al.* Synthesis of Large Area Two-Dimensional MoS $_2$ Films by Sulfurization of Atomic Layer Deposited MoO $_3$ Thin Film for Nanoelectronic Applications. *ACS Appl. Nano Mater.* **2**, 7521–7531 (2019).
150. Chakraborty, B. *et al.* Symmetry-dependent phonon renormalization in monolayer MoS2 transistor. *Phys. Rev. B* **85**, 161403 (2012).

151. Wang, Y., Cong, C., Qiu, C. & Yu, T. Raman Spectroscopy Study of Lattice Vibration and Crystallographic Orientation of Monolayer MoS2 under Uniaxial Strain. *Small* **9**, 2857–2861 (2013).

152. Zribi, R., Foti, A., Donato, M. G., Gucciardi, P. G. & Neri, G. Electrochemical and sensing properties of 2D-MoS2 nanosheets produced via liquid cascade centrifugation. *Electrochimica Acta* **436**, 141433 (2022).

153. Shi, H. *et al.* Exciton Dynamics in Suspended Monolayer and Few-Layer MoS $_2$ 2D Crystals. *ACS Nano* **7**, 1072–1080 (2013).

154. Giordano, M. C., Zambito, G., Gardella, M. & Buatier de Mongeot, F. Deterministic Thermal Sculpting of Large-Scale 2D Semiconductor Nanocircuits. *Adv Materials Inter* 2201408 (2022) doi:10.1002/admi.202201408.

155. Spreyer, F., Ruppert, C., Georgi, P. & Zentgraf, T. Influence of Plasmon Resonances and Symmetry Effects on Second Harmonic Generation in WS $_2$ – Plasmonic Hybrid Metasurfaces. *ACS Nano* **15**, 16719–16728 (2021).

156. Bhatnagar, M. *et al.* Broadband and Tunable Light Harvesting in Nanorippled MoS $_2$ Ultrathin Films. *ACS Appl. Mater. Interfaces* **13**, 13508–13516 (2021).

157. Giordano, M. C., Viti, L., Mitrofanov, O. & Vitiello, M. S. Phase-sensitive terahertz imaging using room-temperature near-field nanodetectors. *Optica* **5**, 651 (2018).

158. Telesio, F. *et al.* Ohmic contact engineering in few–layer black phosphorus: approaching the quantum limit. *Nanotechnology* **31**, 334002 (2020).

159. Ly, T. H. *et al.* Vertically Conductive MoS $_2$ Spiral Pyramid. *Adv. Mater.* **28**, 7723–7728 (2016).

160. Wang, B. *et al.* Enhanced current rectification and self-powered photoresponse in multilayer p-MoTe $_2$ /n-MoS $_2$ van der Waals heterojunctions. *Nanoscale* **9**, 10733–10740 (2017).

161. Ma, L., Chen, R., Dong, S. & Yu, T. In situ strain electrical atomic force microscopy study on two-dimensional ternary transition metal dichalcogenides. *InfoMat* (2022) doi:10.1002/inf2.12310.

162. Palacios-Berraquero, C. *et al.* Large-scale quantum-emitter arrays in atomically thin semiconductors. *Nat Commun* **8**, 15093 (2017).

163. Munkhbat, B. *et al.* Transition metal dichalcogenide metamaterials with atomic precision. *Nat Commun* **11**, 4604 (2020).

164. Guo, Y. *et al.* Additive manufacturing of patterned 2D semiconductor through recyclable masked growth. *Proc. Natl. Acad. Sci. U.S.A.* **116**, 3437–3442 (2019).

165. Sun, H., Dong, J., Liu, F. & Ding, F. Etching of two-dimensional materials. *Materials Today* **42**, 192–213 (2021).

166. He, T. *et al.* Etching Techniques in 2D Materials. *Adv. Mater. Technol.* **4**, 1900064 (2019).

167. Garcia, R., Knoll, A. W. & Riedo, E. Advanced scanning probe lithography. *Nature Nanotech* **9**, 577–587 (2014).

168. Albisetti, E. *et al.* Thermal scanning probe lithography. *Nat Rev Methods Primers* **2**, 32 (2022).

169. Zheng, X. *et al.* Patterning metal contacts on monolayer MoS2 with vanishing Schottky barriers using thermal nanolithography. *Nat Electron* **2**, 17–25 (2019).

170. Liu, X., Howell, S. T., Conde-Rubio, A., Boero, G. & Brugger, J. Thermomechanical Nanocutting of 2D Materials. *Adv. Mater.* **32**, 2001232 (2020).

171. Liu, X. *et al.* Thermomechanical Nanostraining of Two-Dimensional Materials. *Nano Lett.* **20**, 8250–8257 (2020).

172. Jeon, M. H. *et al.* Controlled MoS $_2$ layer etching using CF $_4$ plasma. *Nanotechnology* **26**, 355706 (2015).

173. Choi, S., Shaolin, Z. & Yang, W. Layer-number-dependent work function of MoS2 nanoflakes. *Journal of the Korean Physical Society* **64**, 1550–1555 (2014).
174. Kim, J. H. *et al.* Work function variation of MoS $_2$ atomic layers grown with chemical vapor deposition: The effects of thickness and the adsorption of water/oxygen molecules. *Appl. Phys. Lett.* **106**, 251606 (2015).
175. Pacheco, L. & Martinez, N. F. Enhanced Current Dynamic Range Using ResiScope^{TM} and Soft-ResiScope^{TM} AFM Modes. in *Conductive Atomic Force Microscopy* 263–276 (John Wiley & Sons, Ltd, 2017). doi:https://doi.org/10.1002/9783527699773.ch12.
176. Greene, J. E. Quantitative Electrical Measurements with Atomic Force Microscopy. *Micros. Today* **23**, 32–37 (2015).
177. Panasci, S. E. *et al.* Multiscale Investigation of the Structural, Electrical and Photoluminescence Properties of MoS2 Obtained by MoO3 Sulfurization. *Nanomaterials* **12**, 182 (2022).
178. Hamada, T. *et al.* Sheet Resistance Reduction of MoS$_2$ Film Using Sputtering and Chlorine Plasma Treatment Followed by Sulfur Vapor Annealing. *IEEE J. Electron Devices Soc.* **9**, 278–285 (2021).
179. Barelli, M., Ferrando, G., Giordano, M. C. & Buatier de Mongeot, F. Wavelength-Dependent Plasmonic Photobleaching of Dye Molecules by Large-Area Au Nanostripe Arrays. *ACS Appl. Nano Mater.* **5**, 3470–3479 (2022).
180. Patil, K., Pawar, R. & Talap, P. Self-aggregation of Methylene Blue in aqueous medium and aqueous solutions of Bu 4 NBr and urea. *Physical Chemistry Chemical Physics* **2**, 4313–4317 (2000).
181. Ozdemir, F. A., Demirata, B. & Apak, R. Adsorptive removal of methylene blue from simulated dyeing wastewater with melamine-formaldehyde-urea resin. *Journal of Applied Polymer Science* **112**, 3442–3448 (2009).
182. Qin, C. *et al.* Observation of Hole Transfer in MoS $_2$ /WS $_2$ Van der Waals Heterostructures. *ACS Photonics* **9**, 1709–1716 (2022).
183. Song, S. *et al.* Rapid thermal annealing of ITO films. *Applied Surface Science* **257**, 7061–7064 (2011).
184. Ali, A. I., Ibrahim, M. & Hassen, A. New fabrication method for di-indium tri-sulfuric (In2S3) thin films. *Sci Rep* **12**, 7033 (2022).
185. Spasevska, H., Kitts, C. C., Ancora, C. & Ruani, G. Optimised In $_2$ S $_3$ Thin Films Deposited by Spray Pyrolysis. *International Journal of Photoenergy* **2012**, 1–7 (2012).
186. Raj Mohamed, J. & Amalraj, L. Effect of precursor concentration on physical properties of nebulized spray deposited In $_2$ S $_3$ thin films. *Journal of Asian Ceramic Societies* **4**, 357–366 (2016).
187. Surucu, O., Isik, M., Terlemezoglu, M., Gasanly, N. M. & Parlak, M. Structural and temperature-tuned bandgap characteristics of thermally evaporated β-In2S3 thin films. *J Mater Sci: Mater Electron* **32**, 15851–15856 (2021).
188. Chen, J.-H., Jang, C., Xiao, S., Ishigami, M. & Fuhrer, M. S. Intrinsic and extrinsic performance limits of graphene devices on SiO2. *Nature Nanotech* **3**, 206–209 (2008).
189. Nair, R. R. *et al.* Fine Structure Constant Defines Visual Transparency of Graphene. *Science* **320**, 1308–1308 (2008).
190. Reina, A. *et al.* Transferring and Identification of Single- and Few-Layer Graphene on Arbitrary Substrates. *J. Phys. Chem. C* **112**, 17741–17744 (2008).
191. Wu, J.-B., Lin, M.-L., Cong, X., Liu, H.-N. & Tan, P.-H. Raman spectroscopy of graphene-based materials and its applications in related devices. *Chem. Soc. Rev.* **47**, 1822–1873 (2018).

192. Ferrari, A. C. Raman spectroscopy of graphene and graphite: Disorder, electron–phonon coupling, doping and nonadiabatic effects. *Solid State Communications* **143**, 47–57 (2007).
193. Kang, Z. *et al.* MXene-Silicon Van Der Waals Heterostructures for High-Speed Self-Driven Photodetectors. *Adv. Electron. Mater.* **3**, 1700165 (2017).
194. Huo, N. *et al.* Novel and Enhanced Optoelectronic Performances of Multilayer MoS_2-WS_2 Heterostructure Transistors. *Adv. Funct. Mater.* **24**, 7025–7031 (2014).
195. Qi, T. *et al.* Interlayer Transition in a vdW Heterostructure toward Ultrahigh Detectivity Shortwave Infrared Photodetectors. *Adv. Funct. Mater.* **30**, 1905687 (2020).
196. Chen, Y. *et al.* Unipolar barrier photodetectors based on van der Waals heterostructures. *Nat Electron* **4**, 357–363 (2021).
197. Li, Q., Zhang, N., Yang, Y., Wang, G. & Ng, D. H. L. High Efficiency Photocatalysis for Pollutant Degradation with MoS_2/C_3N_4 Heterostructures. *Langmuir* **30**, 8965–8972 (2014).
198. Wang, Y., Ding, Z., Arif, N., Jiang, W.-C. & Zeng, Y.-J. 2D material based heterostructures for solar light driven photocatalytic H_2 production. *Mater. Adv.* **3**, 3389–3417 (2022).
199. Zhu, K. *et al.* The development of integrated circuits based on two-dimensional materials. *Nat Electron* **4**, 775–785 (2021).
200. Zhang, W. *et al.* Ultrahigh-Gain Photodetectors Based on Atomically Thin Graphene-MoS2 Heterostructures. *Sci Rep* **4**, 3826 (2014).
201. Wan, X. *et al.* Controlled Electrochemical Deposition of Large-Area MoS_2 on Graphene for High-Responsivity Photodetectors. *Adv. Funct. Mater.* **27**, 1603998 (2017).
202. Lineykin, S., Averbukh, M. & Kuperman, A. An improved approach to extract the single-diode equivalent circuit parameters of a photovoltaic cell/panel. *Renewable and Sustainable Energy Reviews* **30**, 282–289 (2014).
203. Kim, J. S. *et al.* Characterisation of the properties of surface-treated indium-tin oxide thin films. *Synthetic Metals* **101**, 111–112 (1999).
204. Gu, Y. *et al.* Sulfurization Engineering of One-Step Low-Temperature MoS_2 and WS_2 Thin Films for Memristor Device Applications. *Adv Elect Materials* **8**, 2100515 (2022).
205. Fabbri, F. *et al.* Novel near-infrared emission from crystal defects in MoS2 multilayer flakes. *Nat Commun* **7**, 13044 (2016).
206. Liu, H. *et al.* High-harmonic generation from an atomically thin semiconductor. *Nature Phys* **13**, 262–265 (2017).
207. Chhowalla, M. *et al.* The chemistry of two-dimensional layered transition metal dichalcogenide nanosheets. *Nature Chem* **5**, 263–275 (2013).
208. Arnold, A. J. *et al.* Mimicking Neurotransmitter Release in Chemical Synapses *via* Hysteresis Engineering in MoS_2 Transistors. *ACS Nano* **11**, 3110–3118 (2017).
209. Purcell-Milton, F. *et al.* Induction of Chirality in Two-Dimensional Nanomaterials: Chiral 2D MoS_2 Nanostructures. *ACS Nano* **12**, 954–964 (2018).
210. Yu, Y. *et al.* Equally Efficient Interlayer Exciton Relaxation and Improved Absorption in Epitaxial and Nonepitaxial MoS_2/WS_2 Heterostructures. *Nano Lett.* **15**, 486–491 (2015).
211. Deng, D. *et al.* Catalysis with two-dimensional materials and their heterostructures. *Nature Nanotech* **11**, 218–230 (2016).
212. Huo, N. & Konstantatos, G. Recent Progress and Future Prospects of 2D-Based Photodetectors. *Adv. Mater.* **30**, 1801164 (2018).

213. Toth, M. & Aharonovich, I. Single Photon Sources in Atomically Thin Materials. *Annu. Rev. Phys. Chem.* **70**, 123–142 (2019).

214. Mahyavanshi, R. D., Desai, P., Ranade, A., Tanemura, M. & Kalita, G. Observing Charge Transfer Interaction in CuI and MoS $_2$ Heterojunction for Photoresponsive Device Application. *ACS Applied Electronic Materials* **1**, 302–310 (2019).

215. Wang, Q. H., Kalantar-Zadeh, K., Kis, A., Coleman, J. N. & Strano, M. S. Electronics and optoelectronics of two-dimensional transition metal dichalcogenides. *Nature Nanotech* **7**, 699–712 (2012).

216. Matković, A. *et al.* 2D Semiconductors: Interfacial Band Engineering of MoS $_2$ /Gold Interfaces Using Pyrimidine-Containing Self-Assembled Monolayers: Toward Contact-Resistance-Free Bottom-Contacts (Adv. Electron. Mater. 5/2020). *Advanced Electronic Materials* **6**, 2070026 (2020).

217. Schaibley, J. R. *et al.* Valleytronics in 2D materials. *Nat Rev Mater* **1**, 16055 (2016).

218. Cortés, N., Ávalos-Ovando, O., Rosales, L., Orellana, P. A. & Ulloa, S. E. Tunable Spin-Polarized Edge Currents in Proximitized Transition Metal Dichalcogenides. *Phys. Rev. Lett.* **122**, 086401 (2019).

219. Voiry, D., Yang, J. & Chhowalla, M. Recent Strategies for Improving the Catalytic Activity of 2D TMD Nanosheets Toward the Hydrogen Evolution Reaction. *Adv. Mater.* **28**, 6197–6206 (2016).

220. Krasnok, A., Lepeshov, S. & Alú, A. Nanophotonics with 2D transition metal dichalcogenides [Invited]. *Opt. Express* **26**, 15972 (2018).

221. Luo, Z. *et al.* Two-dimensional material-based saturable absorbers: towards compact visible-wavelength all-fiber pulsed lasers. *Nanoscale* **8**, 1066–1072 (2016).

222. Wang, G., Baker-Murray, A. A. & Blau, W. J. Saturable Absorption in 2D Nanomaterials and Related Photonic Devices. *Laser & Photonics Reviews* **13**, 1800282 (2019).

223. Zhang, S. *et al.* Direct Observation of Degenerate Two-Photon Absorption and Its Saturation in WS $_2$ and MoS $_2$ Monolayer and Few-Layer Films. *ACS Nano* **9**, 7142–7150 (2015).

224. Dai, X. *et al.* Enhanced two-photon absorption and two-photon luminescence in monolayer MoS $_2$ and WS $_2$ by defect repairing. *Opt. Express* **27**, 13744 (2019).

225. Lin, K.-I. *et al.* Atom-Dependent Edge-Enhanced Second-Harmonic Generation on MoS $_2$ Monolayers. *Nano Lett.* **18**, 793–797 (2018).

226. Lin, X. *et al.* Two-Dimensional Pyramid-like WS $_2$ Layered Structures for Highly Efficient Edge Second-Harmonic Generation. *ACS Nano* **12**, 689–696 (2018).

227. Zhang, J. *et al.* Enhanced second and third harmonic generations of vertical and planar spiral MoS $_2$ nanosheets. *Nanotechnology* **28**, 295301 (2017).

228. Autere, A. *et al.* Optical harmonic generation in monolayer group-VI transition metal dichalcogenides. *Phys. Rev. B* **98**, 115426 (2018).

229. Bernardi, M., Palummo, M. & Grossman, J. C. Extraordinary Sunlight Absorption and One Nanometer Thick Photovoltaics Using Two-Dimensional Monolayer Materials. *Nano Lett.* **13**, 3664–3670 (2013).

230. Ferrando, G. *et al.* Flat-optics hybrid MoS $_2$ /polymer films for photochemical conversion. *Nanoscale* **15**, 1953–1961 (2023).

231. Lu, C. & Lipson, R. H. Interference lithography: a powerful tool for fabricating periodic structures: Interference lithography. *Laser & Photon. Rev.* **4**, 568–580 (2010).

232. Seo, J.-H. *et al.* Nanopatterning by Laser Interference Lithography: Applications to Optical Devices. *j. nanosci. nanotech.* **14**, 1521–1532 (2014).

233. Ellman, M. *et al.* High-power laser interference lithography process on photoresist: Effect of laser fluence and polarisation. *Applied Surface Science* **255**, 5537–5541 (2009).

234. Xie, Q. *et al.* Fabrication of nanostructures with laser interference lithography. *Journal of Alloys and Compounds* **449**, 261–264 (2008).

235. Fattal, D., Li, J., Peng, Z., Fiorentino, M. & Beausoleil, R. G. Flat dielectric grating reflectors with focusing abilities. *Nature Photon* **4**, 466–470 (2010).

236. Khorasaninejad, M. & Capasso, F. Broadband Multifunctional Efficient Meta-Gratings Based on Dielectric Waveguide Phase Shifters. *Nano Lett.* **15**, 6709–6715 (2015).

237. Chang-Hasnain, C. J. & Yang, W. High-contrast gratings for integrated optoelectronics. *Adv. Opt. Photon.* **4**, 379 (2012).

238. Giordano, M. C. & de Mongeot, F. B. Anisotropic Nanoscale Wrinkling in Solid-State Substrates. *Advanced Materials* **30**, 1801840 (2018).

239. Quaranta, G., Basset, G., Martin, O. J. F. & Gallinet, B. Recent Advances in Resonant Waveguide Gratings. *Laser & Photonics Reviews* **12**, 1800017 (2018).

240. Zhou, W. *et al.* Extraordinary optical absorption based on guided-mode resonance. *Opt. Lett.* **38**, 5393 (2013).

241. Dumcenco, D. *et al.* Large-Area Epitaxial Monolayer MoS $_2$. *ACS Nano* **9**, 4611–4620 (2015).

242. Hung, Y.-H. *et al.* Scalable Patterning of MoS $_2$ Nanoribbons by Micromolding in Capillaries. *ACS Appl. Mater. Interfaces* **8**, 20993–21001 (2016).

243. Qi, R. *et al.* Towards well-defined MoS $_2$ nanoribbons on a large scale. *Chem. Commun.* **53**, 9757–9760 (2017).

244. Martella, C. *et al.* Large-area patterning of substrate-conformal MoS2 nano-trenches. *Nano Res.* **12**, 1851–1854 (2019).

245. Camellini, A. *et al.* Ultrafast Anisotropic Exciton Dynamics in Nanopatterned MoS $_2$ Sheets. *ACS Photonics* **5**, 3363–3371 (2018).

246. Kuo, W.-K., Hsu, J.-J., Nien, C.-K. & Yu, H. H. Moth-Eye-Inspired Biophotonic Surfaces with Antireflective and Hydrophobic Characteristics. *ACS Applied Materials & Interfaces* **8**, 32021–32030 (2016).

247. Mennucci, C. *et al.* Broadband light trapping in nanotextured thin film photovoltaic devices. *Applied Surface Science* **446**, 74–82 (2018).

248. Ji, S., Song, K., Nguyen, T. B., Kim, N. & Lim, H. Optimal Moth Eye Nanostructure Array on Transparent Glass Towards Broadband Antireflection. *ACS Appl. Mater. Interfaces* **5**, 10731–10737 (2013).

249. Mueller, T. & Malic, E. Exciton physics and device application of two-dimensional transition metal dichalcogenide semiconductors. *npj 2D Mater Appl* **2**, 29 (2018).

250. Wang, S. S., Moharam, M. G., Magnusson, R. & Bagby, J. S. Guided-mode resonances in planar dielectric-layer diffraction gratings. *J. Opt. Soc. Am. A* **7**, 1470 (1990).

251. Mazulquim, D. B. *et al.* Efficient band-pass color filters enabled by resonant modes and plasmons near the Rayleigh anomaly. *Opt. Express* **22**, 30843 (2014).

252. Ahmadi, M. *et al.* 2D transition metal dichalcogenide nanomaterials: advances, opportunities, and challenges in multi-functional polymer nanocomposites. *Journal of Materials Chemistry A* **8**, 845–883 (2020).

253. Kundu, S. & Patra, A. Nanoscale Strategies for Light Harvesting. *Chemical Reviews* **117**, 712–757 (2017).

254. Chang, K. *et al.* MoS 2 /Graphene Cocatalyst for Efficient Photocatalytic H 2 Evolution under Visible Light Irradiation. *ACS Nano* **8**, 7078–7087 (2014).
255. Merki, D. & Hu, X. Recent developments of molybdenum and tungsten sulfides as hydrogen evolution catalysts. *Energy & Environmental Science* **4**, 3878 (2011).
256. Gao, Y., Chen, C., Tan, X., Xu, H. & Zhu, K. Polyaniline-modified 3D-flower-like molybdenum disulfide composite for efficient adsorption/photocatalytic reduction of Cr(VI). *Journal of Colloid and Interface Science* **476**, 62–70 (2016).
257. Wu, M. *et al.* Fabrication of ternary GO/g-C3N4/MoS2 flower-like heterojunctions with enhanced photocatalytic activity for water remediation. *Applied Catalysis B: Environmental* **228**, 103–112 (2018).
258. Yim, C. *et al.* Investigation of the optical properties of MoS 2 thin films using spectroscopic ellipsometry. *Applied Physics Letters* **104**, 103114 (2014).
259. He, Z. & Que, W. Molybdenum disulfide nanomaterials: Structures, properties, synthesis and recent progress on hydrogen evolution reaction. *Applied Materials Today* **3**, 23–56 (2016).
260. Castellanos-Gomez, A., Quereda, J., Van Der Meulen, H. P., Agraït, N. & Rubio-Bollinger, G. Spatially resolved optical absorption spectroscopy of single- and few-layer MoS2 by hyperspectral imaging. *Nanotechnology* **27**, 0 (2016).
261. Verre, R. *et al.* Transition metal dichalcogenide nanodisks as high-index dielectric Mie nanoresonators. *Nat. Nanotechnol.* **14**, 679–683 (2019).
262. Bradley, R. M. & Harper, J. M. E. Theory of ripple topography induced by ion bombardment. *Journal of Vacuum Science & Technology A* **6**, 2390–2395 (1988).
263. Valbusa, U., Boragno, C. & Mongeot, F. B. D. Nanostructuring surfaces by ion sputtering. *J. Phys.: Condens. Matter* **14**, 8153–8175 (2002).
264. Chan, W. L. & Chason, E. Making waves: Kinetic processes controlling surface evolution during low energy ion sputtering. *Journal of Applied Physics* **101**, 121301 (2007).
265. Keller, A., Facsko, S. & Möller, W. The morphology of amorphous SiO_2 surfaces during low energy ion sputtering. *J. Phys.: Condens. Matter* **21**, 495305 (2009).
266. Pachmajer, S., Werzer, O., Mennucci, C., Buatier De Mongeot, F. & Resel, R. Biaxial growth of pentacene on rippled silica surfaces studied by rotating grazing incidence X-ray diffraction. *Journal of Crystal Growth* **519**, 69–76 (2019).
267. Belardini, A. *et al.* Tailored second harmonic generation from self-organized metal nano-wires arrays. *Opt. Express* **17**, 3603 (2009).
268. Barelli, M., Mazzanti, A., Giordano, M. C., Della Valle, G. & Buatier De Mongeot, F. Color Routing via Cross-Polarized Detuned Plasmonic Nanoantennas in Large-Area Metasurfaces. *Nano Lett.* **20**, 4121–4128 (2020).
269. Huang, X. *et al.* Fabry-Perot cavity enhanced light-matter interactions in two-dimensional van der Waals heterostructure. *Nano Energy* **62**, 667–673 (2019).
270. Song, B. *et al.* Layer-Dependent Dielectric Function of Wafer-Scale 2D MoS_2. *Advanced Optical Materials* **7**, 1801250 (2019).
271. Li, H. *et al.* From Bulk to Monolayer MoS2: Evolution of Raman Scattering. *Adv. Funct. Mater.* **22**, 1385–1390 (2012).
272. Berkdemir, A. *et al.* Identification of individual and few layers of WS2 using Raman Spectroscopy. *Sci Rep* **3**, 1755 (2013).
273. Vega-Mayoral, V. *et al.* Exciton and charge carrier dynamics in few-layer WS_2. *Nanoscale* **8**, 5428–5434 (2016).
274. Bhatnagar, M. *et al.* Ultra-broadband photon harvesting in large-area few-layer MoS_2 nanostripe gratings. *Nanoscale* **12**, 24385–24393 (2020).